Institut für Physik und Astronomie

Astrophysik II

A study of the absorption characteristics of gaseous galaxy halos in the local Universe

Dissertation

zur Erlangung des akademischen Grades

"doctor rerum naturalium"

(Dr. rer. nat.)

in der Wissenschaftsdisziplin "Astrophysik"

eingereicht an der
Mathematisch-Naturwissenschaftlichen Fakultät
der Universität Potsdam
von

Peter Herenz

Potsdam, den 8. Januar 2014

Published online at the
Institutional Repository of the University of Potsdam:
URL http://opus.kobv.de/ubp/volltexte/2014/7051/
URN urn:nbn:de:kobv:517-opus-70513
http://nbn-resolving.de/urn:nbn:de:kobv:517-opus-70513

"The important thing is not to stop questioning. Curiosity has its own reason for existing. One cannot help but be in awe when he contemplates the mysteries of eternity, of life, of the marvelous structure of reality. It is enough if one tries merely to comprehend a little of this mystery every day. Never lose a holy curiosity."

Albert Einstein

Abstract

Today, it is well known that galaxies like the Milky Way consist not only of stars but also of gas and dust. The galactic halo, a sphere of gas that surrounds the stellar disk of a galaxy, is especially interesting. It provides a wealth of information about in and outflowing gaseous material towards and away from galaxies and their hierarchical evolution. For the Milky Way, the so-called high-velocity clouds (HVCs), fast moving neutral gas complexes in the halo that can be traced by absorption-line measurements, are believed to play a crucial role in the overall matter cycle in our Galaxy. Over the last decades, the properties of these halo structures and their connection to the local circumgalactic and intergalactic medium (CGM and IGM, respectively) have been investigated in great detail by many different groups. So far it remains unclear, however, to what extent the results of these studies can be transferred to other galaxies in the local Universe.

In this thesis, we study the absorption properties of Galactic HVCs and compare the HVC absorption characteristics with those of intervening QSO absorption-line systems at low redshift. The goal of this project is to improve our understanding of the spatial extent and physical conditions of gaseous galaxy halos in the local Universe.

In the first part of the thesis we use *HST*/STIS ultraviolet spectra of more than 40 extragalactic background sources to statistically analyze the absorption properties of the HVCs in the Galactic halo. We determine fundamental absorption line parameters including covering fractions of different weakly/intermediately/highly ionized metals with a particular focus on Si II and Mg II. Due to the similarity in the ionization properties of Si II and Mg II, we are able to estimate the contribution of HVC-like halo structures to the cross section of intervening strong Mg II absorbers at $z = 0$. Our study implies that only the most massive HVCs would be regarded as strong Mg II absorbers, if the Milky Way halo would be seen as a QSO absorption line system from an exterior vantage point. Combining the observed absorption-cross section of Galactic HVCs with the well-known number density of intervening strong Mg II absorbers at $z = 0$, we conclude that the contribution of infalling gas clouds (i.e., HVC analogs) in the halos of Milky Way-type galaxies to the cross section of strong Mg II absorbers is 34%. This result indicates that only about one third of the strong Mg II absorption can be associated with HVC analogs around other galaxies, while the majority of the strong Mg II systems possibly is related to galaxy outflows and winds.

The second part of this thesis focuses on the properties of intervening metal absorbers at low redshift. The analysis of the frequency and physical conditions of intervening metal systems in QSO spectra and their relation to nearby galaxies offers new insights into the typical conditions of gaseous galaxy halos. One major aspect in our study was to regard intervening metal systems as possible HVC analogs. We perform a detailed analysis of absorption line properties and line statistics for 57 metal absorbers along 78 QSO sightlines using newly-obtained ultraviolet spectra obtained with *HST*/COS. We find clear evidence for bimodal distribution in the H I column density in the absorbers, a trend that we interpret as sign for two different classes of absorption systems (with HVC analogs at the high-column density end). With the help of the strong transitions of Si II λ1260, Si III λ1206, and C III λ977 we have set up Cloudy photoionization models to estimate the local ionization conditions, gas densities, and metallicities. We find that the intervening absorption systems studied by us have, on average, similar physical conditions as Galactic HVC absorbers, providing evidence that many of them represent HVC analogs in the vicinity of other galaxies. We therefore determine typical halo sizes for Si II, Si III, and C III for $L = 0.01L^*$ and $L = 0.05L^*$ galaxies. Based on the covering fractions of the different ions in the Galactic halo, we find that, for example, the typical halo size for Si III is $\sim$160 kpc for $L = 0.05L^*$ galaxies. We test the plausibility of this result by searching for known galaxies close to the QSO sightlines and at similar redshifts as the absorbers. We find that more than 34% of the measured Si III absorbers have galaxies associated with them, with the majority of the absorbers indeed being at impact parameters $\rho \leq$160 kpc.

In summary, our study provides important new information about the absorption properties of gaseous strucures in the halo and circumgalactic environment of the Milky Way and other galaxies in the local Universe. Combining information on the Milky Way HVCs and intervening metal absorbers we conclude that circumgalactic metal absorption in low and intermediate ions typically arises within the virial radius of low-z galaxies. The absorber properties reflect a complex distribution of multi-phase gas around galaxies being a result of the on-going formation and evolution of galaxies.

Zusammenfassung

Galaxien bestehen nicht nur aus Sternen, sondern zum größten Teil auch aus interstellarem Gas und Staub. Der gasförmige Halo von Galaxien, welcher die stellare Scheibe umgibt, ist dabei von besonderem Interesse für die Astrophysik, denn hier finden sich viele Hinweise auf den Zustrom und den Ausfluss gasförmigen Materials von Galaxien; Prozesse, die die Entwicklung von Galaxien massgeblich mitbestimmen. Für die Erforschung des Materiekreislaufs der Milchstraße sind inbesondere die sogenannten Hochgeschwindigkeitswolken (HVCs) von Bedeutung. Diese Halo-Wolken lassen sich besonders gut mit Hilfe von Quasar-Absorptionsspektren analysieren. In den vergangenen Jahren konnten eine Vielzahl von Studien unser Verständnis dieser Wolken und ihrer morphologische Verbindung zum zirkumgalaktischen und intergalaktischen Medium (CGM und IGM) erweitern. Unklar bleibt jedoch, in welcher Weise sich die Resultate dieser Studien auch auf *andere* Galaxien übertragen lassen.

In dieser Arbeit untersuchen wir die Absorptions-Characteristika Galaktischer HVCs und vergleichen diese mit den Eigenschaften intergalaktischer Absorptionssysteme bei niedriger Rotverschiebung. Ziel des Projektes ist es, neue Erkenntnisse über die räumliche Ausdehnung gasförmiger Galaxienhalos und dere physikalische Eigenschaften zu erlangen.

Im ersten Teil der Arbeit verwenden wir *HST*/STIS Spektren von mehr als 40 extragalaktischen Hintergrundquellen, um die Absorptionscharakteristika der HVCs im Galaktischen Halo statistisch zu untersuchen. Dafür bestimmen wir fundamentale Absorptionsparameter, u.a. den Bedeckungsanteil verschiedener niedrig/mittel/hochionisierter Metalle unter spezieller Berücksichtigung der Ionen Si II und Mg II. Wegen der Ähnlichkeit der Ionisationseigenschaften von Si II und Mg II ist es möglich, den Beitrag von HVCs zum Absorptionsquerschnitt von intergalaktischen Mg II Absorptionssystemen bei $z = 0$ zu bestimmen. Es stellt sich heraus, dass nur die HVCs mit der größten Masse als sog. starke Mg II Systeme auftreten würden, wenn man den Milchstraßen-Halo als ein Absorptionssystem von einem äußeren Standpunkt aus betrachten würde. Aus der Kombination der ermittelten Absorptionsquerschnitte der Galaktischen HVCs mit der wohl-bekannten Anzahldichte von intergalaktischen Metall-Absorptionssystemen bei $z = 0$ leiten wir ab, daß der Anteil von einfallenden Gaswolken (HVC-Analoga) in den Halos anderer (Milchstraßen-ähnlicher) Galaxien zum Absorptionsquerschnitt von starken Mg II Absorptionssystemen weniger als 34% beträgt. Anscheinend stellen HVCs also nur weniger als ein Drittel der Population starker Mg II Systeme, während der überwiegende Anteil vermutlich durch galaktische Winde und andere gasförmige Ausflüsse von Galaxien erzeugt wird.

Der zweite Teil dieser Arbeit widmet sich den Eigenschaften von Metall-Absorptionssystemen bei niedriger Rotverschiebung. Untersuchungen der Häufigkeit und physikalischen Eigenschaften solcher Absorptionssysteme in Quasarspektren und des Zusammenhangs zwischen Absorptionssystemen und Galaxien sind für unser Verständnis gasförmiger Galaxienhalos von zentraler Bedeutung. Ein Kernaspekt unserer Untersuchungen war daher der mögliche Zusammenhang zwischen HVCs und intergalaktischen Absorptionssystemen. Dazu wurden insgesamt 57 Metall-Absorptionssysteme in 78 Quasarspektren basierend auf Daten von *HST*/COS statistisch untersucht. Wir finden eine signifikante zweikomponentige Struktur in der Säulendichteverteilung von neutralem Wasserstoff in den Absorptionssystemen. Diese Bimodalität interpretieren wir durch die Existenz zweier verschiedener Populationen von Absorptionssystemen, wobei die HVC-ähnlichen Systeme am oberen Ende der Säulendichteverteilung anzusiedeln sind. Mit Hilfe der starken Linienübergänge von Si II λ1260, Si III λ1206 und C III λ977 wurden anschließend Photoionisationsmodelle für die Bestimmung der lokalen Ionisationsbedingungen, der Gasdichten und der Metallizitäten gerechnet. Es stellt sich heraus, dass die physikalischen Bedingungen in diesen (ausgewählten) Absorptionssystemen denen der Galaktischen HVCs im Mittel sehr ähnlich sind, was auf einen morphologischen Zusammenhang zwischen beiden Gruppen hindeutet. Diese Ergebnisse können nun genutzt werden, um den typischen Haloradius von Si II, Si III und C III für $L = 0.01L^*$ und $L = 0.05L^*$ Galaxien zu bestimmen. Basierend auf den Galaktischen Bedeckungsanteilen der verschiedenen Ionen errechnen wir zum Beispiel für Si III und $L = 0.05L^*$ Galaxien eine charakteristischen Haloradius von ~ 160 kpc. Wir testen die Plausibilität dieser Ergebnisse mittels einer direkten Suche von Galaxien in der unmittelbaren Nähe der Sichtlinien bei gleicher Rotverschiebung wie die Absorptionssysteme. Für etwa 34% der gemessenen Si III Absorptionssysteme konnten Galaxien in der umittelbaren Nähe zur Sichtlinie identifiziert werden, wobei die Mehrzahl dieser Galaxien in der Tat innerhalb von 160 kpc von den Absorptionssystemen liegen.

Insgesamt ergeben sich aus unserer Studie ein Vielzahl von neuen Erkenntnissen über die Absorptionseigenschaften gasförmiger Strukturen in den Halos von Galaxien im lokalen Universum. Die Kombination von Informationen zu den Galaktischen HVCs und intergalaktischen Absorptionssystemen impliziert,

dass die Absorption von nierigen und mittleren Metallionen in solchen Systemen aus Gas stammt, welches sich überwiegend innerhalb der Virialradius von Galaxien befindet. Die Eigenschaften der Absorptionssysteme weisen ferner auf eine komplexe räumliche Verteilung eines Multi- Phasen-Gases im Halo von Galaxien hin, welche sich auf die anhaltende dynamische Entwicklung von Galaxien bei $z = 0$ zurückführen lässt.

Contents

List of Tables

List of Figures

Chapter 1

Introduction

1.1 The Universe – as we see it today

From the time when the first humans looked at the stars and recognized that the moon and the sun were no natural miracles until todays astronomical state of arts, a tremendous amount of progress and knowledge has been achieved. Over the first few thousand years all available astronomical information was limited by the physical possibilities of the human eye. But even with this very insensitive instrument, compared with todays telescopes, many remarkable developments have been made (e.g., calendar, seafaring, agriculture).
The beginning of the 17th century can be claimed as the beginning of modern astronomy. World-famous academics like Johannes Kepler and Isaac Newton discovered new natural laws which are, with little confinements, still valid today, and can be found in almost all basic physics books (Kepler 1609; Newton 1722). With the help of the newly invented telescopes by Galileo Galilei a whole new world filled with planets, stars, and galaxies has been discovered (e.g., Galilei et al. 1663). These new optical instruments enabled scientists to prove the new astronomical laws which again leads to new insights and even change the whole view of the world. With the telescopes becoming larger and more sensitive over the next centuries, new planets were discovered (Neptune 1612, Uranus 1781). Even new astronomical objects like planetary nebulae and stellar clusters were integrated in the developing picture of the Universe (Herschel 1815).
For the current theories of the Universe the beginning of the 20th century was essential. Since Edwin Hubble discovered that other galaxies are not part of our own Milky Way but instead own objects with hundreds of millions of stars, and that they are moving away from our home galaxy, well-known terms like the Big Bang, redshift or the expansion of the Universe became part of the vocabulary of the astronomers and the picture of a static straightforward Universe had to be changed again (Hubble 1929). After the invention of the first spectrographs, Johannes Franz Hartmann discovered the first evidence of interstellar material during his work on the spectra of the δ Orionis star (Hartmann 1904).
Since these days, we know that stars and galaxies are neither the only nor the most frequent form of matter in the Universe. Instead, the space between luminous objects is filled with a very thin (~ 1 particle/m^3), but usually very hot gas or plasma (e.g. Stocke et al. 2004; Richter et al. 2006). Due to the enormous volume filled by this interstellar and intergalactic medium (ISM/IGM) some surveys suppose that, for the low-redshift Universe, it might account for up to 70 % of the overall baryonic matter content and its contribution was even higher in the earlier stages of the Universe (e.g. Danforth 2009; Shull et al. 2012a). However, this material is not evenly distributed but instead it forms a filamentary structure between the galaxies and galaxy clusters. Such filaments have been detected partly with large sky surveys (e.g., the Sloan Digital Sky Survey, SDSS) and could be reproduced in complex simulations by different groups over the last decades (see Figure 1.1, e.g., Springel et al. 2006). The model behind these simulations is the so-called standard model of cosmology or Lambda Cold Dark Matter model (ΛCDM model, see Section 2.1). It describes the evolution of the Universe beginning with the Big Bang, evolving through the Dark Ages and the Reionization Epoch until todays structure formation. One of the main predictions is a hierarchical evolution of large scale structures which should lead to a filamentary matter distribution. As shown in Figure 1.1 the predictions of the ΛCDM model are in very good agreement with observations.
In this work, we focus on the gaseous component of the Universe. This matter can only be detected by the absence of light (with some exceptions like the H I 21 cm or the Hα emission line). The intervening matter absorbs the light of bright background sources (e.g., quasars) and can be detected in their spectra. The examination of these spectra is called quasars absorption line spectroscopy (QSO spectroscopy). These quasars and their fainter and younger equivalents, the Seyfert galaxies, are only two candidates of the group of objects called active galactic nuclei (AGNs). Located at high distances

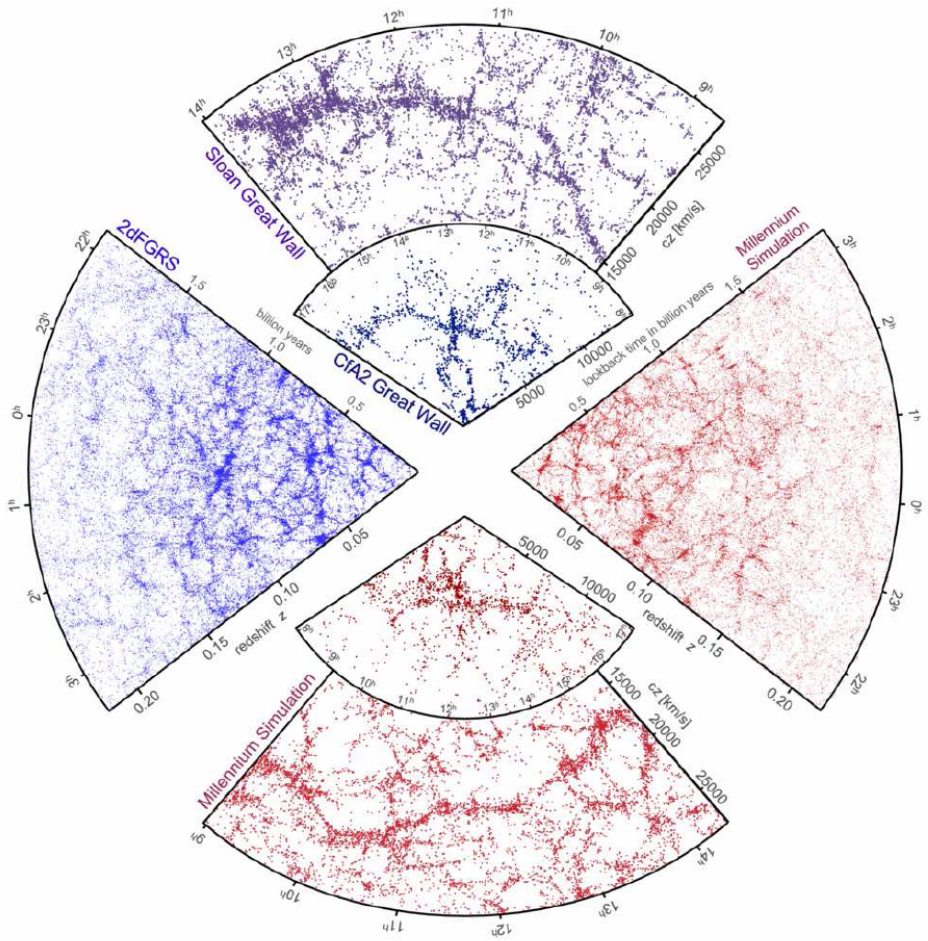

Figure 1.1: Comparison between observations (Sloan Digital Sky Survey, or SDSS and the 2-degree Field Galaxy Redshift Survey, or 2dFGRS) and simulations of the large scale structure of the Universe. The small highlighted wedges in the center show the Center for Astrophysics (CfA) galaxy redshift survey produced in the 1980s (Springel et al. 2006).

up to redshifts $z > 7$ (Mortlock et al. 2011), these galaxies have an extremely bright inner core. It is supposed that a central supermassive black hole accretes the surrounding material which then starts to radiate because of the conservation of angular momentum and of resulting non-thermal processes like friction. These processes produce a rather smooth continuum over a wide wavelength range.
Depending on the distance, the composition, and the physical properties of the intervening material along the sightline towards the quasar, different absorption patterns with a certain shape appear in the spectrum. These absorption lines allow detailed studies of the gas properties of the interstellar and intergalactic medium and have been analyzed extensively over the last decades (e.g., Wakker 1991; Tripp et al. 2004; Stocke et al. 2004; Richter et al. 2006; Danforth 2009; Oppenheimer et al. 2012, and many others). From these investigations we know that, for instance, the baryon content of the IGM has changed over time and that a large portion of ~ 30 % is still missing or undetected in the low-z Universe (see also Figure 1.7).
The study of the IGM is closely connected to the study of the formation and evolution of galaxies. Apart from neutral hydrogen, metals, which can only be produced in galaxies, can be used to probe infalling, outflowing and recycling processes (e.g., winds, starbursts, shocks etc.) of the gaseous material in nearby galaxies. Therefore, metal enrichment can deliver key information for the comprehension of the global galactic formation and evolution.
This is especially interesting for the Milky Way. Due to the relative small distances and our unique position inside this galaxy, we have the possibility to probe the gas distribution in the Galactic halo in many different directions in great detail and high resolution. This allows us, for instance, to identify structures like the so-called high velocity clouds (HVCs) which exhibit a variety of different physical parameters like metallicity, velocity or distance, and which spread over a huge portion of the sky. Despite the fact that they have been studied extensively over the last years, there are still many open questions.

Table 1.1: Main phases of the ISM and their properties.

Component	f_V	T [K]	$n_{\rm H}$ [cm^{-3}]	Formation Process	Detection method
Coronal gas	0.5	$> 10^{5.5}$	~ 0.004	shocks, collisional ionization	UV, X-ray and synchrotron emission
H II gas	0.1	10^4	0.3 - 10^4	Photoionization	line emission
Warm neutral medium	0.4	~ 5000	0.6	Photoionization	H I 21 cm emission, absorption lines
Cool neutral medium	0.01	~ 100	30	Photoionization	H I 21 cm emission, absorption lines
Diffuse H_2	0.001	~ 50	~ 100	Photoionization	H I 21 cm emission, CO 2.6 mm emission, absorption lines
Dense H_2	10^{-4}	10 - 50	10^3 - 10^6	heated by photoelectrons, cosmic rays, self-gravitating	CO 2.6 mm emission, dust FIR emission

f_V: volume filling factor

The most important ones refer to their origin, their composition, or their contribution to the total gas accretion rate or the cross section of the Milky Way (e.g., Fox et al. 2006; Ben Bekhti et al. 2008; Collins et al. 2009; Richter et al. 2009, and many others). Furthermore, it is not clear whether these objects are only restricted to the Milky Way or represent a common feature of Milky Way-type galaxies. Recent studies have shown that gaseous halo structures, which can represent HVC analogs, are also detected around other galaxies (see Section 1.3). Thus, it is essential to improve our knowledge about the gas distribution and the metal content of the gas around and between galaxies to improve the picture of the galaxies and the evolving Universe in general.

1.2 The Interstellar Medium

Because the inner parts of the ISM are not the main interest of this thesis, only the most important properties and concepts are explained briefly. The different gas phases (in terms of temperature and density) in the halo of the Milky Way, with special focus on HVCs, are discussed in more detail in Subsection 1.3.

The ISM contains all matter between the stars in galaxies. The amount of material bound in this phase strongly depends on the age of a galaxy and its star-forming rate (e.g., Schruba 2013). Due to processes like ejections by galactic winds and infalling matter from the IGM, the ISM content is not constant but will evolve over time.

The ISM is basically composed of three main phases: a non-relativistic gas phase with its ions and molecules, the dust phase with small particles ($\lesssim 1\mu$m), and the dark matter with its unknown properties. Other constituents like cosmic rays, electromagnetic radiation and magnetic fields are also part of the ISM, but will not be discussed here. All of these phases have different physical properties spanning a wide range in terms of temperature, density and composition. Following Draine (2010), we summarize the subcomponents of the ISM gas phases with their individual properties in Table 1.1.

One can distinguish between old red elliptical galaxies with almost no star formation and young blue spirals or irregular galaxies with a high star-forming rate. Since new galaxies are born out of the IGM and the intra cluster medium (ICM), they are at first filled with hydrogen and helium which will subsequently be converted into stars which produce heavier elements. As only a few stars eject all their material back into the ISM, a substantial fraction of baryonic material will be bound in stellar remnants over time. Therefore, the older a galaxy the smaller is its gas-mass fraction. In ISM-rich spiral galaxies, most of the dense and cool ISM resides in a thin gaseous disk where most of the star formation takes place (see Figure 1.2). When a new star has been formed, the surrounding ISM can get photoionized by high-energy UV photons. This ionized bubble is called a H II region. These regions extend only over a few parsec and they exist only a few Myrs like their host star. Another process that produces photoionized gas is the ejection of a planetary nebulae by evolved intermediate mass stars (0.8 $M_\odot <$

$M < 6\ M_\odot$). In this case, at first, the gas is ejected during the last period of the lifetime of the star. Subsequently, the ejected gas is ionized by the radiation of the stellar remnant. Considering a whole galaxy, the ionized gas phase with temperatures up to $T > 10^4$ K can account for a significant portion of the ISM mass (e.g., $\sim 1.1 \times 10^9\ M_\odot$ for the Milky Way; Draine 2010, and references therein).
Going to lower temperatures and higher densities, the warm neutral medium provides another large fraction to the overall ISM content. It contains predominantly H I with an ISM mass fraction of $\sim 60\%$ and exists at temperatures of $T \sim 10^4$ K. For observations, this phase has not been accessible for a long time until the radio astronomy became available and the 21 cm "hyperfine" transition of neutral hydrogen could be used (Kerr 1958, e.g.,).
At the cold and dense end of the parameter scale, the molecular and dusty part of the ISM is located. As we know today, dust grains are essential for the creation of molecules and, thus, play an important role in the galactic evolution. Dust is also interesting because of the possible depletion of elements out of the gas phase onto the dust grains. A detailed discussion of the effects of dust to the abundance of elements will be presented Section 6.1.
In contrast to the cold and dense phases, there exists a collisionally highly ionized medium surrounding the whole galaxy which was already predicted in the mid 1950s (Spitzer 1956). Heated, for instance, by shocks of supernovae (SN) or gravitational forces, temperatures will rise up to $T > 10^5$ K and even higher combined with very low densities. This phase can be traced through a variety of highly ionized species as (Si IV), C IV, O VI, N V or Ne VIII (see Subsection 1.3).
The hot and thin gas bubble around galaxies on the edge of the IGM is also often referred to as the Circumgalactic Medium (CGM) or the halo. Since there is no clear cutoff between the halo and the space between the galaxies, one cannot define a sharp edge of the IGM. Due to many different heating, cooling, and recombination processes, all these ISM phases are not static but highly dynamic with phase transitions between them.
Because of the input of free energy in form of UV radiation from stars and kinetic energy from SN ejecta, the ISM is far from the thermal equilibrium but instead is in a high non-equilibrium state. This has to be kept in mind since almost all theories assume local thermal equilibrium (LTE) conditions because of simplifications in the underlying equations. However, the reality is always a highly non-LTE state and, therefore, many models can only be considered as rough approximations.

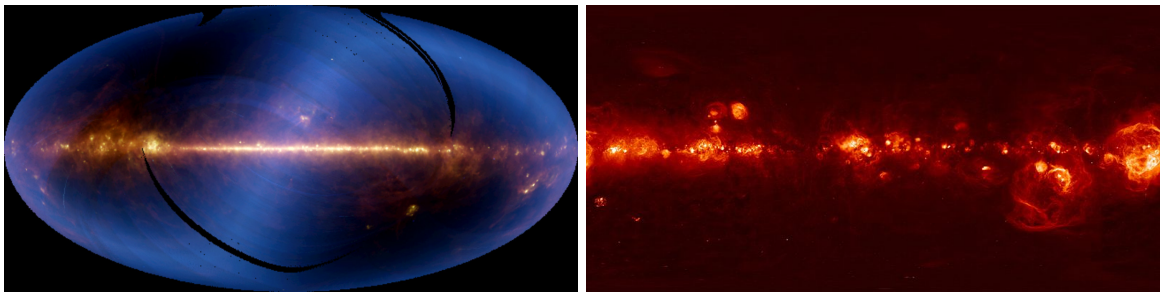

Figure 1.2: Two images of the entire sky with the Milky Way disk visible in the center, recorded at different wavelengths. The left image was generated with the Infrared Astronomical Satellite (IRAS) and shows the infrared radiation emitted by dust. The right picture is a composition of the Virginia Tech Spectral line Survey (VTSS) and the Southern H-Alpha Sky Survey Atlas (SHASSA) showing the Hα emission from photoionized gas (Finkbeiner 2003).

1.3 The gas distribution around the Milky Way

Beyond the inner part of the disk and the star-forming regions, the halo gas forms an interphase and connects the outer parts of a galactic disk to the surrounding IGM which contains a substantial fraction of unprocessed material. Because of its intermediate position, the halo consists new material from the IGM and satellite galaxies as well as highly enriched and recycled disk material that has been blown out by galactic winds or supernova shocks. Concerning the spatial extent, there are at least three different approaches to define gas as part of the halo. Following Putman et al. (2012), gas within the virial radius[1] and beyond the star-forming disk of a galaxy has to be counted as halo gas. Another approach is the definition by the expected velocities of the gas compared to those of a rotation model of the disk.

[1]Defined as $R_{\rm vir} \approx (200\ {\rm kpc}) M_h / 10^{12}\ M_\odot]^{1/3} (\Delta_{200})^{-1/3}$ with M_h being the mass of the halo and Δ_{200} being an overdensity of 200 compared to the critical density of the Universe.

Finally, one can also define the halo of a galaxy as to lie a few kpcs above the plane but not being part of the galactic disk. However, none of these definitions is absolutely accurate due to the smooth transition and the absence of a sharp edge between the phases.
To categorize the different phases of halo gas, the temperature is the best-suited parameter (see, for instance, Figure 1.3). Thus, we follow this scheme and refer the explanations to the Milky Way (MW) as the best investigated galactic environment although recent observations hypothesize that many of the findings can be transferred to other galaxies.

Recent studies have shown that a significant fraction of $\sim$37% of the sky is covered by neutral

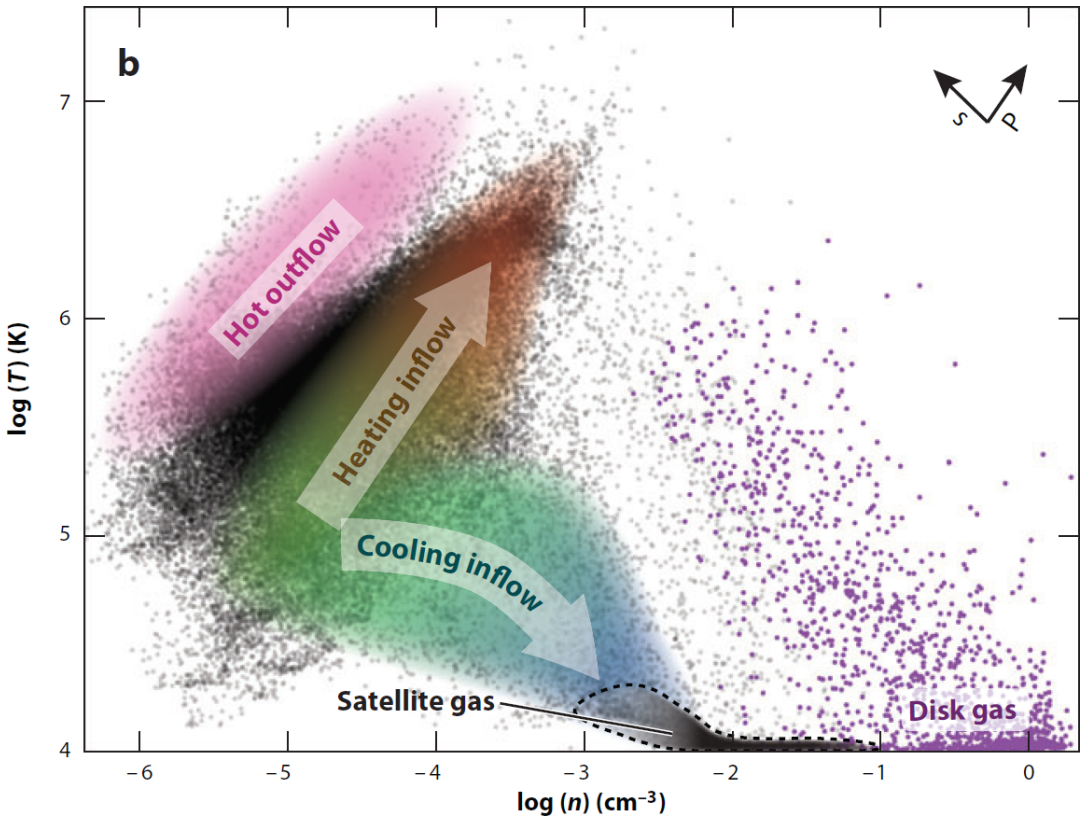

Figure 1.3: Density-temperature diagram of the Milky Way gas components at $z = 0$. The colors indicate the different gas phases and the arrows in the top right corner point in the directions of increasing pressure (p) and entropy (s) (Putman et al. 2012).

hydrogen at temperatures of $T < 10^4$ K at a column density of $N(\mathrm{H\,I}) \sim 7 \times 10^{17}$ cm^{-2} (see Figure 1.4 and Lockman et al. 2002). Visible in the H I 21 cm emission line, these halo clouds are often referred to as high velocity clouds (HVCs) because of their large kinematic range (-500 to $+450$ km s^{-1}) in the local-standard-of-rest (LSR) velocity frame. Compared to a simple model of differential galactic rotation, Wakker (1991) has shown that these HVCs are incompatible with the expected disk velocities at the considered positions. In the MW, the most massive clouds are typically found at $17.2 \leq \log N(\mathrm{H\,I}) \leq 20.2$, but there is evidence for the existence of a large number of clouds with lower H I column densities that can be detected very well with QSO absorption line studies. Current H I 21 cm studies suggest that these smaller HVCs (in terms of H I column density) are the outer parts or the extended diffuse envelopes of the large HVCs that are seen in H I emission (Lehner et al. 2012). Note that not all accreted gas necessarily cools down to temperatures where it can be detected via H I 21 cm emission. In fact, it is expected that a substantial portion of the infalling gas remains "warm" and diffuse ($n_\mathrm{H} < 10^{-2}$ cm^{-3}, $T = 10^4 - 10^5$ K) with only a small fraction of cold, neutral gas. As H I 21 cm emission is not sensitive for this "warm" mode of gas accretion, intermediately and highly ionized species, like Si III, C III, Si IV and C IV, are used to trace this phase in the halo of the MW as well as in the Circumgalactic Medium of other galaxies (see Sections 2.4 and 4, and Richter 2012).
At lower LSR velocities of 40 km s^{-1} $< |v_\mathrm{LSR}| <$ 90 km s^{-1}, the picture of HVCs has to be extended with the intermediate velocity clouds (IVCs), which can be detected typically at lower scale-heights of $z \sim 1 - 2$ kpc above the Galactic plane. Note that these LSR velocities are not necessarily the same like the infall velocities of these clouds. For the precise calculation of v_infall, the balance equation between the gravitational force and the ram pressure force is needed. This requires knowledge about the density distribution of the surrounding hot coronal gas. Typically, one can assume that both velocities are almost

Table 1.2: Most important Milky Way HVC complexes.

HVC name	$f^b_{\rm HVC}$	D^c [kpc]
Complex A	0.01	$8-10$
Complex C	0.04	~ 10
Complex H	0.01	>5
Magellanic Stream	0.04	~ 50
Complexes WA, WB	0.01	$8-20$

This Table was originally presented in Richter (2012). For more references regarding the individual complexes see Richter (2012) and references therein.
[b] Sky-covering fraction
[c] Distance

on the same order of magnitude ($v_{\rm infall,HVC} \sim 100$ km s^{-1}, $v_{\rm infall,IVC} \sim 50$ km s^{-1}) which is supported by grid-based hydrodynamical simulations (see also Heitsch and Putman 2009; Richter 2012). However, with an H I mass of roughly $0.5-8 \times 10^5\ M_\odot$ and a roughly solar metallicity, the IVCs are thought to represent a rather evenly distributed class of objects that are located in the disk-halo interface region. Ongoing studies have shown that there are large numbers of even smaller H I clouds of $1-700\ M_\odot$ (see Ford et al. 2010; Saul et al. 2012). It will be the task of future high-resolution studies to uncover the nature of these objects.
The third class of objects are the so-called compact high velocity clouds (CHVCs). These are very small and dense objects largely associated to HVCs or HVC complexes. With an angular size of less than 1°, they are thought to represent the link between dwarf galaxies and theoretically expected low-mass objects like the dark-matter satellites around the big Local Group galaxies as predicted from simulations. Westmeier has argued that also M31 harbors a population of CHVCs which can be used to compare their H I brightness temperatures with those of the local CHVC population. This enables us to determine a rough estimate of the distance of CHVCs around the Milky Way. It turns out that most of them are located at distances $\lesssim 60$ kpc from the Milky Way disk.
As shown in Figure 1.4, HVCs form large and wide-spread complexes like the Magellanic Stream (MS) or Complex C, which are the two most prominent examples and which will be discussed in detail in a subsequent passage. Very small and dense clumps like the CHVCs can be associated with the big complexes in position and velocity in most of the cases. In Table 1.2, a short list of the most important HVC complexes, their sky covering fraction, and their approximate distance is given.
Current projects suppose that with increasing resolution power even the large clouds will degrade into smaller subclumps which has to be taken into account for the formation process of HVCs (Putman et al. 2002; Ben Bekhti et al. 2012).
The nowadays favored model of HVCs expects a two-phase structure with a cold ($T \lesssim 500$ K) inner core and a warmer neutral outer shell with linewidths of $20-30$ km s^{-1} indicating a temperature of $T \sim 10^4$ K (Kalberla and Haud 2006). Wolfire et al. (1995) have shown that such a two-phase structure is a result of the HVCs being in thermal pressure equilibrium with the surrounding hot ($T \sim 10^6$ K) halo gas, which can also explain the lack of the inner cores for HVCs located at distances $d > 20$ kpc like the Magellanic Stream.
The measurement of the distance is one of the key tasks for the investigation of HVCs. Usually looking for the optical Ca II or Na II absorption line doublets, spectra of stars with known distances are used to define upper or lower limits depending on whether the absorption of the HVC is seen or not. It turns out that almost all HVCs (except the MS) reside at distances of $2-15$ kpc within a 30° angle as seen from the Galactic Center. Richter (2006) has discussed to use the two phase model to estimate the distances to these clouds in an indirect manner using Hα emission. Recent studies have shown that the clouds are in fact surrounded by a highly ionized medium which radiates in Hα (Putman et al. 2003). However, due to the high temperatures in the corona, collisional ionization effects play a role and may effect the overall interpretation. Thus, the estimation of distances using the Hα method is still afflicted with high uncertainties. Combining the estimates for HVCs using the "star-approximation" method described here and the distances for CHVCs explained earlier, one can conclude that these H I HVCs rather represent a circumgalactic then an intergalactic/Local Group phenomenon (see Richter 2006).
With typical H I maximum column densities ranging from $\sim 10^{19} - 10^{20}$ cm^{-2}, HVC complexes contain a significant fraction of H I mass circulating around the Milky Way. Depending on the distance and excluding the MS, observations and calculations result in a total neutral hydrogen mass bound in HVCs

of $2.6 \times 10^7\ M_\odot$ (Putman et al. 2012).
At higher temperatures of $T \sim 10^4 - 10^5$ K, high velocity gas can also be detected by Hα emission line observations as well as by absorption lines of lowly and intermediately ionized metals like C II/III or Si II/III through QSO absorption line measurement. With the metallicity of HVCs ranging from sub-solar, $(Z/Z_\odot) = 0.1$ (e.g., Complex A), up to solar, $(Z/Z_\odot) = 1.0$ (in some IVCs), the creation processes of these objects are manifold (e.g., Richter et al. 1999; Wakker 2001a; Richter et al. 2001; Tripp et al. 2003). On the one hand, the metal-poor gas from the IGM hints to infalling and accreting processes (e.g., gravitation, stripping out of companions) whereas, on the other hand, the metal-enriched part is driven out of the disk by supernova shocks or galactic winds (e.g., the galactic fountain model). In contrast to the galactic winds, the galactic fountain is thought to appear over the whole range of the disk. Thereby, supernova explosions and adiabatic expansion drive material out of the disk where it can condense due to radiative cooling, followed by a fall-back onto the disk. This model is supported by simulations of the disk-halo interface region and also by the near solar metallicities of IVCs (see, for instance, Putman et al. 2012, and references therein).
With the possible detection of low column density gas through absorption lines, the covering fraction of this warm-photoionized component rises up to $\sim$81% for Si III or >60% for primarily collisionally ionized O VI at $T > 10^5 - 10^6$ K. This indicates that almost the entire sky is covered with ionized hydrogen in the halo containing a mass on the order of that for neutral hydrogen, $\sim 3 - 4 \times 10^7\ M_\odot$, which then leads to a total hydrogen mass of $\sim 10^8\ M_\odot$ and a contribution of $\sim 0.7\ M_\odot\ \mathrm{yr}^{-1}$ to the total mass accretion rate of the Milky Way (Richter 2012). In fact, these numbers are still afflicted with large uncertainties. For instance, Lehner et al. (2012) estimate the total fraction of infalling HVC material being on the order of $0.4 - 1.4\ M_\odot\ \mathrm{yr}^{-1}$, which would be sufficient to maintain the present day star-formation rate, which is $1.9 \pm 0.4\ M_\odot\ \mathrm{yr}^{-1}$. Note that the infall rate does not necessarily needs to be as high as the star-formation rate because of internal chemical evolution and stellar outflows.
Since the Magellanic Stream and Complex C cover a huge portion of the entire sky, it is important to

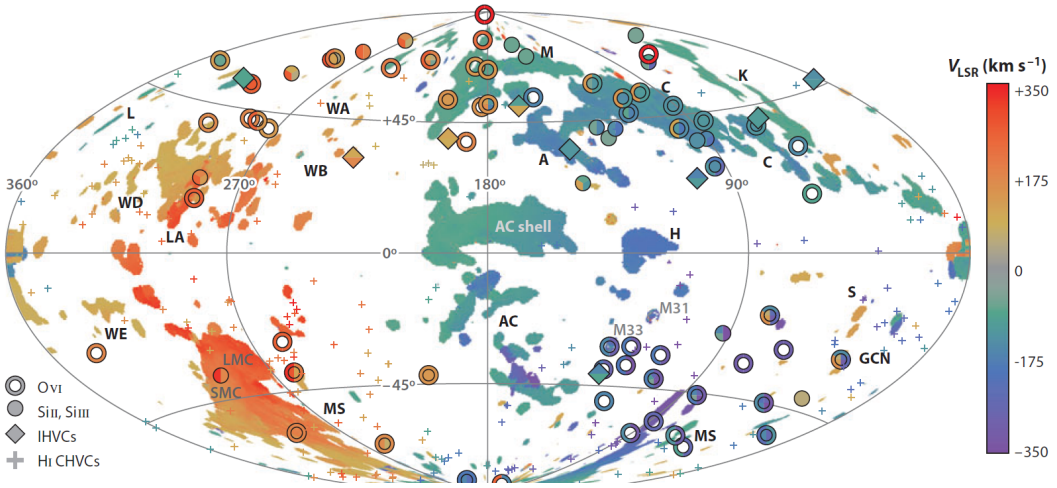

Figure 1.4: Anticentered 21cm all sky map of the known HVC complexes based on the LAB survey and combined with additional data of compact HVCs shown as the little crosses (Putman et al. 2002; Kalberla 2003; Kalberla et al. 2005). Color-coded is the local-standard-of-rest velocity and the symbols mark ionized high-velocity gas. Multiple colored symbols imply that more than one ion is found along this sightline. Additionally, most of the known complexes are labeled like the Magellanic Stream (MS) in the southern hemisphere or Complex C at the northern part of the sky. Figure taken from Putman et al. (2012).

provide some more details about these two HVC complexes.

- **The Magellanic Stream**
  The Magellanic Stream is the largest complex of high velocity gas, formed as a tidal tail with its origin at the Small and Large Magellanic Cloud (SMC/LMC), respectively. With a spatial dimension of $\sim 120°$ it dominates the southern hemisphere of the sky and it is complemented by Complex EP, also know as the leading arm (LA) of the MS. Only this huge complex is responsible for $\sim$27% of the covering fraction of HVCs in H I ($f_c = 0.04$ for $\log N(\mathrm{H\,I}) > 18.3$; Richter 2012). Due to its size, the MS is one of the best analyzed HVC structures (see Wakker 2004; Putman 2004; Mastropietro et al. 2004; Westmeier and Koribalski 2008, and many others). Some years

ago, there was a debate whether the MS is a result of ram-pressure stripping or tidal forces, but since the identification of the LA as part of the MS, the tidal model has been more accepted. In principal, it assumes that roughly 2 Gyr ago the combined tidal force between the LMC/SMC and the Milky Way was strongest and ripped out material of about 2.5×10^8 $M_\odot$, which then separated into a leading arm and a tidal tail feature following the dwarf galaxies. This assumption is confirmed by the metallicity of ~ 0.2 solar which is roughly the same as in the SMC.
Compared to other HVC complexes, the MS stands out in several physical parameters. For instance, located at a mean distance of $\bar{d} \sim 55$ kpc, it is much farther away than other HVCs and it contains a larger amount of mass than all other members of the HVC population. Moreover, recent studies have shown that the metallicity might be changing over the extend of the MS.
Finally, the LSR velocity dispersion within this one complex ranges from -440 to $+412$ km s^{-1}. That is almost the full range detected in all other HVC complexes.

- **Complex C**
  Complex C is the second-largest high velocity gas complex covering almost 10% of the northern sky (~ 1500 deg^2). Depending on the sensitivity limit, the covering fraction is almost as large as that of the Magellanic Stream ($f_c \approx 0.04$). With a H I column density range of $N_{\rm HI} = 1.6 - 11.5 \times 10^{19}$ cm^{-2} and a H I $v_{\rm LSR}$ velocity distribution ranging from $v \sim -100$ to -200 km s^{-1} it is much more defined than the MS, but, in contrast to the MS, the distance is still quite unclear (between 5 – 20 kpc). With a sub-solar metallicity of 0.1 – 0.2 $Z_\odot$, the origin of the gas is thought to be basically intergalactic, but many abundance and ratio measurements of heavy elements suggest that the included metals should be a result of SN-Type II enrichment (Wakker 2001b; Richter et al. 2001). In general, this low metallicity gas represents one of the best candidates for the fuel of Galactic star formation that the Milky Way accretes from the surrounding IGM. With a detailed analysis of different sightlines passing through this complex, Gibson et al. (2001, for Mrk 290/817/279) have found evidence for abundance variations within the complex.

To complete the picture, we want to summarize some properties of the hot ($T > 10^6$ K) halo gas phase. Detectable in X-ray emission and QSO absorption by highly ionized metals (C IV, O VI, Ne VIII), this phase is thought to trace feedback mechanisms from the disk or may represent shock-heated material from the IGM. Because of its "expected" extent up to the virial radius of our galaxy and a covering fraction of more than 60%, this phase accounts for a mass up to $\sim 10^{10}$ $M_\odot$ within 100 kpc and, therefore, a substantial baryon fraction of the MW (Sembach et al. 2003). Furthermore, there are several indirect signs that support the idea of a low density (typically $10^{-5} - 10^{-4}$ particles/cm^{-3}) hot halo medium out to distances of at least the Magellanic Stream:

- possible detection of O VI around cool halo clouds, which hints to an interaction with a surrounding hot and low density medium (Sembach et al. 2003).
- the head-tail structure of compact halo clouds (see Putman et al. 2012).
- gas stripping out of satellite galaxies because of their passage through this medium (Grcevich and Putman 2009).
- a low-density bipolar structure in X-ray and gamma-ray maps (Su et al. 2010).

In general, this hot halo phase is difficult to detect and so far not well understood. Even though this medium contains about 2 orders of magnitude more mass than all other halo gas phases, simulations still predict a higher fraction to be consistent with cosmological models.

In contrast to dust, the metallicity has been estimated for many HVCs especially for Complex C and the MS. In general, it is assumed that complexes with a metallicity less than $< 2\%$ solar (like Complex A) are good candidates for the so-called cold stream accretion (see Section 1.4), whereas gas that has been enriched to levels found in the LMC (usually ~ 0.2 $Z_\odot$) could be a tracer for interactions with nearby satellites or outflows. Thus, HVCs with near solar metallicities can be claimed as candidates produced by Galactic fountains (Lehner et al. 2012). Finally, molecules like H_2 and CO have been detected in only a few cases usually connected to the MS like the Magellanic Bridge or the Leading Arm (Richter et al. 2001; Lehner 2002).
For a better understanding of these clouds, it is important to extend the detection limit for HVCs down

to low column densities of log N(H I) ≤ 17.2 (sub-Lyman-Limit-Systems, subLLS) to complete the HVC map of the Milky Way. It is not yet clear whether the HVC distribution is representative for other Local Group members like the Andromeda nebula (M31) or NGC 891, but there are a lot of hints that HVCs represent a common feature of Milky Way-type spirals (see Section 1.3.1). Nevertheless, even with respect to the Milky Way, there are a lot of open questions. Current and future 21 cm radio surveys and UV absorption line analyses of the Mg II $\lambda\lambda$2796, 2803 doublet will help to deepen the insight into halo processes at other galaxies and hopefully create a consistent picture of galaxy formation and evolution (Richter et al. 2009).

1.3.1 The gas distribution around other galaxies

With the numerous detections and information of Galactic HVCs and IVCs, one would expect that these circumgalactic neutral gas clouds are essential for the evolution of, at least, Milky Way-type galaxies in general. Thus, it is expected that the HVC phenomenon should be quite common for other galaxies in the local Universe. During the last years, the focus of the analysis of distant galaxies was on the H I gas distribution around these objects for various reasons. On the one hand, radio telescopes with a sufficient resolution enable us to create a whole H I map of the galaxy and its environment and, on the other hand, H I provides a direct measure of the accreting gas and is also a powerful tracer of merger events. Despite the challenging task of identifying individual neutral H I clouds in the halos of other galaxies, a lot of progress has been made during the last decade. One can find positive detections, for instance, for M31, M51, M81, M101, NGC 891 and many others (see review of Richter 2006, and references therein). In the more general case of extended H I halos, the list can be continued. In the same way as for the Milky Way, some of these structures extend more than 10 kpc away from the disk with a similar contribution of outflows and tidal interactions with surrounding satellites.
One of the best candidates to study HVCs and the gas distribution around other galaxies is M31, the Andromeda galaxy. Next to the Milky Way, it is the closest "big" Milky Way-type galaxy in the Local Group and, therefore, well suited for this kind of study. One of the first and most extensive studies of the extended CGM of M31 has been done by Thilker et al. (2004, see left panel of Figure 1.5). They observed a population of about 20 discrete H I halo clouds at systemic velocities of $\sim$200 km s^{-1} and H I masses in the range of $0.15 - 1.3 \times 10^6$ $M_\odot$. Furthermore, an extended, low H I column density gas phase at a velocity of $\sim$80 km s^{-1} relative to M31 has been detected. They have concluded, based on the

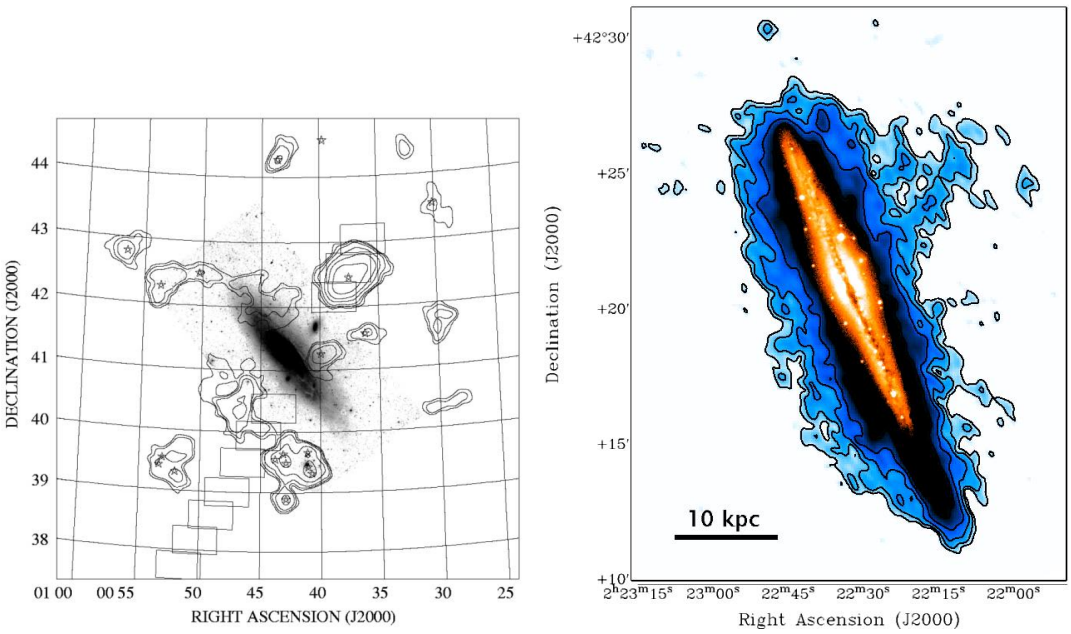

Figure 1.5: **Left panel:** high-velocity H I map around M31 observed with the Green Bank Telescope. The stars mark the positions of individual clouds (Thilker et al. 2004).
Right panel: the blue contours show the H I gas distribution around NGC 891 with an extended filament in the northern part. The blue labeled gas is kinematically separated from the "normal" disk gas. Overlaid is an optical image (Fraternali et al. 2007)

observed cloud mass function, $\mathrm{d}N(M_{\mathrm{HI}}) \propto M_{\mathrm{HI}}^{-2}\mathrm{d}M$, that the overall H I halo cloud population mass is in the range of $\sim 3 - 4 \times 10^7$ $M_\odot$, which is in very good agreement with the amount of neutral hydrogen found in the Milky Way halo. However, this estimate assumes that most of these possible HVC objects

around M31 are still undetected. Finally, also M31 is surrounded by several satellite galaxies which implies that some of these M31 HVCs have their origin in tidal interactions, whereas others are produced by outflowing galactic-fountain material or by infalling IGM gas (Thilker et al. 2004). In general, it has been revealed that the phenomenon of tidal interactions with satellite galaxies is very common in the local Universe. Sancisi et al. (2008) have published a list of more than 18 individual galaxies where extended H I features or even gas-rich dwarf companions are known. All of them have typical velocities close to the main galaxy and, in most of the cases, the mass of the companion is below 10% to that of the host galaxy. Inspecting the H I maps of these systems, it is evident that usually H I tails and bridges are formed between both participants. That means that there is much interaction between both objects with a large amount of gas being accreted by the main galaxy. For systems without individual visible companions, one assumes that extended H I tails and envelopes are the remaining evidence for merging processes that took place earlier (Sancisi et al. 2008). The right panel of Figure 1.5 shows another example of a galaxy with a known extended H I halo. Here, one can see that the neutral gas around NGC 891 is more extended in the northern part of the disk where also the star formation rate is higher than in the southern extension. That is another direct evidence for the important connection of infalling gas clouds to the ongoing star formation in the main galaxy. Furthermore, one can see a clear filament which extends up to $\sim 22\,\mathrm{kpc}$ above the disk and contains $\sim 1.6 \times 10^7\ M_\odot$ which is $\sim 1.3\%$ of the total H I mass ($\sim 1.2 \times 10^9\ M_\odot$) bound in the halo. With this high mass, NGC 891 is one of the galaxies with the highest mass of neutral halo gas known today (30% of total). However, also smaller, more compact clouds with masses in the range of Galactic HVCs ($1 - 3 \times 10^6\ M_\odot$) can be observed. In both panels of Figure 1.5, the normal symmetric disk and halo component has been subtracted which leads to the conclusion that the remaining features might be the analogs of HVCs in the Milky Way. With respect to the accretion rate, these neutral filaments are expected to contribute with $0.1 - 0.2\ M_\odot\ \mathrm{yr}^{-1}$, which is on the order of what is known for the Milky Way (see Section 1.3).

Concerning the more diffuse and hot gas component, many studies have found such a component especially around observed edge-on spiral galaxies (e.g., Richter 2006, and references therein). This gas phase, usually analyzed through Hα emission, extends several kpc above the galactic plane which indicates that the galactic fountain model can be applied to these types of galaxies (see Section 1.3). Furthermore, some gas properties (Hα brightness, vertical extent) lead to the conclusion that the ionized gas is directly connected to the particular star formation rate. Thus, for Milky Way-type spirals one can conclude that the hot ionized gas component traces outflowing processes of metal-enriched interstellar gas, whereas the neutral H I structures are tracers of the backflow and the infall of intergalactic material. Due to the high importance of the circumgalactic medium a lot of studies focus on the ionization conditions and the composition of this gas phase around the MW and other galaxies. For instance, Shull et al. (2009) and Collins et al. (2009) have used the newly available COS instrument to study various aspects and properties of the CGM around the Milky Way. They model the ionization parameters and metallicities for Galactic HVCs with respect to Si III, finding values of $\log U \approx -3.0 \pm 0.3$ and $\langle \log (Z_{\mathrm{Si}}/Z_\odot) \rangle = -1.4 \pm 0.3$.

Since it is difficult to transfer our knowledge to distant galaxies, local studies can be used to uncover connections between the MW and other galaxies. Nevertheless, there are already numerous studies which consider individual absorption systems (see, for instance, Jenkins et al. 2005; Richter et al. 2006; Savage et al. 2011a; Shull et al. 2011; Narayanan et al. 2012; Keeney et al. 2013; Stocke et al. 2013, and many others). Most of them have found ionization conditions similar to the results of this work, but also large differences between particular systems are found. For an overall coherent picture, it is necessary to combine the results of all these studies and extract a general picture of the typical properties of the CGM around Milky Way-type galaxies.

Additionally to these analyses, some of these galaxies have also been observed in the IR and X-ray regime. It turns out that many of these spirals exhibit a significant amount of dust features with high scale-heights and masses up to $\sim 10^5\ M_\odot$ (Richter 2006, and references therein). Besides, X-ray telescopes like Chandra or XMM-Newton revealed an extended corona of very hot, ionized gas which looks similar to the Galactic hot Halo of the Milky Way. For regions close to the disk, the X-ray emission turns out to be closely related to the Hα emission, which leads to the conclusion that both signals trace the same gas, but at different temperatures, densities and ionization stages.

In general, it seems that the properties of the Galactic CGM in terms of tidal interactions, gas phases, gas distribution and structure are very similar to those of other spiral galaxies. However, despite the fact that there have been detections of H I halo clouds around other galaxies down to $\sim 10^5\ M_\odot$, high resolution observations still provide only a column density sensitivity of $\sim 10^{19}\,\mathrm{cm}^{-2}$, which is on the order of the peak column densities for HVCs. Even for M31, current H I maps only reach kpc resolution with $\log N(\mathrm{H\,I}) \gtrsim 18$. Nevertheless, these maps indicate, that the HVC phenomenon, embedded in a hot halo component with almost the same physical properties as in our own halo, is a common feature of at least MW-type spirals (e.g., see Figure 1.5; Putman et al. 2012, and references therein).

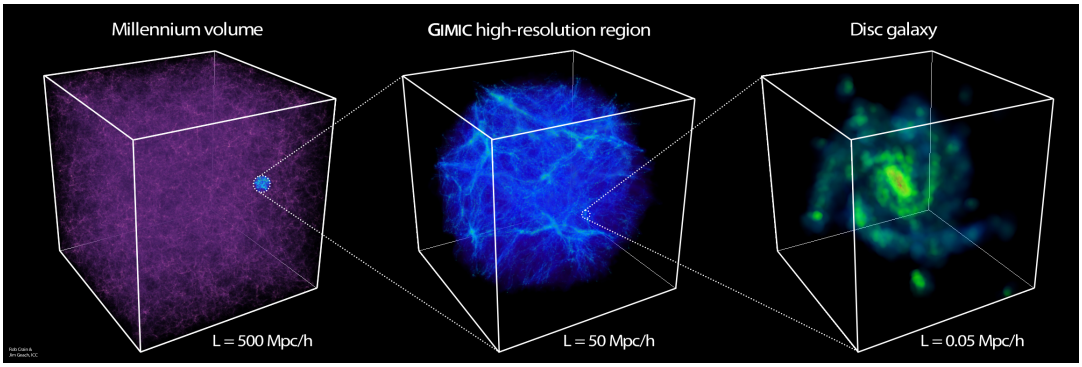

Figure 1.6: Picture from the GIMIC (Galaxies-Intergalactic Medium Interaction Calculation) simulation, started in 2008. The left and middle cube show the distribution of the IGM in the cosmic web, whereas the rightmost cube goes down to the resolution of possible disk galaxies (0.05 Mpc boxsize, Crain et al. 2009).

1.4 The Intergalactic Medium

As mentioned in Section 1.1, almost all baryonic matter in the Universe is bound in the gas phases in, around and between galaxies (see Figure 1.6 and right panel of Figure 1.7). The gas distribution offers the possibility to probe the large-scale structure of the Universe, and to understand the ongoing formation and evolution of galaxies and stars. Therefore, it is essential to understand the different phases of the intergalactic gas and the matter cycles between this gas reservoir and the galaxies.
Just after the Big Bang, the Universe harbors no structure or any objects, but due to small inhomogeneities and density fluctuations the structure formation starts. During these times, stars and galaxies were formed and caused the reionization. The material left over, which is located between the galaxies, is called the IGM. The result of this process is a clumpy and filamentary structure of the Universe. In the old classical (spherical) picture, the baryons enter the environment and the virial radius of a galaxy in an almost symmetric way. In fact, this is not observed (see Section 1.1 and 2.1 Putman et al. 2012). Instead, under ΛCDM conditions, the majority of the gas/baryons will follow the Dark Matter potentials along the cosmic filaments, and partly become shock-heated to the virial temperature (hot mode accretion with $T > 10^6$ K). Nowadays, there is consensus that, for the $z = 0$ Universe, this mode is dominant for massive galaxies with DM halos $> 10^{12}\,M_\odot$. On the other hand, for galaxies at high redshift ($z > 2$) and for low mass galaxies ($M_{\rm halo} \leq 10^{12}\ M_\odot$) at $z = 0$, the so-called "cold accretion mode" has to be considered as well. In this scenario, "cold" gas with temperatures of $T \leq 10^{5.5}$ K, which resides in the shielded, more compressed, core regions of the filaments, is accreted. Due to the protection from the interaction with the surrounding "hot mode" gas, this gas has the possibility to remain cold and directly feed the star formation in the disks of galaxies (Brooks et al. 2009). The covering fraction of such streams of cold material varies between 5% – 40%, depending on the parameters of the considered model and the redshift. Furthermore, it is expected that only for galaxies with $M_{\rm Halo} \lesssim 10^{12}\,M_\odot$ this material remains cold while it is accreted to the inner parts of the galaxy (Ribaudo et al. 2011b, and references therein). This part of the IGM infall might be seen as HVCs.
With an expected lower metallicity compared to the ISM, the IGM could provide new material to power the star formation in galaxies. The IGM itself is enriched by metals that are produced in galaxies and carried out by galactic winds or SN explosions. To characterize the IGM, one has to distinguish between high ($z > 2$) and low ($z < 2$) redshift. Recent CMB studies done by Komatsu et al. (2011) found a baryon fraction of $\Omega_b = 0.0455 \pm 0.0028$ in the IGM that should be conserved over time. At high redshift, almost all the baryons can be traced in galaxies and in the IGM, which mainly contains the Lyα forest at that time. At low redshift, it turns out that the composition of the IGM has changed with the baryons crossing over to other phases that partly cannot be detected and, therefore, are still missing at low redshift (see Figure 1.7, e.g., Fukugita et al. 1998; Shull et al. 2012a). This so-called "missing baryon problem" is one of the most studied topics in todays IGM astrophysics.
Nevertheless, recent simulations have shown that the IGM contains a wide range of temperatures and densities (see Figure 1.7 left panel; Hui and Gnedin 1997). It turns out that the so-called warm-hot intergalactic medium phase (WHIM) probed by O VI absorbers (with $\rho/\bar{\rho} \leq 100$ and $\sim 1/50\,Z_\odot$ at $z = 0$) becomes one of the possible candidates for a substantial fraction of the missing baryons. However,

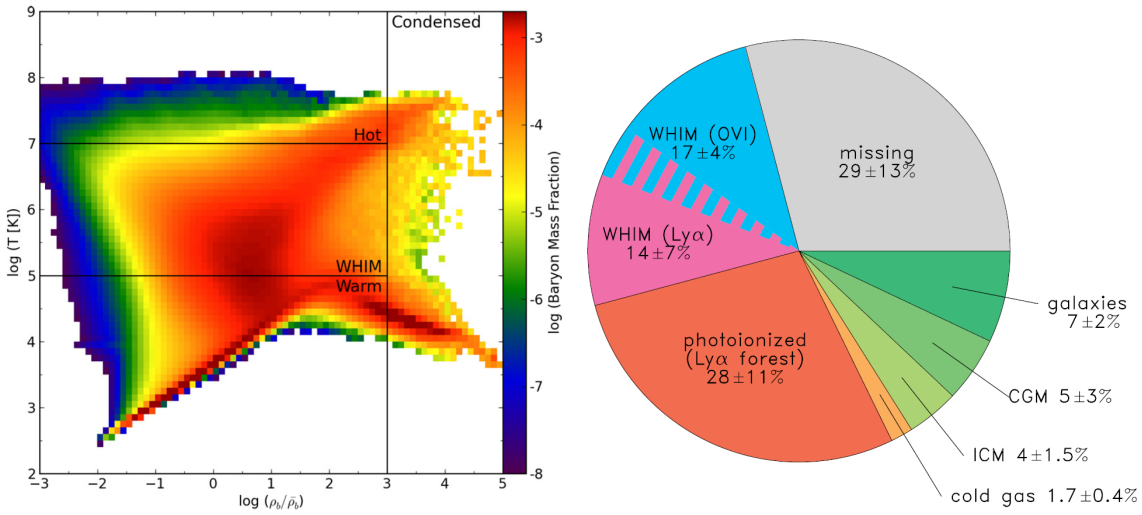

Figure 1.7: The left panel shows the temperature-baryon overdensity ($\Delta b = \rho_b/\bar{\rho_b}$) distribution of the IGM, color-coded with the baryon mass fraction. The most common phases are labeled. In the right panel, the fragmentation of the low-redshift baryonic matter is shown. Collapsed structures like galaxies and clusters provide only $\approx 7\%$, whereas most of the matter is bound in different gas phases with a large portion of $\approx 30\%$ still missing at low redshift (Shull et al. 2012a).

there is still a big part missing, possibly having temperatures higher than $T > 10^6$ K, and, therefore, only detectable through X-ray observations.
To probe the composition and the metal content of the IGM in detail, it is necessary to analyze QSO absorption lines of all different elements and their ions. Recent observations, done with the Cosmic Origin Spectrograph (COS), suggest that galactic superwind outflows are necessary to enrich the IGM to the detected metallicity (Oppenheimer et al. 2012, hereafter OD11) (see also next Section).
O VI, Ne VIII, and other highly ionized species offer the possibility to study gas with temperatures higher than $T > 10^5$ K , whereas the abundance of weakly ionized species like Si III and C III indicates that also denser metal systems exist. It is still not clear whether these are coupled to galaxies or whether they are created in other processes.

1.4.1 H I in the IGM

Shortly after the first observations of QSO spectra with the newly developed QSO absorption line technique in the middle of the last century, scientists noticed that most of the spectra at wavelengths shorter than the redshifted hydrogen emission line of the quasar were "polluted" with hundreds of lines. Because the number of these lines is higher in longer sightlines, one can conclude that they are a result of gaseous material that resides between the quasar and the observer. These intergalactic filaments contain highly ionized material with only a little fraction of neutral hydrogen which, nevertheless, produces most of these lines due to its strong Lyα absorption transition at $\lambda_0 = 1215.67$ Å (see Figure 1.8). Simulations suggest that the diffuse Lyα forest accounts for $\sim 30\%$ of the baryons at low redshift, whereas an equally high fraction is expected to reside in the shock-heated, highly-ionized, warm-hot intergalactic medium (WHIM).
The Lyα forest can be used to analyze some of the properties of the IGM and the early structure formation in the Universe directly. On the other hand, blends with Lyα absorbers are a problem for the analysis of metals in the IGM. In most cases, the metal lines arise in the Lyα forest. With a typical volume density of only $n_{\rm H} < 10^{-4}$ cm^{-3}, the Lyα forest typically traces extended, highly ionized intergalactic structures, which are basically photoionized by the diffuse background radiation of AGNs. As explained in Section 1.4, it is assumed that these intergalactic filaments originate from density fluctuations in the early Universe. With ongoing structure formation, the gas falls into the potential wells of the evolving condensed structures where it is shock-heated up to temperatures of $T \sim 10^5 - 10^7$ K (Richter 2006, and references therein). Most of the "diffuse" Lyα forest has H I column densities below $< 10^{15}$ cm^{-2}, whereas structures with N(H I) $> 10^{15}$ cm^{-2} are believed to trace condensed structures like galaxy disks and halos. These systems are referred to as Lyman-Limit Systems (LLS, log N(H I) $>$ 17) or damped Lyα Systems (DLAs, log N(H I) > 21). Based on observations done for the Milky Way, one would expect HVC analogs to appear as sub-damped Lyα systems (sub-DLAs) and Lyman-limit

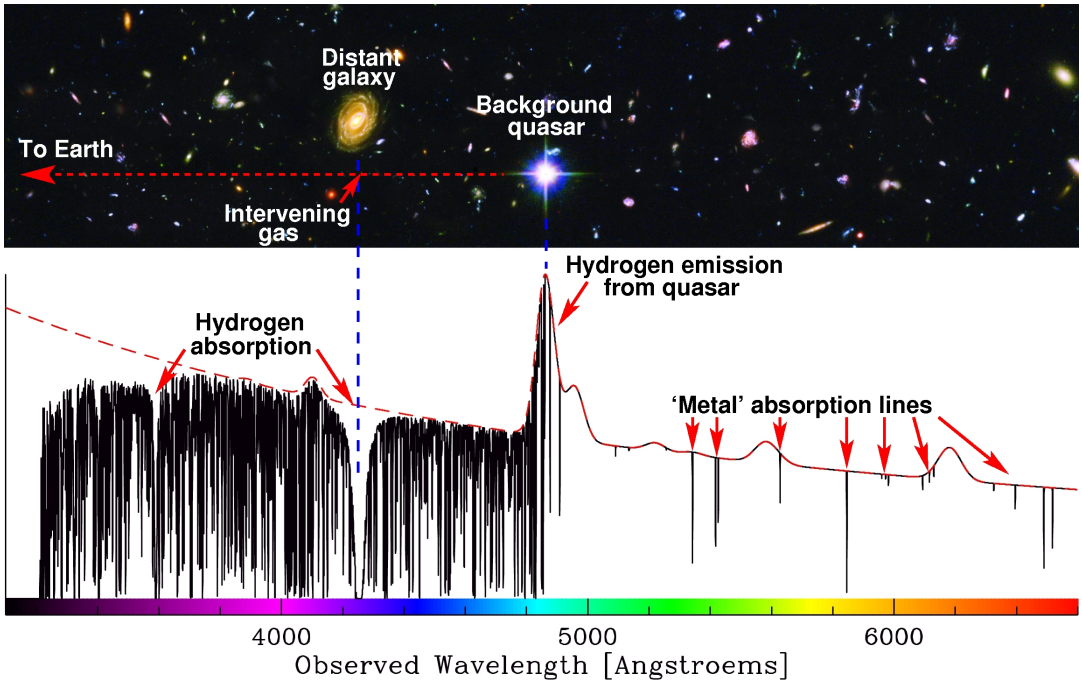

Figure 1.8: Illustrating scheme of the QSO absorption spectroscopy technique. In the bottom panel, a typical quasar spectrum with the dense Lyα forest at $\lambda \lesssim 4800$ Å, a DLA system at ~ 4250 Å, as well as some metal absorption lines redwards of the hydrogen emission line of the quasar are shown[2].

systems, whereas DLAs are typically thought to be the central parts of galactic disks (see Richter 2012). In Figure 1.9, the H I column density distribution function with some classification marks is shown.

It is evident that the number density of H I absorbers strongly decreases with increasing column density. This behavior can be approximated by $\mathrm{d}\mathcal{N}/\mathrm{d}N_{\mathrm{HI}} \propto N_{\mathrm{HI}}^{-\beta}$ with $\beta \approx 1.3 - 1.5$ (Richter 2012, and references therein). Furthermore, Richter (2006) has reviewed that measurements done with *FUSE* suggest that there might be an ongoing evolution apparent in the redshift dependent number density $\mathrm{d}\mathcal{N}/\mathrm{d}z$(H I) between $1.5 < z < 4.0$ in the form $\mathrm{d}\mathcal{N}/\mathrm{d}z \propto (1+z)^{\gamma}$ which seems to disappear for $z < 1.0$. This behavior can be understood in terms of the ongoing expansion of the Universe and the change of the ionizing background flux. For high redshifts, the Lyα forest density strongly decreases because of the rapidly expanding Universe combined with only a slightly decreasing background ionization flux. For low z, simulations suggest that the intensity of the background radiation has been decreased about one order of magnitude, which forces the evolution of the Lyα forest density to slow down (Richter 2006, and references therein). This process is also reflected in the contribution of the Lyα forest to the baryon density of about $\sim 30\%$ for $z = 0$ and $\sim 90\%$ at $z = 2$.

Another open question concerning H I in the IGM is the possible existence of isolated H I clouds (dark galaxies) with masses on the order of $\sim 10^7\ M_{\odot}$ that feed the star formation in galaxies. Sancisi et al. (2008) have argued that these "intergalactic HVCs" might, theoretically, be another possible source of fresh material that can be accreted to galaxies. However, researchers have searched for such objects, but there is no clear evidence for a population of isolated H I clouds that came directly from the IGM. That could imply that most of the gas accretion originates from merger events with small satellite galaxies, which is not possible due to cosmic timescales and the observed star-formation rates. Therefore, a significant portion of the infalling material has to stream directly from the IGM to the galaxies in the form of filaments or clouds, which is also supported by metallicity measurements. Thus, it is still an open question why such clouds are not observed at larger impact parameters than usually estimated for HVCs. One hypothesis is that the hot galactic halo confines the incoming clouds, whereas it is more diffuse in the outer CGM. Another possible approach is that such clouds are just too small, with masses $< 10^6\ M_{\odot}$, for current sensitivity limits and that they fall down to the galaxy more like a smooth rain rather than in the form of massive compact objects.

[2] from http://www.eso.org/ jliske/qsoal/qsoabs.jpg

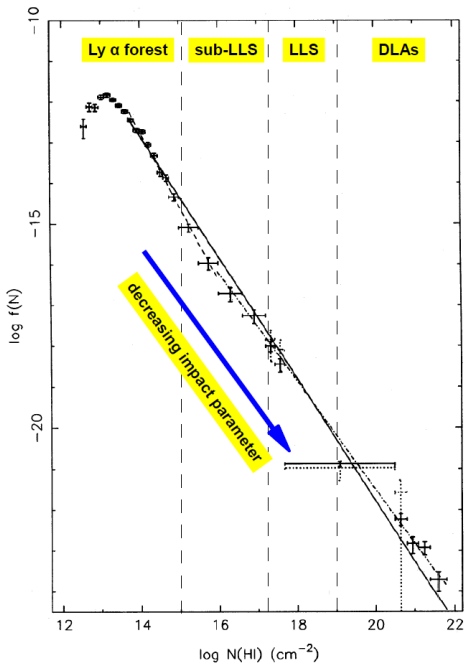

Figure 1.9: H I column-density-distribution function (CDDF) of neutral hydrogen in the IGM over several orders of magnitude. The cutoff at log N(H I) ~ 13 is due to sensitivity limits. Labeled are the different classification marks. Basic image taken from Petitjean et al. (1993).

1.4.2 Metals in the IGM

Apart from the Lyα forest, a variety of more narrow absorption features can be found in quasar spectra which can be identified as metal lines. These arise from elements that are heavier than hydrogen and helium and are called metals in astrophysics. Compared to the Lyα forest, these lines contribute only a small fraction to the overall absorption, but the content of information stored in them is still significant. They are usually harder to detect than the Lyα forest for several reasons. On the one hand, they are usually weaker and, thus, may be hidden between strong Lyα lines. On the other hand, some key transitions occur at wavelengths that are not covered by the observed spectra.
Since the metals have been produced in galaxies or rather in their stars, they trace the enrichment history of the IGM (e.g., Danforth and Shull 2008; Tripp et al. 2008, OD11). Furthermore, with these intervening metal systems and their connections to galaxies, it is possible to deduce outflow mechanisms and the star formation history of the host galaxies. In fact, in the review of Richter (2006) it is mentioned that one of the prime candidates for the metal enrichment of the IGM are starbursting dwarf galaxies which produce outflows that are able to enrich the surrounding IGM to the level that can be observed today. Finally, as the "missing baryons problem", there is also a so-called "missing metals problem" at $z \sim 2 - 3$. It describes the lack of metals in the galaxies, and also the IGM at that time, compared to the expected amount from the overall cosmic star-formation rate (Davé and Oppenheimer 2007, hereafter DO07).
To establish a coherent picture about metals in the IGM, at first, one has to describe the enrichment history of baryons in the Universe. This topic has become more and more important during the last 15 years, also because of the availability of hydrodynamical cosmological simulations. Since the outstanding work of Cen and Ostriker (1999a), these simulations are able to connect the models with the observations. Following DO07, it has been proven that even the most distant quasars as well as the IGM at $z \gtrsim 6$ show a substantial amount of enrichment. During the last $10 - 20$ years, the IGM has been observed in metal lines through all epochs from $z \sim 6$ to $z = 0$. In Figure 1.10, the results of a hydrodynamical simulation for the $z = 6 \rightarrow 0$ evolution of the metal fraction, the baryon fraction, and the mean metallicty are shown for several phases. In principle, the different phases are defined through their temperatures and densities (see DO07). One can see that at high redshift the diffuse IGM holds most of the metals. This is required to, for instance, slow down the star formation at early times which needs to be in agreement with observables, like the high-redshift galaxy luminosity functions. Therefore, in the model of DO07, early outflows are quite effective, which results in an IGM metal reservoir at $z = 6$. As time goes on, the diffuse structures start to collapse and outflows become less efficient. Finally, the baryons and metals cross over to more dense phases with the effect of increasing metallicity in halos

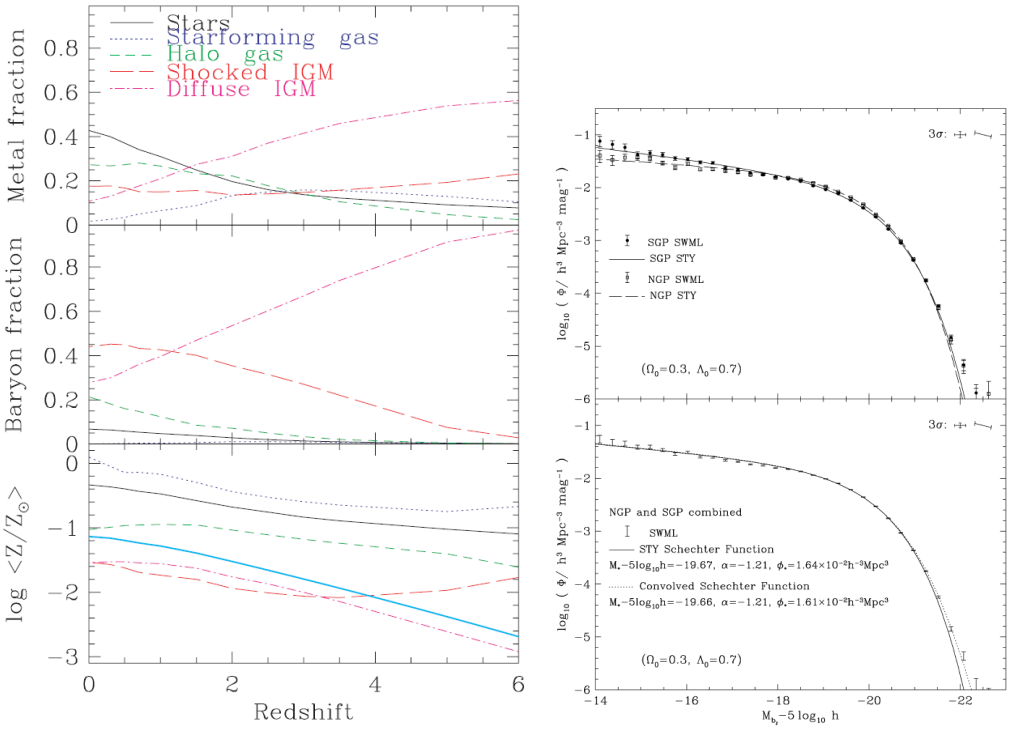

Figure 1.10: **Left panel:** the three panels show the results of a simulation of the evolution of the metal fraction, the baryon fraction and the logarithmic metallicity in solar units over the redshift range $z = 0 - 6$. The different lines represent different phases of the IGM. The thick cyan line in the bottom panel represent the mean mass weighted metallicity of the Universe (Davé and Oppenheimer 2007).
Right panel: example of a Schechter galaxy luminosity function. The upper panel shows the data points and the estimates for the noth and south galactic pole regions, whereas the bottom panel shows the combined results for $z = 0$. In the bottom panel, the parameters for the applied Schechter functions are labeled (Norberg et al. 2002).

and galaxies.

For the present epoch, most of the baryons reside in shock-heated gas with metallicities of $Z/Z_\odot \sim 0.2$, whereas most of the metals are bound in stars and the halos of galaxies. In the top panel of Figure 1.10, it is shown that stars have already obtained a mean metallicity of $\sim 0.1\ Z_\odot$ at early times, which has increased up to $\sim 0.5\ Z_\odot$ today. However, stars that are formed today are expected to have up to $\sim 1.0\ Z_\odot$. Here, one has to keep in mind that these numbers represent only mean metallicities. It is possible that the individual metallicity for particular regions in the IGM varies substantially. However, apart from the metal-enriched IGM at early times, one can say that current models predict a wide distribution of metals over all phases at all ($z < 6$) epochs with no clear dominant state, but with increasing cosmic age a trend to the more condensed phases like stars and galaxies is clearly visible.
Referring to the missing metals problem, these simulations suggest that at $z = 2.5$ half of the metals are still bound in the diffuse IGM phase. In this environment, the temperature is expected to be higher ($10^4\,\mathrm{K} \leq T \leq 10^5\,\mathrm{K}$) than possible only by photoionization. This high-redshift, warm-hot intergalactic medium (WHIM), which is not directly bound to galaxies but more wide spread, is heated due to a combination of gravitational forces and feedback effects and contains a substantial amount of baryons and metals. It is difficult to trace this hot gas phase by observations. That could be the reason for the "hidden" metals.
For the current research, OD11 have claimed three main questions as most important concerning the local IGM. These are:

- **What is the metallicity of the IGM?**
  As shown in Figure 1.10, current simulations suggest an increasing metallicity over time due to ongoing star formation. In the present-day Universe, at $z = 0$, a typical mean value on the order of 0.1 $Z_\odot$ is measured, whereas at earlier times, at $z = 2 - 3$, observations favor lower values in the range of 0.0003 – 0.01 $Z_\odot$ (Davé et al. 1998; Schaye et al. 2003). The problem concerning the

Table 1.3: Possible separation of different IGM phases.

Phase	T	δ
Diffuse	$< T_{\rm th}$	$< \delta_{\rm th}$
WHIM	$> T_{\rm th}$	$< \delta_{\rm th}$
Hot halo	$> T_{\rm th}$	$> \delta_{\rm th}$
Condensed	$< T_{\rm th}$	$> \delta_{\rm th}$

$T_{\rm th}$ is the transition temperature between the cold and the hot IGM state and $\delta_{\rm th}$ is a density parameter that describes whether the gas is bound or unbound.

metallicity at different times is that these systems do not necessarily reflect the same conditions at every point in time because of the cosmic expansion, increasing photoionization rates and ongoing metal production. This means that there are many corrections necessary to transform the sum of the metal column densities into an overall metallicity. Recent simulations done by OD11 have shown that, with ongoing structure formation, metals are typically found in overdense regions like halos. Depending on the favored wind model and enrichment model, the amount of metals bound outside halos drops from $\sim$ 20% at $z = 2$ to only $\sim$4% at $z = 0$. There are models that predict a higher fraction of metals outside of halos, but bound in the WHIM phase. It is part of ongoing research to investigate this hard-to-detect, warm-hot intergalactic medium to establish firm values for the metallicity to confirm or disprove these models or not.
In this work, the study of intermediate ions like Si III and C III in the IGM will help to discover the nature of intervening metal absorbers in the mildly ionized regime and provide additional information about the ionization and enrichment conditions of these systems.

- **What is the temperature of the enriched IGM gas?**
  Without any doubt, the temperature represents an excellent parameter to classify different gas phases in the IGM and ISM. With its indirect detectability via QSO absorption lines of metals, it is one of the connecting parameters between observations and simulations. Furthermore, it controls the ionization state of the gas and the included ions, and it is therefore crucial to understand the underlying physical processes, like shock-heating or cooling. To describe the properties of, for instance, the diffuse gas phase, it is of crucial importance to define the temperature by ion observations and to compare it to the available models and simulations.
  A possible temperature classification for the gas phases has been presented by OD11. They have distinguished between four main parts, summarized in Table 1.3, on the basis of their temperatures and related densities. They have defined $T_{\rm th} = 10^5\,{\rm K}$ as the transition temperature between the cold and the hot IGM state and $\delta_{\rm th}$ as a density parameter that describes whether the gas is bound or unbound. With this classification of the IGM, it is possible to study the amount and the distribution of metals in each phase individually, and to compare the detected results to those of simulations. It turns out that, for all studied models in OD11, most of the metals either reside in the cool condensed phase at $T < 10^4\,{\rm K}$, or in the intra-cluster medium at temperatures $T > 10^6\,{\rm K}$. The reason for the missing metals in the intermediate temperature range is that metal-line cooling is very efficient in this regime. Therefore, metal enriched gas in the range of $10^4\,{\rm K} < T < 10^6\,{\rm K}$ does not populate this gas phase for significant cosmic time scales, but rather transits to more stable phases.

- **How homogeneously are metals distributed in the IGM?**
  The transportation and mixing history of metals in the past and present directly leads to the question how metals are distributed in the Universe and especially in the IGM. As shown in Figure 1.10, in the early Universe, metal ejection from the first stars (Population III) was very efficient and enriched the IGM to an initial amount that can be detected at very high redshift ($z \sim 6$). As explained in the previous Sections, this behavior is required to be in line with other observations at high redshift (e.g., star formation rate, see D07). It is a matter of debate how the metal distribution evolves over time and what effects are triggered. For instance, well mixed metals will result in more efficient baryonic cooling processes that could result in an increased accretion rate, and, consequently a higher star-formation rate. However, this is not observed. Instead, observations suggest that metals are rather poorly mixed, which leads to the conclusion that the detection of a metal "cloud" does not necessarily imply anything about the overall distribution or the surrounding environment at all.

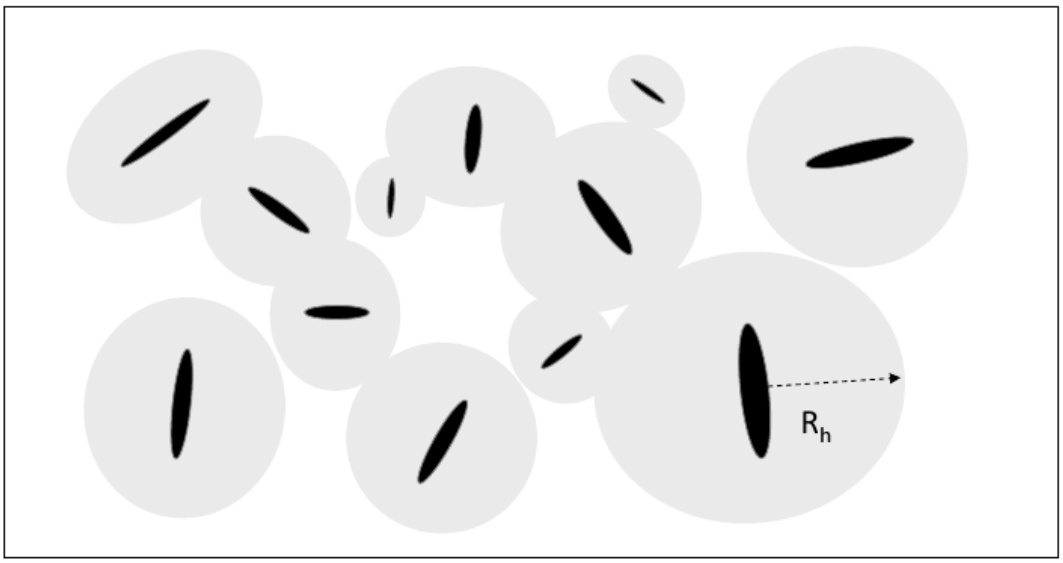

Figure 1.11: Schematic illustration of a typical distribution of galaxies. The grey-shaded areas indicate the projected cross section of their H I halos.[3]

The task for the future will be to increase the amount of studied systems and environments at all cosmic epochs. Finally, a full metal census in the IGM at all times may be possible with the next set of instruments. Future observations will be able to prove the simulations, with regard to the detailed interactions between all baryonic phases, at a new level. Therefore, new insights in galaxy formation and feedback, gas accretion and interaction, and the evolution of cosmic baryons over the whole lifetime of the Universe might be achieved.

[3]With kind approval of P. Richter, taken from his lecture of the intergalactic medium.

Table 1.4: Number densities for different ions.

Ion/absorbers	$d\mathcal{N}/dz$	Reference
strong Mg II	0.8 at $z = 0.5$	Kacprzak et al. (2008)
weak Mg II	1.06 at $z = 0.6$	Narayanan et al. (2007)
Ca II	0.117 at $z = 0.4$	Richter et al. (2011)
DLAs	0.045 at $z = 0$	Zwaan et al. (2005)

1.4.3 The connection between QSO absorbers and galactic halos

The next section is designed to provide some more detailed information about the connection between QSO absorbers and galactic halos. In Figure 1.11, a schematic random distribution of galaxies with their halos is shown. It is evident that the cross section of galaxies strongly depend on the size of the individual halos, which can be expressed in terms of their mean radius. Additionally, one has to consider the covering fraction, f_c, of the ion that is used for the observation. In that way, one can find a relation between the number density of absorbers in a given redshift interval, $d\mathcal{N}/dz$, and the covering fraction, $f_c \leq 1$, of an ion X in a galactic halo for a given (mean) radius R_h. Kacprzak et al. (2008) have shown that for the local Universe ($z = 0$), these parameters are directly related to each other by

$$\frac{d\mathcal{N}}{dz} = \frac{n_g \langle f_c \rangle c\pi R_h^2}{H_z}. \tag{1.1}$$

Here, n_g is the space density of galaxies, which can also be written as $n_g = \Phi^* \Gamma(x, y)$ with Φ^* being the number density of L^* galaxies and $\Gamma(x, y)$ the incomplete Gamma function. Furthermore, x is defined as $x = \alpha + 1$, with α being the slope of the faint end of the Schechter luminosity function for galaxies and $y = L_{min}/L^*$ where L_{min} is the minimum luminosity of galaxies that are considered in the observation (see right panel of Figure 1.10). It is possible to calculate the typical radius of the absorbing region around galaxies for individual ions if the corresponding covering fraction, the number density, and the galaxy density is known. In general, the number density is a common parameter for many different absorption systems. It describes their occurrence in the Universe and is often used to compare different types of absorbers (e.g. Richter et al. 2011). In Table 1.4, some of the most frequently used values for $d\mathcal{N}/dz$ for different ions and absorption systems are listed. Detailed considerations on the number density for Si II, Si III and C III can be found in Sections 4 and 5. More information about the individual parameters used in Equation 1.1 can be found in Richter (2012).
The crucial parameter is the covering fraction of the individual ions. It is a challenging task to estimate reasonable values for f_c(X) in the halos of distant galaxies due to the absence of a "scan" tool for the halos in different wavelength ranges. With the QSO absorption line spectroscopy technique it is, at least, possible to estimate reasonable values for f_c(X) for the Milky Way, which can be used to evaluate covering fractions for Milky Way-type galaxies. Thus, one has to transfer these local results to other distant galaxies with a special focus on the changing point of view (see Section 4). The space- and number density of galaxies, in turn, are more easily accessible through large sky surveys and statistic evaluations of the resulting density functions.
With respect to the galaxy-absorber relation, one has to add that, in most cases, the foreground galaxy is a few parsec separated to the line-of-sight of the background quasar, and usually very faint compared to the AGN. As explained in the previous Sections, this characteristic results in the appearance of intervening metal systems that can be used to serve as a tracer for the faint host galaxies. In Figure 5.11, a few galaxy-absorber pairs from the *HST*/COS data sample with labeled angular separations are shown (see Section 3.2).

1.4.4 The Mg II ion

The Mg II ion is of higher importance for the main part of this thesis than most of the other investigated ions. Therefore, the current state of the research connected to Mg II absorbers is discussed here. For short descriptions of other ions see Section 2.4.
One of the key tasks for ISM/IGM studies is the comprehension of the connection between the surrounding medium of the Milky Way and halos of other distant galaxies. Depending on the impact parameter, the previously described QSO absorption line technique provides a unique tool to investigate the inner and outer parts of halos over a large range of redshifts.
The best tracer for this metal-enriched environment around other galaxies is the Mg II $\lambda\lambda$2796, 2803 doublet. It is easily detectable in quasar spectra since it is shifted to optical wavelengths even for low

redshifts. Therefore, it is of great interest and has become one of the best studied ions referring to the gaseous halos of galaxies (e.g. MAGIICAT II catalog, see also Figure 5.10; Bergeron and Boisse 1991; Churchill et al. 2005; Kacprzak et al. 2007, and many others).
Being an α-element, ejected by SN type II, Mg II probes both weakly ionized outflowing CGM structures as well as infalling metal-enriched gas. It has presumably been produced by the first generation of stars, and, thus, it was able to enrich the intergroup and intergalactic space. Therefore, the understanding of the history and morphology of the Mg II absorbers probes the star-forming and enrichment history of the associated galaxies and the involved gas structures.
Mg II is detectable in H I environments from $\log N(\mathrm{H\,I}/\mathrm{cm}^{-2}) \simeq 16.5$ up to 21.5 and is expected to trace almost the same neutral and ionized gas phases like, for instance, Si II. During the last two decades, Mg II has been used to estimate various galactic parameters like galaxy luminosities, galaxy mass, star forming rates, galaxy morphologies and galaxy orientations (see Nielsen et al. 2013, and references therein). Steidel (1995) has shown that there is a weak correlation in the form of $R(L_K) \simeq 38h^{-1}(L_K/L_K^*)^{0.15}$ kpc between the size of Mg II halos and the luminosity of the host galaxy. Furthermore, Chen et al. (2010) have found that the extent of Mg II absorbing gas depends strongly on the total stellar mass, M_{star}, and weakly on the specific star-formation rate (sSFR):

$$R_{\mathrm{MgII}} \propto (M_{\mathrm{star}})^{0.28} \times (\mathrm{sSFR})^{0.11} \quad \text{with} \quad \mathrm{sSFR} = \mathrm{SFR/M_{star}}. \tag{1.2}$$

Nowadays, there is consensus that the class of Mg II absorbers can be divided into two main subclasses, the weak Mg II absorbers with equivalent widths $W_{\mathrm{r}}(2796) < 0.3$ Å and the strong Mg II absorbers with $W_{\mathrm{r}}(2796) > 0.3$ Å. The latter are thought to arise within impact parameters $< 35\ h^{-1}$ kpc of luminous $L > 0.05\ L^*$ galaxies, whereas the weak Mg II absorbers represent a more distinct population of objects at higher impact parameters of 35 – 100 kpc. Thus, they are more likely correlated to the star formation in dwarf galaxies (Narayanan et al. 2007). Apart from the confirmed connection of strong Mg II absorbers to luminous galaxies, it is still not clear whether such absorbers trace outflowing or rather infalling material (Ribaudo et al. 2011b). As shown in Figure 5.10, there is a clear transition in the $\partial\mathcal{N}/\partial W_{\lambda 2796}$ distribution at $W_0^{\lambda 2796} \approx 0.3$ Å that cannot be described by a simple power law or an exponential function and, thus, supports the concept of different populations (Nestor et al. 2005).
Referring to the evolution of Mg II systems in general, Nestor et al. (2005) and Narayanan et al. (2007) have demonstrated that there is a declining evolution in the redshift dependent number density $\mathrm{d}\mathcal{N}/\mathrm{d}z$ for weak absorbers with a peak at $z \sim 1.2$ (see left panel of Figure 4.8), as well as for the very strong absorbers ($W_0^{\lambda 2796} \geq 2$ Å) from $z = 1.9$ to 0.8, but not for those lying in the range of $0.3 < W_{\mathrm{r}}(2796) < 2.0$ Å. This strange behavior is only one example for our lack of knowledge of Mg II absorbers.
In this work the connection between HVCs in the Milky Way, other galaxies and Mg II absorbers is especially important. Many studies have shown that Mg II can be detected in HVCs around the MW. These would represent strong Mg II absorbers, if classified in the common scheme. Richter (2012) has shown that the number density of strong intervening Mg II absorbers,$(\mathrm{d}\mathcal{N}/\mathrm{d}z)_{\mathrm{MgII_{strong}}} \approx 0.5$, calculated by Kacprzak et al. (2008), is 2 – 3 times higher than the estimated $(\mathrm{d}\mathcal{N}/\mathrm{d}z)_{\mathrm{HVC}}$ for HVC. That means that the cross section of intervening Mg II absorbers is substantially larger, compared to H I absorbers with $\log N(\mathrm{H\,I}) \geq 17.5$. The reason for that is the Mg II ionization potential of 15 eV, meaning that it traces both the neutral and the lowly ionized phase, compared to only the neutral phase traced by H I. To confirm these results, it is necessary to estimate the Mg scii covering fraction of Milky Way HVCs in order to understand the relation between the HVCs and weak/strong Mg II absorbers, which is one of the purpose of this thesis.

1.5 Motivation

Since the main topic of this thesis are the gaseous environments and the CGM of the MW and other distant galaxies, the scientific goals can be summarized in the following questions.

a) *What is the contribution of HVCs to the cross section of strong Mg* II *absorbers in the halo of the Milky Way?*

The gaseous CGM plays an important role in the evolution of galaxies and their halo characteristics. We have explained that the HVCs play a crucial role in the MW, and, consequently, have been studied intensively during the last decades. Thus, we have a good idea about their nature and characteristics. However, these facts are basically limited to our own galaxy since it is challenging to observe HVCs in distant halos directly.
The idea is now, to investigate the connection between Galactic HVCs and weak/strong Mg II absorbers, since this class of objects has been studied in detail in the halos of distant galaxies. To achieve this, it is necessary to set up a well analyzed data set of HVC detections. To be comparable to the general Mg II statistics, one also has to take into account the internal point of view for our MW. This means that the MW has to be handeled as a QSO absorption line system. Finally, one can draw conclusions on the contribution of HVCs to the cross section of strong Mg II absorbers in the halo of the Milky Way.

b) *What is the contribution of HVCs to the overall number density of strong Mg* II *absorbers in the local Universe?*

We want to know how these conclusions for the MW can be applied to other MW-type galaxies. The contribution of HVCs to the overall number density, $\mathrm{d}\mathcal{N}/\mathrm{d}z$, of strong Mg II absorbers from the halos of distant galaxies is of interest since this result helps to unveil the nature of the strong Mg II absorbers. Consequently, these measurements allow us to conclude on the frequency of HVCs in the local Universe in general, and their contribution to gaseous in- and outflows.

c) *What information can be obtained from the absorption line and ionization parameters of intervening metal systems in relation to Galactic metal systems?*

In the second part of this thesis, we want to focus on the intervening metal systems in general. We use the newly available *HST*/COS data to obtain a detailed absorption-line statistics. Depending on the data quality, we use the photoionization program Cloudy to model local photoionization conditions in these systems. The results are compared to measurements of the Galactic metal systems. Then, we draw conclusions about the connection between intervening metal absorbers and the CGM of the Milky Way in general. Especially for the rarely analyzed intermediate ions like Si III and C III, we get new results for their typical detection radii and ionization parameters.

d) *Do intervening metal absorbers represent HVC analogs with similar properties as Galactic HVCs?*

Finally, the main question is whether intervening metal absorbers can be identified as distant HVC analogs. Certainly, to achieve this goal, many different aspects have to be considered. We want to compare parameters like the column density distribution functions, the component structure and the ionization conditions of both classes of objects. Furhermore, there should be host galaxies detectable within a certain impact parameter of intervening metal systems. However, we find evidence for the HVC phenomen being common at least for MW-type galaxies in the local Universe besides the known H I 21cm detections. We show that intervening metal systems can be handeled as tracers for HVCs around other MW-type galaxies.

Chapter 2

Fundamentals

The next chapter introduces detailed explanations and discussions on basic concepts and methods, that are used in this work. The first section describes the current model of cosmology, the cosmological redshift, the process of radiative transfer and some important parameters related to absorption lines and line profiles. The later sections explain the most common analyzing procedures with their properties, potentials, and constraints.

2.1 The ΛCDM Model

As mentioned in the introduction, the nowadays accepted model to describe the evolving Universe is the so-called Lambda Cold Dark Matter Model, or standard model of Big Bang cosmology. Beside others (e.g., cyclic model, steady-state model), it is in very good agreement with the observations and its predictions have been proved in multiple cases (e.g., large scale structure, CMB).
In the ΛCDM cosmology, Λ represents the cosmological constant, introduced by Albert Einstein in his general theory of relativity in 1916, and, nowadays, identified as the dark energy driving the accelerated expansion of the Universe. For the mysterious dark matter, first introduced in 1933 by Fritz Zwicky, a direct evidence is still missing. Indirect indications are the galactic rotation curves, the structure of galaxy groups, and clusters and gravitational lensing (e.g., Zwicky 1933; Wilson et al. 2001). In contrast to the formerly considered hot dark matter model, in the CDM model the dark matter particles have low velocities, which match the observations much better. That is why it is called "cold". In principal, the ΛCDM model predicts many effects that should be observable. The four most essential ones are described here in brief.

- **The metric expansion of the Universe**
  First discovered in 1928, Edwin Hubble showed that almost all galaxies are moving away from us. This results in a redshift of their spectra (Hubble 1929). Six years before, based on Einsteins field equations, Alexander Friedman developed a pair of equations, called the Friedmann Equations (2.1), which, depending on the used parameters, can describe an expanding Universe with a certain shape:

$$H^2 = \left(\frac{\dot{a}}{a}\right)^2 = \frac{8\pi G}{3}\rho - \frac{kc^2}{a^2} \qquad \dot{H} + H^2 = \frac{\ddot{a}}{a} = -\frac{4\pi G}{3}\left(\rho + \frac{3p}{c^2}\right). \tag{2.1}$$

  Here, H is the Hubble parameter, G and c are universal constants with G being the gravitational constant and c is the vacuum speed of light. Finally, ρ is the energy density, p is the pressure, k is the bending parameter, and a the scale factor of the Universe.
  Based on the simple assumption that the Universe is spatially isotropic and homogeneous in all directions, and that no point of view stands out (Cosmological principle), these equations connect the energy density of the Universe with its topology. Hence, one of the most important parameters included in this theory are the so-called density parameters,

$$\Omega_{\mathrm{dm}} = 0.20 \pm 0.020 \qquad \Omega_{\mathrm{b}} = 0.042 \pm 0.002 \qquad \Omega_\Lambda = \frac{\Lambda}{3H_0^2} = 0.76 \pm 0.020, \tag{2.2}$$

  with Ω_{dm}, being the dark matter density parameter, Ω_{b} the baryonic matter density parameter and Ω_Λ the dark energy density parameter (Springel et al. 2006). The combination and strength of these parameters in the well-known expansion equation (see Equation 2.3) combined with the Hubble constant H and the scale factor a will define the shape and the rate of the expansion in the Universe. In Equation 2.3, Ω_{R} is the radiation density parameter and Ω_{M} is the matter density

(dark + baryonic). With the detection of Edwin Hubble in 1928, the expectations of this theory were proven and the Friedmann Equations became one of the fundamental astronomical concepts:

$$H^2(t) = \left(\frac{\dot{a}}{a}\right)^2 = H_0^2[a^{-4}(t)\Omega_\mathrm{R} + a^{-3}(t)\Omega_\mathrm{M} + a^{-2}(t)(1 - \Omega_\mathrm{M} - \Omega_\Lambda) + \Omega_\Lambda]. \tag{2.3}$$

- **The CMB and the large scale structure**
  The expansion of the Universe implies that, at a certain point in the past, everything was concentrated at one point of infinite temperature and density. This incident is known as the Big Bang, where space and time were created. Despite this event happened roughly 13.7 billion years ago, astronomers predicted an afterglow that should be measurable even today (Dicke et al. 1946; Gamow 1948). Indeed, this microwave radiation was detected in 1965 by Arno Penzias and Robert Wilson with their Dicke radiometer at the Bell Laboratories in New Jersey (Penzias and Wilson 1965). During the next decades it turned out that this radiation is not distributed evenly over the whole sky, but has an anisotropy in the order of $\frac{\Delta T}{T} \sim 10^{-5}$ (see Figure 2.1; Bennett et al. 2003). Tiny density fluctuations in the early epochs of the Universe are the reason for these oscillations in the CMB. Primarily driven only by gravity, large simulations established that these inhomogenities are the reason for the large-scale structure in the Universe (see Figure 1.1). The formation over time is very well described by the hierarchical model of matter aggregation (Press and Schechter 1974).

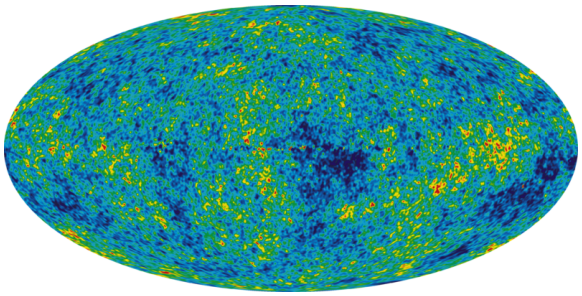

Figure 2.1: All-sky map of the anisotropy of the microwave background, recorded with the WMAP (Wilkinson Microwave Anisotropy Probe; Bennett et al. 2003).

- **The abundance of the most frequent elements**
  Because of the use of spectrosopic methods, we know that hydrogen with $\sim$75% is by far the most abundant element in the Universe. All other elements, except a small fraction of helium and lithium, have been produced in stars through different stages of nuclear fusion and stellar explosions. The theory of the Big Bang nucleosynthesis, developed in 1948 by Ralph Alpher and George Gamow, says, that during the first few minutes after the Big Bang, hydrogen, helium and a small fraction of lithium have been produced in a specific relation and up to a certain mass (Alpher et al. 1948; Coc et al. 2004). Within the ΛCDM model, this theory is combined with the postulation and indirect detection of dark matter, which predicts the actual observed matter density and composition in the Universe very well.

With these observations and theories, the ΛCDM model respresents the most complete and best verified theory of the Universe we have today. Even in 1998, one of the last big predictions of an accelerating expansion was proven right through supernova type Ia measurements (Riess et al. 1998). Nevertheless, there are still open questions. Especially, with the dark matter and dark energy, there exist two important **theoretical** concepts, which represent $\sim$95% of the Universe with a **direct** observational evidence still missing.

2.1.1 Cosmological redshift

In the previous section, we have discussed that the Universe itself is expanding. This behaviour has consequences for the light that travels through space, and which is used to observe extragalactic objects. From the comparison to laboratory experiments, we know that most of the transition lines in the spectra of distant galaxies are shifted to longer wavelengths. In the early times, the scientists tried to explain this phenomenon with the well-known Doppler effect that is also observable on earth and in experiments. Shortly after this discovery, E. Hubble verified a law, which originally was predicted by Georges Lemâitre

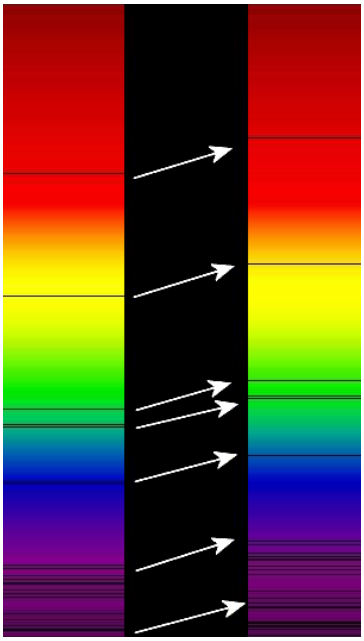

Figure 2.2: Example for a set of cosmologically redshifted lines (right panel) in a spectrum of a galaxy cluster, compared to the same lines in the spectrum of the sun (left panel)[1]

two years before. It connects the distance of a galaxy with its velocity. This relation is now known as Hubble's law, one of the most important basic concepts in modern cosmology,

$$v = H_0 \cdot D. \tag{2.4}$$

Today, we know that the Hubble constant, H_0, is connected to the scale factor, a, and the density parameter of an expanding Universe as described in Equation 2.3. To understand the relation between the definition of the redshift, $(1 + z) = \lambda_{\mathrm{obs}}/\lambda_0$, and this property of space, one has to assume two observers, which are positioned with a certain separation, $\mathrm{d}r$, along a line of sight towards a light emitting object. Following the explanations given by Schneider (2006), these two comoving observers will see each other at relative velocities of $\mathrm{d}v = H(t)\mathrm{d}r$ due to the cosmic expansion. Assuming that there was light emitted at t_{e}, these two observers will measure their relative movement as a redshift of that light in the form

$$\frac{\mathrm{d}\lambda}{\lambda} = \mathrm{d}z = \frac{\mathrm{d}v}{c}. \tag{2.5}$$

Thus, the light needs the time $\mathrm{d}t = \mathrm{d}r/c$ to travel from one observer to the other. With the Hubble parameter and the scale factor $\dot{a} = \mathrm{d}a/\mathrm{d}t = H(t)a$, one can find that

$$\frac{\mathrm{d}\lambda}{\lambda} = \frac{\mathrm{d}v}{c} = \frac{H(t)}{c}\mathrm{d}r = H(t)\mathrm{d}t = \frac{\mathrm{d}a}{a}, \tag{2.6}$$

which can be integrated. Thus, one gets $\lambda = Ca$ with C being the integration constant that is defined as the wavelength of the object that is observed today at $a = 1$, $C = \lambda_{\mathrm{obs}}$. Finally, one can estimate the wavelength of the light when it was emitted as $\lambda_{\mathrm{e}} = a \cdot \lambda_{\mathrm{obs}}$. It is clear that there is a direct relation between the redshift and the scale factor,

$$1 + z = \frac{1}{a}. \tag{2.7}$$

This relation is of significant importance for cosmology. It means that the observed redshift of an object is a measure of its age and its approximate distance. And therefore, the properties of the Universe at earlier times can be probed. Furthermore, there is a clear difference between the Doppler redshift and this cosmological redshift. The reason for the Doppler effect is a real radial motion of the object. In case of the cosmological redshift, the change in wavelength does not necessarily result from a peculiar velocity, but from the expanding space between the observer and the object. Thus, one can conclude that observed redshifts, for small distances, are basically caused by the Doppler motion of those systems, due to the dominance of the gravity force at small scales (e.g., Galaxies, solar system etc.), which

[1] Based on a public domain image created by Harold T. Stokes, and amended by Ian Tresman. Original upload in English Wikipedia.

neglects the expansion of the space and keeps the objects bound. Nevertheless, for low redshifts, $z \ll 1$, one can approximate $z = H_0 D/c$ with $v \approx zc$. Figure 2.2 shows an example of a set of redshifted lines in the spectrum of a distant galaxy cluster, compared to those lines in the spectrum of the sun.
Closely connected to the cosmological redshift is the so-called **comoving distance**. In an expanding Universe there are many different possibilities for a definition of distance. The most known ones are the parallax distance, the luminosity distance, the angular diameter distance, the comoving distance, or the proper distance. The explanation of every of these distances is beyond the scope of this work, but the comoving distance will be discussed briefly.
The individual redshifts that result from the Hubble expansion can be transformed into a distance, X, which is defined as the proper distance divided by the ratio of the scale factors at different times. In other words, X is the comoving distance between two objects that stays constant over time if both objects are only moving with the Hubble flow. Using the definition for the redshift-dependent Hubble constant,

$$H(z) = \sqrt{\Omega_{\mathrm{M}}(1+z)^3 + \Omega_{\mathrm{R}}(1+z)^2 + \Omega_{\Lambda}} \tag{2.8}$$

one can now calculate the comoving distance as

$$X = D_H \int_0^z \frac{\mathrm{d}z'}{H(z')} = \int_{t_\mathrm{e}}^t c \frac{\mathrm{d}t'}{a(t')}, \tag{2.9}$$

with $D_H = c/H_0$ being the Hubble distance. This integral can be solved numerically. With the combination of the ΛCDM constants described in Section 2.1 it is possible to convert each redshift into a corresponding distance that stays constant if the object is only moving with the Hubble flow. This distance measure is the most frequently used in modern cosmology since all other measures on large scales can be expressed in terms of the comoving distance. For more detailed information and discussions about the relation between expansion, redshift and comoving distance in the sense of general relativity see, for instance, Davis and Lineweaver (2004).

2.2 Absorption line theory

In order to understand the different procedures used in this work, we have to provide some information about the physics of the processes which take place in the interstellar and intergalactic gas. Within the following section, the properties and conditions of the absorption processes are discussed and the resulting absorption lines with their behavior and intrinsic physics are described (following de Boer 2007; Draine 2010).
To apply absorption line spectroscopy, a bright background object, which provides continuum radiation, is necessary. Since we use active galactic nuclei (AGNs), like quasi stellar objects (QSOs) and Seyfert galaxies, this procedure is called QSO absorption line spectroscopy. Figure 1.8 illustrates this method. Assuming a bright background object, which provides a certain frequency-dependent intensity, I_ν, an intervening cloud of material will interact with this emitted radiation only through emission and absorption, if scattering (e.g., by dust grains or electrons) is neglected. The change in the intensity of the radiation is described by the equation of radiative transfer,

$$\mathrm{d}I_\nu = -I_\nu \kappa_\nu \mathrm{d}s + j_\nu \mathrm{d}s, \tag{2.10}$$

with the attenuation coefficient κ_ν, the path length $\mathrm{d}s$, and the emissivity j_ν. The first term, $-I_\nu \kappa_\nu \mathrm{d}s$, describes the loss in intensity due to absorption and stimulated emission processes, whereas the second term, $j_\nu \mathrm{d}s$, describes the gain of intensity due to spontaneous emission. Equation 2.10 is often used in the form

$$\mathrm{d}I_\nu = -I_\nu \mathrm{d}\tau_\nu + S_\nu \mathrm{d}\tau_\nu \quad \text{with} \quad \mathrm{d}\tau_\nu \equiv \kappa_\nu \mathrm{d}s \quad \text{and} \quad S_\nu \equiv j_\nu/\kappa_\nu. \tag{2.11}$$

Here, τ is the **optical depth** of the absorption and S_ν is the so-called source function. Integration over $\mathrm{d}\tau$ leads into the integral form of the equation of radiative transfer

$$I_\nu(\tau_\nu) = I_\nu(0) e^{-\tau_\nu} + \int_0^{\tau_\nu} e^{-(\tau_\nu - \tau')} S_\nu \mathrm{d}\tau', \tag{2.12}$$

which solves Equation 2.11 under the assumption that no scattering takes place. If emission can also be neglected, the second term of Equation 2.12 can be eliminated, and the optical depth-dependend intensity is only defined by the exponential decline of the initial intensity, $I_\nu(\tau_\nu) = I_\nu(0) e^{-\tau_\nu}$.

In the next step, we want to have a detailed look at the intrinsic shape of absorption lines and the parameters which are necessary to describe them. The rate, at which photons are absorbed by material at the transition $l \rightarrow u$, can be estimated as

$$\left(\frac{\mathrm{d}n_\nu}{\mathrm{d}t}\right) \approx n_l u_\nu \frac{c}{h\nu} \int \sigma_{lu}(\nu)\mathrm{d}\nu, \tag{2.13}$$

with n_l, the number of absorbers at level l, $\sigma_{lu}(\nu)$, the cross section for photons with frequency ν for the transition $l \rightarrow u$, and u_ν the photon density at ν. Here, l always means the lower transition state and u the upper one. We assume that the photon density and energy can be approached as constant over ν. Additionally, the cross section, $\sigma_{lu}(\nu)$, of a transition $l \rightarrow u$ depends on the normalized line profile Φ_ν and the Einstein coefficient A_{ul}, or the **oscillator strength** f_{lu}, which are both measures of the strength of the absorption,

$$\sigma_{lu}(\nu) = \frac{g_u}{g_l}\frac{c^2}{8\pi\nu_{lu}^2}A_{ul}\phi_\nu = \frac{\pi e^2}{m_e c} f_{lu}\Phi_\nu \qquad \text{with} \qquad f_{lu} \equiv \frac{m_e c}{\pi e^2}\int \sigma_{lu}(\nu)d\nu. \tag{2.14}$$

In this work, the oscillator strength is usually used as a given parameter taken from different tables (e.g., Morton 2003), to estimate other properties of the absorbers, like the column densities or equivalent widths. In the 6th column of Table 2.1, the used values are listed.
The shape of an absorption profile results from the ratio of the intrinsic profile, Φ^{intr} (see Equation 2.15), and the thermal velocity distribution, $\Delta v^{\mathrm{therm}}$, of the absorbing gas. Due to the uncertainty of the energy levels of the different transition states, Φ^{intr} is no δ-function but can be approximated by a Lorentz profile,

$$\Phi_\nu^{\mathrm{intr}} = \frac{4\gamma_{ul}}{16\pi^2(\nu-\nu_{ul})^2 + \gamma_{ul}^2}. \tag{2.15}$$

To compare the intrinsic broadening of the line to other effects, Φ_ν^{intr} can be transformed into a velocity width $(\Delta v)_{\mathrm{FWHM}}^{\mathrm{intr}}$ which depends on the energy and the oscillator strength of the transition (see Equation 2.16),

$$(\Delta v)_{\mathrm{FWHM}}^{\mathrm{intr}} = 0.116\left(\frac{h\nu}{I_{\mathrm{H}}}\right)\frac{g_l}{g_u} f_{lu}\mathrm{km\,s^{-1}}, \tag{2.16}$$

with I_{H}= 13.6 eV, the ionization energy of hydrogen and $g_{l/u}$ the degree of degeneracy of the lower and upper transition level. Even though, most of the considered lines have very small intrinsic line widths (see Table 2.1, 7th column), this effect has to be considered for detailed fitting or modeling procedures.
The second important line forming effect results from the general spatial motion of the absorbing material. Therefore, it has a velocity distribution, p_ν, which is often approximated by a Gaussian profile (see Equation 2.17). This assumption is completely valid if the line broadening is only an effect of the thermal motion (thermal Doppler broadening). In this case, the velocity distribution can be approximated as

$$p_\nu = \frac{1}{\sqrt{2\pi}}\frac{1}{\sigma_\nu}e^{-(\nu-\nu_0)^2/2\sigma_\nu^2} \qquad \text{with} \qquad \Delta v_{\mathrm{FWHM}}^{\mathrm{therm}} = \sqrt{8\ln 2}\sigma_\nu = 2\sqrt{\ln 2}b. \tag{2.17}$$

Here, σ_ν, is the one dimensional velocity dispersion, which often is referred to as the **Doppler parameter**, $b = \sqrt{2}\sigma_\nu$, when the $\sqrt{2}$ factor is included. Another frequently used relation for the Doppler parameter is

$$b^2 = b_{\mathrm{th}}^2 + b_{\mathrm{non-th}}^2 \qquad \text{with} \qquad b_{\mathrm{th}} = \sqrt{\frac{2kT}{m}} \approx 0.129\sqrt{\frac{T}{A}}\mathrm{km\ s^{-1}}. \tag{2.18}$$

Here m is the particle mass, T the temperature, and A the atomic weight of the element (e.g., Richter et al. 2006). With the assumption of pure thermal broadening, this correlation can be used to define temperatures of the analyzed gas phase. But in reality, it is appropriate to expect other additional broadening effects, which also imprint a certain velocity distribution on the gas (e.g., turbulence, shocks etc.).
To describe the absorption lines, we have to combine both discussed effects to get the combined line profile, Φ_ν. This can be done by a convolution of the intrinsic line profile Φ_ν^{intr} (see Equation 2.15) and the velocity distribution p_ν (see Equation 2.17) with the result of $\Phi_\nu = \int p_\nu(\nu) \otimes \Phi_\nu^{\mathrm{intr}}\cdot\mathrm{d}\nu$. This profile is called a **Voigt-profile**,

$$\Phi_\nu^{\mathrm{Voigt}} \equiv \frac{1}{\sqrt{2\pi}}\int \frac{1}{\sigma_v}\cdot e^{-v^2/2\sigma_v^2}\cdot\frac{4\gamma_{ul}}{16\pi^2[\nu-(1-v/c)\nu_{ul}]^2+\gamma_{ul}^2}\mathrm{d}v, \tag{2.19}$$

which is often used in fitting procedures. Unfortunately, this profile cannot be computed analytically, but there are some approximation procedures, which will not be discussed here but can be found in the literature (e.g., Draine 2010).
Another important parameter related to absorption lines is the resolution, R, of the used instrument (see also Chapter 3). It is defined as $R = \lambda/\Delta\lambda$ and, thus, depends on the construction properties of the used grating. Typical resolutions of $R \approx 19\,000$ mean that, in the velocity frame, structures with a velocity dispersion of ~ 16 km s^{-1} can be resolved.
For the characterization of the investigated lines, we have to discuss three main parameters briefly. They are called the **column density** N, the **equivalent width** W and the **Doppler parameter** b. Since each of them having different significance, all are used in analyzing techniques, as described in Section 1.4. For instance, on the one hand, for different regimes of the optical depth (e.g., $\tau \ll 1$, $\tau \gg 1$), the column density is strongly coupled with the equivalent width, which is important in the curve of growth analysis. On the other hand the equivalent width contains no information about the component and velocity structure of the absorption. This information can be obtained with the line-profile fitting/modeling. Basically, the column density and the equivalent width contain information about the amount of material present along the line of sight, whereas the Doppler parameter is a measure of the internal velocity structure resulting from thermal and turbulent motions. For a detailed discussion see the following sections.
If one wants to compile ionization models like we do in Chapter 5, it is useful to define the ionization parameter, U, as the ratio of the density of the ionizing photons to the total density of the material. In general, it is used for hydrogen with $n(\mathrm{H})$, the total hydrogen density, $Q(\mathrm{H})$, the number of hydrogen-ionizing photons and $\Phi(\mathrm{H})$, the flux of ionizing photons hitting the surface of the modeled area. Hence, the ionization parameter can be defined as

$$U \equiv \frac{Q(\mathrm{H})}{4c\pi r_0^2 n(\mathrm{H})} \equiv \frac{\Phi(\mathrm{H})}{n(\mathrm{H})c}, \tag{2.20}$$

with r_0, being the distance between the ionized surface and the core of the modeled region.

2.3 Analysing procedures

In the following, techniques to analyze absorption lines and their advantages and disadvantages are discussed. In general, there are three main approaches, which are called the curve of growth method (COG), the apparent optical depth method (AOD), and direct line-profile fitting.

2.3.1 Curve of growth method

It is possible to estimate the total strength of the absorption via the the **equivalent width**, W, as

$$W \equiv \frac{1}{\nu_0}\int\left(1 - \frac{I_\nu}{I_\nu(0)}\right)\mathrm{d}\nu = \frac{1}{\nu_0}\int(1 - e^{-\tau_\nu})\mathrm{d}\nu, \tag{2.21}$$

with I_ν being the intensity of the flux and $I_\nu(0)$ the intensity without any absorption (e.g., Draine 2010). That means, the total absorbed flux can be measured even when there are unresolved subcomponents in the absorption feature because of the $W \sim I_\nu/I_\nu(0)$ behavior. Additionally, the optical depth, τ_ν, can be related to the column density as

$$\tau_\nu = \frac{\pi e^2}{m_e c} f_{lu} N_l \phi_\nu \left[1 - \frac{N_u/g_u}{N_l/g_l}\right] \qquad \text{with} \qquad N_l = \int n_l \mathrm{d}s \qquad \text{and} \qquad \int \phi_\nu \mathrm{d}\nu = 1. \tag{2.22}$$

In Equation 2.22, we neglect stimulated emission assuming $\frac{N_u/g_u}{N_l/g_l} \ll 1$, which is true for interstellar and intergalactic absorption. Therefore, one can directly conclude that $\left[1 - \frac{N_u/g_u}{N_l/g_l}\right] \approx 1$.
To obtain a relation between the column density and the equivalent width, we have to distinguish between different types of lines in terms of the optical depth. The most frequent assumption is optically thin absorption ($\tau \ll 1$). An example for such a line is shown in the upper panel of Figure 2.3. For these cases, the $(1 - e^{-\tau})$ term in Equation 2.21 can be approximated as $(1 - e^{-\tau}) \approx \tau - \tau^2/2$ in the first order, which leads to

$$W = k \cdot N_l f_{lu} \lambda_{lu} \cdot \frac{1}{1 + \tau/(2\sqrt{2})} \qquad \text{with} \qquad k = 8.853 \times 10^{-13}\,\mathrm{cm}. \tag{2.23}$$

For small values of the optical depth ($\tau \to 0$), Equation 2.23 results in a very simple relation between the column density and the equivalent width

$$W = k \cdot N_l f_{lu} \lambda_{lu}. \tag{2.24}$$

The assumption for the linear part of the $N_l - W$ relation gets invalid at higher optical depths. This fact has to be considered as the absorption feature is saturated (see middle panel of Figure 2.3). In this case, there is no exact solution for the $N_l - W$ relation, but the equivalent width can be approximated as dominated by Doppler-broadening and, therefore,

$$W \approx \frac{(\Delta\nu)_{\mathrm{FWHM}}}{\nu_0} \approx \frac{2b}{c}\sqrt{\ln(\tau_0/\ln 2)} \qquad [\text{Å}]. \tag{2.25}$$

Finally, for this case one gets the relation

$$W \approx \sqrt{\ln\left(N_l f_{lu}\lambda_{lu} \cdot \frac{k}{b}\right) \cdot \frac{2b}{c}} \quad \text{with} \quad k = \frac{\sqrt{\pi}e^2}{\ln 2 m_e c}, \tag{2.26}$$

which shows that in this particular case, W depends on $N_l f_{lu}\lambda_{lu}$, but **also** on the Doppler parameter b. Due to the weak increase of the equivalent width with increasing column density, this regime is often called the flat portion of the curve of growth. As shown in Figure 2.4, slight changes in W will result in significant changes in N. Because of this fact and due to the dependence on the Doppler parameter, in practice, one needs very accurate measurements of these parameters to use the COG-technique if applied to saturated lines.

Finally, for very high values of the optical depth ($\tau \gg 1$), the line starts to produce damping wings

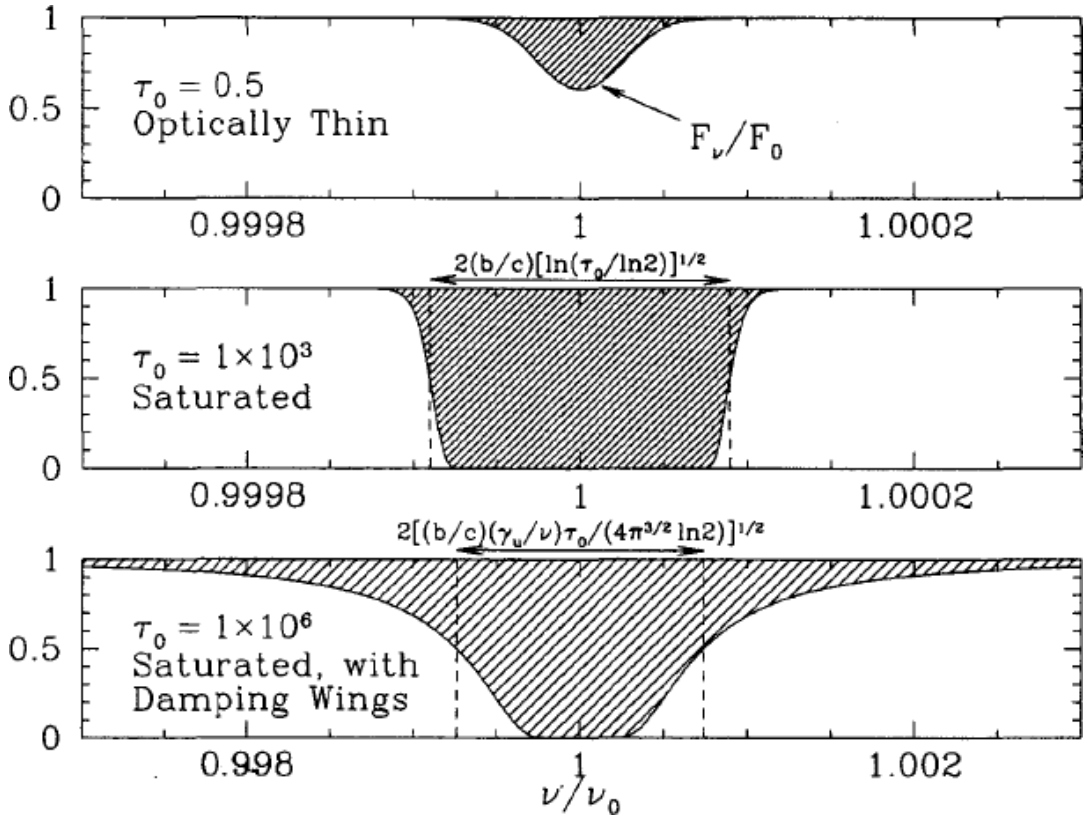

Figure 2.3: Three absorption lines with different optical depths, representing the three regimes ($\tau \ll 1$, $\tau \approx \tau_{\mathrm{sat}}$, $\tau \gg 1$), which are important for the COG-analyses.[2]

due to the complete saturation of the Doppler core, as shown in the lower panel of Figure 2.3. This behavior is often approximated with Lorentz profiles and, therefore,

$$\tau_\nu \approx \frac{\pi e^2}{m_e c} N_l f_{lu} \frac{4\gamma_{lu}}{16\pi^2(\nu - \nu_0^2) + \gamma_{lu}^2} \tag{2.27}$$

[2]from Draine,B.T., "Physics of the interstellar and intergalactic Medium", p.78.

can be assumed. Thus, the $N_l - W$ relation for the damped regime can be written as

$$W = \sqrt{k \cdot N_l f_{lu} \lambda_{lu}} \quad \text{with} \quad k = \frac{e^2}{m_e c^2} \cdot \frac{\gamma_{lu} \lambda_{lu}}{c}. \tag{2.28}$$

Consequently, there is again a rather weak dependence of the equivalent width on the column density in this regime.
Since we have discussed all three important parts of the $N_l - W$ relation, we are able to introduce a complete picture of the curve of growth (COG) for different Doppler parameters (see Figure 2.4).
Assuming there is an optical thin absorption line, $N_l f_{lu} \lambda_{lu}$ can be estimated easily with the equivalent width and the linear relation between W and N (see Equation 2.24). If one has two or more saturated lines available, that only differ in the product of $f\lambda$, then the (pure thermal) Doppler parameter can be defined. Thus, $N_l f_{lu} \lambda_{lu}$ can be estimated, while the absorption takes place on the flat part of the curve of growth. In this case, one has to keep in mind that $N_l f_{lu} \lambda_{lu}$ is extremely sensitive for small changes in W.
In general, the COG-method is useful to get rough estimates of the column density without knowing anything about the internal velocity and component structure of the absorption. This, clearly, is a problem if there are several clouds which cover each other, or if internal clumping has to be considered. Even broadening effects due to turbulent mixing will result in errors when analyzed with the COG-method.

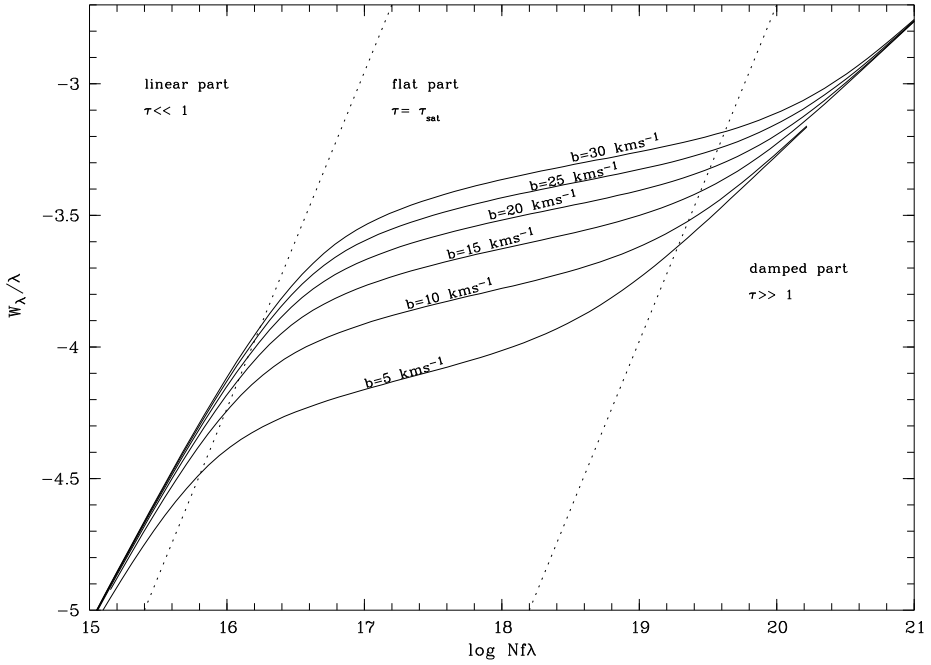

Figure 2.4: Curves of growth for different Doppler parameters. Indicated are the three regimes for the optical depths where the COG behaviour changes.

2.3.2 The Apparent Optical Depth (AOD) method

In Section 2.2, we have shown that the radiation intensity of any galactic object detected with a certain instrument can be described as $I(\lambda) = I_0(\lambda) \cdot \exp[-\tau(\lambda)]$, with τ being the optical depth of the absorption line (Savage and Sembach 1991). Since the data is affected by the recording instrument itself, we can define an apparent optical depth τ_a as

$$\tau_a(\lambda) = \ln\left(\frac{I_0(\lambda)}{I_{\rm obs}(\lambda)}\right). \tag{2.29}$$

The relation between τ and τ_a is given by a parameter called the Line-Spread-Function (LSF), Φ, which has an individual shape for each instrument (see, for instance, Figure 3.2),

$$\tau_a(\lambda) = \ln\left[\frac{1}{\exp(-\tau(\lambda) \otimes \Phi(\Delta\lambda)}\right]. \tag{2.30}$$

To simplify this relation, one can assume that we are only analyzing non-saturated lines which means $\tau \ll 1$. This will result in

$$\tau_a(\lambda) = \tau(\lambda) \otimes \Phi(\Delta\lambda). \tag{2.31}$$

The LSF has to be considered since it is related to the resolution of the instrument indirectly (FWHM(Φ) $\sim 1/R$). Therefore, one can assume that $\tau_a \approx \tau$ for FWHM(line) $\gg$ FWHM(Φ).
For appropriate data one can use the relation

$$\tau(\lambda) = \frac{\pi e^2}{m_e c^2} f\lambda^2 N(\lambda) \tag{2.32}$$

to estimate the observed optical depth profile in a direct way. Equation 2.32 can be expressed in terms of the velocity,

$$\tau(v) = \frac{\pi e^2}{m_e c} f\lambda N(v) = 2.654 \times 10^{-15} f\lambda N(v). \tag{2.33}$$

Finally, the total column density N can be estimated by the complete integration over $N(v)$ in Equation 2.33

$$N = \frac{m_e c}{\pi e^2 f\lambda} \int \ln \frac{I_0(v)}{I(v)} \mathrm{d}v. \tag{2.34}$$

The column densities derived with the AOD method can be taken as lower limits if there are no unresolved subcomponents. Compared to the COG-method, these lower limits provide better column densities, because the lines have not to be on the linear part of the COG. There is also no need to know the Doppler parameter as it is for the COG-method. On the other hand, this means a loss of information. But, if there are two or more absorption features of one ion available which differ in $f\lambda$, additional information concerning line saturation can be gained (see Savage and Sembach 1991). These facts lead to the conclusion that for high-resolution instruments like STIS ($R \sim 45\,000$, see Section 3), one can apply the AOD method straight-forward for unsaturated lines. For low-resolution instruments like COS ($R \sim 18\,000$), one has consider the LSF due to the instrumental effects on the absorption profiles.

2.3.3 Voigt-profile fitting

Another important technique is the Voigt-profile fitting. First, one needs a program which is able to produce Voigt profiles (see Section 2.2, Equation 2.19). In our case we use the `Fitlyman` routine of the *Midas* package, which is an European Southern Observatory (ESO) program, designed for astronomical data reduction and other applications[3] (see Fontana and Ballester 1995). With this program we are able to approximate absorption features within normalized data with Voigt profiles of high complexity. Additionally, `Fitlyman` allows the input of Doppler parameters and multi-component systems, as well as fixing several input parameters. This offers the potential to resolve multi-component structures, even in systems where the absorption lines are blended. In practice, with a set of input parameters, `Fitlyman` even allows to apply a χ^2 goodness test of the fit, scaling with the data quality or the S/N ratio, respectively,

$$\chi^2 = \sum \frac{(\mathrm{data} - \mathrm{fit})^2}{\mathrm{fit}}. \tag{2.35}$$

That means, after each iteration, one can compare the resulting fit to the imported data and starts the next iteration with new parameters. In general, `Fitlyman` is able to execute a χ^2 minimization which results in a final set of column densities, Doppler parameters, and central wavelengths. Even the statistical errors are included. Note that, in case of an available line doublet (e.g., Si II $\lambda\lambda$1260, 1526, 1304, C IV $\lambda\lambda$1548, 1550), it is possible to measure Doppler parameters below the instrumental resolution because of the simultaneous fit of these doublets.
In the subsequent paragraph we want to discuss some of the problems of this method. The first one is the data quality, that needs to be sufficient in terms of resolution and the S/N ratio. If the data quality is too low, the fit will not be representative due to possibly missed subcomponents. On the other hand, on very strong saturated lines, the minimization procedure leads to ambiguous results. In the same way, the minimization can fail with slightly wrong start parameters due to the complexity of the minimization function.
An example of Voigt-profile fits, applied to a spectrum, is shown in both panels of Figure 4.2. In this work we use this method to study the data samples presented in Chapter 4 and 5.

[3] see http://www.eso.org/sci/software/esomidas/

2.3.4 Component modeling

Here, component modeling means the analysis of absorption features with a program that uses the `Fitlyman` package, but enables the accurate adjustment of individual key parameters for single absorption components. Furthermore, the instrumental LSF can be considered (Richter et al. 2013).
For the detailed analysis of the absorption lines in our data sets we use different approaches. The so-called component modeling technique includes the same continuum-normalization routines that were used in the normal Voigt-profile fitting. That implies low-order polynomials that are fitted locally to the specific spectral regions. Basically, there is little difference between the modeling of an absorption component and the fitting procedure. In both cases, the `Fitlyman` routines of *Midas* are used. The basic difference to the Voigt-profile routines is that no χ^2-minimization is performed. Instead, it is possible to define the column density, the velocity structure and other important absorption parameters by hand. With this given set of parameters, an artificial spectra is created with `Fitlyman` that contains Voigt-profiles with these parameters. Afterwards, this artificial function can be used as a model that can be combined with the real data to confirm the used parameters. Thus, with this technique, we use the `Fitlyman` routine of *Midas* only to produce well-defined Voigt-functions.
With this self-written code it was possible to distinguish between the thermal and the turbulent part of the Doppler parameters. The code allows us to define a turbulent Doppler parameter for each individual component, which can be held constant for aligned velocity components of different ions. In a subsequent step, the program can estimate the thermal part of the Doppler parameter individually, based on an assumed temperature of $T = 10^4$ K. We choose this temperature because weakly and intermediately ionized species are believed to arise in gas at these temperatures (see Oppenheimer et al. 2012). Note that the thermal Doppler parameter strongly depends on the mass of each ion (see Section 2.2). The particular laboratory wavelengths and oscillator strengths have been taken from Morton (2003). To ensure a reliable basis for the choice of the parameters, one can reconsider Voigt-profile fits which give a good approximation for the line centers of the components, for instance.
In contrast to Voigt-profil fitting one does not need the assumption that for one component the combined Doppler parameter stays constant in the different ions, which is only true for ions of heavy elements or low temperatures. This is especially not true for hydrogen. Therefore, the distinction between the turbulent and thermal part of the Doppler parameter provides more detailed information of the physical quantities of an individual absorber. In Figure 2.5 the differences between the combined Doppler parameters of different ions are shown.
Furthermore, with the component modeling technique it is possible to include the complex non-gaussian LSF of the used spectrograph. As will be described in Section 3, this LSF shape produces artificially broadened wings in the absorption lines which mimic a higher column density. With the component modeling it is possible to convolve the COS LSF with an initial Voigt-profile in order to consider also the instrumental effects on the absorption.
With respect to the effects of the change of column densities and Doppler parameters, strong and saturated lines are less affected than weak and narrow lines. That means that the possible errors in the modeled parameters strongly increase with increasing line strength. Weak lines, in turn, represent a very sensitive tool to determine these parameters.
This method is, basically, only a "by eye" analyzing technique. Since no χ^2 minimization is performed, the quality of the model is hard to determine. Thus, the estimated uncertainty of each parameter is larger, and, the quality of the model is, in general, quantitatively unknown.
The modeling technique is an alternative to the implemented complete `Fitlyman` program. With the access to the code, written in *Midas*, more detailed physical processes and even the instrumental LSF can be included. A possible task for the future will be, to include also a procedure that compute the residuals for the applied model. Thus, with each iteration of a new set of parameters, also model quality information will be given. That would be more confidential than the "by eye" estimate. For more information about this method, see, for instance, Richter et al. (2013).

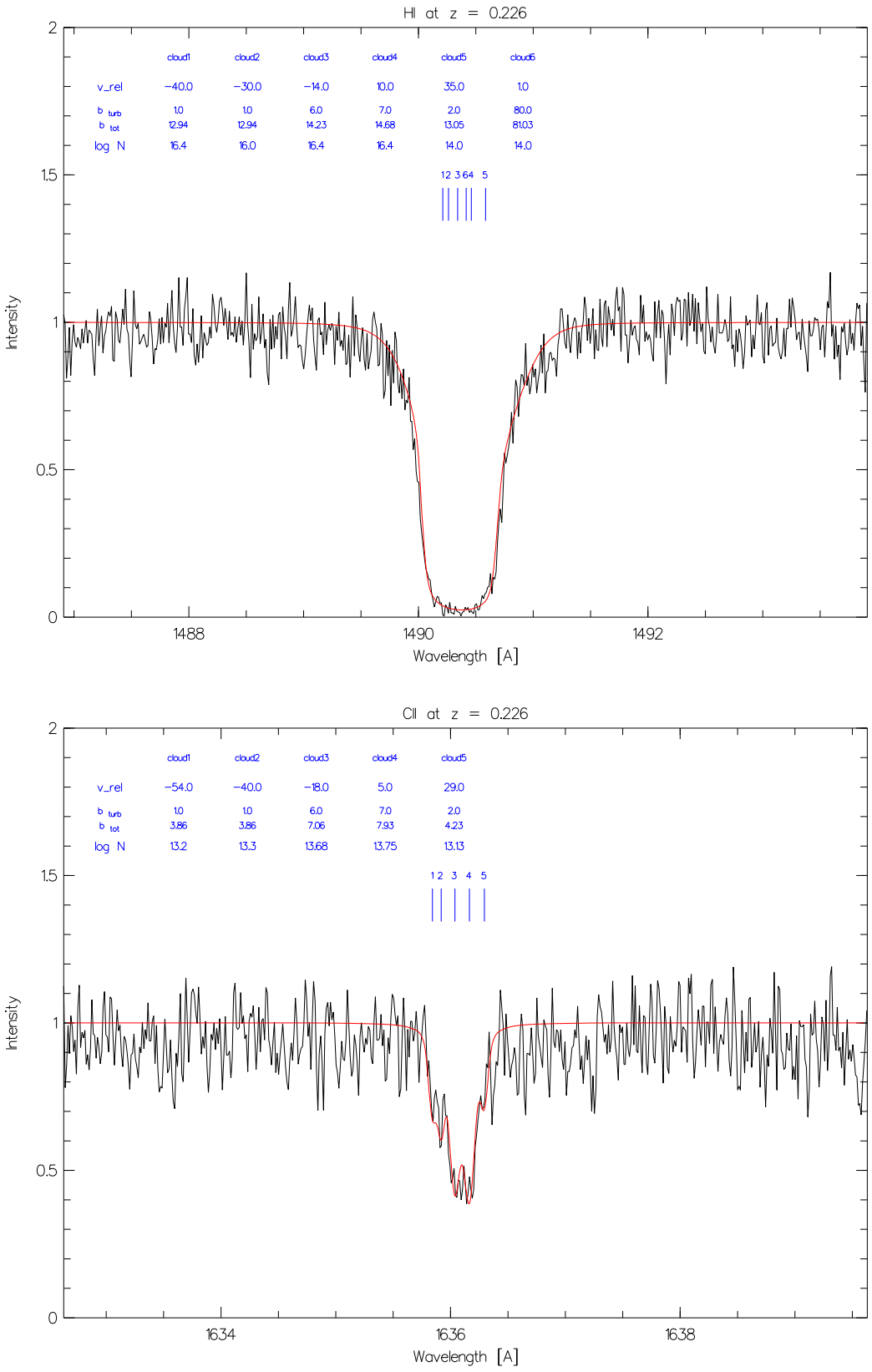

Figure 2.5: Two examples of the component modeling technique for the system at $z = 0.226$ along the sightline towards the quasar HE 0153-4520. The bottom panel shows the detailed velocity structure visible in the C II ion, whereas in the top panel the equal components with the same turbulent Doppler parameters are applied to the saturated absorption of H I. We identify two components as part of one cloud when their velocities are aligned within $\Delta v \leq \pm$ 20 km s^{-1}. Cloud 6 has no counterpart in the bottom panel.

2.4 Metal ions in the ISM and IGM

In the next subsections, the properties of the various ions used in this study are described. For further analyses and discussions see Chapters 4 and 5.

Table 2.1: List of the species, their main transitions and some of their properties used in this work.

Ion[1]	Transition[2]	Wavelength[3] [Å]	$h\nu$[4] [eV]	I(X)[5] [eV]	f_{lu}^{6}	$\Delta v_{\mathrm{FWHM}}^{\mathrm{intr.}}$ [7] [km s^{-1}]
H I Lyα	$1s$ – $2p$	1215.67	10.19	13.60	0.4164	0.0121
Lyβ	$1s$ – $3p$	1025.72	12.08		0.0791	0.0027
Lyγ	$1s$ – $4p$	972.53	12.74		0.0290	0.0011
Lyδ	$1s$ – $5p$	949.74	13.05		0.0140	0.0005
Lyϵ	$1s$ – $6p$	937.80	13.21		0.0078	0.0003
Si II	$3s^2 3p$ – $3s^2 4s$	1526.71	8.12	16.35	0.133	0.01
	$3s^2 3p$ – $3s 3p^2$	1304.37	9.50		0.086	0.007
	$3s^2 3p$ – $3s^2 3d$	1260.42	9.83		1.180	0.049
	$3s^2 3p$ – $3s 3p^2$	1193.29	10.39		0.582	0.052
	$3s^2 3p$ – $3s 3p^2$	1190.42	10.41		0.292	0.013
Si III	$3s^2$ – $3s3p$	1206.50	10.27	33.49	1.630	0.048
Si IV	$3s$ – $3p$	1402.77	8.83	45.14	0.254	0.019
	$3s$ – $3p$	1393.76	8.89		0.513	0.019
C II	$2s^2 2p$ – $2s 2p^2$	1334.53	9.29	24.38	0.128	0.005
	$2s^2 2p$ – $2s 2p^2$	1036.34	11.96		0.118	0.012
C III	$2s^2$ – $2s2p$	977.02	12.68	47.89	0.757	0.027
C IV	$2s$ – $2p$	1550.78	7.99	64.49	0.095	0.006
	$2s$ – $2p$	1548.20	8.00		0.1899	0.006
O I	$2s^2 2p^4$ – $2s^2 2p^3 3s$	1302.17	9.52	13.62	0.048	0.007
Fe II	$3d^6 4s$ – $3d^6 4p$	2600.17	4.77	16.18	0.239	0.01
	$3d^6 4s$ – $3d^6 4p$	2382.77	5.20		0.320	0.012
Mg II	$3s$ – $3p$	2803.53	4.42	15.04	0.306	0.012
	$3s$ – $3p$	2796.35	4.43		0.616	0.012

Notes: [1]) Name of the ion. [2]) Electronic transition responsible for the absorption line. [3]) Wavelength of the transition. [4]) Energy required to produce the individual transition and absorption line. [5]) Ionization potential for the transition into the next higher ionization state. [6]) Oscillator strength for the transition from the lower (l) into the upper (u) state. [7]) Intrinsic linewidth calculated with Equation 2.16.
Values taken from Morton (1991)

2.4.1 Mg II

The two magnesium transitions at 2803 Å and 2796 Å are usually used as tracers for neutral and weakly-ionized gas in the CGM of distant galaxies. Due to their shift into the optical wavelength regime even for low redshift, they have been used extensively to characterize the extended halos of other galaxies (see Section 1.4.4 for a list of references). Magnesium is an α-element, which enriches the ISM and IGM by supernova Type II explosions and subsequent outflow processes. With an ionization energy of only 15.04 eV it is a perfect tracer of cold, neutral, and weakly-ionized gas in the halos of distant galaxies. With respect to its ionization conditions, models suggest that it has almost the same characteristics like Si II, which is one of the main reasons for its importance for this thesis (see right panel of Figure 4.8). Furthermore, the solar abundance of magnesium (log $(\mathrm{Mg/H})_{\odot} = -4.47$) is similar to that of silicon (see Subsection 2.4.3). For a more detailed discussion see Section 1.4.4.

2.4.2 O I

Besides H I, neutral oxygen is the ion with the lowest ionization potential in this work. Being an α-element, exclusively produced in stars, the ISM and IGM is enriched by oxygen through supernova Type II explosions. With an ionization potential of $I_{\rm OI} = 13.62$ eV, O I has very similar ionization properties like H I and is additionally coupled to H I by a strong charge exchange reaction. That means that neutral oxygen is an excellent tracer for neutral hydrogen at low column densities. Moreover, with log $(\rm O/H)_\odot = -3.34$, it has the highest abundance of all heavy elements, which is a result of its creation in the α-process.
In the wavelength range covered by our data (see Chapter 3), there is only one (strong) transition of O I available at 1302.2 Å (see Table 2.1). Thus, we have to assume that b(O I) = b(Si II) to be able to determine a reasonable value of the O I column density. This assumption will result in uncertainties of the estimated values due to the different atomic weights of oxygen and silicon. With an atomic weight of A(Si II) = 28 u, silicon is 1.75 times as heavy as oxygen. Assuming that both elements are present in the same gas phase and under the same turbulent and thermal conditions, oxygen is substantially more affected by thermal motions than silicon (see error discussion in Chapter 4 for more details). Oxygen is typically not depleted into dust grains.
Being such a good tracer for H I and the neutral phase of the ISM/IGM, weaker O I transitions (with $\lambda_0 < 1040$ Å) have been used in several other studies. They combine data from the Space Telescope Imaging Spectrograph (STIS) with FUV data from the *Far Ultraviolet Spectroscopic Explorer (FUSE)* (e.g., Richter et al. 2001; Sembach et al. 2004b). In this thesis we do not consider any available *FUSE* spectra since these data are not available for all used sightlines.

2.4.3 Si II/III/IV

Besides magnesium, silicon, with its three basic ionization states, is the most important element in this thesis. Being an α-element such as oxygen and magnesium, silicon is synthesized in the α-process in stars. Therefore, the ISM and IGM is enriched with silicon only by supernova Type II explosions. Si II has very similar properties as Mg II, like the ionization potential ($I_{\rm SiII} = 16.4$ eV) or the solar abundance (log $(\rm Si/H)_\odot = -4.44$). Therefore, we can suggest that both ions trace almost exact the same gas phase. In the right panel of Figure 4.8, a Cloudy ionization model is shown, to illustrate the similarity of the ionization properties of both ions. Assuming an H I absorber with log N(H I) = 19.0 and a solar abundance at a distance of 50 kpc from a galactic disk, both ions have almost the same column densities under the same ionization conditions.
Since the wavelength coverage of our data contains five Si II transitions ($\lambda\lambda$1526.7, 1304.4, 1260.4, 1193.3, 1190.4), we use the Si II multiplet to adjust the Doppler parameters. Additionally, the similarity to Mg II allows us to combine the measurements for Mg II and Si II.
Following Richter et al. (2009), these weakly ionized species are expected to live in colder and denser inner regions of HVCs or metal systems, whereas highly ionized species, like Si IV and C IV, live in a spatially separated gas phase. This would support the two-phase model of HVCs introduced in Chapter 1.1 in this thesis, and, as a consequence, these ions cannot be analyzed together assuming the same conditions.

The strongest line considered in this study is the one at λ1206.5 of double-ionized silicon. On the one hand, this has the advantage that even low column densities can be detected. On the other hand, the component structure is often lost due to saturation. Nevertheless, with an ionization potential of $I_{\rm SiIII} = 33.5$ eV, Si III can be found in mildly and intermediately ionized diffuse gas. Due to the existence of only one line in the available data and heavy saturation in many cases, the determination of the column density is very uncertain.
Since it is easy to detect, we use Si III as tracer for intervening metal absorbers and with the generation of Cloudy photoionization models, Si III can help to unveil the nature of these metal systems.

Finally, Si IV is often found in combination with C IV, because it is expected to arise in almost the same gas phase (Oppenheimer et al. 2012). However, with an ionization potential of $I_{\rm SiIV} = 45.1$ eV, which is very similar to C III, Si IV actually cannot be stable under C IV conditions. Thus, the comparison between both ions should be interpreted with caution. Nevertheless, these highly ionized species provide evidence for a hotter, more diffuse gas phase that surrounds the HVC or the cloud complex. In the analyzed data, there are two transitions of Si IV at $\lambda\lambda$ 1393.8, 1402.8 available.

2.4.4 C II/III/IV

With an ionization potential of $I_{\rm CII} = 24.4$ eV, singly-ionized carbon traces neutral and mildly ionized gas in HVCs and intervening metal systems. Despite C II λ1334 has only $f\lambda = 171$ (compared to Si II λ1260 with $f\lambda = 1487$ and Si III λ1206 with $f\lambda = 1967$), it is one of the strongest and most important identification lines for HVC gas since carbon has a $\sim$8 times higher (solar)abundance compared to silicon. For the covered wavelength range there is only this one C II transition observable. Thus, we have to assume that the Doppler parameter is similar to that derived from the Si II multiplet or other weakly ionized species. Again, with an atomic weight of only A(C II) = 12 u, and with the assumption of b(C II) = b(Si II), the error of the thermal Doppler parameter is even higher than for neutral oxygen (35%). Additionally, the ionization potential is a lot higher than for Si II, which means that C II is still abundant under conditions where Si II is already ionized. Therefore, C II is assumed to trace a more diffuse and wide-spread, but still neutral and weakly ionized gas phase of the ISM/IGM. With reference to the solar abundance (log (C/H)$_\odot = -3.61$), carbon is one of the most abundant elements. It is also not significantly depleted.

The double-ionized C III has an ionization potential of $I_{\rm CIII} = 47.9$ eV and therefore traces intermediately ionized gas. With an oscillator strength of $f = 0.757$ it has a very strong transition at a wavelength of $\lambda = 977.02$ Å. Unfortunately, the HVC data do not cover this wavelength range. However, at a redshift of only $z = 0.16$ it is shifted into the detection range of the used spectrograph. Therefore, we use this ion predominantly as a tracer for intervening metal systems and it is one goal of this study to identify the typical ionization conditions of C III absorbing gas.

Finally, three-times ionized carbon, C IV, can be handled as a tracer for the hotter, diffuse, and highly ionized gas component at temperatures $T < 10^5$ K. Like C II and C III, it still arises primarily from photoionization, but can also be produced through collisional ionization. With an ionization potential of $I_{\rm CIV} = 64.5$ eV, it is expected to arise in galactic halos and in the interphase regions between neutral HVC gas and the hot coronal gas at overdensities of $\rho/\bar{\rho} \gtrsim 100$ (Oppenheimer et al. 2012; Herenz et al. 2013). Referring to HVC absorptions, Sembach et al. (2003) have shown that there exists a population of highly ionized HVCs, detectable in C IV that probably represent low-density gas structures in the halo. These structures may arise in diffuse gaseous material that originates in the IGM and that is accreted by the Milky Way ("warm accretion"). Another possible origin is the break-up of more massive HVCs as they interact with the coronal gas in the halo (one prominent example is the HVC Complex GCN, which is detected in C IV and Si IV towards the quasar PKS 2155-304 and the Seyfert 1 galaxy Mrk 509; see Winkel et al. 2011). For this study, C IV is detectable in the HVC survey, as well as in the intervening metal absorbers. Oppenheimer et al. (2012) claimed that for C IV there is a discrepancy between the number density in observations and simulations and it is still a matter of debate, whether photoionization or collisional ionization is the main process that produces these highly ionized metals.

2.4.5 Fe II

The ionization potential of Fe II, $I_{\rm FeII} = 16.2$ eV, is very similar to that of Mg II and Si II. Therefore, singly-ionized iron is expected to arise in the same neutral and weakly ionized gas phase as Mg II and Si II. In the observed wavelength range, there are two detectable lines at 2382.8 Å and 2600.2 Å . With oscillator strengths of f(Fe II$_{2600}$) = 0.239 and f(Fe II$_{2382}$) = 0.320 they are the strongest ones available. In principal, there are also lines with lower oscillator strenghts in the data, but since they are very weak their EW is below the detection limit. In case the Fe II$_{2600/2382}$ doublet can be detected, the assumption that b(Fe II) $\approx$ b(Si II), as applied for O I and C II, is not necessarily needed.
In contrast to oxygen, silicon, and carbon, iron can be produced only in the most massive stars during the last period of their lifetime. Here, iron is the last, in terms of atomic weight, element that can be produced exothermal in SN Ia. With a solar abundance of log (Fe/H)$_\odot = -4.55$ it is almost as abundant as silicon or magnesium. In the same manner, iron is affected by depletion onto dust grains. Because of its large atomic weight of A(Fe II) = 56 u, it is barely affected by thermal motions, which means that its Doppler parameter is completely dominated by the turbulent part and it can be used to define the turbulent properties of the gas phase.

2.4.6 Metallicity

Closely connected to the investigation of the different elements and their ions is the important cosmic parameter of the metallicity, Z. In astronomy, every element other than hydrogen and helium is defined to be a metal. This offers the possibility to express the abundance of such metals in the ISM and

IGM and in stars. Because hydrogen and helium are the most abundant elements in the Universe, the metallicity of an object can be expressed in terms of the mass fraction of elements that are heavier then hydrogen and helium. We assume that $X = m_{\mathrm{H}}/M$ is the mass fraction of hydrogen in a certain system, with m_{H} being the mass of of hydrogen and M being the total mass of the system. If we define Y for helium analogously, the metallicity of a system can be expressed as

$$Z = \sum \frac{m_{\mathrm{i}}}{M} = 1 - X - Y, \tag{2.36}$$

with m_i being the mass of all other elements in that system. Unfortunately, it is often not possible to determine the metallicity of an object directly. Therefore, models or simulations are needed to provide a good estimate for the metallicity from observationally accessible parameters such as the column density. The metallicity is often written in angular brackets like

$$\left[\frac{\mathrm{O}}{\mathrm{H}}\right] = \log\left(\frac{N_{\mathrm{O}}}{N_{\mathrm{H}}}\right)_{\mathrm{system}} - \log\left(\frac{N_{\mathrm{O}}}{N_{\mathrm{H}}}\right)_{\odot}, \tag{2.37}$$

with $N_{\mathrm{O,H}}$ being the column densities of oxygen or hydrogen. Here, the elemental abundance of a system is compared to that of the sun. That means, if an object has a metallicity of [O/H] = –1, it has one tenth of the solar oxygen abundance.
Apart from the abundance of one particular element compared to hydrogen or an other element, the "overall" metallicity can be given. In this context, 0.5 solar metallicity means that most of the elements have 50% of the solar abundance.

2.5 Ionization

Ionization plays an important role in almost all gas phases in the Universe.
Actually, we have to distinguish between positive and negative ionization. The first one means that an electron, e^-, is removed from the potential of the atom, which carries away a negative charge and leaves the remaining atom with a positive charge. In case of the negative ionization, under certain conditions, an electron can be captured by the atom which adds an additional negative charge to the system. Since the latter plays almost no role in interstellar and intergalactic astrophysics, we focus on the processes connected to the positive ionization.
In this case, the electron has to gain enough energy to pass the potential barrier of the atom, if tunneling is omitted. That means, cold gas (with low internal thermal energy), which is not influenced by external effects, almost always stays neutral. These neutral gas clouds often represent very dense and compact cores of gas complexes ($n_\mathrm{H} \gtrsim 1$ cm^{-3}, $T \lesssim 10^3$ K, see Table 1.1) which possibly contains molecules and where star-formation can occur since they are shielded (self shielding) against the surrounding radiation.
Following Draine (2010), in general, one can distinguish between four main processes that can lead to an ionization event and change the ionization state. These are

- **Photoionization:** $\mathrm{X} + h\nu \rightarrow \mathrm{X}^+ + e^-$
- **Collisional ionization:** $\mathrm{X} + e^- \rightarrow \mathrm{X}^+ + 2e^-$
- **Cosmic ray ionization:** $\mathrm{X} + \mathrm{CR} \rightarrow \mathrm{X}^+ + e^- + \mathrm{CR}$
- **Charge exchange:** $\mathrm{X} + \mathrm{Y}^+ \rightarrow \mathrm{X}^+ + \mathrm{Y}$

with X and Y being atoms, ions or molecules of given elements.
Photoionization is caused by the reaction of photons with a certain energy, $h\nu$, with the atom or ion. For hydrogen as the most abundant element in the Universe, the energy needed to photoionize an atom from the ground state is $I_\mathrm{H} = 13.6$ eV. In contrast to collisional ionization processes, where the ions are excited by energetic electrons, the main source for the photoionization energy in the IGM is the UV background, which basically consists of the radiation from quasars and young galaxies. The mean intensity of the UV background, based on simulations, is shown in Figure 2.7.
Assuming a photon with $h\nu \geq 13.6$ eV that interacts with a hydrogen atom, the photon can be absorbed completely, striking out an electron which carries away the remaining energy as kinetic energy ($mv^2/2 = h\nu$ –13.6 eV). In case of the Compton effect, a very high energetic photon is not absorbed completely but delivers some energy to the atom. Here, the photon is scattered by the electron, resulting in a different radiation angle and a higher wavelength (energy-loss) after the scattering process. In case of the inverse Compton Scattering, low energy photons like those of the CMB scatter on high-energetic free electrons or protons which can be produced around AGNs or in supernovae (see also Sunjaev-Zeldovich-Effect). In general, atoms with more than one valence electron are very difficult to describe since quantum effects have to be considered in these multiple-particle systems. The only manageable non-relativistic exceptions are hydrogen and one-electron ions where the cross sections of the ground state can be expressed in an analytic way,

$$\sigma(\nu) = \sigma_0 \left(\frac{Z^2 I_\mathrm{H}}{h\nu}\right)^4 \frac{e^{4-4\arctan(x)/x}}{1-e^{-2\pi/x}} \quad \text{with} \quad x \equiv \sqrt{\frac{h\nu}{Z^2 I_\mathrm{H}} - 1}. \tag{2.38}$$

Here, Z is the atomic number of the nucleus and $\sigma_0 \equiv (2^9\pi/3e^4)Z^{-2}\alpha\pi a_0^2$ is the cross section at threshold with α being the rate coefficient and a_0 the distance to the nucleus. In the special case of hydrogen ($Z = 1$), Equation 2.38 can be simplified to

$$\sigma(\nu) = g_0(\nu) \cdot 7.9 \times 10^{-18} \cdot \left(\frac{\nu_0}{\nu}\right)^3 \quad [\mathrm{cm}^2], \tag{2.39}$$

with $g_0 \backsimeq 1$ being the Gaunt factor that contains all uncertainties due to quantum mechanics. For all other, more complicated ions and atoms, the cross sections have to be calculated or measured in a more complicated way. Figure 2.6 shows the cross section of several ions plotted against the photon energy. The dashed line in the left panel represents a power law approximation for hydrogen. The occurring peaks in some of the trends are results of new available transitions of electrons from other shells.
In general, the total ionization balance, which means the number of ions compared to the number of atoms in the ground state, can be expressed in terms of the total ionization rate and the total recombination rate

$$\frac{n_\mathrm{ion}}{n_\mathrm{atom}} = \frac{\Gamma_\mathrm{tot}}{\Lambda_\mathrm{tot}}. \tag{2.40}$$

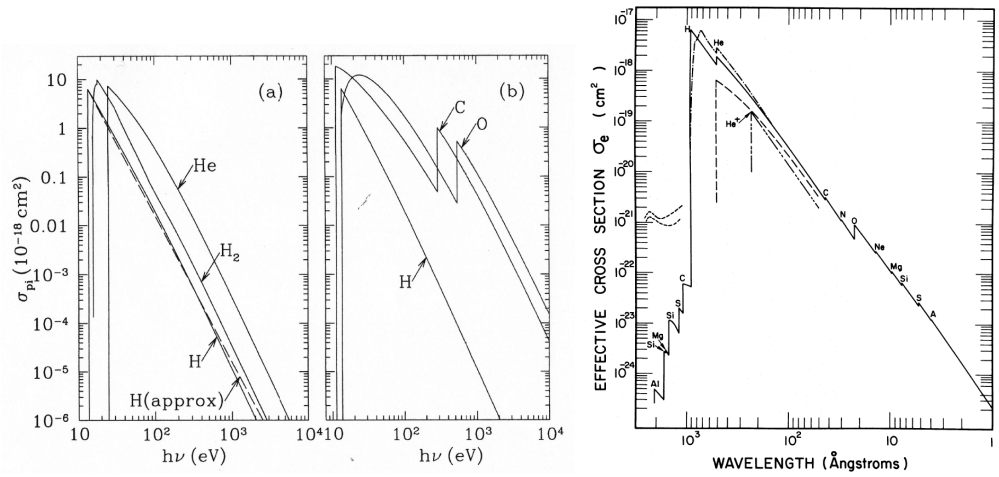

Figure 2.6: **Left panel:** photoionization cross sections for several elements plotted against the photon energy. The dashed line shows a power law approximation for hydrogen.
Right panel: effective photoionization cross section for the ISM, weighted by the abundance of the individual elements and plotted against the wavelength. The dashed and dotted lines represent results for special environments.
Figures taken from Cruddace et al. (1974) and Draine (2010).

Here, Γ_{tot} is the total ionization rate, which is defined as

$$\Gamma_{\mathrm{tot}} = \Gamma_{\mathrm{phot}} + \Gamma_{\mathrm{coll}} + \Gamma_{\mathrm{CR}} + \Gamma_{\mathrm{CE}} \tag{2.41}$$

with Γ_{phot} being the photo ionization rate, Γ_{coll} the collisional ionization rate, Γ_{CR} the ionization rate due to Cosmic rays, and Γ_{CE} the ionization because of charge exchange. In the same way, Λ_{tot} is defined as the sum of all possible de-excitation processes like radiative or dielectric recombination and possible charge exchange.
Since hydrogen is the dominant element in the Universe, there is another way to define the local strength of the ionizing radiation field. In this case, the so-called ionization parameter, U, is used. It is defined as the (dimensionless) ratio of hydrogen-ionizing photons to the total hydrogen density (see Equation 2.20 in Section 2.2 or Section 2.6).

For the absorption characteristics of the ISM and IGM, in general, the abundance of the different elements has to be considered. Assuming on average solar abundances in the ISM, it is clear that the total absorption cross section becomes dominated by hydrogen and helium over a wide wavelength range. Significant peaks caused by other elements can be discovered only for energies below 13.6 eV and at the very high energy end (see right panel of Figure 2.6; de Boer 2007).
Nevertheless, photoionization is one of the most important ways to create weakly and mildly ionized atoms in the Universe, which allows to draw conclusions about the local ionization conditions and other local parameters.

For collisional ionization, all available particle-particle interactions that can change the ionization state of an atom have to be taken into account. Normally, one only needs to consider electrons due to their high mobility compared to other charged particles. Collisional ionization is especially important for the thin and very hot ($T \geq 10^5$ K) parts of the IGM. The dominant ionization state of the species in this gas phase is typically very high (e.g., O VI, Ne VIII). Thus, within the scope of this work, collisional ionization is less important.
Summing up, one can say that ionization processes, in general, play a key role in the evolution of the gas in the Universe. With the understanding of the underlying procedures of the detections of ions like Si II, C IV or O VI, we are able to get a much better idea of interstellar and intergalactic environments and ongoing matter-affecting activities in the Universe on a global and local scale. Further explanations regarding this field would lead to far into atomic physics, and, thus, lie beyond the scope of this work. For the interested reader, there is a wealth of literature available that goes more into the details of this field of physics (e.g. de Boer 2007; Draine 2010).

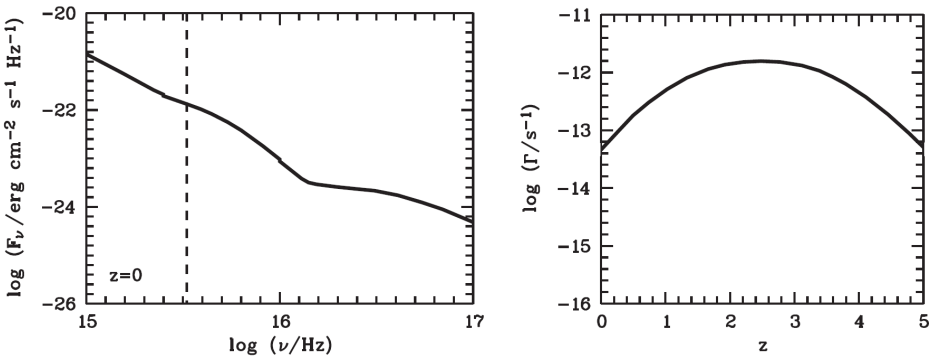

Figure 2.7: **Left panel:** mean spectrum of the UV background at $z = 0$, based on the simulations from Haardt and Madau (1996). The dashed line indicates the corresponding frequency of the Lyman limit.
Right panel: redshift-dependend photoionization rate (see Richter et al. 2008, and referenecs therein).

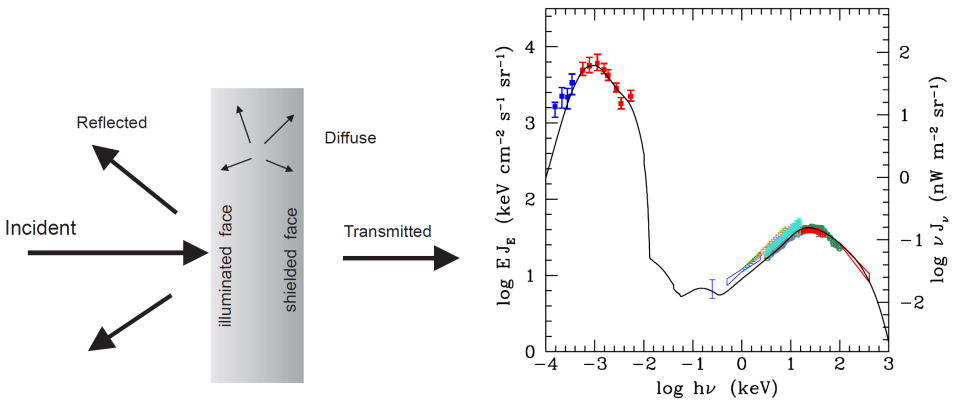

Figure 2.8: **Left panel:** scheme of the different radiation fields that can be considered in the Cloudy simulations [4].
Right panel: predicted broad-band UV background spectrum combined from quasars and galaxies at redshift $z = 0$. The colored points represent data from different observations (Haardt and Madau 2012).

2.6 Cloudy

In this section, a short description of the properties and restrictions of the Cloudy code is given. It is referred to Cloudy version 10.00, last described by Ferland et al. (2013), and can be found in the Quick Start guide and the Hazy manuals available at `http://www.nublado.org/`.
Cloudy is a code that is designed to model the properties of gas clouds with a large number of parameters and over a huge range of physical conditions. With only a few input commands, Cloudy will provide the user with several informations about the internal state of the gas, the chemical composition, the temperature, the size of the clouds and the ionizing conditions. Furthermore, the user can define the shape and strength of the spectra of the ionizing flux that the cloud is exposed to. And, finally, the whole model works with ionization-equilibrium conditions which are more complex to handle but closer to nature than the assumption of thermal or pressure equilibrium that is done in several other theoretical equations or calculations (e.g., see Section 2.2).
In order to be able to calculate the chemical and thermal state of a cloud that becomes irradiated by an external radiation field, Cloudy needs to have the ability to solve different equations. The most important one is the balance equation, which describes the change in the density of atoms in a given ionization state i (see Equation 2.42). The basic assumption is that all atomic processes are time steady, which, in terms of the balance equation, means that the change of the number of atoms of a given ionization state over time is zero (see also the Saha equation):

$$\frac{\partial n_i}{\partial t} = \sum_{j \neq i} n_j R_{ji} + S - n_i \left(\sum_{ji} R_{ij} + D \right) = 0 \quad [\mathrm{cm}^{-3}\mathrm{s}^{-1}]. \tag{2.42}$$

Here, R_{ji} describes the rate of atoms going from the j in the i state, S is the rate of atoms being excited to i and D is the rate they are going down to j. The second important equation is the conservation of charge which describes that in a closed system charge can neither be created nor destroyed. That is, of course, true for the whole Universe but it has to be specified for a limited cloud. In Equation 2.43 this principle is shown, with ρ being the charge density at one point and J the current density. This means the only way to change the charge at one point is a flow of charge in or out of this area which is known as current,

$$\frac{\partial \rho}{\partial t} + \nabla \cdot J = 0. \tag{2.43}$$

And, finally, the conservation of mass and energy in a closed system has to be considered. With these assumptions the whole problem is specified and can be solved numerically.
To define the individual problem, the user has to consider two important points: on the one hand, the incoming radiation field and, on the other hand, the physical parameters of the cloud. For both cases there is a tremendous amount of possibilities and parameters that can be defined and changed. In this case, a UV background spectrum according to Haardt and Madau (2012), which is usually adopted, is used (see right panel of Figure 2.8; Haardt and Madau 2012). In the left panel of Figure 2.8 the

[4] Figure taken from the Cloudy manual.

different parts of the considered radiation field are shown. The individual components can be tuned by hand. Furthermore, one has to define the shape of the cloud which can be open (default), as we use it for a cloud that is located in the ISM/IGM and is illuminated by the background light, or closed like, for instance, a planetary nebulae that surrounds a central star. In addition, we use the "double optical depth" command which means that the cloud should be illuminated from both (all) sides. Furthermore, a plane-parallel geometry is applied. With the set up of this basic properties the next step is to define several parameters of the cloud. In this case these are the solar abundances taken from Asplund et al. (2005), the assumed temperature of the cloud, and the measured H I column density. All of these parameters are set to be constant in the cloud over time which does not necessarily have to be the case. For the purpose of this work, we calculate the column densities for a grid of different hydrogen densities which are coupled with the ionization parameter (see Equation 2.20). This grid allows us to plot the evolution of column densities over a range of different ionization parameters as we did for the study of intervening metal absorbers.

Chapter 3

Instruments and Data

The next chapter is dedicated to give an overview on the two instruments providing the data analyzed in this work, their strengths and problems. Furthermore, the used data sets are presented. In the first part, the Space Telescope Imaging Spectrograph (STIS) is described. In the second part the Cosmic Origins Spectrograph (COS) is presented. In the end of this section a short comparison between both instruments is given.

3.1 Instruments

Since most of the lines of interest are located in the near and far ultraviolet (NUV/FUV) wavelength range, one has to go to space observatories because of the absorption characteristics of the Earth's atmosphere. Both instruments used in this thesis are installed on board the Hubble Space Telescope (*HST*), which is orbiting around the earth in almost 95 minutes at a height of $\sim$560 km.

- **STIS**
  STIS was installed on board of the *HST* with the second service mission in 1997, and it was designed to stay operable for about five years. It replaced the old High Resolution Spectrograph and the Faint Object Spectrograph. After a supply failure in 2004 it was inoperable for almost five years but was repaired during the STS-125 service mission 4 and was working again in the mid of 2009. Until today, STIS has more than doubled its expected five-year lifetime. During the $\sim$11 years of operation, it has made important measurements like, for instance, the first spectrum of an atmosphere of an extra solar planet (HD 209458b, Sing et al. 2008), or the direct imaging of the planet Formalhaut b (Kalas et al. 2005).
  In principle, STIS can use three different detectors to collect the incoming light: a charge coupled device (CCD) chip or two Multi-Anode Micro Channel Array (MAMA) detectors, with all three of them having different properties and application areas. Compared to the 1 $\times$ 512 linear array Digicon detector of the first-generation instruments, the advantage of STIS are the two large, two-dimensional array detectors for the UV, and a 1024 $\times$ 1024 pixel camera for the optical regime. In Table 3.1, we summarize some of the main characteristics of all three detectors. Apart from these three main detectors, there is a variety of different apertures, filters, and gratings available. Table 3.2 lists a selection of the standard settings. For a complete list of all setups, see `http://www.stsci.edu/hst/stis/` or the instrument handbook.
  With this instrument, it is possible to record images in a 25" – 50" field of view over the full 1150

Table 3.1: Main properties of the STIS detectors.

	CCD Chip	NUV-MAMA	FUV-MAMA
Pixel size	$\sim$ 0.5 arcsec^2	$\sim$ 0.024 arcsec^2	$\sim$ 0.024 arcsec^2
Field of view	52 $\times$ 52 arcsec^2	25.1 $\times$ 25.4 arcsec^2	25.1 $\times$ 25.3 arcsec^2
Wavelength range	1640 – 10 300 Å	1600 – 3100 Å	1150 – 1700 Å
Quantum efficiency	$\sim$ 20 % at 3000 Å $\sim$ 67 % at 6000 Å $\sim$ 29 % at 9000 Å	$\sim$ 10 % at 2537 Å	$\sim$ 25 % at 1216 Å
Saturation limit (global/local)	144 000 e$^-$	285 000/340 counts	285 000/220 counts

Table 3.2: Spectral Format and Resolving Power for STIS Primary Spectroscopic Modes.

Mode name	Detector	Nominal λ Range [Å]	Å per Exposure	Exposures (Full Band)	Å per Pixel[a]	Resolving Power λ/Δλ (FWHM)	Slit used (arcsec)
G140L....	FUV MAMA	1150 – 1700	597	1	0.583	950 – 1400	52 × 0.050
G230L....	NUV MAMA	1650 – 3100	1583	1	1.55	500 – 960	52 × 0.050
G230LB...	CCD	1672 – 3077	1405	1	1.37	700 – 1050	52 × 0.100
G430L....	CCD	3050 – 5550	2809	1	2.75	500 – 980	52 × 0.100
G750L....	CCD	5500 – 10 000[b]	4993	1[b]	4.88	560 – 760	52 × 0.100
PRISM....	NUV MAMA	1150 – 3100	11 950	1	0.47 – 48[c]	1200–31[c]	52 × 0.050
G140M....	FUV MAMA	1150 – 1700	54.3	11	0.0530	7800 – 19 200	52 × 0.050
G230M....	NUV MAMA	1650 – 3100	89.2	18	0.0872	8200 – 20 600	52 × 0.050
G230MB...	CCD	1650 – 3100	154	12	0.151	5200 – 11 200	52 × 0.100
G430M....	CCD	3050 – 5550	283	10	0.277	4900 – 10 100	52 × 0.100
G750M....	CCD	5500 – 10 000	567	9	0.555	5100 – 10 400	52 × 0.100
E140M....	FUV MAMA	1150 – 1700	587	1[d]	l/91700	46 000	0.200 × 0.060
E230M....	NUV MAMA	1650 – 3100	808	2	λ/60 000	29 900 – 32 200	0.200 × 0.060
E140H....	FUV MAMA	1150 – 1700	202	3	λ/228 000	99 300 – 114 000[e]	0.200 × 0.090
E230H....	NUV MAMA	1650 – 3100	277	6	λ/228 000	92 300 – 110 900[e]	0.200 × 0.090

[a] For MAMA modes, "pixel" refers to a low-resolution pixel.
[b] A second grating setting can be selected to extend the coverage past the 10 600 Å cutoff of the CCD.
[c] The resolution and Å per pixel are specified at 1200 Å and 3100 Å, respectively.
[d] A second grating setting can be selected to fill in very small gaps between the longest wavelength orders.
[e] Even higher resolution is achievable using narrower slits.
Table take from Kimble et al. (1998).

- 10 000 Å wavelength range. Furthermore, the simultaneous wavelength coverage with several high-resolution UV detectors increases the quality of the data, in terms of resolution and dark rate significantly.
For the HVC analysis, we use data taken with MAMA detectors with the E140M and the E230M echelle grating because of the high resolution and large wavelength coverage in the UV. The first one covers a wavelength range of $\lambda = 1144 - 1729$ Å , whereas the second one covers $\lambda = 1605 - 3110$ Å with possible resolutions of $R = 45\,800$ and $R = 30\,000$, respectively. This is equivalent to a velocity resolution of $v = 7$ km s^{-1} and $v = 10$ km s^{-1}. Both MAMA detectors can operate in two modes: the accumulation mode (ACCUM) and the time-resolved (TIME-TAG) mode. The ACCUM mode can be used to count every photon which arrives the 2048×2048 array, where they are accumulated. Note, that in this mode there is a delay of at least ~ 30 seconds between two exposures due to the storage of the received data in the *HST* accumulator. Additionally, due to the velocity of the *HST* in the Earth orbit of roughly 7.5 km s^{-1}, there is an instrumentally induced Doppler shift of the incoming photons, which result in a ± 8 pixel shift in the high-resolution modes. This effect is considered in the data processing pipeline.
In general, both MAMA detectors are performing as it is expected. For the FUV-MAMA, a little bonus appeared as a 5 – 10 times lower background signal than described in the specifications. This appears because of the successful rejection of Cherenkov photons produced in the detector window. However, with the NUV-MAMA detector it is the complete opposite. Unfortunately, high energetic particles coming from the South Atlantic Anomaly (SAA), a region with a lower geomagnetic field, and, therefore, a higher flux of cosmic particles, cause excitations of impurities in the window of the detector. These high energy states, if they become deexcited, will produce UV photons that can be detected by the MAMA. Nevertheless, this error is known and can be minimized by using optimal extraction techniques or smaller slits.
Concerning the S/N ratio, an on-board deuterium continuum lamp is used to produce flat fields for the NUV MAMA, as well as a krypton continuum lamp for the FUV MAMA, resulting in a very less wavelength dependence of the S/N ratio. Thus, in principle, it should be possible to receive point-source spectroscopy with S/N ~ 70 for the FUV and ~ 110 for the NUV. For more detailed information about STIS, its detectors, and optical performances, instrument operations, and target acquisition etc. see Kimble et al. (1998).

- **COS**
The second data set used in this thesis has been recorded with the Cosmic Origins Spectrograph (COS), which was installed on board of the *HST* in May 2009. In contrast to STIS, COS was designed to increase the capabilities of the *HST* only in the 1150 – 3200 Å wavelength range, but the NUV channel can even be used for imaging. Since COS is a very new instrument, its primary science aims are the answers of the nowadays most important astronomic questions, like the large scale structure of the Universe, the formation and evolution of galaxies, planets and the cold ISM. COS was tried to be designed as simple as possible to reduce the the on-board reflections of the

Table 3.3: Gratings of COS.

Grating	Wavelength Range [Å]	Bandpass per Exposure and FUV Gap [Å]	Resolving Power (PSA) $R = \lambda/\mathrm{FWHM}$	BOA[1] Resolving Power	Dispersion (mÅ pixel^{-1})
		FUV Channel			
G130M	900 – 1236	295/16	$\sim 11\,500$	-	9.97
	1065 – 1365	296/15.7	13 000 – 10 000	-	9.97
	1150 – 1450	292/14.3	16 000 – 21 000	5900	9.97
G160M	1405 – 1775	360/18.1	16 000 – 21 000	4400	12.23
G140L	$<$ 900 – 2150	$>$ 1150/112	1500 – 4000	1100	80.3
		NUV Channel			
G185M	1700 – 2100	3×35	16 000 – 20 000	3500	37
G225M	2100 – 2500	3×35	20 000 – 24 000	4600	33
G285M	2500 – 3200	3×41	20 000 – 24 000	5000	40
G230L	1650 – 3200	(1 or 2) $\times$ 398	2100 – 3900	500	390

[1]: The Bright Object Aperture (BOA) is one of four possible apertures. The others are listet in the instrument handbook Section 3.1.2.

Table from the instruments handbook Section 5.1: "The Capabilities of COS"

incoming light, and, thus, minimize the possibly resulting errors. There are different apertures, filters, and gratings available. In Table 3.3, the three gratings for the FUV and the four for the NUV regime together with some of the most important properties are summarized. For a complete list and detailed information see `http://www.stsci.edu/hst/cos` or the instrument handbook.

Compared to the STIS instrument, the sensitivity, especially for the FUV, is increased. If one compares the effective area of some COS settings with those of STIS, one can see that between $\sim 1150 - 1400$ Å the difference in the sensitivity is in the order of 1 – 2 magnitudes. In general, COS has two major disadvantages. On the one hand, the resolution for some wavelength ranges is rather low. This can result in the loss of information for closely connected individual absorption components (see Figure 3.1). On the other hand, the complex Line Spread Function (LSF) can change the shape of the absorption features in a way that more flux (up to 40%) is transferred to the wings of the absorption because of the non-Gaussian wings, and, thus, simulate a higher column density (see Figure 3.2). Another problem of the COS-LSF is their variability along the spectrum, which requires special routines for detailed fitting. Unfortunately, this problem did not occur before COS was installed onboard the *HST*. It was first described by Ghavamian et al. (2009), who explained this failure as zonal polishing errors on the *HST* optical telescope assembly that produce mid-frequency wave front errors, which are not corrected by any other *HST* instrument. In Green et al. (2012), one can find more information and a complete description of the instrument characteristics. For a more detailed report on the reduction, data processing and co-addition procedures, see, for instance, Meiring et al. (2011) and references therein.

In Figure 3.3, three different examples of spectral parts, which are used in this thesis, are shown. In the top panel, a COS spectrum of the sightline towards the Seyfert 1 galaxy RX J2154.1-4414 in the range of $\lambda = 1200 - 1800$ Å is shown. The red line at $\lambda \sim 1215$ Å indicates the local Galactic Lyα emission line. The pink and green lines mark the positions of the Lyα and Lyβ emission lines of the background source. Due to the comparatively low redshift of this AGN galaxy of $z = 0.344$, there are only a few intervening Lyα absorption lines in the area of the Lyα forest (see also Figure 1.8 in Section 1.4). The middle and bottom panels show the same spectral region of the Seyfert 1 galaxy PHL 1811, observed with COS and STIS, respectively. Here, one can clearly see the different spectral qualities of the two instruments.

In principle, for UV spectroscopy, nowadays two instruments are available onboard the *HST*. Depending on the scientific goals and on the necessary detector capabilities, one has to decide, whether STIS or COS is the appropriate one. In the FUV, COS is up to 10 – 30 times more sensitive and has a much higher discovery potential compared to STIS at an equal resolution. On the other hand, for lower wavelengths (< 1150 Å), the STIS FUV-MAMA is more sensitive. Furthermore, for broad NUV observations, STIS will be the instrument of choice because of the splitting of the COS NUV spectrum in three non-continuous stripes, which require several exposures for a complete NUV spectrum. Since STIS has been used much longer than COS, the calibration is more robust and well understood. Furthermore,

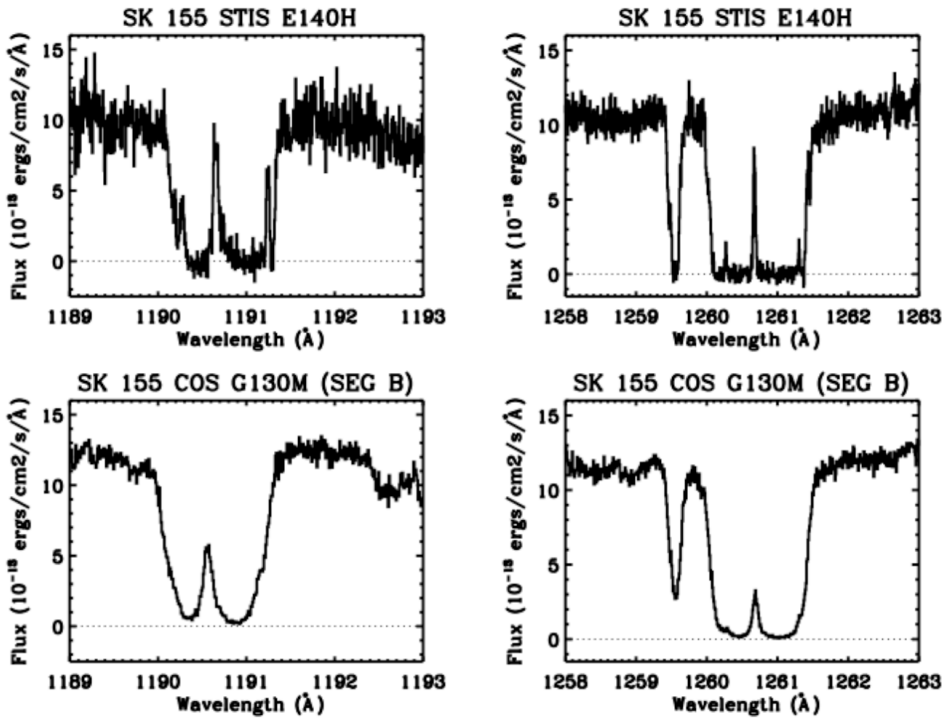

Figure 3.1: Comparison of two different absorption features captured with the E140H grating of STIS (top panels, $R \approx 114\,000$) and with the G130M grating of COS (bottom panels, $R \approx 20\,000$). Figure taken from Ghavamian et al. (2009).

for faint objects, COS will be more appropriate due to the significant lower dark rate of $< 1.0 \times 10^{-3}$ counts pixel^{-1} s^{-1}, compared to 1.8×10^{-3} counts pixel^{-1} s^{-1} for STIS. On the other hand, because of the lower sensitivity, STIS can be used to observe brighter objects than COS. Referring to the complex LSF, even STIS has broad non-Gaussian wings. But here, the influence can be minimized by using narrow apertures that are not available for COS. Finally, STIS is able to produce spectra of much higher resolution and even offers the possibility for optical and near-IR observations up to wavelengths of 10 200 Å.

3.2 Data

This section describes the properties of the data set and the instrumental settings that were used to observe the individual sightlines. Furthermore, the selection and reduction process is described. The first part is about the data obtained from the STIS archive, whereas the second part describes the COS data. In general, all analyzed spectra are public and available in the MAST archive (Mikulski Archive for Space Telescopes)[1].
The data have been further processed with the ESO-*Midas* Program package[2] and the implemented `Fitlyman` routines (Fontana and Ballester 1995). Further discussions and descriptions of the individual sightlines can be found in the subsequent sections and the Appendix.

- **The STIS data**
  The whole data set taken from *HST*/STIS contains 47 sightlines towards background quasars or AGN galaxies. In Table 3.4, the STIS QSO sightlines with their original proposal numbers and the used STIS gratings are listed. We focus on the E130M and the E230M grating because of the high resolution and the wavelength coverage of $\lambda = 1150 - 1700$ Å and $\lambda = 1600 - 3100$ Å. With these gratings, it is guaranteed that either the Si II/III or the Mg II features are within the observed spectral range. For the final spectra, several exposures are combined following the procedures described by Narayanan et al. (2008b). With a resolution of $R \sim 45\,800$ for E140M and $R \sim 30\,000$ for E230M, velocity components can be resolved down to ~ 7 km s^{-1} and ~ 10 km s^{-1}, respectively. The downloaded data was already reduced with the standard STIS reduction pipeline described by Brown (2002). We check the original proposals for a possible bias towards

[1] `http://archive.stsci.edu/index.html`
[2] `http://www.eso.org/sci/software/esomidas/`

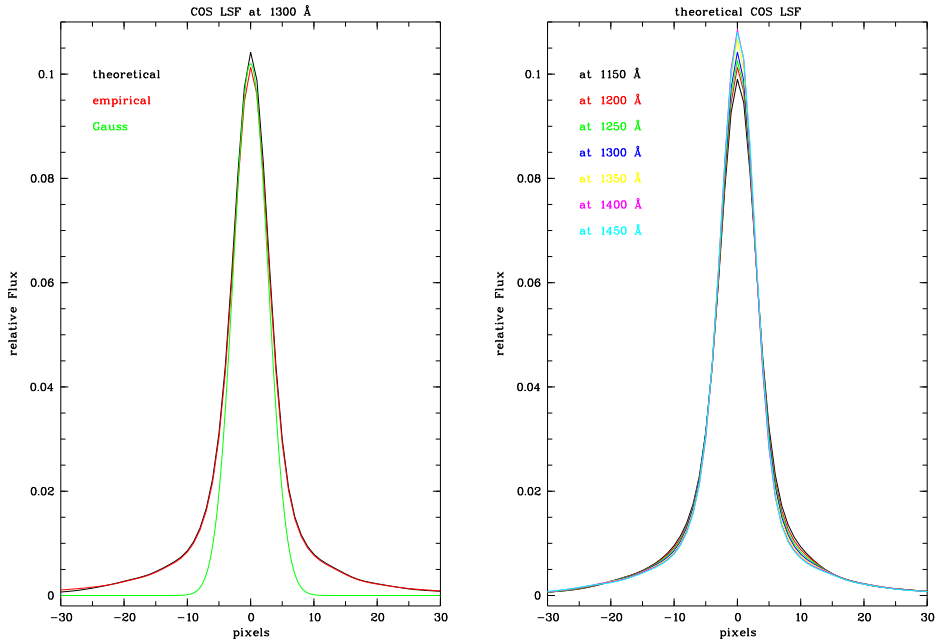

Figure 3.2: **Left panel:** line-spread-function (LSF) of COS compared to a Gaussian-shaped LSF. **Right panel:** theoretical models for the COS LSF at different wavelengths.

HVC detections, but all of them where selected because of QSO brightness or known intervening metal systems. Therefore, our sample should represent a randomly chosen data set. The sky distribution of all 47 sightlines is shown in Figure 4.1 in Chapter 4.

- **The COS data**
  Since COS was first installed at the *HST* in 2009, it is a very new instrument. Hence, the amount of available data is still limited, but will, of course, increase over time. During the data collection time for this work at the end of 2011, there were only few different proposals with appropriate spectra available in the archive. Thus, we decide to include also all available and appropriate COS spectra of SDSS objects in the analysis to ensure the highest possible sky covering fraction. Furthermore, with a higher amount of sightlines the statistics is more robust. Unfortunately, the mean S/N of the subsample of SDSS objects is only $\sim 37\%$ of the S/N of the other COS spectra. For a detailed discussion on the implications of this drawback see the subsequent sections. Finally, our COS sample contains 59 sightlines. In Table 3.5, all considered proposal numbers, as well as the names of the background objects and the available COS gratings are listed. For this study, we use the G130M and G160M gratings with $\lambda = 900 - 1450$ Å and $\lambda = 1405 - 1775$ Å wavelength coverage, respectively. With a resolution of $R = 18\,000 - 19\,000$, the corresponding velocity resolution is in the order of $v_{\rm LSR} \approx 15.8 - 16.7$ km s^{-1}. The reduction was done by the implemented COS reduction and calibration pipeline CALCOS[3].

[3] `http://www.stsci.edu/hst/cos/pipeline/`

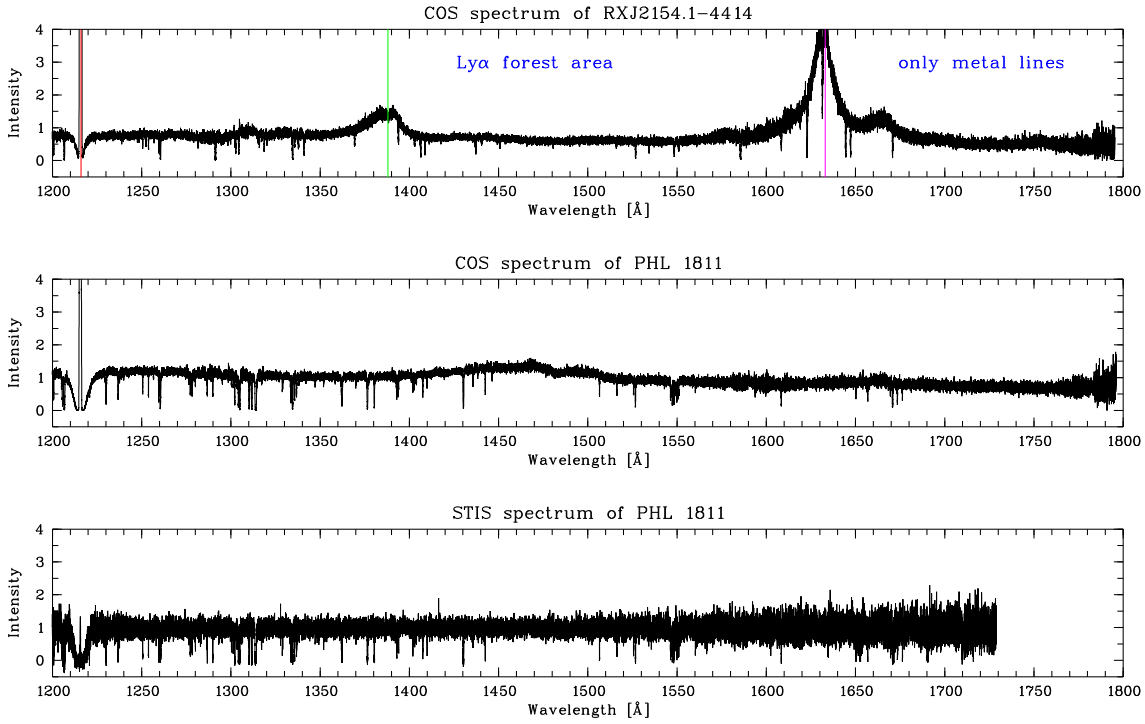

Figure 3.3: The top panel shows an excerpt from a COS spectrum of the sightline towards the background Seyfert 1 galaxy RX J2154.1-4414. Labeled are different important spectral attributes. The middle and bottom panel show a comparison of the same region in the spectra of the Seyfert 1 galaxy PHL 1811 observed with COS and STIS, respectively.

Table 3.4: *HST*/STIS QSO sightlines, gratings used for observation, and original proposals numbers.

Original Proposal ID	Relevant STIS grating	QSO Name
9802	E140M	NGC 7469
9511	E140M, E230M	NGC 5548
9418	E140M	PHL 1811
9415	E140M, E230M	Ton S210
9362	E140M, E230M	NGC 4395
9275	E140M	Mrk 279
9186	E230M	Mrk 132
9184	E140M	3C249.1, HS 0624+6907, Ton 28 PG 1216+069, PG 1444+407
9173	E230M	PKS 1127-145
9040	E230M	HS 0747+4259, HS 0810+2554
8877	E140M, E230M	Mrk 509
8695	E140M	PG 0953+415, PG 1259+593
8673	E230M	PG 0117+213, PG 1630+377, PKS 0232-04
8672	E230M	CSO 873, PG 1206+459, PG 1241+176, PG 1248+401
8651	E140M, E230M	PKS 0312-770
8625	E140M	Mrk 205
8606	E140M, E230M	NGC 3783
8571	E140M	PG 1211+143
8473	E140M	NGC 4151
8321	E140M	NGC 4051
8306	E140M	PKS 1302-102
8288	E230M	HE 0515-4414
8265	E140M	Akn 564
8165	E140M, (E230M)[1]	H 1821+643, PG 1116+215
8150	E230M	Mrk 290
8125	E140M	PKS 2155-304
8051	E140M	3C351
8017	E140M	3C273
7778	E140M	HS 1700+6416
7737	E140M	RX J1230.8+0115
7617	E140M	B 2121-1757
7576	E140M	PKS 0405-123
7355	E140M, E230M	NGC 3516
7292	E230M	PG 1634+706, PG 1718+481

[1]) E230M grating data for PG 1116+215 available in proposal ID 8097.

Table 3.5: *HST*/COS QSO sightlines, gratings used for observation, and original proposals numbers.

Original Proposal ID	Available COS grating	QSO Name
11520	G130M, G160M, G185M	RX J0439.6-5311, HE 0439-5254, PG 1553+11, HE 0435-5304, PKS 2005-489, SBSG 1122+594, PG 0838+770, Mrk 421, PKS 2005-489
11519	G130M, G160M, (G185M)[1]	PG 1115+407, TON 580
11541	G130M, G185M	PG 1259+593, HE 0226-4110, 3C263, HE 0153-4520, HS 1102+3441, PKS 0405-123, HE 0238-1904, RX J2154.1-4414
11524	G130M, G160M, G185M	Mrk 817, Mrk 1513, Mrk 290, Mrk 335, Mrk 876, PG 1011-040
12038	G130M, G160M,	PHL 1811
11598	G130M, G160M	SDSS J161916.54+334238.4, SDSS J004222.29-103743.8, SDSS J022614.46+001529.7, SDSS J040148.98-054056.5, SDSS J091029.75+101413.6, SDSS J091440.38+282330.6, SDSS J094331.61+053131.4, SDSS J100902.06+071343.8, SDSS J102218.99+013218.8, SDSS J111239.11+353928.2, SDSS J113327.78+032719.1, SDSS J115758.72-002220.8, SDSS J122035.10+385316.4, SDSS J123304.05-003134.1, SDSS J123335.07+475800.4, SDSS J124154.02+572107.3, SDSS J124511.25+335610.1, SDSS J133045.15+281321.4, SDSS J143511.53+360437.2, SDSS J144511.28+342825.4, SDSS J151428.64+361957.9, SDSS J155048.29+400144.9, SDSS J155304.92+354828.6, SDSS J155504.39+362848.0, SDSS J161649.42+415416.3, SDSS J225738.20+134045.4, SDSS J234500.43-005936.0, SDSS J141910.20+420746.9, SDSS J101622.60+470643.3, SDSS J082024.21+233450.4, SDSS J092554.70+400414.1, SDSS J080359.23+433258.4, SDSS J161711.42+063833.4

[1]) not available for PG 1115+407

Chapter 4

The MW halo as a QSO absorption-line system[1]

In the next chapter the results of the HVC analysis, based on data from the *HST*/STIS instrument, are presented. We use several sightlines to extragalactic background AGNs to statistically analyze the absorption characteristics of the high-velocity clouds (HVCs) in the Galactic halo. With the detailed information for Si II and Mg II we are able to investigate the contribution of HVCs to the absorption cross section of strong Mg II absorbers in the local Universe. This analysis provides new details on the structure of the Galactic halo as well as new conclusions on HVCs in Milky Way-type galaxies.

The structure of the subsequent sections follows directly the one presented in Herenz et al. (2013). The first part describes the procedure of data analysis and basic assumptions. Subsequently, individual ions and their significance for the investigation as well as the results and conclusions are presented, explained and discussed.

4.1 Data acquisition and analysis method

Our *HST*/STIS data set contains 47 sightlines through the Galactic halo towards QSOs and other AGNs. All spectra are publicly available in the Mikulski Archive for Space Telescope (MAST). Figure 4.1 shows the sky distribution of the 47 sightlines plotted on a H I 21cm map of the Galactic HVCs from the Leiden/Argentine/Bonn (LAB) all-sky survey (Kalberla et al. 2005). From an inspection of the original observing proposals we conclude that more than 70% of the 47 selected AGNs were selected because of their ultraviolet (UV) brightness and/or because of the known presence of intervening metal-absorption systems, as indicated by previous UV data from earlier *HST* spectrographs with lower spectral resolution. We therefore can assume that the 47 sightlines are not biased towards particular HVCs or HVC regions. Figure 4.1 indicates, however, that there is a clear overabundance of QSO sightlines in the northern sky at $b > 30$ deg with both detections and non-detections of high- velocity halo gas in the STIS data. This non-uniform sky distribution of the QSOs in our sample is further discussed in Section 4.4.

All STIS spectra considered in this paper were recorded using the E140M ($\lambda = 1150 - 1700$ Å) and the E230M ($\lambda = 1600 - 3100$ Å) high-resolution Echelle gratings of STIS. These instruments provide a spectral resolution of $R \sim 45\,800$ (E140M) and $R \sim 30\,000$ (E230M), corresponding to a velocity resolution of ~ 7 km s^{-1} and ~ 10 km s^{-1} FWHM, respectively. The STIS data were reduced using the standard STIS reduction pipeline (Brown 2002). Separate exposures were combined following the procedures described by Narayanan et al. (2008a). Table 2.1 lists prominent ions in the two wavelength ranges that can be used to study the absorption properties of Galactic HVCs. The ion transitions considered in this study include C II λ1334.5, C IV $\lambda\lambda$1548.2, 1550.8, O I λ1302.2, Si II $\lambda\lambda$1190.4, 1193.3, 1260.4, 1304.4, 1526.7, Si III λ1206.5, Si IV $\lambda\lambda$1393.8, 1402.8, Mg sc ii λ2796.4, 2803.5, Fe II $\lambda\lambda$2382.8, 2600.2, and Al II λ1670.8. Laboratory wavelengths and oscillator strengths have been taken from the compilation of Morton (2003). For our study we consider only HVCs, i.e., absorption features that have radial velocities $|v_{\rm LSR}| \geq 90$ km s^{-1}, but not the IVCs. All in all, 28 out of the 47 sightlines observed with STIS exhibit significant HVC absorption features in at least one of the ions listed above. Table 4.1 provides a summary of the HVC detections in our STIS QSO sample. This overall detection rate is affected by the strongly varying S/N ratios in the spectra and the resulting differing detection limits for the individual ion lines (see also Section 4.4).

The HVC spectral features have been fitted by multi-component Voigt profiles (see Section 2.3.3), from

[1]This chapter was published as an article in Herenz et al. 2012, A&A, Volume 550, id.A87, 23 pp.

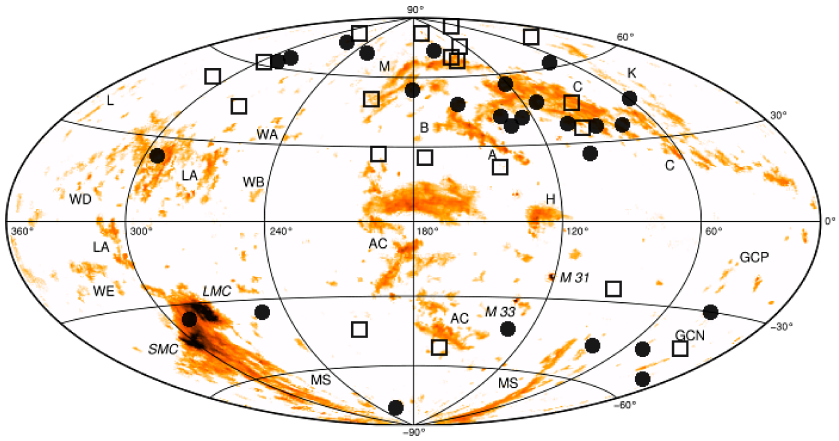

Figure 4.1: H I 21cm sky map of HVC complexes, based on the LAB survey (Kalberla 2003; Kalberla et al. 2005). The symbols mark the STIS sightlines inspected in this paper. Filled circles indicate sightlines with HVC detections, whereas empty squares indicate sightlines where no HVC absorption was found. The LAB all-sky map was kindly provided by T.Westmeier.

which we obtain column densities and Doppler parameters (b-values) for the individual HVC absorption components. For the fitting process we have used the `fitlyman` routine implemented in the ESO-MIDAS software package (Fontana and Ballester 1995). After an initial inspection of the velocity structure in each HVC we have simultaneously fitted all low ions (neutral species and singly-ionized species; e.g., O I, Si II) in each velocity component with a single b-value. This approach is justified, as the low ions are expected to reside in the same gas phase in HVCs where b is dominated by turbulence (i.e., the thermal contribution to b is expected to be negligible). The absorption components of intermediate ions (e.g., Si III) and high ions (e.g., Si IV, C IV) were fitted independently of the low ions (leading to other b-values for these ions), as these ions most likely trace a gas phase different from that traced by the low ions. Because many spectra have relatively low S/N, not all HVC velocity components can be resolved with the current *HST* data set. Moreover, high-resolution, high-S/N optical spectra of HVC sightlines indicate that there often are a large number of velocity sub-components in HVCs whose identification would require a spectral resolution much higher than currently provided by space-based UV spectrographs (e.g., Welty et al. 1999). This systematic uncertainty is, however, not restricted to HVCs but is relevant also for the analysis of intervening metal absorbers at low z using UV data with limited S/N and spectral resolution (e.g., Richter et al. 2004; Ribaudo et al. 2011b). For the Voigt profile fitting presented in this paper our strategy was to find the *minimum* number of velocity components (Voigt components) that are required to obtain a satisfying fit to the STIS HVC absoption profiles. This allows us to compare our results to studies of intervening absorbers, for which similar fitting strategies were chosen (e.g., Churchill et al. 2003). All HVC fitting results are listed in Tables 6.1 - 6.5 of the Appendix.

Table 4.1: Summary of QSO Sightlines and HVC Detections.

QSO Name	z_{em}	l (deg)	b (deg)	HVC status (yes/no)	HVC velocity range ($km\,s^{-1}$)	HVC name (if known)	Relevant STIS grating	Detected ions
PKS 2155−304	0.117	18	−52	yes	−138...−190	...	E140M	Si II, C II, Si III, Si IV, C IV
NGC 5548	0.020	32	+71	no	-	-	E140M, E230M	-
B 2121−1757	0.110	33	−42	no	-	-	E140M	-
Mrk 509	0.034	36	−30	yes	−295...−310	GCN	E140M, E230M	C II, Si III, Si IV, C IV
CSO 873	1.010	38	+84	no	-	-	E230M	-
PHL 1811	0.192	47	−45	yes	−130...−270	GCN	E140M	Si II, C II, O I, Al II, Si III, Si IV, C IV
PG 1630+377	1.480	60	+43	yes	−160...−60	-	E230M	Mg II, Fe II
PG 1444+407	0.270	70	+63	yes	−80...−90	-	E140M	Si II, C II, O I, C IV
PG 1718+481	1.083	74	+35	yes	−100...−215	C Extension	E230M	Fe II
NGC 7469	0.016	83	−45	yes	−190...−400	MS	E140M	Si II, C II, O I, Si III, Si IV, C IV
3C351	0.372	90	+36	yes	−130...−230	Complex C	E140M	Si II, C II, O I, Al II, Si III, Si IV, C IV
Mrk 290	0.030	91	+48	yes	−128	Complex C	E230M	Fe II
Akn 564	0.030	92	−25	no	-	-	E140M	-
H 1821+643	0.297	94	+27	yes	−130...−170	Outer Arm	E140M	Si II, C II, O I, Al II, Si III, Si IV, C IV
HS 1700+6416	2.740	94	+36	no	-	-	E140M	-
PG 1634+706	1.337	103	+37	yes	−100...−215	Complex C	E230M	Fe II
Mrk 279	0.031	115	+47	yes	−150...−200	Complex C south	E140M	Si II, C II, O I, Al II, Si III, Si IV
PG 1259+593	0.472	121	+58	yes	−120...−145	Complex C III	E140M	Si II, C II, O I, Al II, Si III, C IV
PG 1248+401	1.030	123	+77	no	-	-	E230M	-
Mrk 205	0.071	125	+42	yes	−110...−230	Complex C south	E140M	Si II, C II, O I, Al II
3C249.1	0.310	130	+39	yes	−135	-	E140M	Si II, C II, Si III
PG 0117+21	1.500	132	−41	yes	−134	-	E230M	Mg II, Fe II
NGC 3516	0.009	133	+42	yes	−160...−170	-	E140M, E230M	Si II, C II, Fe II, Mg II, Si III
PG 1206+459	1.160	145	+70	no	-	-	E230M	-
HS 0624+6907	0.370	146	+23	no	-	-	E140M	-
NGC 4051	0.002	149	+70	no	-	-	E140M	-
NGC 4151	0.003	155	+75	yes	+120...+145	...	E140M	Si II, C II, Si III, C IV, Fe II, Mg II
Mrk 132	1.760	159	+49	yes	−140...+80	-	E230M	Mg II, Fe II
NGC 4395	0.001	162	+82	no	-	-	E140M, E 230M	-
PKS 0232-04	1.440	174	−56	no	-	-	E230M	-
HS 0747+4259	1.900	177	+29	no	-	-	E230M	-
PG 0953+415	0.239	180	+52	yes	−150	Complex M	E140M	Si II, C II, Si III, Al II
HS 0810+2554	1.510	197	+29	no	-	-	E230M	-
Ton 28	0.330	200	+53	no	-	-	E140M	-
PKS 0405−123	0.570	205	−42	no	-	-	E140M	-
PG 1116+215	0.177	223	+68	yes	+180...+190	-	E140M, E230M	Si II, C II, O I, Fe II, Mg II, Si III, Si IV, C IV
Ton S210	0.117	225	−83	yes	−150...−235	CHVC 224.0−83.4−197	E140M, E230M	Si II, C II, O I, Si III, Si IV, C IV
HE 0515−4414	1.713	250	−35	yes	+120...+230	-	E230M	Mg II, Fe II
PG 1211+143	0.081	268	+74	yes	+169...+184	...	E140M	Si II, C II, O I, Si III, C IV
PKS 1127−145	1.187	275	+44	no	-	-	E230M	-
PG 1216+069	0.330	281	+68	yes	+210...+270	...	E140M	Si II, Si III, C IV
NGC 3783	0.010	287	+23	yes	+180...+250	Leading Arm (MS)	E140M, E230M	Si II, C II, O I, Al II, Fe II, Mg II, Si III
3C273	0.160	290	+64	no	-	EPn	E140M	-
RXJ 1230.8+0115	0.117	291	+63	yes	−216...−310	...	E140M	Si II, C II, O I, Si III, Si IV
PKS 0312−770	0.223	293	−38	yes	+160...+240	MB	E140M, E230M	Si II, C II, O I, Fe II, Mg II, Si III
PG 1241+176	1.280	293	+80	no	-	-	E230M	-
PKS 1302−102	0.290	309	+52	no	-	...	E140M	-

Table 4.2: Summary of HVC Detections in individual Ions and Sightlines.

Sightlines with HVCs	S/N (Si II 1260) per res. element	S/N (Mg II 2796) per res. element	available STIS Gratings	Si II [cm $^{-2}$]^{1}	Si III [cm $^{-2}$]^{1}	Si IV [cm $^{-2}$]^{1}	C II [cm $^{-2}$]^{1}	C IV [cm $^{-2}$]^{1}	O I [cm $^{-2}$]^{1}	Al II [cm $^{-2}$]^{1}	Mg II [cm $^{-2}$]^{1}	Fe II [cm $^{-2}$]^{1}
PKS 0312-77	7	3	E140M. E230M	Yes<11.83	Yes<11.71	No<12.45	Yes<12.77	No<12.53	Yes<13.20	No<11.54	Yes<12.67	Yes<12.80
PG0953+415	8	...	E140M	Yes<11.78	Yes<11.66	No<12.40	Yes<12.72	No<12.48	No<13.15	No<11.49	No	No
3C249.1	8	...	E140M	Yes<11.78	Yes<11.66	No<12.40	Yes<12.72	No<12.48	No<13.15^{2}	No<11.49	No	No
3c351	5	...	E140M	Yes<12.03	Yes<11.91	Yes<12.65	Yes<12.97	Yes<12.73	Yes<13.40	Yes<11.74	No	No
PG 1116+215	12	6	E140M. E230M	Yes<11.58	Yes<11.46	Yes<12.20	Yes<12.52	Yes<12.28	Yes<12.95	No<11.29	Yes<12.32	Yes<12.45
PG 1259+593	7	...	E140M	Yes<11.83	Yes<11.71	No<12.45	Yes<12.77	Yes<12.53	Yes<13.20	Yes<11.54	No	No
PG 1634+706	...	25	E230M	No	No	No	No	No	No	No	Yes<11.72	Yes<11.85
PG 1718+481	...	...	E230M	No	No	No	No	No	No	No	No	Yes
PHL 1811	7	...	E140M	Yes<11.83	Yes<11.71	Yes<12.45	Yes<12.77	Yes<12.53	Yes<13.20	Yes<11.54	No	No
H 1821+643	12	...	E140M	Yes<11.58	Yes<11.46	Yes<12.20	Yes<12.52	Yes<12.28	Yes<12.95	Yes<11.29	No	No
PG 0117+21	...	6	E230M	No	No	No	No	No	No	No	Yes<12.32	Yes<12.45^{3}
PG 1211+143	15	...	E140M	Yes<11.51	Yes<11.39	No<12.13	Yes<12.45	Yes<12.21^{3}	Yes<12.88^{3}	No<11.22	No	No
PG 1216+069	8	...	E140M	Yes<11.78	Yes<11.66	No<12.4	Yes<12.72^{4}	Yes<12.48	No<13.15	No<11.49	No	No
PG 1444+407	8	...	E140M	Yes<11.78	Yes<11.66^{4}	No<12.40	Yes<12.72	Yes<12.48	Yes<13.15	No<11.49	No	No
PG 1630+377	...	8	E230M	No	No	No	No	No	No	No	Yes<12.17	Yes<12.30
RXJ 1230.8+0115	6	...	E140M	Yes<11.88	Yes<11.76	No<12.50	Yes<12.82	No<12.58	Yes<13.25	No<11.59	No	No
NGC 3516	3	7	E140M. E230M	Yes <12.23^{4}	Yes <12.11^{4}	No <12.85	Yes <13.17^{4}	No <12.93	Yes <13.6^{4}	No<11.94	Yes<12.27	Yes<12.40
NGC 3783	26	10	E140M. E230M	Yes<11.28	Yes<11.16	No<11.90	Yes<12.22	No<11.98	Yes<12.65	Yes<10.99	Yes<12.12	Yes<12.25
NGC 4151	18	30	E140M. E230M	Yes<11.43	Yes<11.31	No<12.05	Yes<12.37	Yes<12.13	No<12.80	No<11.14	Yes<11.67^{3}	Yes<11.80^{3}
NGC 7469	10	...	E140M	Yes<11.73	Yes<11.61	Yes<12.35	Yes<12.67	Yes<12.43	Yes<13.10	No<11.44	No	No
He 0515-4414	...	11	E230M	No	No	No	No	No	No	No	Yes<12.02	Yes<12.15^{3}
PKS 2155-304	20	...	E140M	Yes<11.43	Yes<11.31	Yes<12.05^{3}	Yes<12.37	Yes<12.13	No<12.80	No<11.14	No	No
Mrk 132	...	10	E230M	No	No	No	No	No	No	No	Yes<12.12	Yes<12.25
Mrk 205	5	...	E140M	Yes<12.03	Yes<11.91	No<12.65	Yes<12.97	No<12.73	Yes<13.40	No<11.74	No	No
Mrk 279	23	...	E140M	Yes<11.33	Yes<11.21	Yes<11.95^{3}	Yes<12.27	No<12.03	Yes<12.70	Yes<11.04	No	No
Mrk 290	...	...	E230M	No	No	No	No	No	No	No	No	Yes
Mrk 509	16	11	E140M. E230M	No<11.48	Yes<11.36	Yes<12.10	Yes<12.42	Yes<12.18	No<12.85	No<11.19	No<12.02	No<12.15
Ton S210	6	4	E140M. E230M	Yes<11.88	Yes<11.76	Yes<12.50^{3}	Yes<12.82	Yes<12.58	Yes<13.25	No<11.59	Yes<12.47	Yes<12.60

^{1}): The listet numbers correspond to the logarithmic column density detection limits for each individual ion and sightline based on the particular S/N ratios.
^{2}): No statement possible. Was removed from the statistic.
^{3}): Detections below the column density limit. Thus no contribution to the statistic.
^{4}): Expected absorption but not possible to fit due to blends etc. Was considered in statistic.

4.2 Discussion of individual sightlines

In the next section we shortly discuss the HVC absorption properties for each individual sightline and summarize the results from previous studies. The sightlines are sorted by Galactic longitude.

PKS 2155−304. The PKS 2155−304 sightline is located at $l = 17.7$, $b = -52.3$; it thus passes the outer edge of HVC Complex GCN. HVC absorption is seen at high negative velocities. Only E140M data are available for this sightline. The data have good quality with a S/N of ~ 18 per 3.2 km s^{-1}-wide pixel element at 1300 Å. HVC absorption is split into two groups (see Figure 6.2; Table 6.4). The first group near $v_{\rm LSR} = -150$ km s^{-1} is detected in C II, Si II, Si III, Si IV and C IV and has three subcomponents at $-111, -135$ and -157 km s^{-1}. The second group is centered near -260 km s^{-1} and is detected only in Si III, Si IV and C IV. It has three subcomponents at $-232, -254$, and -280 km s^{-1}. Detailed analyses of the PKS 2155−304 sightline are presented by Sembach et al. (1999); Collins et al. (2004). This sightline is also discussed in (Sembach et al. 2003; Fox et al. 2006; Collins et al. 2009; Winkel et al. 2011).

Mrk 509. The Mrk 509 sightline is located at $l = 36.0$, $b = -29.9$ and passes through highly-ionized HVC gas at very high negative velocities. This HVC is associated with Complex GCN (see Winkel et al. 2011). Both E140M and E230M data are available for this sightline, but the S/N in the data is relatively low (~ 7 per 3.2 km s^{-1}-wide pixel element at 1300 Å). Absorption is detected in four components at $v_{\rm LSR} = -263, -287, -273$, and -311 km s^{-1} in the lines of C II, Si III, Si IV, and C IV (see Figure 6.4; Table 6.5). Detailed studies of this HVC are presented in Sembach et al. (2004b) and Collins et al. (2004). Other studies that discuss this sightline are Sembach et al. (2003) and Winkel et al. (2011).

PHL 1811. The line of sight towards the Seyfert 1 galaxy PHL 1811 ($l = 47.5$, $b = -44.8$) passes the outskirts of HVC Complex GCN and shows a complex HVC absorption pattern in the LSR velocity range between -100 and -300 km s^{-1} (see Figure 6.5; Table 6.2). Only E140M data are available for this sightline; the S/N is ~ 7 per 3.2 km s^{-1}-wide pixel element at 1300 Å. Five absorption components are identified at velocities of $v_{\rm LSR} = -163, -206, -240, -263$, and -351 km s^{-1} in the lines of C II, O I, Si II, Al II, Si III, Si IV, and C IV. The large number of components suggests a complex spatial distribution of HVC gas in Complex GCN in this direction (see also Winkel et al. 2011). A detailed study of the Complex GCN absorption towards PHL 1811 is presented in Richter et al. (2009). Other studies of relevance in this context are the ones by Fox et al. (2006), Ben Bekhti et al. (2008), Collins et al. (2009), and Winkel et al. (2011).

PG 1630+377. For the line of sight towards the quasar PG 1630+377 ($l = 60.3$, $b = +42.9$) only STIS data from the E230M grating are available (see Figure 6.5; Table 6.3). HVC absorption is detected in Mg II and Fe II in three individual components at negative velocities at $v_{\rm LSR} = -64, -99$, and -155 km s^{-1}. With a S/N of ~ 8 per 4.8 km s^{-1}-wide pixel element at 2796 Å the data quality is rather low. For the two absorption components near -100 km s^{-1} the Mg II absorption is saturated. We find no previous studies that discuss HVC absorption along this line of sight.

PG 1444+407. Along the line of sight towards the Seyfert 1 galaxy PG 1444+407 at $l = 69.9$ and $b = +62.7$ we identify one double-component high-velocity absorber at $v_{\rm LSR} \approx -85$ km s^{-1} in the lines of Si II, O I, C II, and C IV (see Figure 6.5; Table 6.3). The C IV component seems to be shifted to more negative velocities and the C II absorption is strongly saturated. This indicates a two-phase HVC structure with an inner core that is surrounded by an ionized envelope. The data have a S/N ~ 8 per 3.2 km s^{-1}-wide pixel element at 1260 Å. This HVC absorber is located at the outer edge of Complex C. For further information see the sample of Wakker et al. (2011) and Shull et al. (2009).

PG 1718+481. The line of sight towards the QSO PG 1718+481 is located at $l = 74.4$, $b = +34.8$; it, therefore, pierces the outer environments of the HVC Complexes C and K. Unfortunately, only Fe II λ2600 is covered by the E230M data, while E140M data are not available. The E230M data have a good S/N of ~ 14 per 4.8 km s^{-1}-wide pixel element at 2600 Å. The Fe II line shows three well-defined HVC components at radial velocities of $v_{\rm LSR} = -81, -128$, and -197 km s^{-1} (see Figure 6.5; Table 6.2). We did not find any previous paper that discusses the HVC absorption towards PG 1718+481.

NGC 7469. The line of sight towards NGC 7469 passes directly through the Magellanic Stream at $l = 83.1$, $b = -45.5$. Consequently, the STIS data show a complex absorption pattern at high negative velocities in the range $v_{\rm LSR} = -180$ to -400 km s^{-1}. For this sightline only E140M data are available. The S/N in the data is ~ 10 per 3.2 km s^{-1}-wide pixel element at 1300 Å. We fit five individual absorption components to the data at $v_{\rm LSR} = -185, -251, -293, -335$, and -366 km s^{-1} (Figure 6.4; Table

6.4). A detailed analysis of this sightline is presented in Fox et al. (2010).

3C 351. The 3C 351 sightline passes the HVC Complexes C and K at $l = 90.1$, $b = +36.4$. Only E140M data are available for this sightline. The S/N in the data is relatively low (~ 6 per 3.2 km s^{-1}-wide pixel element at 1500 Å). A complex absorption pattern at high negative velocities is visible in the absorption lines of C II, Al II, Si II, O I, Si III, Si IV, and C IV (see Figure 6.3; Table 6.1). We identify five absorption components at LSR velocities of -76, -89, -131, -166, and -192 km s^{-1}. HVC absorption in Complex C and Complex K has been studied in detail by Tripp et al. (2003) and Collins et al. (2007).

Mrk 290. The line of sight towards Mrk 290 ($l = 91.5$, $b = +48.0$) is known to pass through Complex C. Unfortunately there is only E230M data available, and only the two Fe II lines are covered. We find HVC absorption near $v_{\rm LSR} = -130$ km s^{-1} in three absorption components, but because of the low S/N (~ 8 per 4.8 km s^{-1}-wide pixel element at 2600 Å) and the saturation of the Fe II lines, a reliable measurement is not possible (see Figure 6.4; Table 6.5). HVC absorption along this sightline is discussed also in Shull et al. (2011).

H1821+643. The H1821+643 sightline at $l = 94.0$, $b = +27.4$ is known to pass through the Outer Arm and the HVC Complexes C and K. Thus, the available E140M STIS spectrum shows a complex absorption pattern of high-velocity gas components in the velocity range -80 to -200 km s^{-1}. The E140M data are of good quality with a S/N of ~ 11 per 3.2 km s^{-1}-wide pixel element at 1300 Å. We identify three distinct absorption components at $v_{\rm LSR} = -84$, -126, and -146 km s^{-1} in the lines of C II, O I, Si II, Al II, Si III, Si IV, C IV, and others (see Figure 6.3; Table 6.2). A detailed analysis of the HVCs towards H1821+643 is presented in Tripp et al. (2003). Other studies that discuss HVC absorption along this sightline are the ones by Sembach et al. (2003) and Collins et al. (2009).

PG 1634+706. The PG 1634+706 sightline passes HVC Complex C at $l = 102.8$, $b = +36.6$. Only E230M data are available for this sightline, so that Complex C absorption is detected only in the lines of Fe II and Mg II at LSR velocities in the range -100 to -230 km s^{-1} (see Figure 6.5; Table 6.2). The E230M data have a high S/N of ~ 22 per 4.8 km s^{-1}-wide pixel element at 2800 Å. Three major absorption components are identified at $v_{\rm LSR} = -125$, -164, and -195 km s^{-1}. The latter component appears to be very broad in Mg II and possibly is composed of several (unresolved) sub-components. We did not find any previous study in the literature that investigate the HVC absorption in the STIS E230M data towards PG 1634+706.

Mrk 279. The line of sight towards Mrk 279 pierces HVC Complex C at $l = 115.0$, $b = +46.9$. The available E140M data show strong HVC absorption at negative velocities in the range $v_{\rm LSR} = -100$ to -200 km s^{-1} in the lines of C II, Si II, O I, Al II, Si III, and Si IV. The data have good quality with a S/N of ~ 14 per 3.2 km s^{-1}-wide pixel element at 1500 Å. Three individual components at $v_{\rm LSR} = -145$, -161, and -179 km s^{-1} are fitted to the data (see Figure 6.3; Table 6.5). There exist a number of detailed studies of the Complex C absorption towards Mrk 279 based on different spectral data (e.g., Gibson et al. 2001; Tripp et al. 2003; Collins et al. 2003 2007).

PG 1259+593. The line of sight towards the quasar PG 1259+593 ($l = 120.6$, $b = +58.0$) passes HVC Complex C at negative LSR velocities; it represents one of the best-studied HVC sightlines in the literature. Because PG 1259+593 is relatively faint ($V = 15.84$ mag) the existing E140M data (obtained with more than 350 ksec integration time; see Sembach et al. 2003) has only an intermediate S/N of ~ 7 per 3.2 km s^{-1}-wide pixel element at 1500 Å. Strong HVC absorption associated with Complex C is seen in two distinct absorption components at $v_{\rm LSR} = -134$ km s^{-1} and $v_{\rm LSR} = -116$ km s^{-1} in the lines of Si II, C II, Al II, O I, Si III, and many other ions (see Figure 6.5; Table 6.2; also Richter et al. (2001), their Figure 2). Detailed studies of HVC Complex C towards PG 1259+593 are presented in Richter et al. (2001), Sembach et al. (2003), Collins et al. (2003), and Fox et al. (2004).

Mrk 205. The sightline towards the Seyfert 1 galaxy Mrk 205 passes high-velocity gas at negative velocities at $l = 125.5$, $b = +41.7$, associated with HVC Complex C. The available E140M data have a very good S/N of ~ 22 per 3.2 km s^{-1}-wide pixel element at 1300 Å. Three absorption components at $v_{\rm LSR} = -106$, -138, and -197 km s^{-1} are identified in the lines of Si II, C II and O I (Figure 6.3; Table 6.4). For a more detailed study of this sightline see Collins et al. (2007).

3C 249.1. The sightline towards the Seyfert 1 galaxy 3C 249.1 ($l = 130.4$, $b = +38.5$) passes the outskirts of Complex C. With a S/N of ~ 8 per 3.2 km s^{-1}-wide pixel element at 1260 Å the quality of the available E140M data is relatively low. We identify one HVC absorption component at $v_{\rm LSR} = -135$

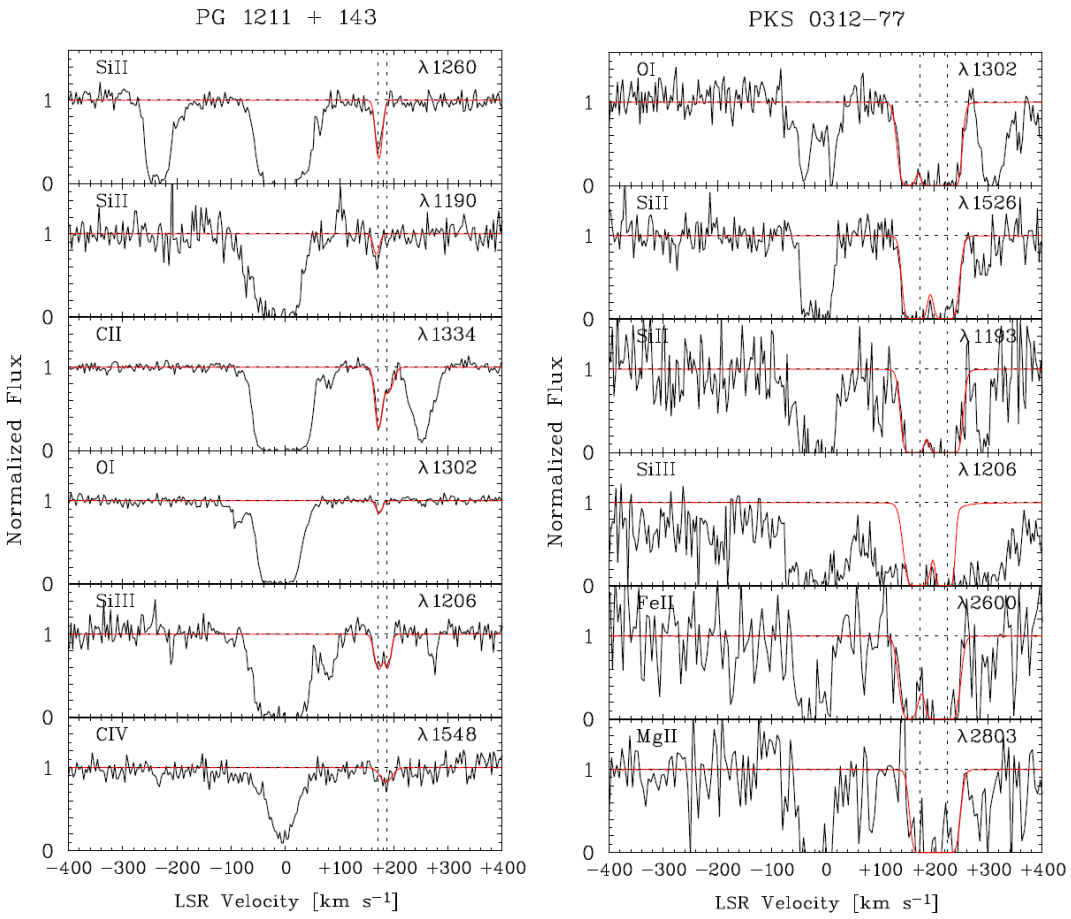

Figure 4.2: Two examples of analyzed HVC components in the STIS spectra. The left panel show the result for the sightline towards PG 1211+143, whereas the right panel does for PKS 0312-770. The red profile indicates the best Voigt-fit with individual component positions marked by the dashed lines. More *HST*/STIS plots can be found in the Appendix A.

km s^{-1} in the lines of Si II, C II, and Si III (see Figure 6.3; Table 6.1). HVC absorption along this sightline is mentioned by Collins et al. (2009).

PG 0117+21. For the line of sight towards the quasar PG 0117+21 (l = 131.8, b = −40.8) only E230M data are available. We identify one weak HVC absorber at $v_{\rm LSR}$ = −134 km s^{-1} in the lines of Mg II and Fe II (see Figure 6.3; Table 6.3). The S/N of the data is low ($\sim$ 6 per 4.8 km s^{-1}-wide pixel element at 2796 Å). The HVC towards PG 0117+21 apparently is not connected with any large HVC complexes. We are not aware of any previous study that discusses the PG 0117+21 sightline with respect to HVC absorption.

NGC 3516. The line of sight toward NGC 3516 (l = 133.2, b = +37.6) passes through the outskirts of HVC Complex C. For this sightline E140M and E230M data are available, but only the E230M data have sufficient quality to measure HVC absorption features (S/N $\sim$ 7 per 4.8 km s^{-1}-wide pixel element at 2800 Å.) One single absorption component is detected at typical Complex C velocities of $v_{\rm LSR}$ = −158 km s^{-1} in the lines of Mg II and Fe II (see Figure 6.4; Table 6.3). HVC absorption towards NGC 3516 is mentioned in the papers from Collins et al. (2009) and Shull et al. (2009).

NGC 4151. Along the sightline towards NGC 4151 (l = 155.1, b = +75.1) weak HVC absorption is observed at high positive radial velocities in the lines of C II, Si II, Fe II, Mg II, Si III, and C IV in a single absorption component centered at $v_{\rm LSR}$ = +143 km s^{-1} (Figure 6.4; Table 6.3). Both the available E140M and E230M data have good S/N ($\sim$ 19 per 3.2 km s^{-1}-wide pixel element at 1300 Å). This HVC appears to be isolated without being connected to any known large HVC complex. A detailed study of this HVC is presented in Richter et al. (2009).

Mrk 132. The line of sight towards Mrk 132 is located at $l = 158.9$, $b = +48.6$, located between the two HVC Complexes B and C. Only E230M data are available to us. We find high-velocity absorption at negative velocities ($v_{\rm LSR} = -139$ km s^{-1} and $v_{\rm LSR} = -98$ km s^{-1}), as well as absorption at positive velocities ($v_{\rm LSR} \approx 80$ km s^{-1}) in the lines of Mg II and Fe II (see Figure 6.3; Table 6.4). The best fit for the positive-velocity absorption yields two components blending each other. With a S/N of ~ 10 per 4.8 km s^{-1}- wide pixel element at 2796 Å the data are of medium quality. We are not aware of any previous paper that discusses the properties of the HVCs towards Mrk 132.

PG 0953+415. The line of sight towards the Seyfert 1 galaxy PG 0953+415 is located at $l = 179.8$ and $b = +51.7$ and passes high-velocity halo gas that possibly is related to HVC Complex M. For this sightline only E140M data with intermediate S/N (~ 9 per 3.2 km s^{-1}-wide pixel element at 1300 Å) are available. We identify one HVC component at $v_{\rm LSR} = -147$ km s^{-1} in the lines of C II, Al II, Si II, and Si III (see Figure 6.4; Table 6.1). No previous study exists that analyzes in detail the low-ion absorption near $v_{\rm LSR} = -147$ km s^{-1}, but the sightline has been studied by several authors to investigate highly-ionized gas in the Milky Way halo at *positive* radial velocities (Collins et al. 2005 2009; Fox et al. 2009; Shull et al. 2009; Fabian et al. 2000).

PG 1116+215. High-velocity absorption towards PG 1116+215 ($l = 223.4, b = +68.2$) is seen at positive LSR velocities between +170 and +220 km s^{-1} in the lines of Si II, C II, O I, Fe II, Mg II, Si III, C IV, and Si IV (see Figure 6.4; Table 6.1). This multi-phase absorber is relatively isolated, but possibly is associated with the Magellanic Stream. For this sightline both E140M and E230M data with relatively good S/N (~ 10 per 3.2 km s^{-1}-wide pixel element at 1300 Å) are available. Two absorption components at $v_{\rm LSR} = +184$ and +203 km s^{-1} can be fitted to the data. The HVC absorption towards PG 1116+215 was studied in detail by Ganguly et al. (2005) and Richter et al. (2009). Other studies that discuss the HVC absorption along this sightlines are Sembach et al. (2004a), Collins et al. (2005), Collins et al. (2009) and Fox et al. (2006).

Ton S210. Along the line of sight towards Ton S210 ($l = 225.0$, $b = -83.2$) high-velocity absorption is seen at high negative velocities between -140 and -260 km s^{-1}. Absorption near -170 km s^{-1} is related to the compact high-velocity cloud CHVC 224.0−83.4 (Putman et al. 2002), while the absorption at higher velocities is of unknown origin. Both E140M and E230M data are available, but the S/N is low (S/N $\sim$4 per 3.2 km s^{-1}-wide pixel element at 1500 Å). Three individual absorption components at $v_{\rm LSR} = -172, -207$, and -241 km s^{-1} are identified in the lines of C II, O I, Si II, Mg II, Fe II, Si III, Si IV and C IV (see Figure 6.2; Table 6.5). A detailed analysis of the high-velocity gas towards Ton S210 is presented in Sembach et al. (2002) and Richter et al. (2009).

HE 0515−4414. The sightline towards HE 0515−4414 is located at $l = 249.6$, $b = -35.0$ and passes through a region with some scattered H I clouds that possibly are connected to the Magellanic Stream. Only E230M data are available for this sightline, and the data have a low S/N of ~ 5 per 4.8 km s^{-1}-wide pixel element at 2400 Å. We identify one HVC absorption component at $v_{\rm LSR} = +103$ km s^{-1} in the lines of Mg II and Fe II. Additional HVC absorption components possibly are present near $\sim +200$ km s^{-1}, but are blended with intergalactic absorption features (Figure 6.3; Table 6.4). We did not find any previous paper that discusses the HVC absorption towards HE 0515−4414.

PG 1211+143. Relatively weak absorption at positive LSR velocities near $v_{\rm LSR} = +180$ km s^{-1} is seen along the line of sight towards the Seyfert 1 galaxy PG 1211+143 ($l = 267.6$, $b = +74.3$) in the lines of Si II, C II, O I, Si III, and C IV (see Figure 6.5; Table 6.3). For this line of sight, only E140M data are available. The S/N in the data is good (~ 15 per 3.2 km s^{-1}-wide pixel element at 1300 Å). Two distinct absorption components are observed at $v_{\rm LSR} = +170$ km s^{-1} and +188 km s^{-1}; the latter component is seen predominantly in the intermediate and high ions. This HVC is isolated, but possibly is associated with a compact high-velocity cloud (CHVC) ~ 1.5 deg away (de Heij et al. 2002). A detailed study of this absorber is presented in Richter et al. (2009); other studies that mention this HVC are Fox et al. (2006) and Collins et al. (2009).

PG 1216+069. The Seyfert 1 galaxy PG 1216+069 is located at $l = 281.1$, $b = +68.1$. We find HVC absorption in the lines of Si II, Si III, and C IV in three individual components at high LSR-velocities of $v_{\rm LSR}$= +212, +256, and +270 km s^{-1} in the available E140M data (see Figure 6.3; Table 6.3). The detected absorbers seem to be unrelated to any known large HVC complex. The data quality is relatively low (S/N ~ 8 per 3.2 km s^{-1}- wide pixel element at 1260 Å). HVC absorption towards PG 1216+069 is also discussed in Shull et al. (2009).

NGC 3783. The line of sight towards the Seyfert 1 galaxy NGC 3783 at $l = 287.5$, $b = +23.0$ is a well-studied HVC sightline that passes through the Leading Arm (LA) of the Magellanic Stream with strong absorption features at high positive velocities. For this sightline both E140M and E230M data are available. The data have superb quality with a S/N of ~ 25 per 3.2 km s^{-1}-wide pixel element at 1300 Å. Very strong disk and halo absorption from local disk and halo gas is seen in a single absorption trough in many lines in the velocity range between -60 and $+120$ km s^{-1}. This absorption component is not further considered in this paper. Absorption from the LA is seen in two strong components at $v_{\rm LSR} = +180$ and $+234$ km s^{-1} in the lines of Si II, O I, Mg II, Fe II, Al II, C II, and Si III (see Figure 6.4; Table 6.3). There are several detailed studies of the LA absorption towards NGC 3783 (e.g., Lu et al. 1998; Sembach et al. 2001).

RXJ 1230.8+0115. In the direction of RXJ 1230.8+0115 ($l = 291.3$, $b = +63.7$) weak HVC absorption in the lines of Si II, C II, O I and Si III is observed in two individual clouds at high positive velocities near $+100$ and $+300$ km s^{-1} (only E140M data are available; Figure 6.47; Table 6.3). The data are of intermediate quality with a S/N of ~ 7 per 3.2 km s^{-1}-wide pixel element at 1300 Å. For each of the two clouds, the HVC absorption can be fitted with a single absorption component centered at $v_{\rm LSR} = +111$ and $+295$ km s^{-1}, respectively (for C II we add another component at $v_{\rm LSR} = +292$ km s^{-1}). Both HVCs do not appear to be associated with any prominent HVC complex, but obviously represent isolated gaseous halo structures. A recent study of this HVC sightline is presented by Richter et al. (2009).

PKS 0312−770. The line of sight towards the Seyfert 1 galaxy PKS 0312−770 ($l = 293.4$, $b = -37.6$) is known to pass the so-called "Magellanic Bridge" (MB), an extended gaseous structure that connects the Large Magellanic Cloud (LMC) and the Small Magellanic Cloud (SMC; see Hindman et al. 1963). The MB is believed to be locted at a distance of $\sim 50 - 60$ kpc (Harries et al. 2003). Thus, the MB does not represent a "classical" Galactic HVC but rather is a tidal feature and gas component of the Magellanic system. For this sightline both E140M and E230M spectra are available, but the average S/N is relatively low (S/N ~ 6 per 3.2 km s^{-1}-wide pixel element at 1500 Å). Strong high-velocity absorption from gas in the MB is visible in the lines of C II, O I, Si II, Si III, Fe II, and Mg II. The STIS data indicate two main absorption components centered at $v_{\rm LSR} = +174$ km s^{-1} and $\rm v_{LSR} = +224$ km s^{-1} (see Figure 6.5; Table 6.1) . A detailed analysis of this sightline and the MB absorption is presented in Misawa et al. (2009).

4.3 Covering fractions of individual ions

The physical conditions in the gas, in particular the ionization conditions, are known to vary substantially among the Galactic HVC population. HVCs span a large range in temperatures and gas densities, they are subject to thermal instabilities, ram-pressure stripping, photoionization from the Galactic disk and from the extragalactic UV background, collisional ionization from hot material ejected by supernova explosions in the disk, gas mixing processes, and other related phenomena. As a result, the characteristic absorption patterns of HVCs (i.e, the observed absorption frequency of metal ions and their relative strengths) can be used to constrain the physical conditions in HVCs.

All in all, we fit 67 individual high-velocity absorption components (Voigt components; see above) in our data set. Of these, 47 components have velocity separations $\Delta v > 30$ km s^{-1} from neighboring HVC absorption components and thus can be regarded as individual entities, hereafter referred to as absorption *systems*.

An important parameter that characterizes the distribution of neutral and ionized HVC gas in the Milky Way halo is the covering fraction, $f_{\rm c}(X)$, for each ion X that is considered. As indicated in Table 4.3, we define the covering fraction as the number of sightlines that exhibit significant HVC absorption in the ion X divided by the total number of sightlines along which HVC absorption above the limiting column density threshold ($\log N_{\rm min}$) could be detected. The column density threshold for each ion was calculated from the relevant ion transitions in the STIS wavelength range (see Section 4.1) together with the local S/N ratio.

Table 4.3 shows the values of $f_{\rm c}$ for the ions O I, C II, Si II, Mg II, Fe II, Si III, Si IV, and C IV, together with the limiting column densities, $\log N_{\rm min}$, as determined from our line-fitting analysis. In this way we obtain covering fractions for the above-listed ions between 0.20 (Si IV) and 0.70 (C II, Si III). Assuming that the sightlines and the HVCs are randomly distributed over the sky with $f_{\rm c} \leq 1$, and considering Poisson-like statistics, the total sky covering fraction of HVC absorption in our data is $f_{\rm c} = 0.70 \pm 0.15$. This HVC covering fraction is in excellent agreement with the value of $f_{\rm c} = 0.68 \pm 0.04$ derived by

Table 4.3: Covering fractions of individual ions in HVCs

Ion	$\mathcal{N}/\mathcal{N}_{\rm tot}$ [a]	$f_{\rm c}$ [b]	$\log N_{\rm min}$ [c]
C II	21/30	0.70	13.20
C IV	12/30	0.40	13.00
O I	14/29	0.48	13.65
Si II	20/30	0.67	12.25
Si III	21/30	0.70	12.15
Si IV	6/30	0.20	12.90
Mg II	10/19	0.53	12.70
Fe II	10/21	0.48	12.90

[a] Number of HVC detections above column-density threshold/total number of sightlines;
[b] covering fraction;
[c] minimum column density threshold considered

Lehner et al. (2012), based on a much larger combined COS/STIS data set. The good agreement with the Lehner et al. results indicates that the non-uniform sky distribution of the QSOs (as mentioned in Section 4.1) has no significant influence on the determination of the HVC covering fraction from our STIS QSO sample.
Note that we do not consider absorption by Al II in our statistical analysis, because for the Al II λ1670.8 line (the only detectable Al II line in our data) there is a gap between $+80\ {\rm km\,s^{-1}} \leq v_{\rm LSR} \leq +200\ {\rm km\,s^{-1}}$ at the red end of the Echelle grating. To compare the covering fractions of the individual ions with each other, and to relate them to H I sky-covering fractions determined from 21cm all-sky surveys, one needs to consider the relative abundance of the elements (C, O, Si, Mg, and Fe) in HVCs. The ionization conditions and dust-depletion properties of the absorbing gas can also affect the interpretation of the covering fractions. These factors will be considered in the subsequent sections.

4.3.1 Si II absorption

In our statistical analysis, we focus on Si II absorption in HVCs. The STIS E140M data contain five Si II transitions (at λ1190.4, λ1193.3, λ1260.4, λ1304.4, and λ1526.7) that span a large range in oscillator strengths ($f = 0.133$ for Si II λ1526.7 and $f = 1.176$ for Si II λ1260.4; Morton (2003)). Our simultaneous fitting of these lines therefore provides particularly reliable values for N(Si II) and b(Si II) in both strong and weak HVC absorption components. The ionization potential of Si II ($E_{\rm Si\,II} = 16.4$ eV) is very similar to that of Mg II ($E_{\rm Mg\,II} = 15.0$ eV), suggesting that both ions trace the same gas phase in HVCs. In addition, the cosmic abundance of Si and Mg are almost identical ($\log({\rm Si/H})_\odot = -4.44$ and $\log({\rm Mg/H})_\odot = -4.42$, assuming solar relative abundance from Asplund et al. (2005)). Because Mg II is the most commonly used ion to study circumgalactic gas at low and intermediate redshift in optical quasar spectra (e.g., Kacprzak et al. 2008; Bouché et al. 2012), the absorption properties of Si II and Mg II in HVCs can be directly compared to the statistical properties of intervening Mg II absorbers at low redshift (see Section 4.4.3).
The covering fraction for HVC Si II absorption in the halo is $f_{\rm c}({\rm Si\,II}) = 0.67$ for $\log N({\rm Si\,II}) \geq 12.25$ (see previous section; Table 4.3). For comparison, the filling factor of H I in HVCs derived from 21cm surveys is $f_{\rm c}({\rm H\,I}) \approx 0.15$ for $\log N({\rm H\,I}) \geq 18.3$ and $f_{\rm c}({\rm H\,I}) \approx 0.30$ for $\log N({\rm H\,I}) \geq 17.8$ (Wakker 2004). The higher detection rate of Si II absorption compared to H I emission suggests that more than half ($0.37/0.67 = 0.55$) of the high-velocity Si II absorbers trace neutral and ionized gas in the halo below the typical detection limit of current 21cm observations at $\log N({\rm H\,I}) < 17.8$.
HVCs that are detected in metal absorption without having an H I 21cm counterpart commonly are referred to as "low-column density HVCs" (LCDHVCs, Richter et al. 2009).

Radial velocities

In the upper panel of Figure 4.3 we show the distribution of LSR velocities of the 19 HVCs for which Si II absorption was detected and accurately measured (only high-velocity Si II absorption towards NGC 3516 is not considered here because of the low data quality). Absolute values for $v_{\rm LSR}$ range between $|v_{\rm LSR}| =$ 90 and 370 ${\rm km\,s^{-1}}$. The highest velocity absorber is found towards NGC 7469 and is related to the Magellanic Stream (see Table 4.2). Note that the region between $v_{\rm LSR} = -90$ to $+90\ {\rm km\,s^{-1}}$ (i.e., the IVC velocity regime) is not considered in this study.

Out of these 19 sightlines, 12 (63%) show absorption at negative velocities. One may argue that large HVC complexes at negative velocities (such as Complex C) together with the limited sample size leads to an observational bias towards negative velocities. However, optical observations of Ca II absorption in HVCs, based on a ten-times larger data sample of randomly distributed QSO sightlines, also indicate that the majority of the neutral HVC absorbers exhibit negative radial velocities (Ben Bekhti et al. 2008 2012). This velocity distribution suggests a net infall of high-velocity neutral and weakly ionized gas towards the Milky Way disk. High ions such as O VI, in contrast, show an equal distribution of positive and negative velocities in the Galactic halo (Sembach et al. 2003), supporting the idea that they trace both infalling and outflowing gas that is highly ionized.

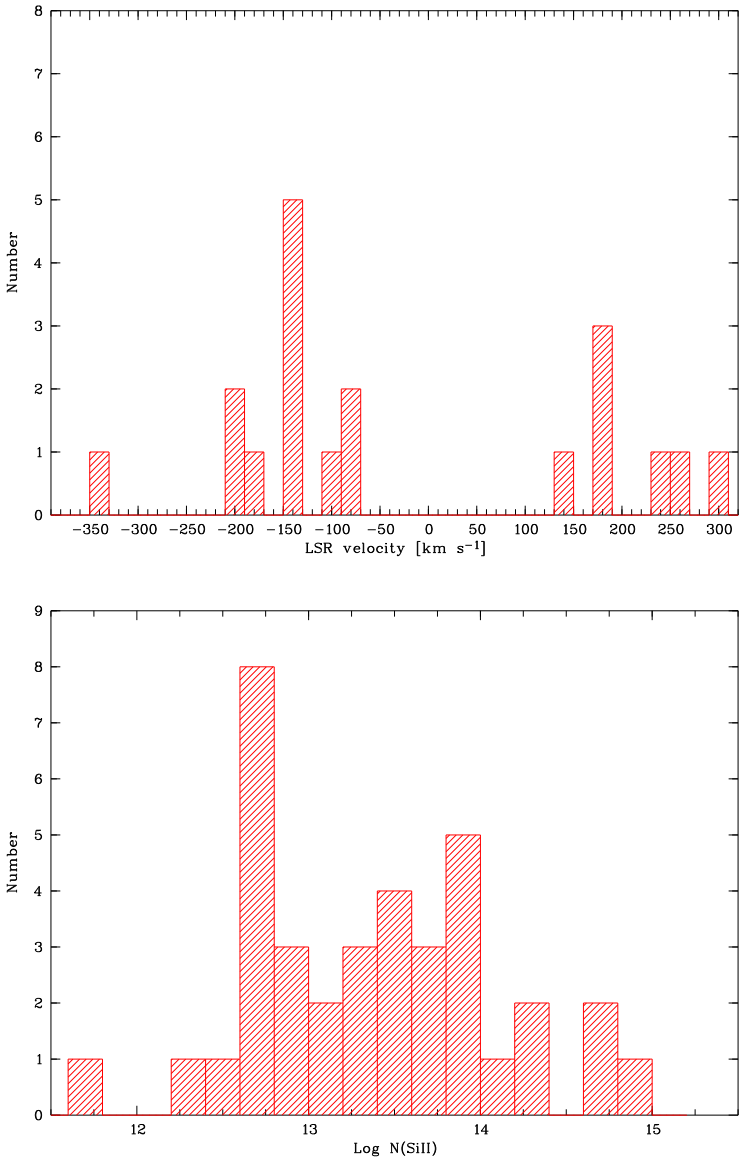

Figure 4.3: **Upper panel:** distribution of LSR velocities of all detected Si II HVC absorption systems. **Lower panel:** distribution of Si II column densities in HVCs, based on Voigt-profile fitting of 38 HVC absorption components.

Column densities

From our line-fitting analysis we find that the 19 HVCs that are detected and accurately measured in Si II absorption are composed of 38 individual absorption components. For these components we obtain typical Si II column densities in the range log $N(\mathrm{Si\,II}) = 12.5 - 15.0$ (see Tables B.1−B.5). A histogram showing the distribution of the Si II column densities is presented in the lower panel of Figure 4.3. The median logarithmic column density is log $N(\mathrm{Si\,II}) = 13.48$.
Figure 4.3 indicates a widespread, inhomogeneous distribution of the Si II column densities in HVC

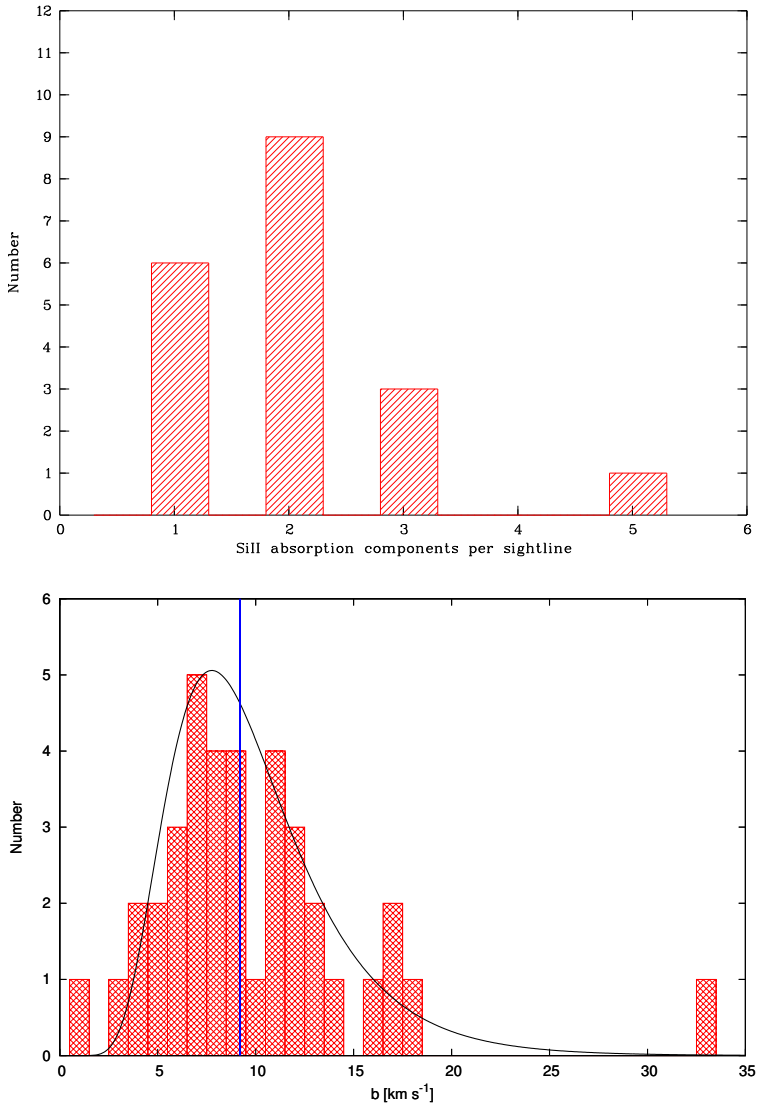

Figure 4.4: **Upper panel:** distribution of Si II velocity-components in HVCs.
Lower panel: distribution of Si II Doppler parameters in HVCs, based on Voigt-profile fitting of 40 HVC absorption components. The black solid line indicates a fit to the distribution with a log-normal function. The blue solid line marks the median value at 9.2 km s^{-1}.

absorption components with a prominent peak near log N(Si II) $\sim$ 12.8 and another maximum near log N(Si II) $\sim$ 13.8. Most (21/31 or 68 %) of the HVC absorption components have log N(Si II) $\geq$ 13.2. Tables 6.1 - 6.5 show that only some of the Si II absorption components with log N(Si II) $<$ 13.0 represent satellite components of stronger HVC absorbers. There exist a distinct population of isolated, weak HVC absorbers with relatively low column densities of Si II and other low ions (e.g., towards PG 1211+143, PKS 2155−304, NGC 4151). These absorbers belong to the class of highly-ionized high-velocity clouds (e.g., Sembach et al. 1999 2003), and to the low-column-density HVCs (Richter et al. 2009). This suggests that the inhomogeneous distribution in Figure 4.3 reflects the actual physical properties of neutral and weakly-ionized gas structures in the Galactic halo, and is not an artifact from our analysis.

Based on the Si II column densities shown in the lower panel of Figure 4.3 we have constructed a column-density distribution function (CDDF) of HVC Si II absorption components (left panel of Figure 4.5). The CDDF can be defined as $f(N) = m/\Delta N$, where m is the number of absorbers in the column-density bin ΔN. The CDDF is usually approximated by a power law in the form $f(N) = C\,N^{-\beta}$, where $\beta \approx 1.5$ for H I in HVCs, as derived from 21cm observations (e.g., Lockman et al. 2002). As can be seen in Figure 4.5, the CDDF of Si II HVC absorption components deviates from a simple power law, showing instead a plateau at log N(Si II) $\sim$ 13.8. The shape of the CDDF thus reflects the inhomogeneous distribution of Si II column densities in HVC absorption components shown in the lower panel of Figure 4.3. If we force a power-law fit with a single slope to the Si II CDDF for column densities log

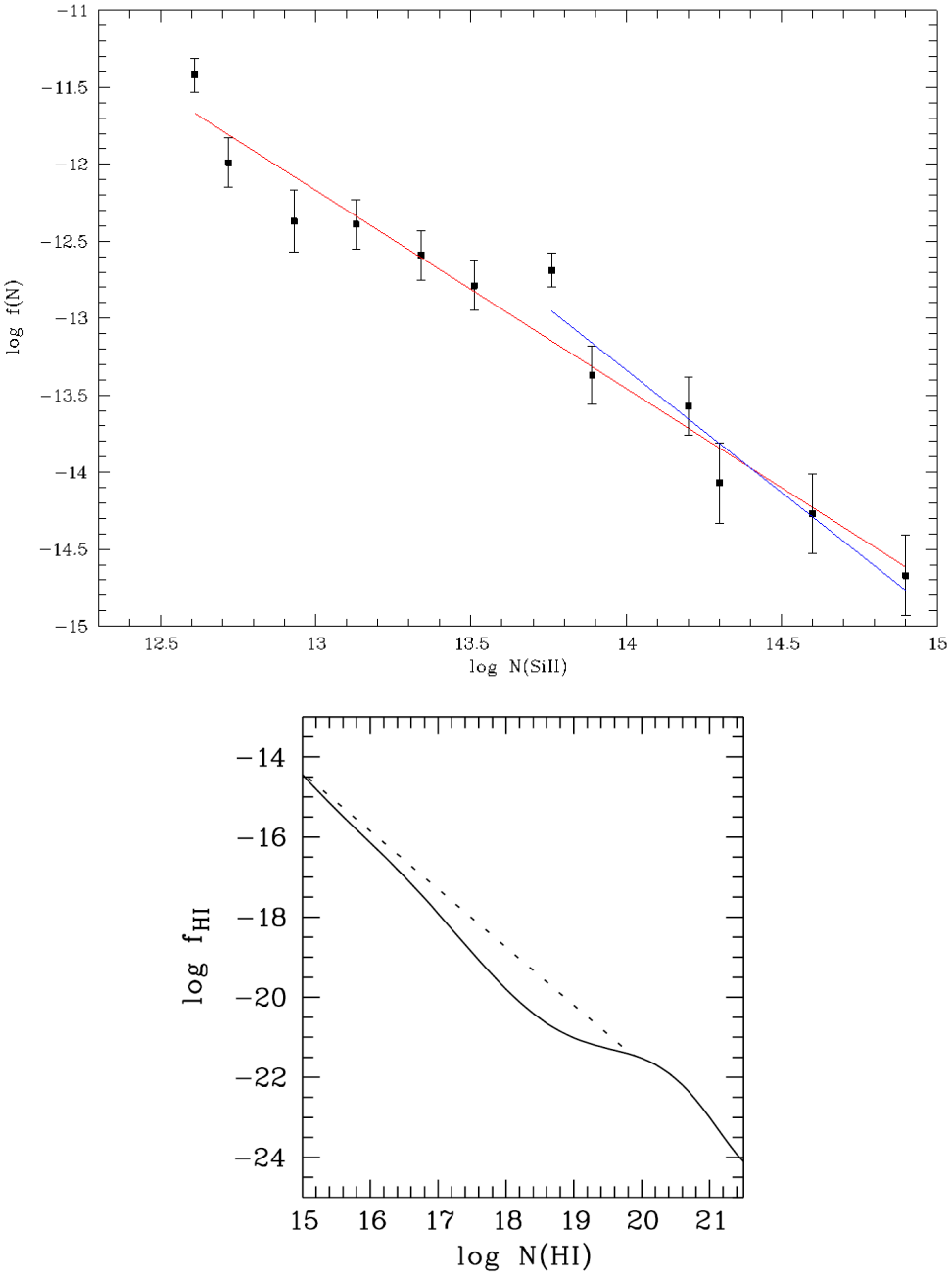

Figure 4.5: **Upper panel:** column-density distribution function of Si II absorption components in HVCs. The data indicate that a simple power law (red and blue solid lines) represents a rather poor approximation to the distribution of Si II column densities.
Lower panel: combined H I CDDF in the range $15.0 \leq \log N(\mathrm{H\,I}) \leq 21.4$. The different lines represent different used data samples. For a detailed description see Richter (2012).

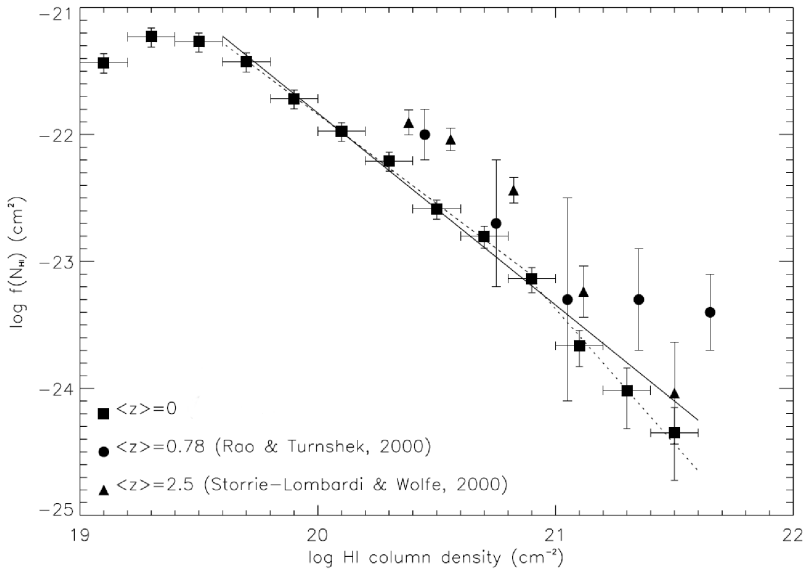

Figure 4.6: Another, more detailed plot for the H I column-density distribution function for $z = 0$ in the range $19.0 \leq \log N(\mathrm{H\,I}) \leq 22.0$, compared with data points from other works. The two different lines represent a single power-law (solid line) and a double power-law (dotted line) (Ryan-Weber et al. 2003).

$N(\mathrm{Si\,II}) \geq 12.5$, we obtain $\beta = 1.29 \pm 0.09$ and $\log C = 4.57 \pm 1.20$ (Figure 4.5, red solid line). This slope is somewhat shallower than the canonical value of $\beta \approx 1.5$ derived from H I 21cm observations of Galactic HVCs (e.g., Lockman et al. 2002). If we instead restrict our fit to the range $\log N(\mathrm{Si\,II}) \geq 13.7$, we obtain a much steeper slope of $\beta = 1.59 \pm 0.23$ and $\log C = 8.94 \pm 3.31$ (Figure 4.5, blue solid line). This slope fits better to the slope derived for H I, but is substantially smaller than the slope derived for optical Ca II absorption in IVCs and HVCs ($\beta = 2.2 \pm 0.3$; Ben Bekhti et al. (2008), Ben Bekhti et al. (2012)). The steeper slope of Ca II compared to Si II most likely is a result of the strong depletion of Ca into dust grains, because high-column density clouds tend to have higher depletion values than low-column density clouds (see also discussion in Ben Bekhti et al. 2012). Note that if some of the HVC absorption components would be composed of several, unresolved velocity components, the slope of the CDDF would be steeper, too.

Doppler parameters

In the lower panel of Figure 4.4 we show the distribution of Si II Doppler parameters (b-values) in HVCs, based on the Voigt-profile fitting of the 38 Si II absorption components. The measured b-values range from 1 to 33 km s^{-1} with a median value of ~ 9.2 km s^{-1}. The distribution can be fitted by a log-normal function (solid line in Figure 4.4), which peaks at $b = 7$ km s^{-1}. The median b value is $b = 9$ km s^{-1}. Note that Si II b-values that are smaller than the instrumental resolution in the E140M grating (~ 7 km s^{-1}) can be reliably determined since we are fitting simultaneously *several* Si II lines with different oscillator strengths (i.e., the corresponding curve-of-growth is well-defined).
It is commonly assumed that the Doppler parameter of an absorber is composed of a thermal component (b_{th}) and a non-thermal component (b_{nth}), so that $b^2 = b_{\mathrm{th}}^2 + b_{\mathrm{nth}}^2$. The thermal component depends on the temperature of the gas, T, and the atomic weight (A) of the absorbing ion: $b_{\mathrm{th}} \approx 0.129\,(T[\mathrm{K}]/A)^{1/2}$ km s^{-1}. The non-thermal component may include turbulent motions in the gas and unresolved velocity structure in the lines.
Since silicon is a relatively heavy element ($A_{\mathrm{Si}} = 28$), it is expected that for neutral and partly ionized HVCs gas with $T \leq 2 \times 10^4$ K (e.g., Ben Bekhti et al. 2012, their Figure 15) the thermal contribution to $b(\mathrm{Si\,II})$ is ≤ 3.5 km s^{-1}. This implies that the observed line widths of most of the Si II HVC absorption features are subject to broadening mechanisms other than thermal broadening, such as macroscopic turbulence and gas flows. Moreover, it is very likely that many of the Si II absorption components seen in the STIS data are composed of smaller (unresolved) substructures. In fact, optical absorption-line studies of IVCs and HVCs at very high spectral resolution and high S/N clearly indicate that there exists substantial velocity-structure in neutral halo clouds at a level of a few km s^{-1} (see, e.g., the IVC and HVC in the direction of the Magellanic Clouds; Welty et al. (1999)).

Sub-component structure

While the smallest substructures in the HVC absorbers obviously are not resolved in the STIS data, most of the detected Si II absorption features do show several individual velocity subcomponents that are separated from each other by > 10 km s^{-1}, typically, and that we have fitted as individual absorption components. Since for intervening QSO absorbers the velocity spread of the detected absorption feature often is used as an observational parameter to constrain the characteristic environment of the absorber host (e.g., Charlton and Churchill 1998), it is interesting to study the velocity structure of Galactic HVCs and compare it to the absorption properties of intervening systems, in particular weak and strong Mg II absorbers.

In the upper panel of Figure 4.4 we show the number distribution of Si II absorption components per HVC for all spectra in which HVC gas is detected in Si II. About 80% of the measured HVCs have one or two velocity components that can be resolved with the STIS data (one component: 32%; two components: 47%). For comparison, Ben Bekhti et al. (2012) find for optical Ca II absorption in IVCs and HVCs that more than 70% of the Ca II absorbers are seen as single-component systems, while the fraction of two-component absorbers is less than 20%. This difference is not surprising, however, since Ca II in IVCs and HVCs is expected to trace relatively confined neutral gas regions in the halo clouds, whereas Si II traces both neutral and weakly ionized gas regions (i.e., multi-phase gas regions) that are spatially more extended.

On a first look, the distribution of absorption components in HVCs appears to be very similar to the distribution found for strong intervening Mg II absorbers (Prochter et al. (2006); one component: ~ 50%; two components: ~ 20%).

However, because intervening Mg II absorbers trace gas in disks and halos of galaxies (and thus often are fully saturated over a large velocity range) and because the spectral resolution of the Mg II SDSS data used by Prochter et al. (2006) is very low ($R \approx 2000$), this similarity does not provide any clues to the connection between strong Mg II systems and HVCs. Using high-resolution optical spectra, Churchill et al. (2003) indeed find a much larger number of ~ 8 absorption components per absorption systems for strong Mg II absorbers with H I column densities below that expected for neutral gas disks, but similar to those in Galactic HVCs.

Even if one considers the longer absorption path length through a galaxy halo from an exterior vantage point (Churchill et al. study) compared to the path length through the Milky Way halo from the position of the Sun (our study), the four-times higher number of absorption components per system clearly indicates that the majority of the strong Mg II absorbers with $\log N(\mathrm{H\,I}) \leq 20.2$ studied by Churchill et al. (2003) trace gaseous structures in halos that are kinematically more complex than the Galactic HVC population. As we will see later, this scenario is supported by the very large absorption cross section of strong Mg II absorbers that are both more common and spatially more extended (Section 4.4.3).

4.3.2 Remarks on other ions

O I

O I is an excellent tracer of H I, because both atoms have the same ionization potential and they are coupled by a strong charge-exchange reaction. There is only one (strong) transition of O I available in the STIS E140M wavelength range (at 1302.2 Å). Thus, $N(\mathrm{O\,I})$ can be determined from the STIS data alone, only under the *assumption* that $b(\mathrm{O\,I}) = b(\mathrm{Si\,II})$.

There are several studies on HVCs that have combined STIS E140M data with FUV data from FUSE (e.g., Richter et al. 2001; Sembach et al. 2004b) to make use of several other (weaker) O I transitions at $\lambda < 1040$ Å. However, only for a few lines of sight in our sample there are FUSE data of sufficient quality to determine $N(\mathrm{O\,I})$ at an accuracy similar to that of $N(\mathrm{Si\,II})$; in this study, we therefore do not consider any available FUSE data.

The covering fraction of HVC O I absorption ($f_c(\mathrm{O\,I}) = 0.48$) is smaller than that of Si II, but the column-density limit above which $f_c(\mathrm{O\,I})$ is considered is 1.4 dex higher than that of Si II (Table 4.3). The relative solar abundance of O compared to Si is $\log(\mathrm{O/Si})_\odot = +1.15$ (Asplund et al. 2005), so that for an HVC with solar relative abundance of O and Si (and with 100% of these elements in the gas phase) our STIS data are slightly (0.25 dex) more sensitive for Si II absorption in HVCs than for absorption by O I. On the one hand, the Si II column density in HVCs may be reduced by the depletion of Si into dust grains (e.g., Richter et al. 2001; Richter and de Boer 2004); on the other hand, Si II traces neutral *and* weakly-ionized gas, so that Si II/O I may be higher than $(\mathrm{O/Si})_\odot$. Consequently, these effects (dust depletion and ionization) are opposite and may even cancel each other out. To estimate whether or not this is the case in an HVC one would need to know the local dust properties and ionization conditions in the gas, which are difficult to determine.

The five sightlines, along which high-velocity Si II is detected without associated O I absorption (see

Table 4.1), exhibit relatively weak HVC absorption in Si II, suggesting that for some of these clouds O I λ1302.2 may be just below the detection limit (see also Richter et al. 2009).

C II

With an ionization potential of $E_{\rm C\,II} = 24.4$ eV singly-ionized carbon traces neutral and mildly ionized gas in HVCs. The only available C II transition in the STIS E140M wavelength range is located at 1334.5 Å. To derive N(C II) from the (mostly fully saturated) λ1334.5 line one needs to assume that b(C II) is similar to the Doppler parameter derived for Si II (or other low or intermediate ions). However, in view of the higher ionization potential of C II compared to Si II, C II absorption may arise in a somewhat different (possibly more extended) gas phase, so that this assumption may be invalid for most of the HVC absorbers. As a consequence, the C II column densities derived for our HVC sample are possibly afflicted with large systematic uncertainties that we cannot account for.
From our data we derive a covering fraction of $f_{\rm c}$(C II) = 0.70 (see Table 4.3), which is insignificantly higher than that of Si II. The column density threshold is $\log N_{\rm min} = 13.20$, which is ~ 1 dex higher than that of Si II (see Table 4.3). This difference compensates the expected abundance difference between these two elements, if solar relative abundances are assumed ($\log$ (C/Si)$_\odot = +0.88$). Therefore, the C II and Si II transitions in the STIS data provide roughly the same sensitivity to neutral and weakly ionized gas in HVCs.

Mg II

The Mg II doublet near 2800 Å is observed only with the STIS E230M grating, so that there are only 19 sightlines along which high-velocity Mg II can be studied in our data sample at intermediate spectral resolution (FWHM ~ 10 km s^{-1}).
As mentioned above, Mg II and Si II are expected to trace a similar gas phase in HVCs and both ions are expected to have very similar column densities. The Mg II filling factor in HVCs is $f_{\rm c}$(Mg II) = 0.53 (Table 4.3), which is somewhat lower than that of Si II. This is not surprising, however, since the Mg II column density threshold ($\log N_{\rm min} = 12.70$) is ~ 0.5 dex higher than that of Si II. In Section 4.4.3 we will combine the E230M data for Mg II and the E140M data for Si II to compare the absorption statistics of HVCs with that of intervening Mg II absorbers.

Fe II

The ionization potential of Fe II ($E_{\rm Fe\,II} = 16.2$ eV) is very similar to that of Si II and Mg II, so these three ions are expected to arise in the same gas phase (neutral and weakly ionized gas). In the E230M wavelength band there are several Fe II transitions available including the two relatively strong transitions at 2382.8 Åand 2600.2 Å. Also the E140M band contains a number of (weaker) Fe II transitions.
The covering fraction of HVC Fe II absorption is $f_{\rm c}$(Fe II) = 0.48 (for $\log N_{\rm min} = 12.90$), thus very similar to that of Mg II (see above). This is expected, since the threshold column density is 0.2 dex higher than for Mg II, while the solar abundance of Fe is 0.08 dex lower ($\log$ (Fe/H)$_\odot = -4.55$, Asplund et al. 2005). In summary, both ions are equally sensitive to trace predominantly neutral and weakly-ionized gas in HVCs. There are two sightlines that show Fe II absorption at high velocities, while these two sightlines are not covered in Mg II (Table 4.3).

Si III

Si III has one very strong transition at 1206.5 Å; with an ionization potential of $E_{\rm Si\,III} = 33.5$ eV this ion traces diffuse ionized gas in HVCs and their (more or less) extended gaseous envelopes. As for C II and O I the determination of a reliable column density for Si III is basically impossible, as the Si III λ1206.5 line is often heavily saturated and the assumption that b(Si III) = b(Si II) may be invalid for most cases. We find $f_{\rm c}$(Si III) = 0.70, which is identical to the value derived for C II (i.e., all HVCs that are reliably detected in Si III in our sample are also detected in C II). The column density threshold considered for this estimate is $\log N_{\rm min}$(Si III) = 12.15 (compared to $\log N_{\rm min}$(C II) = 13.20; see above). Since (C/Si)$_\odot = +0.88$ (Asplund et al. 2005) it follows that Si III and C II trace the same physical regions in HVCs at roughly the same sensitivity. The covering fraction of $f_{\rm c}$(Si III)= 0.70 is lower than that derived by Collins et al. (2009; $f_{\rm c} = 0.84$ for $\log N_{\rm min}$(Si III) = 12.50) based on the same STIS data. The reason for this discrepancy is that these authors also include very weak (and also spurious) absorption features in their statistics that we do not consider as secure HVC Si III detections. In addition, for our analysis we take into account only those HVC components that are (in velocity space) well separated from lower-velocity material (i.e., IVCs). Our value of $f_{\rm c}$(Si III)= 0.70 is, however, in excellent agreement

with the covering fraction of $f_c = 0.68 \pm 0.04$ of UV-selected HVCs based on a much larger STIS/COS data sample recently presented by Lehner et al. (2012).

C IV and Si IV

The high ions C IV and Si IV are known to trace a gas phase in HVCs that is different from that traced by low ions such as O I, C II, Si II, Mg II, and Fe II. High-velocity C IV and Si IV absorption sometimes is associated with common 21cm HVCs (e.g., Fox et al. 2009), or with low-column density HVCs (Richter et al. 2009), where it is thought to arise in the interface regions between neutral HVC gas and the hot coronal gas. In addition, there exists a population of highly-ionized HVCs (e.g., Sembach et al. 1999 2003) that probably represent low-density, gas structures in the halo and that most likely are photoionized. These structures may arise in diffuse gaseous material that originates in the IGM and that is being accreted by the Milky Way ("warm accretion"), or that results from the break-up of more massive HVCs as they interact with the coronal gas in the halo (one prominent example is the HVC Complex GCN, which is detected in C IV and Si IV towards PKS 2155−304 and Mrk 509 ; see Winkel et al. (2011)).
As covering fractions we derive f_c(C IV) = 0.40 for log N_{min}(C IV) = 13.00 and f_c(Si IV) = 0.20 for log N_{min}(Si IV) = 12.90. These covering fractions are smaller than the one derived for O VI in the Milky Way halo (f_c(O VI)$\geq$ 0.59; Sembach et al. (2003)), implying that O VI is more sensitive for detecting highly-ionized halo gas and/or the O VI absorbing gas phase is spatially more extended than the C IV and Si IV absorbing phase.

4.4 HVCs as intervening metal-line absorbers

Deep H I 21cm observations of M31 and other nearby spiral galaxies (e.g., NGC 891) clearly show that the HVC phenomenon is not restricted to the Milky Way, but represents an ubiquitous component of spiral galaxies in the local Universe (e.g., see Section 1.3.1). It indicates the various gas-circulation processes in the inner and outer halos of star-forming galaxies (Thilker et al. 2004; Oosterloo et al. 2007; Fraternali et al. 2007; Richter 2012). Our results on the covering fraction of the different ions in the Milky Way HVCs, together with statistics of intervening metal-line absorbers in QSO spectra, now can be used to investigate the absorption-cross section of HVC analogs in the local Universe and to provide an estimate of the contribution of HVCs to the number density of intervening metal absorbers at low redshift.

In the following, we will first briefly discuss the general relation between the number density of intervening metal absorbers and the absorption-cross section of galaxies and their halos. As a second step, we will then combine the observed sky covering fractions of Si II and Mg II in the Milky Way HVCs with statistics on intervening Mg II absorbers to study the the spatial distribution of neutral and weakly ionized gas in the halos of Milky Way-type galaxies (see also Richter et al. (2011); Richter (2012)).

4.4.1 Absorption-cross section of galaxies and their halos

Let us define $\mathrm{d}\mathcal{N}/\mathrm{d}z\,(X)$ as the absorber number density of QSO metal-line absorbers per unit redshift measured for a given ion X (see also Section 1.4), n_g as the space density of galaxies at $z = 0$, $R_\mathrm{h}(X)$ as the (mean) galaxy halo radius (within which metal absorption takes place), and $f_\mathrm{c}(X) \leq 1$ as the mean covering fraction of the ion X in the disk/halo gas for radii $r \leq R_\mathrm{h}(X)$. Number density and geometric cross section of the gas in and around galaxies are directly related to each other (see Equation 1.1 for $z = 0$, e.g., Kacprzak et al. 2008).
The space density of galaxies can also be expressed as $n_\mathrm{g} = \Phi^* \, \Gamma(x, y)$, where Φ^* is the number density of $L^\star$ galaxies. $\Gamma(x, y)$ is the incomplete Gamma function in which $x = \alpha + 1$, where α is the slope at the faint end of the Schechter galaxy luminosity function. The parameter y is defined as $y = L_\mathrm{min}/L^*$, where L_min is the minimum luminosity of galaxies contributing to the population of absorbing gas halos. Therefore, if n_g is known for a given luminosity range and $\mathrm{d}\mathcal{N}/\mathrm{d}z\,(X)$ and $f_\mathrm{c}(X) \leq 1$ are measured for a given ion, Equation 1.1 allows us to estimate the characteristic size, $R_\mathrm{h}(X)$, of the absorbing region around galaxies. For a more detailed discussion of these parameters see Section 1.4.3 or Richter (2012).

4.4.2 Covering fraction of strong Mg II absorption in the Milky Way Halo

For the study of the physical properties and absorption cross section of gas in and around galaxies at low and high redshift via QSO absorption-line spectroscopy the Mg II ion plays a crucial role. The so-called strong Mg II systems are intervening metal-absorption systems that have Mg II equivalent widths $W_{2796} > 0.3$ Å; they usually are associated with luminous galaxies ($L > 0.05\,L^*$) at impact parameters $< 35\,h^{-1}$ kpc (e.g., Bergeron and Boisse 1991; Steidel et al. 2002; Kacprzak et al. 2010). These absorbers are expected to trace neutral and ionized gas in the disks of galaxies and their gaeous halos (including HVCs). The so-called weak Mg II systems have $W_{2796} \leq 0.3$ Å; they appear to be less tightly associated with galaxies and are typically found at larger distances from luminous galaxies, in the range $35 - 100\,h^{-1}$ kpc (Milutinović et al. 2006; Rigby et al. 2002).
From the LCDHVC survey by Richter et al. (2009) and from this study it is expected that only the most massive HVCs (HVCs with neutral column densities $\log N(\mathrm{H\,I}) \geq 17.2$) display the absorption charcterisitics of strong Mg II absorbers, while there exists a population of HVCs with H I column densities $\log N(\mathrm{H\,I}) < 17.2$ that would appear as weak Mg II absorbers if seen as QSO absorption-line system. The high-velocity absorbers towards Ton S210 and NGC 4151 represent examples for this class of low-column density HVCs. Note that *by definition* all HVCs that have $W_{2796} > 0.3$ Å would be classified as strong Mg II systems if seen as QSO absorbers from far away. However, since all HVCs in the Milky Way halo have $\log N(\mathrm{H\,I}) \leq 20.2$ one would expect that HVC analogs in the halos of Milky Way-type galaxies contribute to the population of strong Mg II absorbers predominantly in the range 0.3 Å $\leq W_{2796} \leq 1.0$ Å while the strongest of the intervening Mg II absorbers with $W_{2796} > 1.0$ Å are related to disks, disk-halo interfaces, and galactic winds (e.g., Bouché et al. 2012). In the usual QSO absorber classification scheme, HVCs would appear as sub-damped Lyman-α systems (sub-DLAs) and Lyman-limit systems (LLS; see Richter 2012).

In Table 4.4, sixth row, we show the measured Mg II equivalent widths for the eleven (out of 19 possible) HVCs in which Mg II absorption has been detected. Strong Mg II absorption with $W_{2796} > 0.3$ Å is measured for six HVCs, suggesting that the covering fraction of HVCs with strong Mg II absorption is

$f_{\rm c,sMg} = 6/19 \approx 0.32$. Because of the limited statistical relevance of this result, we also consider Si II as a proxy for Mg II. As mentioned earlier, Si II and Mg II have very similar ionization potentials and solar abundances, so that it is expected that both ions trace the same gas phase in HVCs and they have very similar column densities. To demonstrate the expected similarity of the Si II and Mg II column densities in HVCs we show in Figure 4.8 an example of a Cloudy photoionization model of a Galactic HVC with a H I column density of 10^{19} cm^{-2}, a distance to the Galactic disk of 50 kpc, and with solar abundances of silicon and magnesium (model from Richter et al. 2009). In this figure, N(Si II) and N(Mg II) are plotted against the ionization parameter, U, and the gas density, $n_{\rm H}$. Over a large range of densities and ionization parameters the expected column densities of Si II and Mg II lie within 0.2 dex of each other, demonstrating that these two ions indeed trace the same gas phase in HVCs with almost identical column densities.
To transform the measured Si II *equivalent widths* along the 19 suited E140M sightlines into Mg II equivalent widths, we consider Si II λ1260, which is the strongest Si II transition covered by our STIS data (Table 4.4, fifth row). From atomic data it follows that $(f\lambda)_{\rm Si\,II\,1260} \approx (f\lambda)_{\rm Mg\,II\,2796}$ (Morton 2003).

For a typical HVC Doppler parameter range of $b = 5 - 12$ km s^{-1} with one or two absorption components and under the above discussed assumption that N(Si II) = N(Mg II), an equivalent width of 300 mÅ in the Mg II λ2796 line corresponds to an equivalent width of $140 - 200$ mÅ in the Si II λ1260 line (see also Narayanan et al. 2008a). We here use the lower threshold of $W_{1260} = 140$ mÅ to separate strong and weak Mg II absorbers in HVCs in an indirect manner. The observed HVC Si II/Mg II absorption strengths towards PG 1116+215 and Ton S210 are in excellent agreement with this conversion scheme (see Table 4.4).
Based on this method, we find that 12 of the 20 Si II HVC absorbers listed in Table 4.4 represent strong Mg II systems. Combining this result with our direct Mg II measurements outlined above we have 6 relevant Mg II plus 8 relevant Si II detections along 41 independent sightlines, so that the total covering fraction of strong Mg II absorption in Galactic HVCs is estimated as $f_{\rm c,sMg} = 14/41 = 0.34 \pm 0.09$. This covering fraction for strong Mg II absorption is identical to the observed covering fraction of H I in HVCs with log N(H I) ≥ 17.8, based on 21cm HVC surveys (see Wakker 2004, and references therein). It is also very similar to the covering fraction of Ca II absorption in HVCs with log N(Ca II) ≥ 11.2, as derived from a large sample of optical QSO spectra (Ben Bekhti et al. 2008 2012). Ca II traces predominantly neutral gas in HVCs with H I column densities log N(H I) ≥ 17.4 (Richter et al. 2011; Ben Bekhti et al. 2012). Therefore, the similar absorption cross sections imply that Ca II and strong Mg II trace the same type of halo clouds, namely massive HVCs that are optically thick in H I; only these clouds would be seen as strong Mg II absorbers if the Milky Way halo would be observed as a QSO absorption-line system from an exterior vantage point.

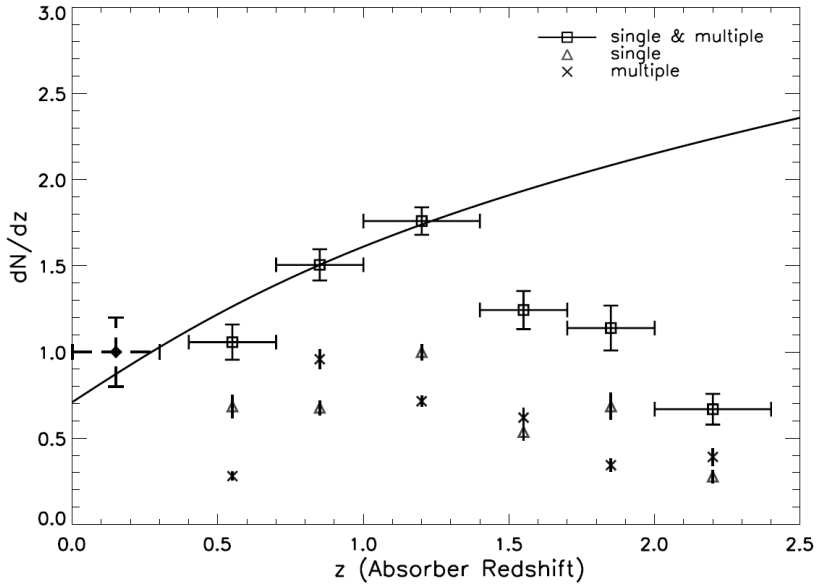

Figure 4.7: Evolution of weak ($W_{\rm r}^{2796} < 0.3$ Å) Mg II absorbers over the $0 < z < 2.5$ redshift interval. The peak at $z \sim 1.2$ is clearly detectable in the single and the multiple cloud systems. The solid line represents the expectations based on a ΛCDM simulation (Narayanan et al. 2007). The $0 < z < 0.3$ data point is from a previous *HST*/STIS survey by Narayanan et al. (2008a).

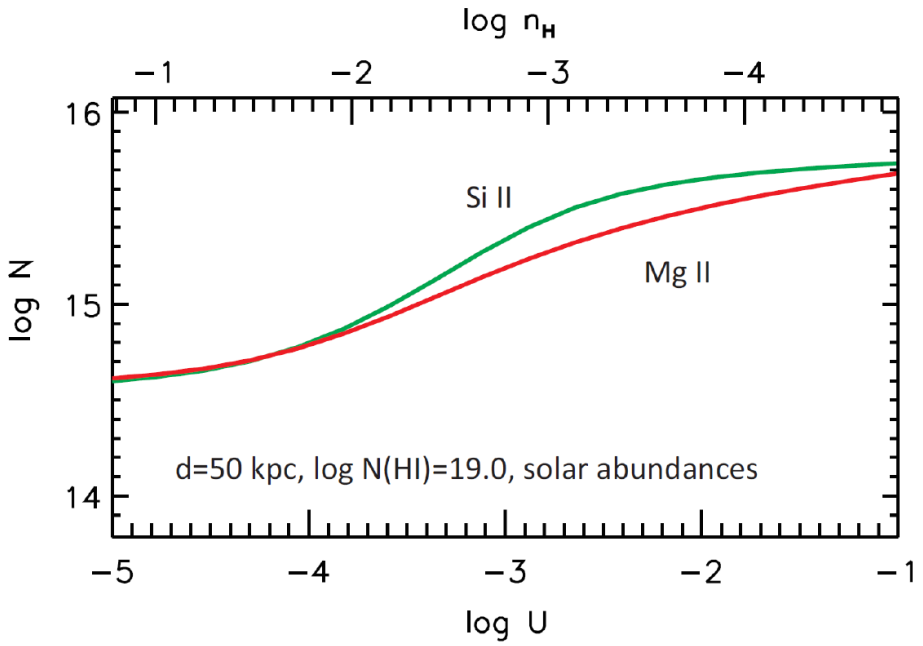

Figure 4.8: Example for a Cloudy photoionization model of Galactic HVC gas at a distance of $D = 50$ kpc from the Galactic disk, with an H I column density of $\log N(\mathrm{H\,I}) = 19$ and a metallicity of 1.0 solar. Shown are the expected column densities of Si II and Mg II as a function of the gas density, n_{H}, and the ionization parameter, U. Because of the similar ionization potentials and cosmic abundances of both elements/ions the column densities of Si II and Mg II in HVCs are expected to be very similar.

4.4.3 On the covering fraction of strong Mg II in the halos of Milky Way-type galaxies

Being located within the Milky Way disk, we see the distribution and covering fraction of HVCs in the Galaxy halo from the inside-out perspective (interior view). For a spherical halo with radius R the absorption path-length through the halo is always $\sim R$ and the observed sky-covering fraction, f_{c}, of HVC gas reflects the spatial distribution of gas integrated from the inner to the outer regions of the Milky Way halo. If a galaxy and its halo is seen from an exterior point of view, the absorption path length through the halo (and disk, eventually) depends on the impact parameter of the sightline, while the observed covering fraction depends on the path length *and* the radial gas distribution in the halo. Therefore, if we want to put into relation the covering fraction of Mg II/Si II in the Milky Way halo with the observed number density of intervening Mg II/Si II absorbers at low redshift (Equation 1.1), the different vantage points need to be considered. In addition, one needs to consider the absorption cross section of gaseous *disks*, as intervening absorbers passes both disk and halo components of galaxies. This important aspect will be discussed in Section 4.4.4.

To investigate the radial distribution of gas in the halos of galaxies and the resulting covering fractions, H I 21cm studies of nearby galaxies are of crucial importance. However, only for a few nearby spiral galaxies (e.g., M31 and NGC 891; Thilker et al. (2004); Oosterloo et al. (2007)) the 21cm observations are deep enough to provide meaningful constraints on the distribution of neutral gas in their halos. In a recent study, Richter (2012) has demonstrated that the projected covering fraction of 21cm HVCs around M31 strongly decreases with radius and can be fitted by an exponential in the form

$$f_{\mathrm{HVC}} = 2.1 \exp\left(-r/h\right), \tag{4.1}$$

where r is the projected radius in [kpc] and $h = 12$ kpc is the scale height for H I in HVCs. An exponential decline of the covering fraction of neutral/ionized gas in the halos of Milky Way-type galaxies is further supported by high-resolution hydrodynamical simulations of galaxies (Fernández et al. (2012)).

Richter (2012) developed the numerical code `halopath` that can be used to calculate the covering fraction of neutral and ionized halo gas from any given vantage point inside and outside the halo sphere. The `halopath` code assumes that the neutral and ionized gas in galaxy halos is distributed spherically around the neutral gas disks of these galaxies. Instead of modeling individual halo clouds or halo-gas

Table 4.4: Equivalent widths of Si II and Mg II absorption in HVCs.

Sightline	HVC velocity range [km s^{-1}]	S/N$_{1260}$ [a]	S/N$_{2796}$ [b]	EW$_{\rm SiII,1260}$ [mÅ]	EW$_{\rm MgII,2796}$ [mÅ]
PG 1211+143	+169...+184	15	...	46±4	...
PKS 2155+304	−138...−190	20	...	59±3	...
Mrk 279	−159...−200	23	...	252±3	...
PG 1116+215	+180...+190	12	6	184±6	341±34
NGC 3783	+180...+250	26	10	356±4	668±28
NGC 4151	+120...+145	18	30	44±5	43±3
PKS 0312−770	+160...+240	7	3	507±13	1191±90
HE 0515−4414	+120...+230	...	11	...	173±15
PG 1634+706	−100...−215	...	25	...	1028±12
NGC 3516	−160...−170	3	7	< 200	203±25
Mrk 205	−110...−230	5	...	253±18	...
PHL 1811	−130...−270	7	...	224±11	...
PG 0953+415	−150	8	...	42±6	...
RXJ 1230.8+0115	−216...−310	6	...	104±10	...
PG 1259+593	−120...−145	7	...	110±7	...
Ton S210	−150...−235	6	4	148±10	305±6
3C351	−130...−230	5	...	389±17	...
H 1821+643	−130...−170	12	...	273±6	...
NGC 7469	−190...−400	10	...	236±8	...
Mrk 132	−140...+80	...	10	...	251±16
PG 0117+21	−134	...	6	...	83±21
PG 1630+377	−160...−60	...	8	...	653±30
PG 1216+069	+210...+270	8	...	168±11	...
PG 1444+407	−80...−90	8	...	175±12	...
3C249	−135	8	...	27±11	...
Mrk 290	−128	...	...	...	...

[a] S/N per 3.17 km s^{-1} wide pixel element
[b] S/N per 4.83 km s^{-1} wide pixel element

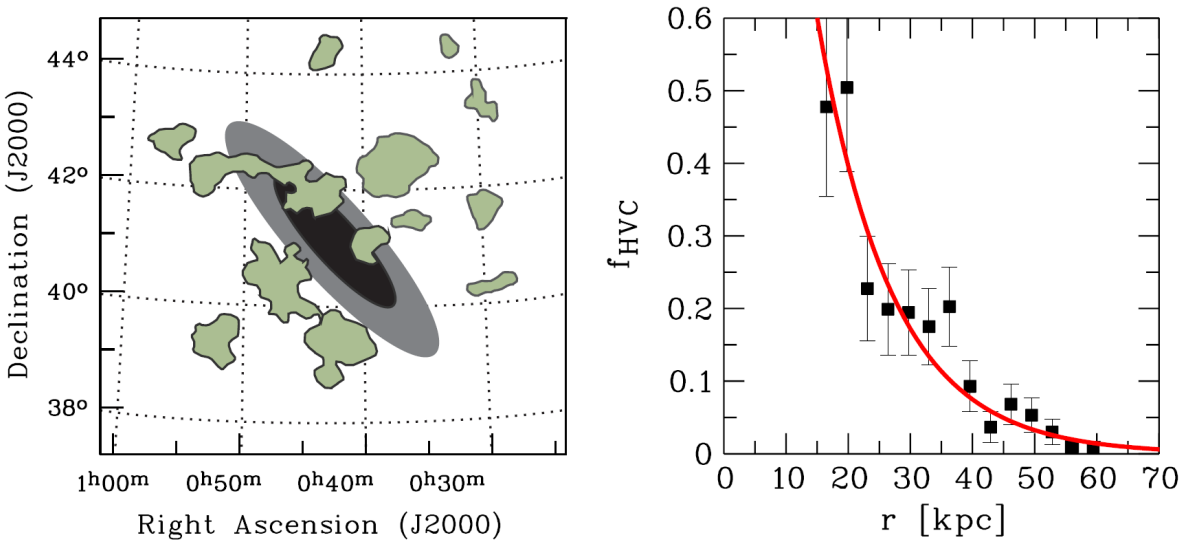

Figure 4.9: **Left panel**: schematic distribution of H I 21cm HVCs around M31 based on the observations from Thilker et al. (2004) done with the Green Bank Telescope. The light grey shaded area indicates the extend of the H I disk.
Right panel: projected covering fraction of HVCs plotted against the impact parameter around M31, based on the distribution shown in the left panel. The red line follows an exponential decline in the form of Equation 4.1. Figures are taken from Richter (2012).

structures (which would require knowledge about the size distribution of such structures), the code uses the *volume* filling factor of a given gas phase (e.g., neutral or ionized gas) as a function of galactocentric distance, $f_{\rm v}(R)$, as main input parameter. The function $f_{\rm v}(R)$ can be parametrized for an individual galaxy or for a population of galaxies. A corresponding model for the gas disks can also be included. The code then delivers the absorption cross section for each gas phase as a function of galaxy impact parameter and the total area covered by gas in the disks and halos of the modeled galaxies from an exterior vantage point. The code also calculates the sky covering fraction of each gas phase if a vantage point *inside* the sphere is chosen; it thus allows us to link the distribution of Milky Way HVCs with the frequency of intervening QSO absorbers. For more details on the code and its application to gaseous galaxy halos see Richter (2012). One important result from the study by Richter (2012) is that the observed sky covering fraction of HVCs in the Milky Way halo (interior view) is fully consistent with the projected covering fraction of H I clouds in the halo of M31 (exterior view). This suggests that the distribution of neutral gas in the halos of both galaxies is similar (in a statistical sense) and that basically all HVCs lie within 50 kpc from the disks.
We now use the code `halopath` to estimate the total absorption cross section and mean covering fraction of strong Mg II in HVC analogs around Milky Way/M31 type galaxies from an external vantage point. As model input we adopt the observed sky covering fraction of $f_{\rm c,sMgII,halo,i} = 0.34$ of strong Mg II in the Milky Way from the *interior* vantage point. We further assume that the observed sky covering fraction of strong Mg II absorption in the Milky Way HVCs (interior view) is representative for non-star forming disk galaxies of similar mass and further assume that the projected covering fraction of halo Mg II (exterior view) declines exponentially (i.e., $f_{\rm MgII}(r)$ declines in a same way as $f_{\rm HI}(r)$; see Equation 4.1).

Under these assumptions, we find that the projected covering fraction of strong Mg II from HVCs in the halos of Milky Way-type galaxies as seen from an external vantage point is $\langle f_{\rm c,sMgII} \rangle \approx 0.2$ for a halo radius of $r_3 = 61$ kpc [1]. The projected halo area covered by strong Mg II in HVCs around Milky Way-type galaxies then turns out to be $A_{\rm sMgII,halo} = 2340$ kpc^2.

4.4.4 On the contribution of HVCs to the absorber density of strong Mg II absorbers

Our STIS measurements imply that HVCs and their distant analogs have a non-negligible absorption cross section in low- and intermediate ions such as Si II and Mg II, and that these objects are expected

[1] We define r_3 as the halo radius beyond which the projected covering fraction of strong Mg II falls below the 3% level.

to contribute to the observed number density of strong Mg II absorbers. However, for a quantitative estimate of the contribution of HVCs to $\mathrm{d}\mathcal{N}/\mathrm{d}z$(Mg II) one also needs to consider the absorption cross section of gaseous *disks*, as intervening absorbers passes both disk and halo components of galaxies. While a detailed discussion of the absorption cross section of gaseous galaxy disks is beyond the scope of this thesis, we provide some simple estimates that help to evaluate the relevance of HVCs for the absorption cross section of strong Mg II absorbers.
For the Mg II-absorbing disk component in our Milky Way/M31 model galaxy we assume a radius of $r_{\mathrm{disk}} = 30$ kpc (for $\log N(\mathrm{H\,I}) > 17.5$), based on the M31 21cm data of Braun et al. (2009), and a covering fraction of $f_{\mathrm{c,sMgII,disk}} = 1$. The mean absorption cross section for strong Mg II of a sample of randomly inclined gas disks with these properties then is $A_{\mathrm{disk}} \approx 1810$ kpc^2, which is $\sim 77\%$ of the cross section of the surrounding HVC population (see previous section). Since the areas covered by disks and halo clouds are overlapping from an exterior vantage point, projection effects need to be taken into account. Using the `halopath` code we calculate that the absorption cross section of strong Mg II of gas disks plus HVCs is $A_{\mathrm{disk+HVC}} \approx 3790$ kpc^2, thus a factor of ~ 2.1 higher than the cross section of gas disks *without* a population of surrounding Milky-Way type HVCs. Our calculations therefore imply that, from an exterior vantage point, $\sim 52\%$ ($f = 1980/3790 = 0.522$) of the cross section of strong Mg II absorption in the Milky Way and M31 comes from the HVC population in their halos. Finally, the mean covering fraction of strong Mg II from the disk plus HVCs in our model halo with radius $r_3 = 61$ kpc, as seen from an exterior vantage point, is $\langle f_{\mathrm{c,sMgII}} \rangle = 0.31$.

While the Milky Way and M31 show very similar properties in their HVC populations, it is unclear whether these two galaxies are representative for the local galaxy population with respect to their halo-gas distribution. Nearby spiral galaxies do show extended H I halos and extraplanar gas features that may be regarded as distant HVC analogs (Oosterloo et al. 2007; Sancisi et al. 2008), but with only few galaxies observed at sufficient 21cm sensitivity no meaningful conclusions can be drawn. Yet, coherent H I structures at relatively large galactocentric distances $d > 30$ kpc, such as tidal features like the Magellanic Stream (MS), appear to be rare. Note that the MS accounts for a substantial fraction of the neutral gas mass and H I covering fraction in the Milky Way halo (see Richter 2012, their Table 1). Many of the high-velocity absorption features in the southern sky (Figure 4.1) may be associated with gas originating in the Magellanic Stream. Therefore, the absorption cross section of gaseous halos of galaxies, that are not surrounded by tidal gas streams, could be substantially smaller. Our STIS sample is not large enough to investigate the absorption cross section of the Milky Way HVCs in different quadrants of the Galaxy on a statistically secure basis to further study this effect in detail. However, using the quickly growing COS data archive, we will address this interesting aspect in a subsequent paper.
Even if one assumes that Milky Way-type HVCs (including the MS) are common in low-redshift galaxies, they cannot dominate the number density of strong Mg II absorbers at $z = 0$: Richter (2012) estimate that the contribution of Milky-Way type HVCs to the number density of intervening absorbers is $\mathrm{d}\mathcal{N}/\mathrm{d}z < 0.167$, assuming that the HVC distribution around the Milky Way and M31 is typical for the local galaxy population. This number density is $< 34\%$ of the expected value for intervening strong Mg II absorbers at $z = 0$ ($\mathrm{d}\mathcal{N}/\mathrm{d}z$(Mg II) $\approx$ 0.5, Nestor et al. 2005).

The contribution of gas disks to the Mg II cross section is expected to be even smaller. From 21cm studies of the H I mass function of nearby galaxies (e.g., Zwaan et al. 2005) follows that neutral gas disks with $\log N(\mathrm{H\,I}) \geq 20.3$ contribute with only $\mathrm{d}\mathcal{N}/\mathrm{d}z \approx 0.045$ to the local population of strong Mg II absorbers, a number density that is one order of magnitude smaller than that of strong Mg II systems. At this H I column density limit, intervening absorbers would be identified as Damped Ly α systems (DLAs) in the common classification scheme for QSO absorption-line systems. One may argue that the radial extent and cross section of strong Mg II absorbing gas disks is much larger for column densities *below* the DLA column density limit. There is, however, no compelling observational evidence for the presence of extended H I disks beyond the DLA column density limit. On the contrary, recent 21cm studies of the radial extent of the H I disks of low-redshift galaxies indicate that gas disks typically are radially truncated with a sharp drop in H I column density at the disk edge from 10^{20} cm^{-2} down to 10^{17} cm^{-2} (Braun et al. 2009; Oosterloo et al. 2007; Portas et al. 2009). From the composite radial H I disk profile of the galaxies in the THINGS survey (Portas et al. 2009, their Figure 5) it follows that the disk radius (disk area) for $\log N(\mathrm{H\,I}) > 17$ is only ~ 10 (~ 21)% larger than for $\log N(\mathrm{H\,I}) > 20$, so that the contribution of extended gas disks to the observed number density of intervening absorbers is is limited to $\mathrm{d}\mathcal{N}/\mathrm{d}z \approx 0.054$, which is $< 11\%$ of $\mathrm{d}\mathcal{N}/\mathrm{d}z$(Mg II) at $z = 0$.

In conclusion, neither the disks of Milky Way-type galaxies nor the HVCs in their halos provide enough cross section in Mg II to explain the large number density of intervening strong Mg II absorbers. Other phenomena that transport neutral and ionized gas outside of galaxies appear to dominate the

absorption cross section of Mg II in the local Universe. This conclusion is supported by *direct* estimates of the absorption cross section of Mg II absorbing galaxies. For intermediate redshifts, Kacprzak et al. (2008) derived a larger mean covering fraction of $\langle f_{\rm c,sMgII} \rangle \approx 0.5$ and larger halo radii for Milky-Way size galaxies in their galaxy sample. Based on observations at low z, Bouché et al. (2012) argued that galaxy outflows and winds must dominate the total cross section of strong Mg II absorption in the local Universe. This, in turn, is in line with our scenario that "quiescent" galaxies (i.e., galaxies that do not drive extended winds and outflows), such as the Milky Way and M31, contribute relatively little to the observed number density of strong Mg II absorption at low redshift. Moreover, Mg II absorption in the halos of such galaxies predominantly indicates material that is *infalling* rather than outflowing.

4.4.5 On the contribution of HVCs to the absorber density of weak Mg II absorbers

Intervening Mg II absorbers with equivalent widths < 300 mÅ in the Mg II λ2796 line are commonly referred to as weak Mg II absorbers. With a number density of $\mathrm{d}\mathcal{N}/\mathrm{d}z = 1.00$ at $z < 0.3$ for rest-frame equivalent widths $W_{2796} = 20 - 300$ mÅ these systems have a similarly high absorption cross section as the strong Mg II absorbers (Narayanan et al. 2008a). However, compared to strong Mg II systems, weak Mg II absorbers probably are located at larger distances from the galaxies, i.e., in their circumgalactic environment (Milutinović et al. 2006).
Richter et al. (2009) have speculated that some of the weak high-velocity O I/Si II/Mg II absorbers in the STIS spectra, that have no associated H I 21cm emission, may be located at larger distances ($d > 60$ kpc) than the more massive 21cm HVCs and thus possibly represent the local analogs of the intervening weak Mg II absorbers found at low and high redshift. From our study we infer a covering fraction of $f_{\rm c,wMg} = 10/41 \approx 0.24$ for weak Mg II absorption at high-velocities for equivalent widths $W_{2796} = 40 - 300$ mÅ; this covering fraction is slightly lower than that of strong Mg II absorption.
For the same line of arguments outlined in the previous section, the contribution of the 21cm HVCs at $d < 60$ kpc to the number density of weak Mg II absorbers must be small. If, however, low-column density Mg II/Si II absorbers in the Milky Way halo were typically located within $R_{\rm h}$ at distances $d > 60$ kpc (as proposed by Richter et al. (2009)), then the absorption cross section of such objects from an exterior vantage point and their contribution to $\mathrm{d}\mathcal{N}/\mathrm{d}z$ would be increased substantially (since $\mathrm{d}\mathcal{N}/\mathrm{d}z \propto A \propto R_{\rm h}^2$; Equation 1.1). The ongoing COS observations of weak Mg II/Si II absorbers along sightlines that pass the inner and outer halos of nearby galaxies will help to further explore this scenario (e.g., Ribaudo et al. 2011b).

4.5 Conclusions

In the last chapter we have discussed and analyzed a set of 47 individual *HST*/STIS spectra towards various AGN sightlines. We focused on Galactic HVC detections for the lines of C II λ1334.5, C IV $\lambda\lambda$1548.2, 1550.8, O I λ1302.2, Si II $\lambda\lambda$1190.4, 1193.3, 1260.4, 1304.4, 1526.7, Si III λ1206.5, Si IV $\lambda\lambda$1393.8, 1402.8, Mg II $\lambda\lambda$2796.4, 2803.5, Fe II $\lambda\lambda$2382.8, 2600.2, and Al II λ1670.8 and found significant absorption for at least two ions in 28 out of 47 sightlines. The covering fractions vary between $f_{\rm c} = 0.20$ for Si IV and $f_{\rm c} = 0.70$ for C II and Si III.
In case of Si II we determined a covering fraction of $f_{\rm c} = 0.67$ for $\log N(\mathrm{Si\,II}) > 12.25$. This is approximately a factor of two higher than what can be found for H I at $\log N(\mathrm{H\,I}) > 17.8$. Thus, Si II is a very good tracer for neutral and weakly ionized gas below the detection limit of recent H I 21cm surveys.
With a fraction of about 70 %, most of the high-velocity Si II absorption is detected at negative velocities. Therefore, we conclude that there is a net infall of neutral and weakly ionized gas in total. The component structure of the Si II absorption turns out to be rather simple with usually 1 - 2 components with Doppler parameters in the range of 5 - 15 km s^{-1}. Furthermore, we created a CDDF out of the column densities of all 38 individual Si II absorbers. If we try to fit a power law to that CDDF it turns out that there is a lack of absorbers with $\log N(\mathrm{Si\,II}) \approx 13$. The derived slope of $\beta = 1.34 \pm 0.12$ is marginally lower than that for H I in HVCs ($\beta \approx 1.5$).
We combined the results for Si II and Mg II to investigate the covering fraction of strong Mg II absorbers in the halo of the Milky Way. It turns out that this value of $f_{\rm c,sMgII,halo,i} = 0.34 \pm 0.09$ is very similar to the covering fraction for H I with $\log N(\mathrm{H\,I}) > 17.8$ in HVCs. Thus we conclude that only the most massive Galactic HVCs would appear as strong Mg II absorbers if seen from an outside point of view.
With the help of the geometrical Milky Way/M31 halo model of Richter (2012) we estimate the cross section of these strong Mg II absorbers based on an exterior vantage point. We found that $\langle f_{\rm c,sMgII} \rangle = 0.31$ for a halo radius of $R = 61$ kpc, which leads to a Galactic HVC/Mg II$_{\rm str}$ fraction of $\sim 52\%$. Furthermore, we come to the conclusion that the contribution of HVCs to the number density ($\mathrm{d}N/\mathrm{d}z$) of

strong Mg II absorbers is below 34%. These results are in line with the idea that most of the intervening strong Mg II absorbers represent gaseous outflows and galactic winds that are present in the extended halos of more actively star-forming galaxies.

Chapter 5

Intervening metal absorbers at low redshift

In this chapter, the results of the *HST*/COS analysis of intervening metal absorbers and their relation to HVCs and nearby host galaxies are presented. We use Voigt-profile/component modeling to pinpoint the statistical properties of intervening metal-absorption systems (see Section 2.3.4). Using a grid of Cloudy photoionzation models for a subsample of sightlines we pin down the ranges for the ionization parameter, the hydrogen volume density, and the metallicity in the intervening absorbers. The values that we derive are in line with the idea that the intervening absorbers trace the halos and CGM of distant galaxies. The results obtained in Chapter 4 are used together with the absorber frequency for intervening Si II, Si III, and C III systems to constrain the typical radii for Si III-absorbing gas halos of galaxies at low z. Furthermore, we search for known nearby galaxies that could be associated with the absorbers and determine their typical impact parameters. With our estimate for the characteristic impact parameters of intervening metal absorbers to low-redshift galaxies, we demonstrate that diffuse, ionized intergalactic metal systems are typically located within $\rho \sim 160$ kpc of their host galaxies, supporting the idea that they trace metal-enriched circumgalactic gas in the local Universe.

5.1 Data selection and handling

For the following analysis we used a set of UV spectral data for 57 QSO sightlines taken with *HST*/COS; these data are all publicly available in the Mikulski Archive for Space Telescope (MAST). To be able to include results from the *HST*/STIS analysis presented in the last chapter, we decided to focus on the same intermediate and low ions that have their transitions in the NUV and FUV. Thus, and because of the necessary resolution and data quality, the possible optical elements for COS are limited to the G130M and G160M gratings. At the time of our data selection procedure (end of 2011), there were only a few appropriate COS spectra publicly available (see subsample analysis). Therefore, we decided to include also a sample of SDSS quasars in our analysis (33 spectra), which have a significant lower mean S/N ratio, but which increase the sample size and increase the significance of our absorber statistics. The final set of sightlines, together with their associated proposal IDs, is given in Table 3.5. From the inspection of the original proposals we conclude that most of the sightlines are selected to study the large-scale structure and the baryon distribution in the Universe. We thus conclude that there is no selection bias towards specific regions or redshifts with regard to intervening metal absorbers. For an overview of all sightlines including basic information on the identified intervening metal absorbers see Table 5.1. The horizontal line marks the separation between the high-quality sample and the additional low-S/N SDSS sightlines.

Each of the spectra has been reduced with the standart COS reduction pipeline and converted into *Midas* tables with the ESO-*Midas* software. We then individually scanned each sightline by eye to identify possible redshift congruence of different absorbers. We count an absorption as positive detection of a metal absorber if we see at least the corresponding H I Lyα line in the data together with the metal absorption. Doubtful or blended features as well as regions with spectral gaps were excluded. For the analysis we focussed on the lines of Si II λ1260, Si III λ1206, and C III λ977 because of the high abundance of these elements and the high oscillator strengths of the listed transitions. Thus, at least for the intermediate ions, the spectra have a relatively low limiting column density despite the limited S/N in the data. In addition, the choice of these ions allows us a statistical comparison to the results obtained for the Milky Way in the first part of this thesis. With the possible determination of the Si II/Si III column-density ratio we are also able to constrain the local ionization conditions. Si III and C III are

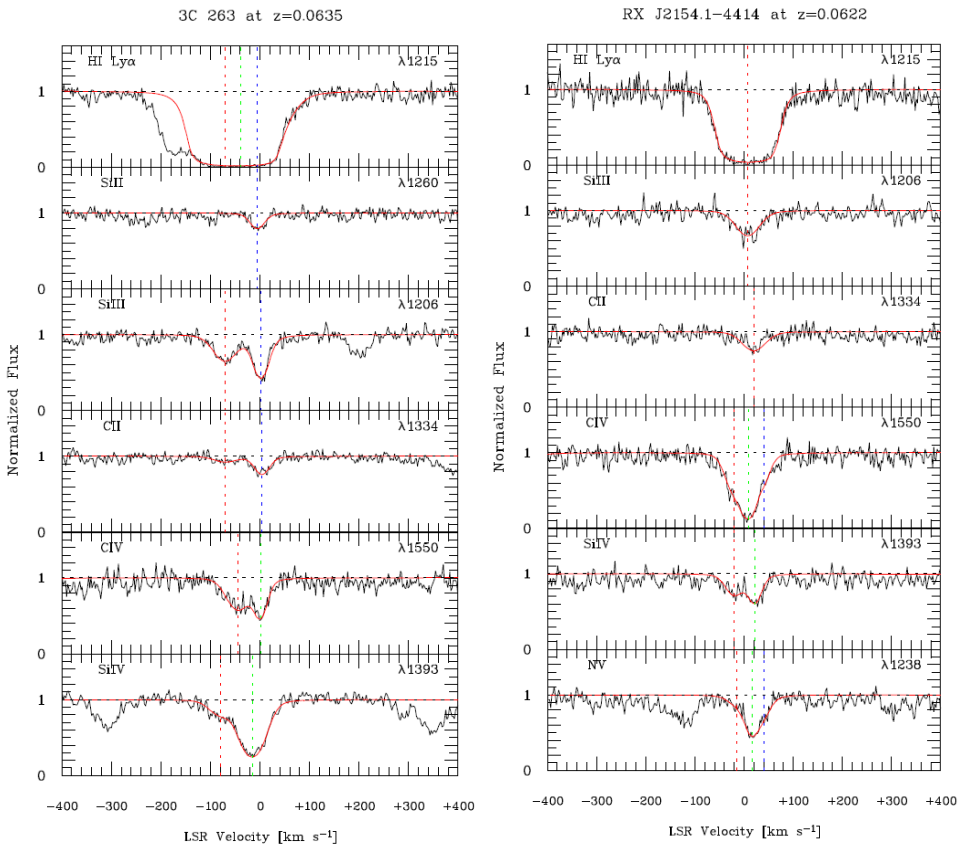

Figure 5.1: Two examples for absorber models of intervening absorbers in the COS spectra. The red solid lines indicates the component model, the colored dashed lines indicate the component structure.

expected to trace a diffuse, extended, mildly ionized gas phase which is expected to be the dominant phase in intervening metal absorbers that trace the outer regions of galaxy halos. Note that because of the intense intergalactic radiation field, the existence of predominantly neutral gas in intervening absorbers would require high gas densities in rather compact cloudlets, which then would have a very small absorption-cross section. Thus, the Si III and C III ion should be most abundant in intervening absorbers and consequently it is more likely to detect them (compared to low ions and neutral atoms). Laboratory wavelengths and oscillator strengths have been again taken from the compilation of Morton (2003). For our analysis we consider a redshift range between $z = 0$ and $z = 0.9$ for the above listed ions.

The mean S/N ratio for sightlines with intervening metal detection in the whole sample is only ~ 7. This value is dominated by the many low-S/N SDSS sightlines. If we divide our sample in two subsamples, which contain the SDSS quasar sightlines in the one subsample and all other sightlines in the other subsample, then the mean S/N ratios are S/N(SDSS) = 4.5 and S/N(rest) = 12.1. Because of this substantial difference in data quality we decided to split the sample for the modeling of the ionization conditions accordingly. Note that with a resolving power of $R \sim 18\,000 - 19\,000$ we require a velocity difference of at least $\Delta v \sim 16$ km s^{-1} to resolve individual velocity sub-components in the absorbers.

To derive initial estimates for the b-parameters, the column densities as well as the number and position of the absorption components of the metal ions and H I in all absorbers in our sample we have used the χ^2 fitting routines of the `fitlyman` package implemented in ESO-*Midas* (Fontana and Ballester 1995). Note that this method does not take into account the complex LSF of COS, but assumes a Gaussian LSF. For most of the low-S/N data sets this method is sufficiently accurate. For the detailed data analysis of the high-S/N subsample we then used the component-modeling technique as described in detail in Section 2.3.4. This technique includes multi-component Voigt profiles, which have been convolved with the varying COS LSF (see Sections 2.3.3 and 2.3.4). This method provides more accurate results than the previous method, but is relevant only for spectra with high S/N (i.e., we do not consider the SDSS sightlines for the modeling analysis due to bad data quality).

In the following, we provide some further details on the modeling procedure for the high-S/N subsample. Based on the initial parameters derived from the Voigt fitting, we have modeled the individual absorption systems, taking into account turbulent broadening mechanisms as well as the COS LSF. The basic intention was to reproduce the absorption profiles with a minimum number of absorption components. In general, we assume one and the same turbulent Doppler-parameter for absorption components within the same system, whereas the thermal contribution to b was calculated for each ion individually (see Equation 2.18) assuming a constant temperature of $T = 10^4$ K, as expected for photoionized gas in the CGM. This approach is justified, because Si III and C III are expected to arise in almost the same gas phase where the turbulent motions dominate the values of Doppler parameter. Due to the (partly) bad data quality it is very likely that some (if not all) of the absorption systems contain a more complex substructure. To resolve this substructure, a much higher spectral resolution than provided by COS would be required (as well as a higher S/N). As already explained in Section 4, this systematic uncertainty affects the whole analysis and should be considered critically in future investigations. Figure 5.1 shows examples of the final model for the two absorbers along sightlines towards the Seyfert 1 galaxies 3C 263 and RX J2154.1−4414. The colored dashed lines indicate the associated components. The final fitting/model results are listed in Tables 6.6 - 6.8 and 6.11 - 6.13 in the Appendix.

Finally, in the case of the sightline towards the quasar SDSS J161649.42+415416.3, we could identify a very strong DLA absorber at $z = 0.3210$, which was impossible to model due to strong saturation in the absorption lines. Therefore, no column densities and Doppler parameters could be derived for this system, but it counts as a detection in all three considered ions.

5.2 Absorption-line statistics

In the following subsections we discuss the results on the component structure, the H I column density distribution, the absorber frequencies ($d\mathcal{N}/dz$), and other statistical properties of the COS absorber sample.

5.2.1 Component structure

During the last decades, there have been several attempts to gain information on the structure of gaseous galaxy halos and their role in the galactic evolution from the analysis of the velocity structure of intervening metal absorbers. For instance, Charlton and Churchill (1998) have shown that it is quite difficult to conclude on the origin of the observed gas with only relying on velocity information of low and intermediate ions. With the application of several models and observational data from the Keck Telescope, these authors argue that one can not clearly distinguish between disk and halo gas. Following their argumentation, it is more appropriate to assume a mixed model which contains contributions from infalling gas as well as a contribution from a rotating gaseous disk. Thus, the high complexity of the component structure of intervening metal systems requires high spectral resolution data to resolve the sub-component structure and the kinematics of these clouds.

In Figure 5.2 the number distribution of the velocity components in the whole COS sample is shown. The component structure was derived from the Voigt-profile fitting of the entire data set (see above). Here we take into account the component structure seen in the metal ions with a higher weight on the strong absorption lines of Si II, Si III and C III. Most of the systems in the COS sample contain only one ($\sim$ 62 %) or at most two ($\sim$ 86 %) absorption components. This is no surprise, because the spectral resolution of the COS instrument is only $R = \lambda/\Delta\lambda \approx 18\,500$ on average, corresponding to a velocity resolution of $v \approx 16.2$ km s^{-1}.

Due to the relatively low resolution, we consider an absorption component as an individual entity, if it has a velocity distance of $v > 20$ km s^{-1} to the adjacent one. Since Si II, Si III, and C III trace neutral and weakly/moderately ionized gas, one would expect to see a more complex velocity distribution for the latter ions because the gas regions traced by them are expected to be spatially more extended. Compared to the results for Si II in local HVCs derived with the STIS instrument (see Section 4), the resolution effect is well visible. In case of STIS, a velocity resolution of $v \approx 7.0$ km s^{-1} is achieved, which results in a higher frequency of two-component systems for Galactic HVCs (see upper panel of Figure 4.4) compared to the intervening absorbers studied with COS. If we additionally consider the results of Ben Bekhti et al. (2012), who found a clear dominance of single-component absorbers in Ca II (tracing relatively dense neutral gas) in HVCs, a more complex velocity structure in intermediate ions in intervening absorbers appears to a natural result of the complex (and spatially more extended) dis-

Table 5.1: Summary of COS sightlines with basic properties and number of intervening absorbers.

QSO name	R.A. (J2000.0)	Decl. (J2000.0)	z_{QSO}	V Flux [mag]	S/N per res. element	$\mathcal{N}$ Si II Systems	$\mathcal{N}$ Si III Systems	$\mathcal{N}$ C III Systems
RX J0439.6-5311	04 39 38.7	-53 11 31	0.243	16.20	8.35	-[1]	-	-
HE 0439-5254	04 40 11.9	-52 48 18	1.053	16.10	7.13	-	1	2
PG 1115+407	11 18 30.3	+40 25 54	0.155	16.02	9.22	-	-	-
PG 1259+593	13 01 12.9	+59 02 07	0.472	15.84	14.87	1	2	2
HE 0435-5304	04 36 50.8	-52 58 49	1.231	16.40	7.42	-	-	-
Mrk 817	14 36 22.1	+58 47 39	0.031	13.80	11.58	-	-	-
Mrk 290	15 35 52.3	+57 54 09	0.030	15.00	11.25	-	-	-
Mrk 421	11 04 27.3	+38 12 32	0.030	12.99	21.25	-	-	-
HE 0226-4110	02 28 15.1	-40 57 14	0.494	15.20	17.67	-	1	1
HE 0153-4520	01 55 13.2	-45 06 12	0.451	n.a.	11.32	1	1	2
3C 263	11 39 57.0	+65 47 49	0.652	16.32	16.26	1	3	2
TON 580	11 31 09.5	+31 14 05	0.289	16.00	10.67	-	1	1
PG 1553+11	15 55 43.0	+11 11 24	0.360	n.a.	9.71	-	-	-
PKS 2005-489	20 09 25.4	-48 49 54	0.071	13.40	10.36	-	-	-
RX J2154.1-4414	21 54 51.1	-44 14 06	0.344	15.80	11.88	-	1	-
SBSG 1122+594	11 25 53.8	+59 10 22	0.852	16.50	6.54	-	2	2
PG 0838+770	08 44 45.3	+76 53 10	0.131	15.70	11.48	-	1	-
Mrk 1513	21 32 27.8	+10 08 19	0.062	14.64	13.48	-	-	-
Mrk 335	00 06 19.5	+20 12 10	0.025	13.85	12.27	-	-	-
HE 0238-1904	02 40 32.5	-18 51 51	0.631	15.00	14.84	-		2
HS 1102+3441	11 05 39.8	+34 25 35	0.510	16.20	10.16	-	2	2
PKS 0405-123	04 07 48.4	-12 11 37	0.574	14.86	n.a.	?	?	?
PG 1011-040	10 14 20.6	-04 18 40	0.058	15.50	12.84	-	-	-
Mrk 876	16 13 57.2	+65 43 10	0.120	15.49	36.42	-	-	-
PHL 1811	21 55 01.5	-09 22 24	0.192	16.80	16	1	1	-
SDSS J161916.54+334238.4	16 19 16.5	+33 42 38	0.471	n.a.	9.5	1	-	-
SDSS J094331.61+053131.4	09 43 31.6	+05 31 31	0.564	17.16	3.19	-	-	2
SDSS J102218.99+013218.8	10 22 19.0	+01 32 19	0.789	17.30	4.45	-	-	-
SDSS J143511.53+360437.2	14 35 11.5	+36 04 37	0.429	17.25	4.04	1	3	3
SDSS J141910.20+420746.9	14 19 10.2	+42 07 47	0.874	17.34	4.4	1	3	2
SDSS J124511.25+335610.1	12 45 11.2	+33 56 10	0.717	17.52	4.4	-	1	2
SDSS J122035.10+385316.4	12 20 35.1	+38 53 16	0.376	16.60	3.4	-	1	1
SDSS J101622.60+470643.3	10 16 22.6	+47 06 43	0.822	17.12	4.25	2	2	2
SDSS J113327.78+032719.1	11 33 27.8	+03 27 19	0.525	17.53	4.4	1	1	1
SDSS J100902.06+071343.8	10 09 02.1	+07 13 44	0.456	17.14	3.7	2	3	1
SDSS J082024.21+233450.4	08 20 24.2	+23 34 50	0.470	n.a.	5.39	-	-	-
SDSS J091440.38+282330.6	09 14 40.4	+28 23 31	0.735	n.a.	4.8	1	2	-
SDSS J092554.70+400414.1	09 25 54.7	+40 04 14	0.471	17.93	4.2	1	1	1
SDSS J111239.11+353928.2	11 12 39.1	+35 39 28	0.636	n.a.	4.2	-	1	-
SDSS J144511.28+342825.4	14 45 11.3	+34 28 25	0.697	n.a.	4.15	-	-	-
SDSS J091029.75+101413.6	09 10 29.7	+10 14 14	0.463	18.11	3.4	1	2	3
SDSS J155304.92+354828.6	15 53 04.9	+35 48 29	0.722	16.76	5.1	1	2	1
SDSS J124154.02+572107.3	12 41 54.0	+57 21 07	0.583	17.58	4.9	1	3	1
SDSS J080359.23+433258.4	08 03 59.2	+43 32 58	0.451	17.20	4.6	-	-	2
SDSS J115758.72-002220.8	11 57 58.7	-00 22 21	0.260	n.a.	5	-	-	1
SDSS J225738.20+134045.4	22 57 38.2	+13 40 45	0.594	17.02	3.5	-	-	1
SDSS J133045.15+281321.4	13 30 45.1	+28 13 21	0.417	n.a.	5.4	1	1	1
SDSS J161649.42+415416.3[2]	16 16 49.4	+41 54 16	0.440	16.98	4.55	1	1	1
SDSS J123335.07+475800.4	12 33 35.1	+47 58 00	0.382	17.40	5.1	1	1	2
SDSS J004222.29-103743.8	00 42 22.3	-10 37 44	0.424	16.38	4.6	1	1	-
SDSS J123304.05-003134.1	12 33 04.0	-00 31 34	0.471	17.90	4.2	-	1	1
SDSS J155048.29+400144.9	15 50 48.3	+40 01 45	0.497	16.99	3.8	-	2	2
SDSS J234500.43-005936.0	23 45 00.4	-00 59 36	0.790	n.a.	4.19	-	-	-
SDSS J161711.42+063833.4	16 17 11.4	+06 38 33	0.23	n.a.	1.60	-	-	-
SDSS J040148.98-054056.5	04 01 49.0	-05 40 57	0.570	16.92	4.11	-	1	2
SDSS J151428.64+361957.9	15 14 28.6	+36 19 58	0.695	18.07	n.a.	?	?	?
SDSS J155504.39+362848.0	15 55 04.4	+36 28 48	0.714	18.13	3.8	1	1	2
SDSS J022614.46+001529.7	02 26 14.4	+00 15 30	0.615	n.a.	n.a.	?	?	?

[1]): No absorber found or analysis not possible because of a gap in the spectrum or other spectral problems.
[2]): Very strong DLA. Impossible to fit, but counts as positive detection.
n.a.: No visual magnitudes available in the simbad database.
?: No statement possible because of problems in the spectral compilation.

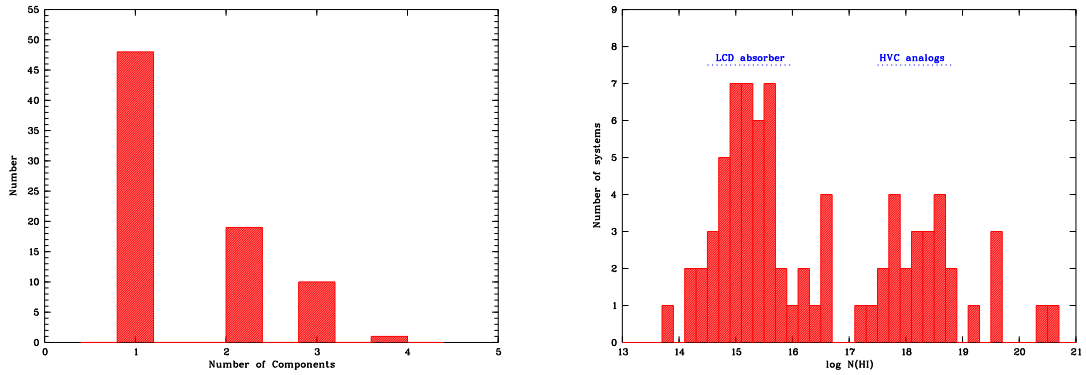

Figure 5.2: **Left panel:** number distribution of the COS velocity-components in intervening metal systems.
Right panel: number distribution of the total H I column density in each system. The two peaks in the this bimodal distribution can be associated with different absorber populations, which are labeled in blue.

tribution of diffuse, ionized gas in these systems. This idea is also supported by the results of Churchill et al. (2003), who found up to 8 components in strong intervening Mg II systems. The overabundance of single/double component systems in our COS sample is, in any way, obviously a result of the low spectral resolution and thus an instrumental effect.

5.2.2 H I column density distribution

In the right panel of Figure 5.2 we show the total H I column density for each system with associated metal detection in the complete COS sample, as derived from the Voigt-profile fitting. The plot clearly indicates a bimodal distribution with the main peak in the range of $14.5 < \log N(\mathrm{H\,I}) \leq 16.0$ and a second accumulation at $17.5 < \log N(\mathrm{H\,I}) \leq 19.0$. If one relies on the definition for the canonical H I column density in galaxy disks ($\log N(\mathrm{H\,I}) \gtrsim 20.0$), one can see that only two disk absorbers (i.e., DLAs) are part of our sample. Furthermore, the observed bimodal distribution suggests that there are two different absorber populations in our data set. From H I 21cm observations of the local Galactic HVC population we know that $\sim 30\%$ of the Milky Way HVCs have neutral hydrogen column densities in the range $17.9 < \log N(\mathrm{H\,I}) < 18.5$ (e.g., Lehner et al. 2012). Combined with the results of Richter (2012), who has shown that HVCs might be responsible for $30\% - 100\%$ of intervening absorption line systems with $\log N(\mathrm{H\,I}) \gtrsim 17.5$, we can conclude that the right peak in the number distribution of the H I column densities possibly indicate HVC analogs around other galaxies. In this scenario, the absorber population at $17.5 < \log N(\mathrm{H\,I}) < 19.0$ is part of a halo of a galaxy and thus belongs to the CGM. To confirm this idea, it will be necessary to identify the corresponding host galaxies; this aspect will be addressed in the later sections.

The reason for the lack of CGM absorbers with $\log N(\mathrm{H\,I}) \approx 17.2$ might be the ionization characteristics of hydrogen. As explained by Corbelli and Bandiera (2002) and Rudie et al. (2013), systems with $\log N(\mathrm{H\,I}) \leq 17.2$ are optically thin for hydrogen-ionizing photons from the UV background. This means that the amount of neutral hydrogen in those systems drops substantially, since the gas cannot self-shield and becomes ionized. Due to this transition in the ionization properties as a function of the neutral hydrogen column density, it is plausible that a break (plateau) in the H I column density distribution occurs near $\log N(\mathrm{H\,I}) = 17.2$. In fact, the H I CDDF shown in Figure 5.3 clearly reveals the expected characteristics. Note that this trend can also be translated into a radial decline of $N(\mathrm{H\,I})$ with increasing impact parameter. Corbelli and Bandiera (2002) suggested that this sharp drop in the H I column density might be related to a transition zone between H I and H II regions. Other particular examples for those breaks in the H I column density distribution can be detected in the two nearby spirals M33 and NGC 3198 (e.g., Maloney 1993; Corbelli and Bandiera 2002, and references therein). If we try to fit our data with a straight power law in the range $14.7 \leq \log N(\mathrm{H\,I}) \leq 20.5$ we find that the observed distribution is not well reproduced (red line in Figure 5.3). Also, the slope of $\beta = 1.1 \pm 0.04$ is ~ 0.4 dex lower than what is found for H I in Galactic HVCs. This discrepancy is not suprising, however, since we are most likely mixing up two different populations of absorbers. Corbelli and Bandiera (2002) discussed that a simple power law cannot reflect the true H I distribution in intervening absorbers in the

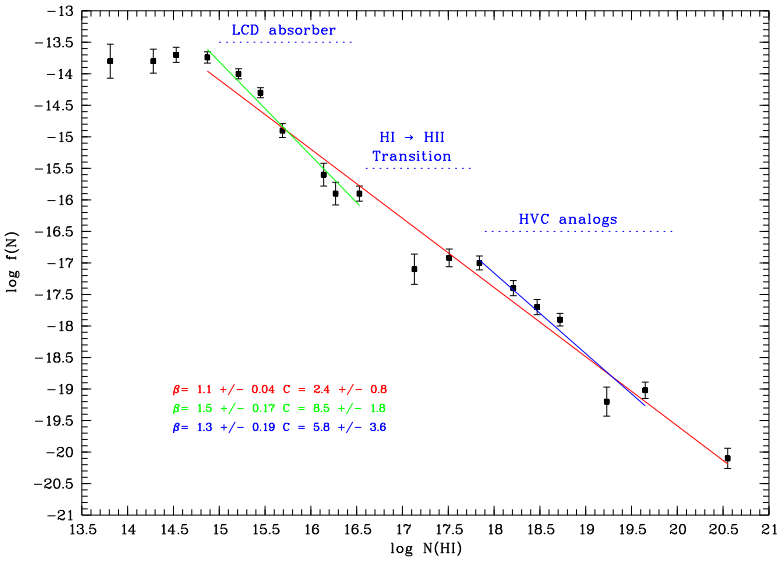

Figure 5.3: H I column-density distribution function for the whole COS data sample. Labeled is the range in which the break in the H I CDDF can be associated with the change in the ionization conditions of hydrogen.

local Universe if it includes the H I - H II transition region. A better solution would be either to consider the total amount of hydrogen (i.e., including the ionized gas component) or to split the H I CDDF into two individual parts, corresponding to each absorber population (green and blue line in Figure 5.3, see also Figure 4.6 in Section 4.3.1). In the study of Ribaudo et al. (2011a), even more (up to four) different parts are identified in the CDDF and fitted individually. For the Lyα forest/LCD absorbers they found a slope of $\beta = 1.7$, while for the high column densities they get slopes between $\beta \sim 0.8$ and 1.4. If we compare our slopes for the splitted CDDF to their results, we find that that they are in much better agreement.

In contrast to the HVC analogs, the population of sub-LLS that have $\log N(\mathrm{H\,I}) < 17.0$ possibly are related to the IGM rather than to the halos of galaxies. On the other hand, on can argue that they might be candidates for the so-called low-column density absorbers that reside in the transition zone between the CGM and the IGM near the virial radius of the galaxies. Low-column density absorbers near the Milky Way are thought to be the counterparts of intervening weak Mg II absorbers, which have been found at impact parameters of $\rho \sim 100$ kpc around Milky Way-type galaxies (see Section 5.10, Richter et al. 2009). This aspect is further discussed in Section 5.2.5. Also for the Milky Way, Richter et al. (2009) have speculated that there should be a distinct absorber population with $\log N(\mathrm{H\,I}) \lesssim 17.0$. Unfortunately, apart from weak Mg II, this absorber population has not been studied in great detail so far. The current discussion circles around the assumption that these systems might represent either faint dwarf galaxies, extragalactic HVC analogs, or metal-enriched gas in intergalactic star clusters. Narayanan et al. (2008b) argue that sub-LLS with $15.8 < \log N(\mathrm{H\,I}) < 16.8$ can account for a substantial fraction ($\sim 25\%$) of the high column density Lyman α forest, which is interesting, since their typical metallicity is on the order of $0.1\,Z_{\odot}$. This scenario is in good agreement with our results presented and discussed in Section 5.3.1.

Summarizing, one can conclude that there are plausible explanations for the bimodal shape of the H I column density distribution and the lack of absorbers with $\log N(\mathrm{H\,I}) \approx 17.2$. Thus, based on H I 21cm observations of the Milky Way halo and the H I distribution around other galaxies and in intervening absorbers, it is possible to relate specific absorber populations to the different peaks in the column-density distribution function.

5.2.3 Absorber frequencies

All in all, we could identify 78 intervening metal absorbers in $\sim 65\%$ (37/57) of all sightlines. Here, we have to mention that this detection rate is affected by the highly varying S/N ratios among the different spectra. Additionally, there is an instrumental effect, which decreases the S/N ratio at the edges of the spectra down to about $\sim 50\%$ of the specified mean value. This means that the actual redshift

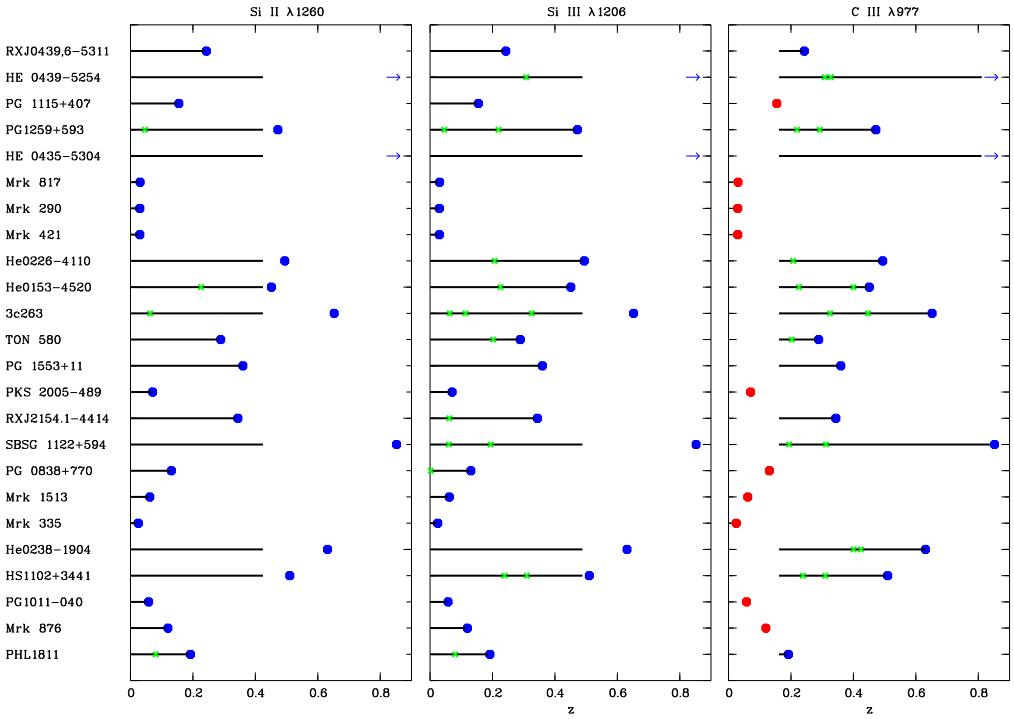

Figure 5.4: This figure illustrates the available redshift coverage for a subsample of 24 sightlines. The three different boxes refer to the lines of Si II λ1260, Si III λ1206, and C III λ977. The blue dots indicate the quasar positions, whereas the red dots showing sightlines, in which the close quasar position does not allows us a detection of that line. The small green crosses indicate the positions of the corresponding absorbers.

pathlength for a given sensitivity limit is somewhat smaller than what is shown in Figure 5.4.

In Figure 5.4, we show the redshift coverage for a *subsamble* of 24 COS sightlines for the three lines of interest: Si II λ1260, Si III λ1206, and C III λ977. The blue dots show the positions of the background AGNs and the red dots indicate AGNs that are too close for a detection of the corresponding line. The small green crosses indicate the identified absorber positions in the individual sightlines. For consistency, we include only absorbers that have 500 km s^{-1} $< cz \leq$ ($cz_{\rm AGN} - 1500$ km s^{-1}) to exclude Galactic HVC absorbers as well as those intrinsic to the AGN (cf., Tilton et al. 2012). This corresponds to a redshift offset of d$z \sim 0.002$ (or $\Delta\lambda \sim 2$ Å) for Si II and Si III for the Galactic environment and a redshift offset of d$z \sim 0.006$ ($\Delta\lambda \sim 7$ Å) for the AGN environment. These ranges are included in Figure 5.4, but they are too small to be seen. The little blue arrows indicate AGN positions that are at higher redshifts outside the plotted range. One can clearly see that Si II absorbers are less abundant, which is not surprising because they are expected to trace partly neutral gas at higher densities, which has a small absorption cross section in the outskirts of galactic halos (as it must reside in relatively small clumps). On the other hand, for the two intermediate ions there is almost the same number of absorbers detectable in the whole sample, which is also in very good agreement with what is expected. Both ions have very strong transitions (see Section 2.1) and are thought to arise in mildly ionized structures tracing almost the same physical conditions. Thus, one expects (and observes) that almost every Si III absorber has a C III counterpart and vice versa.

In the left panel of Figure 5.5 the redshift distribution of all 78 identified intervening metal absorbers is shown. The non-uniform distribution has an accumulation around $z \sim 0.2 - 0.3$. That does not necessarily mean that there is an intrinsic peak in the absorber evolution at that redshift, but rather is a result from the selection bias in the AGN sample. The median absorption redshift for all 78 absorbers in this sample is $\langle z_{\rm abs} \rangle = 0.2525$. The right panel of Figure 5.5 shows the relative spectral coverage for Si III with a sensitivity limit of $\log N_{\rm lim} = 12.02$, which is equivalent to a S/N of 9.0. Following Richter et al. (2011), the redshift coverage, $f_z(z)$, was calculated using $f_z(z) = \sum {\rm d}z(z)/x$, where x is the individual normalization. In our case, the analysis was done for a S/N-selected subsample (black dashed line, $x = 21$) and the whole sample (red dashed line, $x = 57$). As one can see, $f_z(z)$ drops heavily

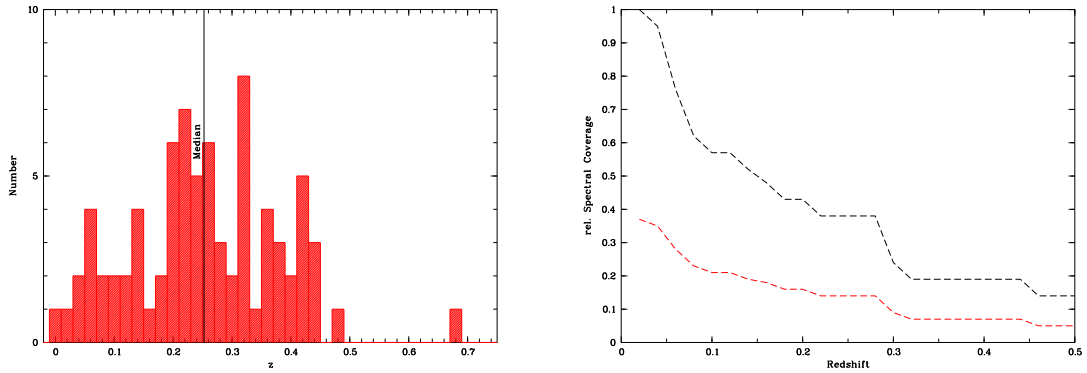

Figure 5.5: **Left panel**: redshift distribution of the 78 intervening metal absorbers.
Right panel: specific relative spectral coverage for Si III with $\log N_{\rm lim} = 12.02$. The black line represents a S/N-selected subsample, whereas the red line shows the spectral coverage (S/N> 9) for the whole sample.

for $z > 0.05$ and declines even more for higher z. The reason for that behavior is, on the one hand, that some of the background AGNs (in particular the brightest ones) are relatively nearby, which limits the redshift path for these sightlines. On the other hand, the redshift distribution is influenced by the flux of the AGN (and the chosen minimum S/N in the data). For this analysis, only spectra (or parts of spectra) with S/N > 9 have been considered for the number counts of intervening Si III, which excludes all SDSS targets. It is clear that, with such a criterion, the possible redshift path is limited. Additionally, the COS instrument is constructed in a way that the S/N ratio decreases for higher wavelengths, which implies that even a spectrum with a good S/N at low wavelengths might have regions where Si III absorption with $\log N_{\rm SiIII} \approx 12$ cannot be detected. For the subsequent analysis, we apply less stringent detection limits, because otherwise the detected absorption in the SDSS AGN sample would drop out of the statistics.

One of the most important parameters in our statistical analysis of the intervening metal absorbers is the redshift-dependent number density of absorbers, $\mathrm{d}\mathcal{N}/\mathrm{d}z$ (see Section 1.4.3). This parameter is an important measure for the statistical occurrence of the investigated objects in the local Universe and is necessary for the calculation of the typical size (cross section) of the absorbing regions. Thus, $\mathrm{d}\mathcal{N}/\mathrm{d}z$ is directly coupled to the covering fraction of the investigated ions and provides information on the gas flows around galaxies, which are important to understand galaxy formation and evolution. With this parameter it is also possible to compare different studies with each other and it allows us to draw conclusions about the selection effects (e.g., as a result of the relatively low data quality) or instrumental effects that may influence the detection statistics. During the analysis, the three sightlines towards PKS 0405−123, SDSS J151428.64+361957.9, and SDSS J022614.46+001529.7 have been sorted out due to compilation-process failures. In the remaining sample of 55 sightlines only the secure (reliable) detections of Si II, Si III, and C III absorbers have been considered. We define an absorption component being part of an absorption *system*, if its velocity offset is lower than ~ 20 km s^{-1} (see also Table 5.1).

Following Tilton et al. (2012), we calculate the individual redshift path for each sightline and ion as shown in Equation 5.1 using the specification described above. In case of gaps in the spectra or the necessary shift of at least $\mathrm{d}z = 0.162$ for C III, these issues have to be considered additionally in Equation 5.1:

$$\mathrm{d}z = (z_{\rm AGN} + 1) \cdot (1 - \frac{1500}{c}) - \frac{500}{c} - 1. \tag{5.1}$$

The resulting redshift ranges are listed in column 10 − 12 of Table 5.3. In total, we derive a statistically relevant cumulative redshift pathlength from all sightlines of $\mathrm{d}z(\mathrm{Si\,II}) = 18.27$, $\mathrm{d}z(\mathrm{Si\,III}) = 20.15$ and $\mathrm{d}z(\mathrm{C\,III}) = 16.49$. With Equation 5.2, a mean redshift of $\langle z \rangle = 0.25$, and the parameters listed in Table 5.7, one can transform $\mathrm{d}z$ into a comoving absorption pathlength $\mathrm{d}X$. Doing so, we derive $\mathrm{d}X(\mathrm{Si\,II}) = 25.02$, $\mathrm{d}X(\mathrm{Si\,III}) = 27.59$, and $\mathrm{d}X(\mathrm{C\,III}) = 22.58$ via the relation:

Table 5.2: $d\mathcal{N}/dz$ for Si II, Si III, and C III depending on the applied EW limit.

EW Limit	Si II λ1260	Si III λ1206	C III λ977
30 mÅ	0.87	2.35	3.01
45 mÅ	1.19	2.47	2.93
60 mÅ	1.25	2.57	3.12

$$dX = (1+z)^2[\Omega_\Lambda + \Omega_m(1+z)^3]^{-0.5}dz. \tag{5.2}$$

If we now ignore any completeness criteria, simply count the number of reliably detected absorbers, and combine this with the derived total redshift paths, then the resulting number densities turn out as $d\mathcal{N}/dz(\mathrm{Si\,II}) = 1.20$, $d\mathcal{N}/dz(\mathrm{Si\,III}) = 2.48$, and $d\mathcal{N}/dz(\mathrm{C\,III}) = 3.09$. Note that these numbers so far do not take into account any data quality issues and column density thresholds.

If we consider the individual S/N ratios in each spectrum, we are able to calculate equivalent-width limits (see Section 4.4.3). Furthermore, with the relation

$$N = 1.13 \times 10^{20} \cdot \frac{W_\lambda}{\lambda^2 f}\mathrm{cm}^{-2}, \tag{5.3}$$

as explained in Draine (2010), it is possible to convert the received EW limits into individual column density limits for each ion and sightline. These limits provide information on whether an absorption signal at a given column density can be securely detected in a particular spectrum (see Table 5.3). Thus, it is now possible to calculate the redshift-dependent number density with respect to the individual detection limits. In Table 5.2, the final results for $d\mathcal{N}/dz$ for Si II, Si III, and C III for different EW limits are shown. Note that the steps for the equivalent widths represent *lower* limits for the allowed individual EW limits for each sightline considered in the resulting data sample. For example, in case of an equivalent width limit of 30 mÅ, only sightlines with an S/N high enough to allow the reliable detection of lines of at least this equivalent width are considered. These sightlines are inspected again, and finally only those absorption features that have a column density above the individual column density limit for this sightline are included in the statistics. This approach allows us to consider the completeness in our data sample for distinct EW limits. Consequently, this approach also implies that for the lowest EW limits only the best spectra with the highest S/N ratios can be used. This means that for $\mathrm{EW_{limit}} = 30$ mÅ the absorber column densities are the most precise ones, but the total redshift path to derive $d\mathcal{N}/dz$ for this limit is quite small, reducing the statistical relevance of the derived number density. On the other extreme, in spectra with very low S/N ratios, that are part of the statistics for *high* EW limits, we might have missed a lot of weak absorbers due to the increased noise in the data. In summary, one can say that with this method one gets appropriate statistical results for a given detection limit, but with the (on average) marginal data quality we rapidly loose appropriate sightlines for the statistics of weak intervening absorbers.

The number density for the comoving pathlength can be calculated in the same way as presented above using the corresponding values for dX. For a 30 mÅ upper limit and $\langle z \rangle = 0.25$ we obtain $d\mathcal{N}/dX(\mathrm{Si\,II}) = 0.636$, $d\mathcal{N}/dX(\mathrm{Si\,III}) = 1.718$, and $d\mathcal{N}/dX(\mathrm{C\,III}) = 3.014$.

Table 5.3: Summary of COS sightlines with individual EW limits for the lines Si II λ1260, Si III λ1206, C III λ977 and effective absorption pathlengths (part 1).

QSO name	S/N	EW limit Si II [mÅ]	$N_{\rm min}$(Si II) Si II	EW limit Si III [mÅ]	$N_{\rm min}$(Si III) Si III	EW limit C III [mÅ]	$N_{\rm min}$(C III) C III	dz(Si II)	dz(Si III)	dz(C III)
RX J0439.6-5311	8.35	24.48	12.17	23.43	12.05	18.97	12.47	0.2351	0.2351	0.0741
HE 0439-5254	7.13	28.67	12.24	27.44	12.12	22.22	12.54	0.4225	0.4861	0.6745•
PG 1115+407	9.22	22.17	12.13	21.22	12.01	17.18	12.43	0.1471	0.1471	-
PG 1259+593	14.87	13.75	11.92	13.16	11.80	10.65	12.22	0.4225	0.4630	0.3019•
HE 0435-5304	7.42	27.55	12.22	26.37	12.10	21.35	12.52	0.4225	0.4861	0.6745
Mrk 817	11.58	17.65	12.03	16.90	11.91	13.68	12.33	0.0244	0.0244	-
Mrk 290	11.25	18.17	12.04	17.39	11.92	14.08	12.34	0.0236	0.0236	-
Mrk 421	21.25	9.62	11.76	9.21	11.64	7.46	12.07	0.0232	0.0232	-
HE 0226-4110	17.67	11.57	11.84	11.07	11.72	8.97	12.15	0.4225	0.4861	0.3238•
HE 0153-4520	11.32	18.06	12.04	17.28	11.92	14.00	12.34	0.4225	0.4421	0.2810•
3C263	16.26	12.57	11.88	12.03	11.76	9.74	12.18	0.4225	0.4861	0.4810•
TON 580	10.67	19.16	12.06	18.34	11.94	14.85	12.37	0.2809	0.2809	0.1198•
PG 1553+11	9.71	21.05	12.10	20.15	11.98	16.32	12.41	0.3515	0.3515	0.1905
PKS 2005-489	10.36	19.73	12.08	18.89	11.95	15.29	12.38	0.0640	0.0640	-
RX J2154.1-4414	11.88	17.20	12.02	16.47	11.90	13.34	12.32	0.3356	0.3356	0.1746•
SBS G1122+594	6.54	31.25	12.28	29.92	12.15	24.23	12.58	0.4225	0.4861	0.6745•
PG 0838+770	11.48	17.80	12.03	17.04	11.91	13.80	12.33	0.1240	0.1240	-•
Mrk 1513	13.48	15.16	11.96	14.51	11.84	11.75	12.26	0.0550	0.0550	-
Mrk 335	12.27	16.66	12.00	15.95	11.88	12.91	12.31	0.0186	0.0186	-
HE 0238-1904	14.84	13.77	11.92	13.18	11.80	10.68	12.22	0.4225	0.4861	0.4601•
HS 1102+3441	10.16	20.12	12.09	19.26	11.96	15.59	12.39	0.4225	0.4861	0.3397•
PKS 0405-123	n.a.	–	–	–	–	–	–	0.4225	0.4861	0.4034
PG 1011-040	12.84	15.92	11.98	15.24	11.86	12.34	12.29	0.0510	0.0511	-
Mrk 876	36.42	5.61	11.53	5.37	11.41	4.35	11.83	0.1127	0.1127	-
PHL 1811	16.00	12.77	11.89	12.23	11.77	9.90	12.19	0.1844	0.1844	0.0233•

[1]): These sightlines are not considered in the statistic because of data compilation problems.
•: Part of a more detailed subsample analysis.

Table 5.4: Summary of COS sightlines with individual EW limits for the lines Si II λ1260, Si III λ1206, C III λ977 and effective absorption pathlengths (part 2).

QSO name	S/N	EW limit Si II [mÅ]	$N_{\rm min}$(Si II) Si II	EW limit Si III [mÅ]	$N_{\rm min}$(Si III) Si III	EW limit C III [mÅ]	$N_{\rm min}$(C III) C III	dz(Si II)	dz(Si III)	dz(C III)
SDSS J161916.54+334238.4	9.50	21.51	12.11	20.59	11.99	16.68	12.42	0.4225	0.4620	0.3009
SDSS J094331.61+053131.4	3.19	64.07	12.59	61.33	12.47	49.67	12.89	0.4225	0.4861	0.3935
SDSS J102218.99+013218.8	4.45	45.93	12.44	43.97	12.32	35.60	12.75	0.4225	0.4861	0.6173
SDSS J143511.53+360437.2	4.04	50.59	12.49	48.43	12.36	39.22	12.79	0.4225	0.4202	0.2591
SDSS J141910.20+420746.9	4.40	46.45	12.45	44.47	12.33	36.01	12.75	0.4225	0.4861	0.6745
SDSS J124511.25+335610.1	4.40	46.45	12.45	44.47	12.33	36.01	12.75	0.4225	0.4861	0.5457
SDSS J122035.10+385316.4	3.40	60.12	12.56	57.54	12.44	46.60	12.86	0.3619	0.3617	0.1992
SDSS J101622.60+470643.3	4.25	48.09	12.46	46.03	12.34	37.28	12.77	0.4168	0.4801	0.6225
SDSS J113327.78+032719.1	4.40	46.45	12.45	44.47	12.33	36.01	12.75	0.4225	0.4861	0.3473
SDSS J100902.06+071343.8	3.70	55.24	12.52	52.88	12.40	42.82	12.83	0.4225	0.4471	0.2860
SDSS J082024.21+233450.4	5.39	37.92	12.36	36.30	12.24	29.39	12.66	0.4225	0.4610	0.2999
SDSS J091440.38+282330.6	4.80	42.58	12.41	40.76	12.29	33.01	12.71	0.4225	0.4861	0.5636
SDSS J092554.70+400414.1	4.20	48.66	12.47	46.58	12.35	37.72	12.77	0.4164	0.4557	0.2931
SDSS J111239.11+353928.2	4.20	48.66	12.47	46.58	12.35	37.72	12.77	0.4225	0.4861	0.4456
SDSS J144511.28+342825.4	4.15	49.25	12.47	47.14	12.35	38.18	12.78	0.4095	0.4725	0.5090
SDSS J091029.75+101413.6	3.40	60.12	12.56	57.54	12.44	46.60	12.86	0.4225	0.4540	0.2930
SDSS J155304.92+354828.6	5.10	40.08	12.38	38.36	12.26	31.07	12.69	0.4225	0.4861	0.5507
SDSS J124154.02+572107.3	4.90	41.71	12.40	39.93	12.28	32.33	12.70	0.4225	0.4861	0.4124
SDSS J080359.23+433258.4	4.60	44.43	12.43	42.53	12.31	34.44	12.73	0.4166	0.4360	0.2734
SDSS J115758.72-002220.8	5.00	40.88	12.39	39.13	12.27	31.69	12.70	0.2520	0.2520	0.0910
SDSS J225738.20+134045.4	3.5	58.40	12.55	55.90	12.43	45.27	12.85	0.4225	0.4861	0.4233
SDSS J133045.15+281321.4	5.40	37.85	12.36	36.23	12.24	29.34	12.66	0.4083	0.4083	0.2472
SDSS J161649.42+415416.3	4.55	44.92	12.43	43.00	12.31	34.82	12.74	0.4087	0.4167	0.2523
SDSS J123335.07+475800.4	5.10	40.08	12.38	38.36	12.26	31.07	12.69	0.3734	0.3734	0.2124
SDSS J004222.29-103743.8	4.60	44.43	12.43	42.53	12.31	34.44	12.73	0.4020	0.4015	0.2372
SDSS J123304.05-003134.1	4.20	48.66	12.47	46.58	12.35	37.72	12.77	0.4225	0.4861	0.3009
SDSS J155048.29+400144.9	3.80	53.79	12.51	51.49	12.39	41.69	12.81	0.4225	0.4861	0.3268
SDSS J234500.43-005936.0	4.19	48.78	12.47	46.69	12.35	37.81	12.77	0.4171	0.4805	0.6104
SDSS J161711.42+063833.4	1.60	127.75	12.89	122.28	12.77	99.02	13.19	0.2212	0.2212	0.0601
SDSS J040148.98-054056.5	4.11	49.73	12.48	47.60	12.36	38.55	12.78	0.4225	0.4861	0.3994
SDSS J151428.64+361957.9	n.a.	–	–	–	–	–	–	–	–	–
SDSS J155504.39+362848.0	3.80	53.79	12.51	51.49	12.39	41.69	12.81	0.4225	0.4861	0.5427
SDSS J022614.46+001529.7	n.a.	–	–	–	–	–	–	–	–	–

[1]): These sightlines are not considered in the statistic because of data compilation problems.

5.2.4 Column-density distribution function for metal ions

The two panels in Figure 5.6 illustrate the measured column density distribution for Si II, Si III, and C III in the COS data sample. In the same way as described in Section 4, the CDDF is defined as $f(N) = C\,N^{-\beta}$ with errors reflecting a Poisson-like statistics. As one can see, the simple power law approximation is fairly adequate for logarithmic column densities $\gtrsim 13.1$ for Si II, $\gtrsim 12.5$ for Si III, and $\gtrsim 13.3$ for C III. Below these limits the effect of incompleteness, which explains the lack of weak absorbers due to instrumental limitations, is evident. If we force a single-slope power-law fit to the data we derive $\beta = 1.55 \pm 0.22$ with $\log C = 8.02 \pm 3.0$ for Si II, $\beta = 1.41 \pm 0.09$ with $\log C = 6.45 \pm 1.2$ for Si III, and $\beta = 1.38 \pm 0.09$ with $\log C = 6.26 \pm 1.4$ for C III. As already described earlier for the HVC analysis in Section 4, there might be plateaus visible in the CDDFs of Si II, Si III, and C III at $\log N(\mathrm{Si\,II}) \sim 13.6$, $\log N(\mathrm{Si\,III}) \sim 14.0$, and $\log N(\mathrm{C\,III}) \sim 15.4$. As explained in Section 5.2.2, such plateaus typcially indicate regions where the gaseous medium changes its opacity. Since a Si II column density of $\log N(\mathrm{Si\,II}) \sim 13.6$ typically traces a neutral hydrogen column density on the order of $\log N(\mathrm{H\,I}) \approx 18.1$, which is close to the measured CDDF plateau for H I (see Section 5.2.2), it is plausible that this behavior is also a result of changes in the ionization properties. However, this aspect is less clear for Si III and C III, since these ions are typically found in regions that have substantially higher ionization fractions compared to regions traced by Si II and H I. In any case, one can conclude that the variance of the data points clearly indicates a inhomogeneous and non-uniform distribution of column densities of metal ions in intervening metal absorbers.

In the lower panel of Figure 5.6, this trend can also be seen. Here, the logarithmic column densities range from ~ 11.5 for Si III up to > 16.5 for C III for the case of the quasar SDSS J124154.02+572107.3, with median values of $\log N(\mathrm{Si\,II}) = 13.12$, $\log N(\mathrm{Si\,III}) = 12.93$, and $\log N(\mathrm{C\,III}) = 13.57$. The corresponding mean column densities are $\langle \log N(\mathrm{Si\,II}) \rangle = 13.58 \pm 0.13$, $\langle \log N(\mathrm{Si\,III}) \rangle = 13.70 \pm 0.12$, and $\langle \log N(\mathrm{C\,III}) \rangle = 13.89 \pm 0.09$. Assuming that C III is the dominant ionization stage of carbon and predominantly traces ionized hydrogen, one can make a rough estimate that a C III column density of $\log N(\mathrm{C\,III}) = 16.7$ traces an H II column density of $\log N(\mathrm{H\,II}) \sim 20.8$ (assuming a typical metallicity in the CGM of ~ 0.3 solar). The inspection of the spectra as well as a fit to the corresponding H I absorption indicates a H I column density on the order of $\log N(\mathrm{H\,I}) = 18.5$. The absorber thus would be classified as a sub-DLA. Consequently this would result in an ionization fraction of $f = N(\mathrm{H\,II})/[N(\mathrm{H\,I})+N(\mathrm{H\,II})] \approx 0.995$, which seems very high for optically thick H I gas. Typical values for LLS are in the order of $f = N(\mathrm{H\,II})/[N(\mathrm{H\,I}) + N(\mathrm{H\,I})] \approx 0.980$ (see Lehner et al. 2013, for a detailed discussion). This implies that estimates for such high H II column densities in LLS can be a result of unresolved sub-component structure and thus should be taken with care. On the other hand, Sembach et al. (1999 2003); Richter et al. (2009) have demonstrated that there exists a population of highly-ionized gas clouds in the Galactic halo that contain only low column densities of neutral/weakly ionized gas. With respect to the peak value of the logarithmic absorber column densities in our study, we find that they range between ~ 12.5 and 13.5 for Si II, ~ 12.8 and 13.5 for Si III, and ~ 13.0 and 14.5 for C III; these values are in very good agreement with previous results (see next section).

5.2.5 Comparison with previous results

In this study of intervening metal absorbers we found 22 Si II absorption systems along 20 sightlines. Thus, the sample size is comparable to the one for the Galactic HVCs, as presented earlier (20 Si II detections in 19 HVCs, see Chapter 4). If we now compare the results for the column densities and the CDDF with those found for the Galactic HVCs, one can see that both absorber samples show a number of similar properties. For instance, both samples show plateaus in the CDDFs of Si II at almost the same logarithmic column density of $\sim 13.6 - 13.8$. It is quite unlikely that this similarity is by chance. Instead, there might be a physical reason of a lack of Si II absorbers in this column density region. This dip is also detectable for Si III (at almost the same column density) and possibly for C III, too (at a higher column density). With an ionization potential of ~ 16.35 eV, Si II is expected to trace predominantly neutral (and weakly ionized) gas. If the majority of the intervening Si II absorbers represent the analogs of Galactic HVCs, one would expect that the slope of the Si II CDDF is similar to that for H I of the local HVC population. In fact, we measure a mean slope of $\beta = 1.55 \pm 0.22$ for Si II, which is in good agreement to the results of Lockman et al. (2002) ($\beta = 1.5$ for H I in the Galactic HVCs).

If we now compare the result for the median column density of Si II in the intervening absorbers ($\log N = 13.12$) with the one measured in Milky Way HVCs ($\log N = 13.48$), we find a difference of ~ 0.4 dex. This can be explained by the different geometry: it is more likely to detect high-column density gas in the halo of the Milky Way because of our position inside the disk. For the intervening

metal systems (that we regard as HVC analogs), it is, on the contrary, more likely to trace the *outer* regions of the galaxy halos (as these regions have the largest geometrical cross section), where the ionization fraction in the gas is higher. In other words, if we observe galaxy halos from an outside vantage point via absorption spectroscopy of randomly distributed background sources, the chance to intersect the inner halo and the disk-halo interface of a galaxy is relatively small.

There are not many other studies that provide comparable statistics for the above mentioned ions in intervening systems at low z, so that a comparison with results from other groups is difficult. Most of the relevant earlier studies that have been carried out concentrate on DLAs or Mg II absorbers, as described in Section 1.4.4. However, with a focus on Si II and Mg II (see previous sections), it is again possible to draw some conclusions. If we assume that every Si II absorber corresponds to a Mg II system (either weak or strong), we again can apply the conversion between Mg II and Si II presented in Section 4.4.2. If we do so, we find that the majority ($\sim 72\%$) of the intervening Si II systems would represent strong Mg II absorbers. This fraction is in very good agreement with our previous results discussed in Section 4.4.2. There, we had shown that for the Milky Way the majority of the HVCs seen in Si II ($\sim 60\%$) would be regarded as strong Mg II absorbers if seen from an outside vantage point. It is therefore not surprising that a similar fraction of the intervening Si II absorbers, which are supposed to be the HVC analogs, are related to strong Mg II absorbers. On the other hand, it is known that strong Mg II systems arise typically within an impact parameter of less than 35 kpc to their host galaxies (Steidel et al. 2002; Kacprzak et al. 2010) and on would thus expect host galaxies to be located close to most of the intervening metal absorbers. This aspect is further discussed in Section 5.4.

If we now turn to the Si III ion, Collins et al. (2009) have analyzed high-velocity Si III around the Milky Way using the *HST*/STIS instrument. They find Si III absorption in the Milky Way halo in more than 90% of their sightlines, with mean column densities of $\langle \log N(\mathrm{Si\ III}) \rangle = 12.92 \pm 0.46$. This is approximately 0.8 dex below our result for the intervening systems based on the COS analysis ($\langle \log N(\mathrm{Si\ III}) \rangle = 13.70 \pm 0.12$). One can explain this discrepancy with the different instruments used. Since STIS has twice the velocity resolution of COS, it is much more likely to resolve smaller sub-components with less column density in the STIS data. Moreover, the average S/N ratio in the STIS data is substantially higher than, for instance, for the SDSS quasar sample in the COS data used in this thesis, providing a higher sensitivity. With respect to the related H I column densities, Collins et al. (2009) have shown that typical values for Milky Way high-velocity H I associated with Si III are in the range $17 \leq \log N(\mathrm{H\ I}) < 19$, which is in good agreement with our H I measurements (see right panel of Figure 5.2). However, Collins et al. (2009) noted that a similar analysis done by Shull et al. (2009) found lower corresponding H I column densities in the range $15.7 \leq \log N(\mathrm{H\ I}) < 16.7$ at a mean Si III column density of $\langle \log N(\mathrm{Si\ III}) \rangle = 13.42 \pm 0.21$. Such low-column density absorbers can also be seen in our H I distribution. In addition, their mean Si III column density is in better agreement with our results. Future measurements are required to further investigate these similarities and discrepancies between Galactic HVCs and intervening absorbers and to clarify the issue of unresolved sub-component structure in the absorbers. Nevertheless, our results for the mean column densities of Si III and H I in intervening absorbers are - in priniciple - in line with the scenario, that they represent a similar class of mildly ionized absorbers as found in the Milky Way halo.

In view of the results for Si III and C III, one can see that for intervening metal systems, C III has (on average) a ~ 1 order of magnitude higher column density. This is expected, because C has also a ~ 1 order of magnitude higher abundance ($(\mathrm{C/Si})_{\odot} = 0.83$, assuming solar reference abudances, Asplund et al. 2005). Furthermore, C III has a somewhat higher ionization potential compared to Si III (see Table 2.1).

For the intervening absorbers, the slopes for the CDDFs of all three ions can be compared to what has been derived by Tilton et al. (2012). These authors derive slopes for Si II, Si III, and C III of $\beta(\mathrm{Si\ II}) = 1.57 \pm 0.2$, $\beta(\mathrm{Si\ III}) = 1.74 \pm 0.1$, and $\beta(\mathrm{C\ III}) = 1.86 \pm 0.1$ based on an absorber sample of similar size. In contrast to this work, they used basically STIS data for their analysis, with the addition of *FUSE* and COS data, if available. Because of the different spectral resolutions, sensitivities, and completeness corrections, the results may not be directly comparable to each other. Yet, the slope in their CDDF for Si II is in very good agreement with the one derived by us. In contrast, their slopes for Si III and C III differ by 0.33 dex and 0.48 dex. The reason for this discrepancy could be the much lower total redshift path in their study. Surprisingly, they found almost the same number of absorbers (Si II: 15/22, Si III: 62/50, C III: 51/51) along a ~ 4 times smaller redshift pathlength. A large fraction of their detected features have $W_{\mathrm{r}} < 50$ mÅ (e.g., for Si III). We generally ignore such weak features because of their uncertain origin. As a result, their redshift-dependent number density is ~ 4 times higher. Note

that if we use their values for $d\mathcal{N}/dz$, we derive unrealistically high values for the statistical halo sizes, as explained in the following sections.

Another, earlier analysis was done by Danforth and Shull (2008). They used a sample of 35 STIS sightlines to search for absorbers at $z < 0.4$. These authors basically focused on Lyα absorbers, but received also a lot of information about different metal ions in intervening absorbers. The overall redshift pathlength in their study ($\Delta z = 5.27$) is a factor of ~ 4 smaller compared to the data set used in this thesis, but, again, they detect almost the same number of absorbers (53 vs. 48 for Si III and 39 vs. 47 for C III). That leads to higher values for $d\mathcal{N}/dz$ ($d\mathcal{N}/dz$(Si III) $= 6^{+2}_{-1}$ and $d\mathcal{N}/dz$(C III) $= 10^{+3}_{-2}$) and slightly different slopes of β(Si III) $= 1.80 \pm 0.9$ and β(C III) $= 1.79 \pm 0.1$. These differences again can be attributed to the different data characteristics of STIS and COS. For instance, they might be caused by the higher sensitivity of the STIS data to detect weak absorbers, but also the limited redshift range of the Danforth and Shull (2008) study ($z < 0.4$) might be of relevance here.

Richter et al. (2011) has investigated intervening neutral-gas absorbers as HVCs analogs around galaxies at $z \leq 0.5$ with a focus on the Ca II ion, based on a large sample of ~ 300 QSO sightlines observed in the optical with VLT/UVES. They find a slightly steeper slope for the CDDF of Ca II of β(Ca II) $= -1.68 \pm 0.2$ compared to the one we find for Si II in this thesis. This difference can be explained with the strong dust depletion of Ca in interstellar and circumgalactic gas, especially in high-column density systems. Dust depletion thus leads to a steepening of the slope of the CDDF. Note that calcium is also much less abundant in the CGM than silicon, if solar relative abundances are assumed ($\log (\mathrm{Si/Ca})_{\odot} = 1.47$, (Asplund et al. 2005)) and therefore, high-column density Ca II systems are expected to be rare.

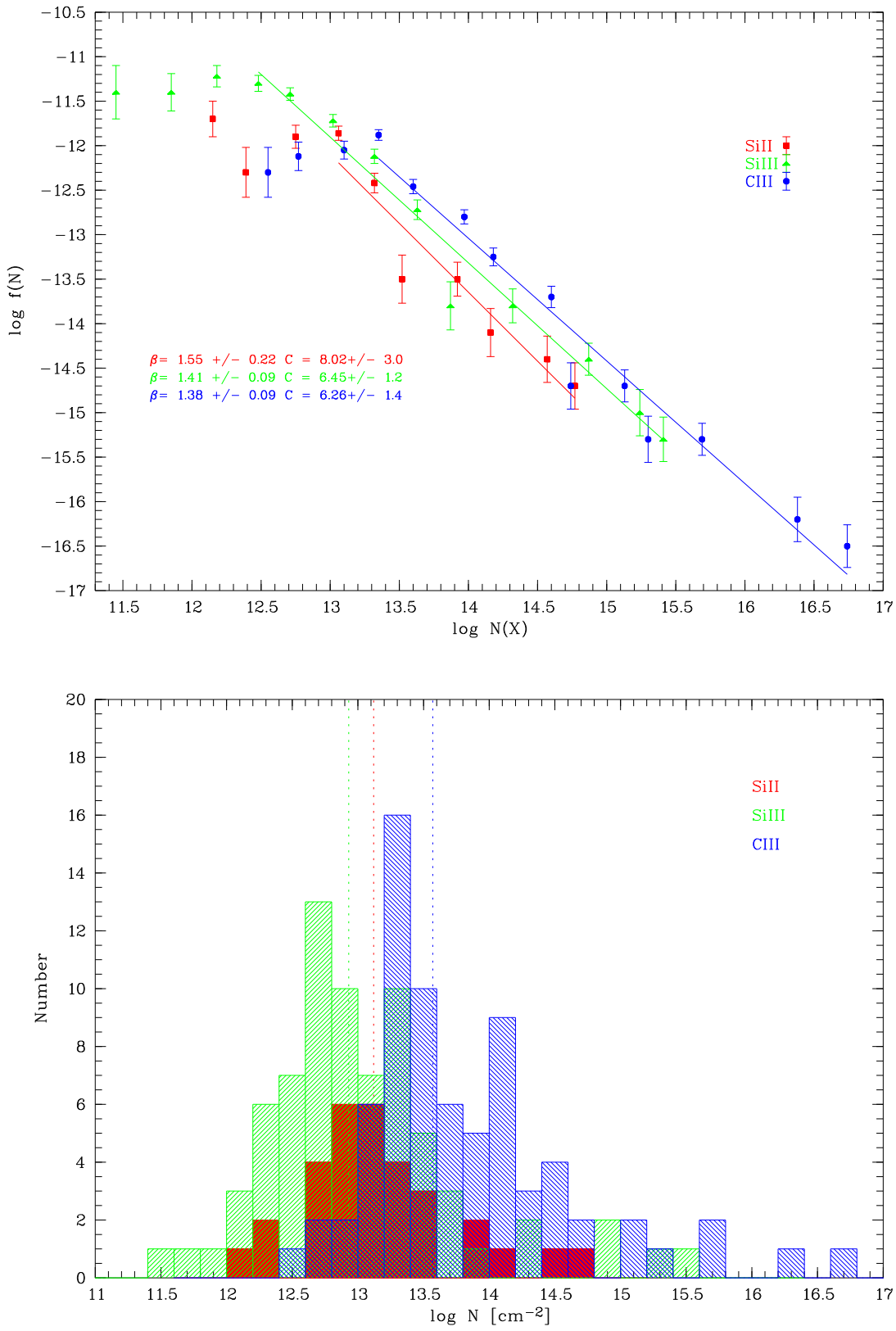

Figure 5.6: **Upper panel**: column density distribution functions for Si II, Si III, and C III based on the COS data sample. The bin size in $\log N$ is 0.2 and the error bars result from a poisson-like statistics.
Lower panel: column density histogram for all three investigated ions in the COS data sample.

5.3 Subsample Analysis

For the further analysis of the ionization conditions in the individual absorbers it was necessary to split the COS data sample into two subsamples. Because of the partly low data quality (see Table 5.3), we decided to consider only spectra with S/N $\gtrsim$ 7 and significant absorption in two or more ions for at least one absorber per sightline. This approach basically excludes all sightlines towards SDSS quasars. The 12 sightlines considered for the further analysis can be found in the upper part of Table 5.3; they are marked with a filled bullet symbol. The mean S/N ratio per pixel in these 12 spectra is $\sim$ 12, which is somewhat higher than for the total COS sample (S/N $\sim$ 7). For each of the selected systems we searched for nearby galaxies within an impact parameter of $\sim$ 160 kpc and looked for a matching ionization model calculated with Cloudy. Furthermore, we analyzed all absorption components in this sample using the model technique described in Section 2.3.4.

The following subsections are organized as follow: first, the Cloudy results of the 12 systems and their resulting ionization conditions are presented and discussed in detail. In a second step, we compare our results for the intervening absorbers to previous HVC and H I studies. Finally, we present a search for associated host galaxies for the whole COS data sample and discuss the typical halo radii for Si II, Si III, and C III.

5.3.1 Ionization Conditions

One of the key aspects in ISM and IGM science is the understanding of the local gas physics that determines the ionization conditions and the individual properties of the different ISM/IGM gas phases. With detailed information on the physical conditions it is possible to characterize the evolution of gaseous matter in and around galaxies as well as in the cosmic web.

With the Cloudy ionization code described in Section 2.6 it is possible to model in detail the ionization conditions of individual gas clouds. For the input of the code it is necessary to establish a set of basic parameters, such as column density, Doppler parameter, temperature, and the background radiation field. For the following, we decided to use the modeling technique to re-analyze all identified absorption systems in the COS subsample described above. With this method, it is possible to include a temperature constraint into the calculation of the absorption profile, which enables us to differentiate between thermal and turbulent gas motions for the Doppler parameter, an aspect that becomes important for the lighter elements hydrogen to carbon.
Furthermore, it is possible to set the contribution of turbulent motions to the Doppler parameter as constant, as it is expected for ions with similar ionizations potentials within the same cloud. The impact of thermal broadening on the total Doppler parameter can be clearly seen in the 6th column of Table 6.6 - 6.8 (Appendix).
Because of the absence of a χ^2 minimization routine in the modeling software, we adjusted the individual properties manually to obtain a satisfying match between the model spectrum and the COS data. The draw-back of this approach is that no statistical estimate for the goodness of the fit (adjustment) is provided (see discussion in Section 2.3.4). A major advantage of the modeling software is, that the wavelength-dependend COS line-spread-function can be included in the modeling of the line profiles, which can make a significant difference in the estimated values for N and b.

In the selected COS subsample, most of the sightlines (7/12 or 58%) inhabit more than one IGM absorber, leading to a total set of 24 absorbers. Unfortunately, not all of these 24 absorbers are suited for a detailed Cloudy modeling due to the fact, that one needs the column densities of at least two different ions for a reliable determination of the ionization parameters. Therefore, our strategy was to identify absorption systems with two or more metal lines from different ions of one or more elements.
Because of the limited spectral range, the only potentially available ion ratios were the Si II/Si III and the C II/C III pairs. Thus, the optimal case would be a detection of all four ions within the same system. For the modeling, we assume a constant gas temperature of $T = 10\,000$ K, the canonical value for diffuse neutral and ionized gas, where the low and intermediate ions of most metals are expected to represent the dominant ionization stages. In addition, we assume solar relative abundances taken from Asplund et al. (2005), which is justified in view of the low redshift of the absorbers. Note that we do not consider Cloudy routines which calculate possible dust depletion effects, because it is not possible (in principle) to distinguish between, for instance, underabundant silicon or a dust depletion effect in a given system without further information on line ratios of other (non-depleted) elements. For the ionizing radiation, we adopt the spectra of the ionizing background radiation at $z = 0$ published by Haardt and Madau (2012), which are implemented in the code (see right panel of Figure 2.8). The two remaining free

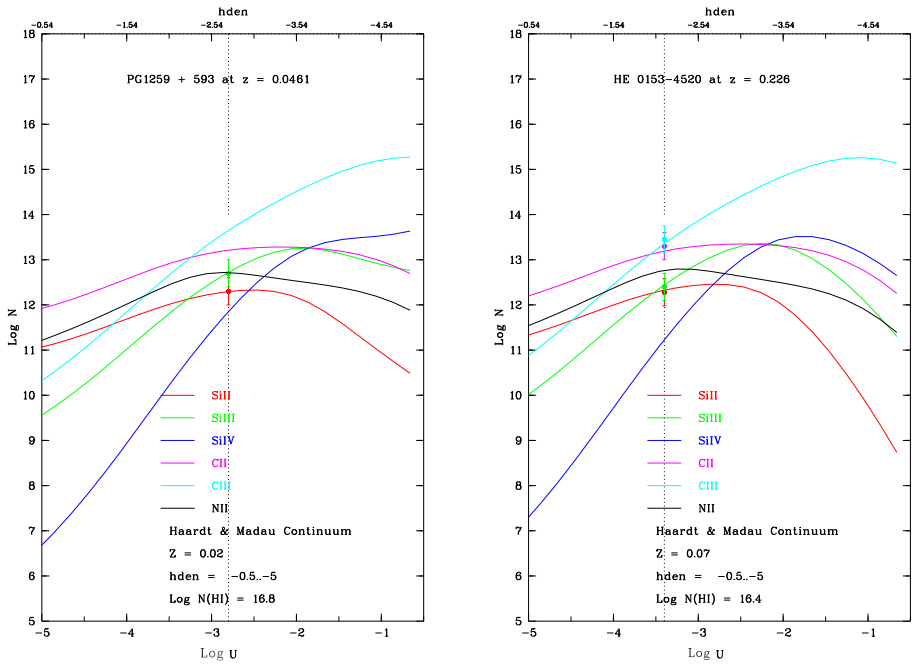

Figure 5.7: Two examples for Cloudy models of the ionization conditions in absorption systems along the sightlines towards the Seyfert 1 galaxy PG 1259+593 and teh quasar HE 0153−4520.

parameters are the column density of neutral hydrogen and the overall metallicity. With the use of our modeling results for the absorbers, it was possible to estimate the neutral hydrogen column density and thus the metallicity remains as an output parameter. As strategy for our modeling we decided to create a grid of data points with a hydrogen volume density ($h_{\rm den} = \log n_{\rm H}$) varying in the range $-5 < \log n_{\rm H} < -0.5$, which is equivalent to an ionization parameter range of $-0.5 < \log U < -5$. Cloudy then calculates the column densities for each ion of interest over the range of ionization conditions (see Figure 5.7). Thus, it is possible to compare the observational results for the column density with a given Cloudy grid model to identify a matching solution for a chosen metallicity. As an example, Figure 5.7 shows two resulting models for the systems at $z = 0.0461$ and $z = 0.2260$ along the sightlines towards the Seyfert 1 galaxy PG 1259+593 and the quasar HE 0153−4520. Both systems are well suited for an ionization analysis due to the availability of several transitions of different ionization stages for one and the same element. In both cases, the simultaneous detection of Si II and Si III, together with a measurement of the neutral hydrogen column density, allows an exact determination of the metallicity and the ionization parameter (Z and $\log U$) for both absorption systems. For the absorber towards HE 0153−4520 also the ion ratio of C II/C III is available, which increases the reliability of the results. For a complete list of the derived model values and all the corresponding Figures see Tables 6.6 - 6.8 in Section 6.2 in the Appendix. A short overview is given in Table 5.5.

In general, one can say that it remains difficult to come to a final conclusion about the typical ionization parameters of intervening metal systems. With only a small number of suited sightlines (10) and absorption systems (14), the amount of spectral information is just too limited to establish a meaningful statistics. In most cases, we could detect only the two strong lines of Si III λ1206.5 and C III λ977.0, which typically leads to more than one valid solution for the ionization modeling. Also for the absorbers towards HE 0153−4520, 3C 263, and PHL 1811, for which three or more ion transitions are detected, the ionization modeling implies possible deviations from a simple single-gas-phase model and these absorbers deserve a more detailed investigation in the future. Consequently, more detailed spectral information from a larger number of sightlines is desired to confirm and extend the ionization results presented in the following passages.

From our ionzation modeling we find that the metallicities in the absorbers range from $0.003 < Z/Z_{\odot} \leq 1.50$, while the hydrogen volume densities are in the range of $-4.34 < \log n_{\rm H} \leq -1.94$. For the ionization parameters we find a range of $-3.60 < \log U \leq -1.20$. Therefore, all three parameters in our modeling span a range of ~ 2.5 orders of magnitude, which illustrates a large variety of physical conditions in the absorbers.

Table 5.5: Ionization parameters and metallicities derived for the COS subsample of intervening absorbers.

QSO	$z_{\rm abs}$	log U	log $n_{\rm H}$ [cm^{-3}]	$Z/Z_{\odot}$	log Z
HE 0439-5254	0.3084	-2.00	-3.54	0.100	-1.0
PG 1259+593	0.0461	-2.80	-2.34	0.020	-1.7
		-3.50	-2.04	0.020	-1.7
		-3.60	-1.94	0.020	-1.7
		-3.55	-1.99	0.020	-1.7
	0.2195	-2.20	-3.34	0.005	-2.3
HE 0226-4110	0.2071	-2.20	-3.34	0.100	-1.0
		-2.25	-3.29	0.100	-1.0
HE 0153-4520	0.2260	-3.40	-2.14	0.070	-1.2
		-2.80	-2.74	0.130	-0.9
		-3.10	-2.44	0.200	-0.7
		-2.20	-3.34	0.200	-0.7
		-3.00	-2.54	1.000	0.0
3C263	0.0635	-2.70	-2.84	0.040	-1.4
		-2.80	-2.40	0.600	-0.2
	0.3256	-2.30	-3.34	0.015	-1.8
		-2.50	-3.04	1.500	0.2
RX J2154.1-4414	0.0622	-3.20	-2.34	1.200	0.08
SBSS G1122+594	0.0602	-2.70	-2.74	0.500	-0.3
	0.1944	-3.40	-2.14	1.000	0.0
		-1.20	-4.34	1.000	0.0
		-3.40	-2.14	0.010	-2.0
PG 0838+770	0.0024	-2.70	-2.84	0.060	-1.2
HS 1102+34	0.2388	-2.40	-3.14	0.003	-2.5
		-2.40	-3.14	0.003	-2.5
		-2.50	-3.04	0.005	-2.3
	0.3102	-2.90	-2.64	0.300	-0.5
PHL 1811	0.0807	-2.00	-3.54	0.032	-1.5
		-4.00	-1.54	0.110	-0.96

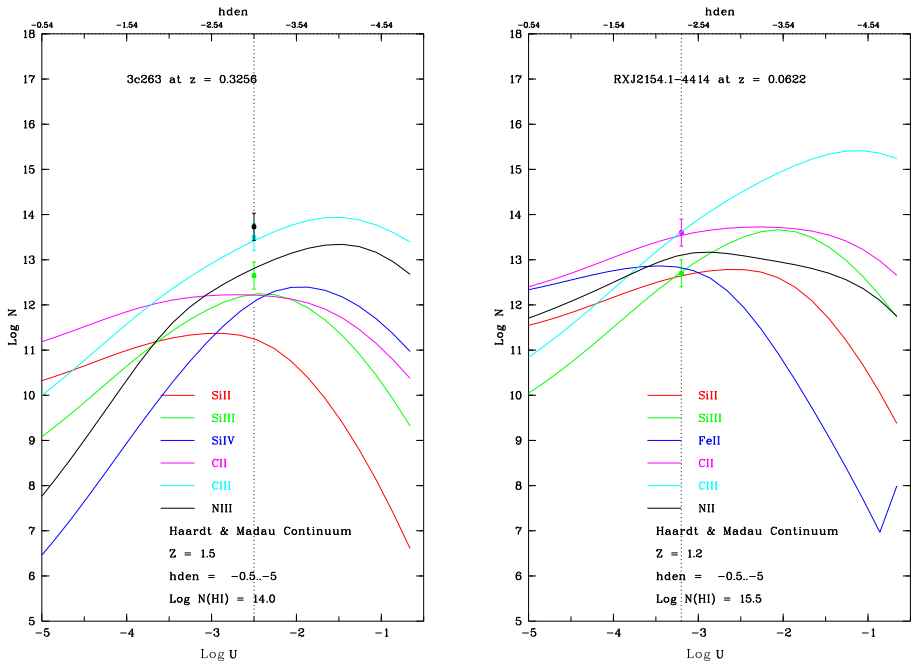

Figure 5.8: Two examples for Cloudy models of the ionization conditions in absorption systems along the sightlines towards the Seyfert 1 galaxies 3C 263 and RX J2154.1−4414.

For the two systems at $z = 0.3256$ towards 3C 263 and at $z = 0.0622$ towards RX J2154.1−4414 we find supersolar metallicities, which appears implausible. In Figure 5.8 both cases are illustrated. In the left panel, one can see that the neutral hydrogen column density ($\log N(\mathrm{H\,I})$) possibly is underestimated. Even at this high metallicity, the column densities of Si III and N III come out too low. To substantially lower the metallicity, one would need a H I column density of $\log N(\mathrm{H\,I}) \sim 16$ or higher. The origin for the underestimation of the H I column density might lie in the existence of broad wings in the H I Lyman α absorption. We decided to apply a three-component model for the H I Lyman α absorption with a broad central component. Apparently, the metal absorption suggests a two-component absorption (for the spectral model see the Appendix). We conclude that in this case the systematic errors from the COS LSF, which can produce broad artificial wings in the spectra, might be a possible source for the problems described above and the separation of the overall H I column density into three sub-components might be the reason for the underestimation of the total $\log N(\mathrm{H\,I})$. However, the inspection of a two-component fit indicates that even with this approach the H I column density will only increase by approximately one order of magnitude, which would not fully solve the problem of the high metallicity. Dust and depletion effects can be excluded, because our model (without the depletion routines) alread predicts *too low* column densities. To solve the problems in this particular system, one needs more information on other ion ratios, which could possibly be used to disentangle the multi-phase nature of this absorber.

For the system at $z = 0.0622$ towards RX J2154.1−4414 the discrepancy is not as large as in the previous example, but with a H I column density of $\log N(\mathrm{H\,I}) < 16$ there might be a similar systematic problem. In this case, we detected additional high ions such as Si IV, C IV, and N V. But with the simultaneous presence of C II, it is more likely that the high ions trace a different gas phase within the absorber than the low and intermediate ions. Therefore, we consider only C II and Si III for the ionization modeling. From a closer look into the spectral data one can see that the applied component separation in the high ions might be present also in Si III. If true, we would overestimate the Si III column density and the true metallicity would be smaller than the one estimated in our photoionization model. To further investigate this issue, more accurate data with a better S/N ratio would be necessary.

Apart from these two problematic cases, our ionization modeling yields realistic values for the metallcities, densities, and ionization parameters in the selected intervening Si III and C III systems. For our absorber sample we derive mean logarithmic values for the metallicity, the hydrogen volume density, and the ionization parameter of $\langle \log (Z/Z_\odot) \rangle = -1.07$, $\langle \log n_\mathrm{H} \rangle = -2.75$, and $\langle \log U \rangle = -2.73$, respectively. In Table 5.6 an overview of the most important statistical parameters is given. For this

Table 5.6: Statistical parameters for the ionization condition measurements

	arithmetical mean $\langle \log X \rangle$	median $\log X$
U	-2.73 ± 0.09	-2.70
$n_{\rm H}$	-2.75 ± 0.10	-2.74
$Z/Z_{\odot}$	-1.07 ± 0.15	-1.07

calculation, the highest and lowest values of each parameter have been omitted. The two panels of Figure 5.9 show the resulting number distribution of the three considered parameters.

Refering to the metallicity, one can see that $\sim 75\%$ of the systems have metallicities $\lesssim 0.4$ solar, which is in good agreement with the expectation for gas outside galaxy disks at $z = 0$. Since our main tracers are Si III and C III, we are observing diffuse ionized gas in the outer interface regions of galaxies to the IGM. The two systems with apparent "supersolar" metallicities have been already discussed above. The upper panel of Figure 5.9 shows, however, that there is a large spread in the metallicity distribution, a trend that is reflected in the large standard deviation. Yet, such a spread is not too surprising, since we know that these ions trace a gas phase which builds the transition region between the neutral, dense gas in and near the disks and the surrounding hot coronal gas. Most likely, mixing and gas circulation processes, including galactic outflows as well as accretion processes, are important and introduce a large scatter in the metallicity distribution of such interface gas.
Considering the ionization parameters and gas densities, which are plotted in the middle and lower panel of Figure 5.9, no clear trend is visible. This could be due to the limited sample size, or also because of a large range in physical conditions in such circumgalactic gas absorbers. Similar trends have also been found by other groups, as discussed below.

5.3.2 Comparison to other studies

In the previous section we have presented the results from the ionization modeling of our selected metal absorbers. We now want to move forward with our idea that intervening Si III and C III systems can be regarded as tracers for the metal-enriched halos of galaxies and their CGM (see for instance Savage et al. 2011a; Narayanan et al. 2012; Keeney et al. 2013; Stocke et al. 2013, for examples). With a mean logarithmic metallicity of $\langle \log (Z/Z_{\odot}) \rangle = -1.07$, most absorption systems contain less metals than the central parts of galaxies (see Section 1.4.2), but are more close to the metallicity of the low-redshift IGM. The derived mean hydrogen density of $\langle \log n_{\rm H} \rangle = -2.75$ further supports the idea that the absorbers are part of a diffuse, warm gas phase at low densities, which is associated with the outer parts of galactic halos (Richter 2012). While our sample of absorbers is relatively limited, our results can be compared (and combined) with results from other recent COS studies of metal absorbers at low z to further constrain the physical conditions that are typical for the CGM around galaxies. For instance, Yao et al. (2011) have investigated the IGM/CGM along the 1ES 1553+113 sightline with a detailed look on an absorber at $z \sim 0.1877$. With the detection of several intermediate and high ions these authors tried to apply different Cloudy models to reproduce their observational results, but they conclude that it is quite difficult to establish a satisfying model which complies all requirements. Nevertheless, they constrain ranges for the hydrogen density and the metallicity in the absorber ($\log n_{\rm H} = -4.6$ to -4.7 and $Z = 0.43 - 0.67\, Z_{\odot}$). These values are quite far away from those calculated in this thesis, which probably reflects the fact that they consider mostly high ions such as O VI and N V, which are expected to live in gas with other ionization conditions than intermediate ions such as Si III.

With respect to Si III, Shull et al. (2009); Collins et al. (2009) both have prepared detailed analyses on high-velocity Si III absorption around the Milky Way. Based on *HST*/STIS and *FUSE* data, they analyzed a set of 37 respectively 58 sightlines towards AGNs with up to 90 identified HVC components in case of Collins et al. (2009). Thus, their data set is comparable with our COS data set of intervening Si III absorbers. Shull et al. (2009); Collins et al. (2009) tried to model the typical ionization conditions in their HVC absorbers. In the same way as we did in this thesis, they used the ion ratios of Si II/Si III/Si IV to constrain a best-fitting Cloudy model for the HVCs. They derived a relatively uncertain value for the mean metallicity in their HVC sample from Si III of $\langle \log (Z_{\rm Si}/Z_{\odot}) \rangle = -1.4 \pm 0.3$, which is a bit lower than our result. In both studies the authors suggest that their metallicity estimate is probably too low in view of the fact that Collins et al. (2007) found a substantially higher value of $\langle \log (Z/Z_{\odot}) \rangle = -0.89$ for HVC Complex C. Instead, our mean value for the metallictiy in the intervening

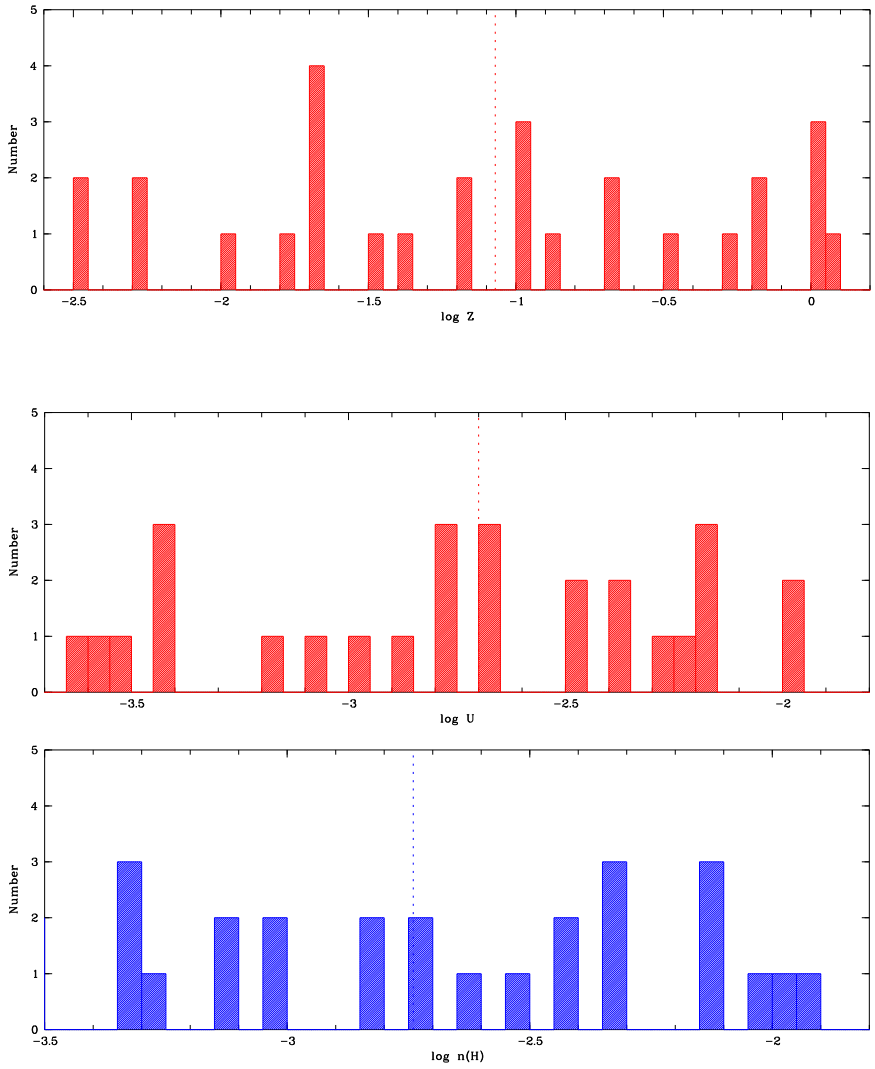

Figure 5.9: **Upper panel:** this panel shows the number distribution of the modeled logarithmic metallicity. The dashed line indicates the median value.
Lower panels: in the middle panel, the distribution for the logarithmic ionization parameter, log U, is plotted, while in the lower panel the number distribution of the logarithmic hydrogen volume density is shown. The dashed lines indicate the median values.

absorbers is relatively close to that found in Complex C, supporting our idea that those Si III systems represent infalling streams of low metallicity gas from the IGM towards galaxies, as it is supposed for Complex C in the Milky Way halo.

Considering the ionization parameter, our results fit very well to the above mentioned previous studies of HVCs. Shull et al. (2009) derived a value of $\log U \approx -3.0 \pm 0.3$, whereas Collins et al. (2009) favoured a model with $\log U \approx -3.1$. Both values are mildly below our result, which is not surprising, as we will explain in the following. We know that most Galactic HVCs reside at distances $\lesssim 15$ kpc from the Galactic disk (except the MS; see Richter 2012). From the analysis of the typical impact parameters of intervening Si III systems later in this section we will see that these systems span a much larger distance range of up to ~ 160 kpc from their host galaxy. From IGM observations we know that the typical ionization parameter for low-redshift absorbers in a diffuse background radiation field is $\log U \approx -2.1 \pm 0.5$ (Danforth and Shull 2008). Thus, we can conclude that our intermediate value of $\log U \approx -2.73 \pm 0.09$ reflects the properties of an absorber population which is spatially more extended than the Galactic HVC population, but which still resides in the circumgalactic environment of galaxies. An additional comparison to an analysis of weak metal absorbers detected in the CGM of the Milky Way can be made. Richter et al. (2009) have analyzed a set of low- and intermediate ions in Milky Way CGM absorbers along six AGN sightlines in detail. Combining their results with ours, one can conclude that the intermediate ions form the connecting gas phase from the inner to the outer regions of the halos of galaxies (see their Figure 6).

In summary, we conclude that there is compelling evidence for a morphological connection between Galactic high-velocity Si III and intervening Si III absorbers at low z. Since both absorber populations have similar ionization parameters, it is likely that they also have similar physical properties. This, together with the large cross section of Si III absorbers compared to galactic disks, implies that many intervening Si III absorbers represent HVC analogs around low-redshift galaxies. To underline this statement, it is also necessary to analyze the relation between these absorbers and their host galaxies. As we will see in the next sections, the expectation is that within a range of ~ 160 kpc the host galaxies of the absorption systems should be detectable.

5.3.3 Discussion of individual sightlines

The following subsection discusses in detail all sightlines that have been used for the ionization modeling. In cases, in which those sightlines have been analyzed in previous studies, we list the corresponding references and provide a comparison between the results.

- **HE 0439−5254**

  Along this sightline, we found two absorbers at $z = 0.3084$ and $z = 0.3282$. Only for the first one in the component at $\bar{v}_{\rm LSR} = -27.3$ km s^{-1} an ionization model makes sense because of the detection of Si III and C III. A problem with this absorber is the very low H I column density compared to the very high Si III column density (note that in the corresponding panel of Figure 6.10 in the Appendix the green Si III dot lies behind that for C III because of identical column densities). There is no Cloudy model than can reproduce such a high Si III column density within a reasonable metallicity range. If we assume a metallicity of 0.1 solar and let C III match in a corresponding Cloudy model, the measured Si III column density is ~ 1.5 dex above the model prediction. Possibly, this line is blended by another intervening absorber and thus the Cloudy model for this system remains inconclusive. All other absorption components along this sightline are not suitable for a Cloudy modeling.

  Keeney et al. (2013) also analyzed this sightline with respect to intervening metal absorption of low- and intermediate ions associated to two nearby galaxies at $z \approx 0.005$ (ESO 157-49) and $z \approx 0.012$ (ESO 157-50). They found possible absorption at impact parameters of $\rho = 93$ kpc and $\rho = 88$ kpc that might be related to these two galaxies, but this conclusion remains uncertain. If we assume that their absorbers are of the same type as those we find for the system at $z = 0.3084$, one can compare the ionization conditions for these absorbers. With their ionization modeling, Keeney et al. (2013) find similar values for the ionization parameter and hydrogen density ($\log U = -2.42$ and $\log n_{\rm H} = -3.66$) as we derive for the absorber at $z = 0.3084$. In contrast to their results, we could not identify any nearby galaxy for this absorber within $\rho \approx 160$ kpc. These authors also come to the conclusion that distant intervening Si III absorbers can be regarded as "transition" objects

between typical Galactic HVCs and the diffuse IGM. Additional information on this sightline can be also found in Stocke et al. (2013).

- **PG 1259+593**

For the system at $z = 0.0461$ we constrain the ionization parameter based on the detection of Si II and Si III in the first component. This approach results in a metallicity of $Z = 0.02$ solar and an ionization parameter of $\log U = -2.8$. Under the assumption that the metallicity is constant in the system (see Section 1.3 or Gibson et al. (2001)), we used this metallicity to estimate U for the other components, where only Si III was detected. The resulting parameters are listed in Table 6.6. Interestingly, we find a galaxy at an impact parameter of $\rho \approx 138$ kpc to this absorber. Thus, this case fits very well in our generalized model of intervening Si III absorbers.

For the absorber at $z = 0.2195$, the metallicity drops down to $Z = 0.005$ with still underabundant Si III. This means that the high H I column density compared to the column density of the metal ions forces Cloudy to reduce the metallicity down to this limit.

In general, this sightline has been widely studied during the last decade (see for instance Richter et al. 2004; Fox et al. 2004; Richter et al. 2006; Shull et al. 2011, and many others). Most of these studies concentrate on Galactic HVC absorption, since this sightline passes the HVC Complex C. Richter et al. (2004) have combined *FUSE* and STIS data to analyze the WHIM along this sightline. They found 72 intervening absorption systems with eight being metal systems that have been confirmed with the detection of Si III, C III, O III, C IV, and other ions. For the system at $z = 0.0461$ they derived very similar column densities for Si III and C IV, but they also mention that there might be unresolved substructures. For the system at $z = 0.2195$ we found almost the same column density for the main component in H I and Si III and a similar Doppler parameter. Richter et al. (2004) modeled the system with Cloudy using the ratio O III/O VI. They derived an ionization parameter of $\log U = -1.5$, which is a bit higher than our result ($\log U = -2.2$). They also come to the conclusion that one need more high-resolution data to resolve the complex sub-structure of the absorbers along this sightline.

- **HE 0226−4110**

For this sightline we produce two Cloudy models for the absorber at $z = 0.2071$: a first one for component at $\bar{v}_{\rm LSR} = -25.0$ km s^{-1} and a second one for the component at $\bar{v}_{\rm LSR} = 1.0$ km s^{-1}. Both components contain a relatively small amount of H I with column densities on the order of $\log N({\rm H\,I}) = 15.0$. The differences between the C III and Si III column densities can be fit best to a Cloudy model with a metallicity of $Z = 0.1$ solar and ionization parameters of $\log U = -2.2$ and -2.3, respectively.

Savage et al. (2011a) has presented an extensive study of this absorption system, which continues the earlier work done by these authors on this system (Savage et al. (2005)). With the help of COS data, they are able to identify a broad Lyman α absorber that is responsible for the O VI and Ne VIII absorption. Savage et al. (2011a) find neutral hydrogen column densities that are similar to those derived in this thesis ($\log N({\rm H\,I}) \approx 15.1$) but their derived total hydrogen volume density is a factor of ~ 10 lower. Furthermore, they point out that the detection of high ions suggest the existence of collisionally ionized gas, which complicates the determination of the ionizing conditions. Savage et al. (2011a) identify three possible foreground galaxies with $L = 0.25\,L^*$, $L = 0.25\,L^*$, and $L = 0.05\,L^*$ which might be the host galaxies of this absorber. Nevertheless, it remains difficult to claim a secure affiliation to these galaxies and more high quality data are required to further investigate these issues.

- **HE 0153−4520**

The sightline towards HE 0153-4520 is a more complex one because of the additional detection of low ions such as Si II, C II, and N II in the considered absorber at $z = 0.2260$. We have generated Cloudy models for the components at $\bar{v}_{\rm LSR} = -39.0$ km s^{-1}, $\bar{v}_{\rm LSR} = -28.3$ km s^{-1}, $\bar{v}_{\rm LSR} = -15.5$ km s^{-1}, $\bar{v}_{\rm LSR} = 7.2$km s^{-1}, and $\bar{v}_{\rm LSR} = 30.2$ km s^{-1}. For the first component, a very solid solution with $\log U = -3.4$ and $Z = 0.07$ is determined. For the second component the metallicity is slightly higher ($Z = 0.13$ solar) with an ionization parameter of $\log U = -2.8$. For the third

and fourth component the very high C III column density turns out to be very problematic. Due to saturation it is not possible to resolve the individual components for C III, and, therefore, the column density determination for the individual components are highly uncertain. Hence, we tried to include the other ions to the predictions of Cloudy. However, the results for the metallicity and the ionization parameters remain afflicted with large systematic uncertainties.

For a comparison with previous results we refer to the paper of Savage et al. (2011b), who prepared a detailed study of the absorber at $z = 0.2260$. They found similar values for $\log U$, $\log n_{\rm H}$, and Z and had a more detailed look on the highly ionized gas seen in O VI absorption. These authors speculate that parts of the high-ionized gas may trace the hot halo of a foreground galaxy, whereas the weakly ionized metals might be related to a circumgalactic tidal-tail structure like the Magellanic Stream in the MW.

- **3C 263**

This sightline is also a very complex one. With the detected ions we could set up four different Cloudy models. For the first and second one for the components at $\bar{v}_{\rm LSR} = -70.0$ km s^{-1} and $\bar{v}_{\rm LSR} = -1.0$ km s^{-1} in the system at $z = 0.0635$ we achieved ionization parameters of $\log U = -2.6$ and -2.8, respectively. The metallicities differ around one order of magnitude, which is also the case for the H I column densities. This could indicate, for instance, that the sightline passes different regions of a cloud, e.g., a metal-rich core region and a low-metallicity outer shell. However, because of the strong saturation of the H I Ly$\,\alpha$ absorption it remains unclear which component is the one that carries most of the neutral gas. The detection of Si II in the second component suggests that this component traces the inner part of the cloud, where the gas is more dense and cold and thus silicon can exist in the form of singly-ionized silicon. For the two Cloudy-modeled components at $z = 0.3256$ the first one could be reproduced very well, whereas for the second one some problems occur due to the low H I column density. Because of the detection of intermediate ions in C, Si, and N, these components characterize a "typical" diffuse intervening metal absorber without a shielded inner core region where low ions are stable. Nevertheless, also in this case it is required to measure the exact distribution of the H I column density within the absorber to produce a reliable Cloudy model.

For comparison, Narayanan et al. (2012) have also analyzed the absorber at $z = 0.3256$ in detail using COS data. They identify the same ions as we do but with the addition of O VI and Ne VIII (which we generally ignore in this study). Similar as in our study, these authors assume at least two components with a possibly more complex substructure. For the ionization conditions they used almost the same neutral hydrogen column density of $\log N({\rm H\,I}) = 15.1$. Their result for the ionization parameter as well as the hydrogen volume density ($\log U = -2.2$ and $\log n_{\rm H} = -3.3$) is in very good agreement with our results ($\log U = -2.3$ and $\log n_{\rm H} = -3.34$). Furthermore, they also speculate that the multiphase character of this absorber might be analogous to the highly ionized HVCs that can be detected around the MW. For more information on this sightline see also the study of Savage et al. (2012). This team focused on the O VI absorption in the absorber at $z = 0.0635$ and find similar ionization conditions than we did in this thesis. They argued that it is very likely that this absorber is linked to a close-by spiral galaxy which has an impact parameter of ~ 63 kpc. They also analyzed another highly ionized absorber at $z = 0.1407$ which we do not consider in this study.

- **RXJ 2154.1−44414**

The sightline towards RX J2154.1−4414 contains only one prominent metal absorber at $z = 0.0622$. In general, it seems that the highly ionized species like Si IV, C IV, and N V are more dominant in this system compared to other absorbers. Even the strong Si III transition is not very well-defined in this system. Nevertheless, in the middle component C II is visible, which is indicative for a more dense, compact core region. The Cloudy model for this component suggests a supersolar metallicity of $Z = 1.2$ solar, which appears very high for an intervening metal system with no associated galaxy nearby (see discussion in previous section). We did not find any other study that presents an analysis of this sightline.

- **SBSSG 1122+594**

  Along the sightline towards SBSS G1122+594 we identify three different absorption systems at $z = 0.0602$, $z = 0.1944$, and $z = 0.3124$. Si III (and partly C III) absorption is clearly detected. A general problem for the modeling of these absorbers are the partly very low H I column densities, which lead to rather high metallicities in the Cloudy models (see Table 5.5). More accurate spectral data (with high spectral resolution) would be required to better resolve the sub-component structure in these absorbers and to yield the information necessary to improve our Cloudy models, which currently rely only on the above mentioned two ions.

  Stocke et al. (2013) included this sightline in their study of a larger sample, which they analyzed as part of a detailed search for nearby galaxies that have associated metal systems. In contrast to our study, they claim the detection of an absorption system at $z \approx 0.004$ with an associated galaxy at $\rho \approx 32$ kpc, but made no statement on the other absorbers along this sightline. In their discussion, these authors state that, despite a huge covering factor of those warm CGM absorbers, they believe that only a small fraction of these objects would represent distant HVC analogs. We do not agree with this statement.

- **PG 0838+770**

  Assuming that depletion effects for Si III are unimportant, the ionization parameter for the system at $z = 0.0024$ towards the Seyfert 1 galaxy PG 0838+770 is well defined in our study. We derive $\log U = -2.7$ at a metallicity of $Z = 0.06$ solar. Due to the relatively high H I column density of $\log N(\mathrm{H\,I}) = 16.8$ there exist no other valid Cloudy solutions that would reproduce the column densities of C II and Si III.

  In the same way as the previous sightline, this one is included in the sample of Stocke et al. (2013). They identified the same absorber as well as the same associated galaxy. Their ionization parameter is in very good agreement with our results, but they derive a ~ 10 times higher metallicity. This difference possibly arises from systematic errors in the model setup or might just be an effect of the high uncertainty of this parameter within the Cloudy model. This sightline is also part of the extensive study of Wakker and Savage (2009), who analyzed the relationship between intergalactic H I/O VI absorption and nearby galaxies.

- **HS 1102+34**

  For this sightline, the most striking aspect is the unusually high C III column density in the absorber at $z = 0.2388$. As shown in the corresponding panel of Figure 6.8, C III absorption is saturated in all components, and, therefore, the column density determination is highly uncertain. The apparent carbon absorption clearly shows damping wings, which possibly suggests that intervening C III at $z = 0.2388$ is blended by H I Ly α absorption from another intervening system. We therefore focused on the component structure seen in Si III and N III absorption and also for the Cloudy models the saturated/blended C III absorption was not considered. Without C III, the system can be modeled as a two-component absorber with a very low metallicity of $Z = 0.003 - 0.005$ solar with consistent ionization parameters. For the second system at $z = 0.3102$ we derive a higher metallicity of $Z = 0.3$, which has to be regarded as a lower limit, as depletion for Si III is neglected.

  This sightline was studied by Shull et al. (2012b), who concentrated on the ionizing flux from background AGNs. We are not aware of any other studies that focused on the analysis of the intervening metal absorbers along this line of sight, so no further comparison can be made.

- **PHL 1811**

  In the last sightline discussed here, many weakly ionized metals are detected in one remarkable intervening system at $z = 0.0807$. This absorber has two main absorption components at $\bar{v}_{\mathrm{LSR}} = 10.6$ km s^{-1} and $\bar{v}_{\mathrm{LSR}} = 62.8$ km s^{-1}. Both components have very high H I column densities (in the range typical for LLS), which explains the presence of many low ions due to the self-shielding in the cloud core. The Cloudy modeling suggests that both components may be very different in metallicity and ionization conditions. In both cases, we use the Si II/Si III ratio to define the modeling parameters. In the first component, there is good agreement also in Fe II,

Table 5.7: Parameters used for the radius calculation

parameter	value
$\bar{z}_{\rm abs}$	0.255
H_0	67.11 km s^{-1}Mpc^{-1}
$\Omega_{\rm m}$	0.317
Ω_Λ	0.683
$H(z)$	76.80 km s^{-1}Mpc^{-1}
$n_{\rm g}(0.01\ {\rm L}^*)$	0.0903 Mpc^{-3}
$n_{\rm g}(0.05\ {\rm L}^*)$	0.0107 Mpc^{-3}

but in the second component Fe II and N II are substantially overpredicted in the model, whereas C II is underabundant (assuming that Si II/Si III is tracing one and the same phase). Also the metallicities come out very different (see Table 5.5), possibly indicating that both components belong to two spatially distinct clouds with very different properties. This idea is supported by the clear separation of both components in velocity (except for H I), which is strongly saturated. Note that there are at least two galaxies close to this absorber with impact parameters of $\rho = 36$ kpc and $\rho = 93$ kpc. The absorption towards PHL 1811 could very well trace the halos of these galaxies.

This sightline has been studied intensively over the last decade (e.g., Richter et al. (2011); Tilton et al. (2012); Stocke et al. (2013)). A very detailed investigation of the absorber at $z = 0.0807$ is presented by Jenkins et al. (2005). They used *HST*/STIS and *FUSE* data to analyze the abundance of various atomic species and the ionization conditions. They favour an ionization parameter in the range of $-4.4 < \log U \leq -3.6$, which is in very good agreement with our result for the component at negative velocity ($\log U = -4.0$). On the other hand, for the second component we found a very different value of $\log U = -2.0$. This discrepancy might be caused by the different modeling approach: we used the Si II/Si III ratio as main model input, whereas Jenkins et al. (2005) basically focussed on low ions like N II, Si II, and O I. Nevertheless, they note that their modeling results may be affected by systematic errors (e.g, from the choice of certain ions for the model input). Indeed, to explain the presence of intermediate ions like Si III a higher ionization parameter than the one presented by Jenkins et al. (2005) would be required.

5.4 Statistical Halo Radii

In Chapter 4 we have investigated the CGM of the Milky Way with a particular focus on HVCs, their properties, and the connection between HVC Si II absorption and intervening weak/strong Mg II absorbers at low redshift. It is now possible to combine the results of the measured HVC covering fractions, $f_{\rm c}$, with our measurements of intervening Si II and Si III from the COS data to gather new information about the typical statistical radius of the metal-absorbing gas halos of galaxies in the local Universe.
If we solve Equation 1.1 for $R_{\rm h}$ (see Section 1.4.3), we obtain:

$$R_{\rm h} = \sqrt{H_z \cdot \frac{{\rm d}\mathcal{N}}{{\rm d}z} \cdot \frac{1}{n_{\rm g}\langle f_c \rangle c\pi}}. \tag{5.4}$$

Now it is possible to combine the results on the space density of galaxies, $n_{\rm g}$, the number density ${\rm d}\mathcal{N}/{\rm d}z$ with the mean covering fraction of individual ions in galaxy halos (outside view) to estimate a statistical halo radius for galaxies at low z (Kacprzak et al. 2008). This has been already done for low ions like H I 21cm, Mg II, and Ca II (Thilker et al. 2004; Kacprzak et al. 2008; Richter et al. 2011). These authors have derived values for the above mentioned ions ranging from $R_{\rm h}$(Ca II) ~ 55 kpc, $R_{\rm h}$(H I 21cm) ~ 60 kpc up to $R_{\rm h}$(Mg II) ~ 91 kpc. Note that here a luminosity scaling has to be considered and that these values are only valid for $L \geq 0.05L^*$ galaxies. As one can see, the statistical halo radius increases for Mg II because of the higher sensitivity for neutral *and* ionized gas. Thus, the expectation for the intermediate ions Si III and C III, which have been investigated in this thesis, is that the typical halo radius for these ions is substantially larger than that for Mg II and Ca II, i.e., $R_{\rm h}$(Si III) ≥ 100 kpc.

In Table 5.7 a summary of the parameters used here is presented, which will be explained in the following. For the total COS sample, that has been investigated by us (58 sightlines, 77 absorbers), the mean redshift is $\bar{z}_{\rm abs} = 0.255$. Using the equation $H(z) = H_0(\Omega_m(1+z)^3 + \Omega_\Lambda)^{1/2}$ and the most recent

Table 5.8: Estimated halo radii in kpc for different parameters

L	f_c	$d\mathcal{N}/dz$(Si II)			$d\mathcal{N}/dz$(Si III)			$d\mathcal{N}/dz$(C III)		
		0.87	1.19	1.25	2.35	2.47	2.57	3.01	2.93	3.12
	0.2	63	73	75	103	106	108	117	115	119
	0.4	44	52	53	73	75	76	82	81	84
0.01 L*	0.6	36	42	43	59	61	62	67	66	69
	0.8	31	37	38	52	53	54	58	58	59
	1.0	28	33	34	46	47	48	52	51	53
	0.2	182	213	218	299	308	313	339	334	345
	0.4	129	151	154	212	217	221	239	236	244
0.05 L*	0.6	105	123	126	173	177	181	196	193	199
	0.8	91	106	109	150	153	156	169	167	172
	1.0	81	95	98	134	137	140	151	149	154

cosmological parameter estimates of $H_0 = 67.11\ \mathrm{km\,s^{-1}\,Mpc^{-1}}$, $\Omega_m = 0.317$, and $\Omega_\Lambda = 0.683$ (Planck Collaboration et al. 2013) we derive $H(z) = 76.8\ \mathrm{km\,s^{-1}\,Mpc^{-1}}$ for the redshift-dependent Hubble parameter. For the space density of galaxies, n_g, we use the value $n_\mathrm{g} = 0.0107\ \mathrm{Mpc^{-3}}$ for $L \geq 0.05L^*$ galaxies and $n_g = 0.0903\ \mathrm{Mpc^{-3}}$ for $L = 0.01L^*$ galaxies based on the results of Faber et al. (2007) and Richter et al. (2011). Here, one has to add that the shape of the galaxy luminosity function is still a matter of debate and afflicted with systematic errors. Therefore, the used values of n_g have to be taken with caution, as they are different from the ones used in other studies (see for instance Zaninetti 2008; Jaacks et al. 2012; Bian et al. 2013). Moreover, we use the values derived for the redshift dependent number density $d\mathcal{N}/dz$ for Si III estimated in Section 5.2.3 combined with a 0.2 dex graduation in the covering fraction for a better demonstration of the evolution of R_h in the $0.05L^*$ and $0.01L^*$ cases.

In Table 5.8 the results for $L/L^* = 0.05$ and $L/L^* = 0.01$ galaxies are shown. Apart from the differences because of the luminosity scaling one can clearly see the $R_\mathrm{h} \sim \sqrt{\frac{d\mathcal{N}/dz}{f_c}}$ dependency of the results. If we assume $d\mathcal{N}/dz(\mathrm{Si\ III}) = 16.6$, as derived by Tilton et al. (2012), this would lead to $R_\mathrm{h}(0.05L^*,\ f_\mathrm{c} = 0.8) = 397.66$ kpc and $R_\mathrm{h}(0.01L^*,\ f_c = 0.8) = 136.87$, thus values near and clearly beyond the virial radius of Milky Way-type galaxies. For H I, these authors derive $d\mathcal{N}/dz$(H I, > 10mÅ) $= 283.9$, which would imply $R_\mathrm{h}(0.05L^*,\ f_\mathrm{c} = 0.8) = 1.64$ Mpc if the H I absorbing gas would be distributed around galaxies. Most of the weak H I absorbers that do *not* show associated metal absorption are expected to reside in the network of cosmological filaments far away from galaxies, so that the derivation of R_h for H I from $d\mathcal{N}/dz$(H I) alone does not provide meaningful insights into the neutral gas distribution around galaxies. From 21cm measurements of the CGM of M31 Thilker et al. (2004) find $R_\mathrm{h}(0.05L^*) = 60$ kpc for H I. As can be easily seen, the covering fraction f_c clearly triggers the estimated halo size for each ion. If we use the value $f_\mathrm{c}(\mathrm{Si\ III}) = 0.7$ derived from the STIS HVC data in this thesis, combined with the determined number density $d\mathcal{N}/dz = 2.35$, we derive $R_{\mathrm{h,SiIII}}(0.05L^*) \approx 160$ kpc and $R_{\mathrm{h,SiIII}}(0.01L^*) \approx 55$ kpc. On the other hand, the gas distribution around brighter galaxies can be tested directly with the search for galaxies that are close to the line of sight along which intervening metal absorbers are identified. This will be further discussed in the next section. Relying on the results presented above, one would expect that most of the intermediate absorbers are located within $150 - 200$ kpc from their host galaxies (i.e., most of them are located within the virial radius of their host galaxies).

5.4.1 Absorber-galaxy connection

As mentioned above, one interesting key question regarding the nature of intervening metal absorbers concerns their connection to nearby galaxies. The absorber-galaxy connection has gained a lot of attention during the last decade, in which our understanding of the IGM, CGM, and the WHIM has improved considerably. For the warm-hot component of the IGM and CGM (i.e., for gas with temperatures $T > 10^5$ K), thermally broadened Lyα lines (Lehner et al. 2007) as well as highly ionized species like O VI and Ne VIII have been studied in great amount and detail (e.g., Tripp 2008; Savage et al. 2005). Despite a well established picture of the frequency and distribution of these absorbers, their origin and their importance for the evolution of galaxies is still a matter of debate. Since the 1950s there have been predictions (and observations) that indicate that hot, diffuse gas should be located in the inner

and outer halos of galaxies and in the filamentary network of the IGM (e.g., Spitzer 1956). Thus, there is consensus that, for instance, O VI is a very good tracer for the various processes that transport highly ionized metals into the CGM and IGM and the conditions in these environments (Oppenheimer and Davé 2009). It yet remains unclear whether O VI is more likely to trace the WHIM phase (collisionally ionized) or a cooler photoionized phase (e.g., Tepper-García et al. 2011; Draganova 2013).

Similar considerations concern also the nature of intervening Ly α absorbers. These systems have been the first ones that have been analyzed systematically together with a parallel search for nearby galactic systems to characterize their connection to the overall large-scale structure (Morris et al. 1993; Spinrad et al. 1993). Moderate to strong Ly α absorption is found in the CGM around galaxies at a high covering fraction at impact parameters of $\rho \lesssim 250$ kpc, which points towards a widespread presence of diffuse, ionized circumgalactic gas even beyond the virial radius of galaxies (Wakker and Savage 2009). Such studies have beend extended also to higher redshifts ($z \sim 1$), implying a significant clustering between strong Ly α absorbers (defined as absorbers with $\log N(\mathrm{H\,I}) > 15$) and galaxies (Shone et al. 2010). The fact that weak Lyα absorbers do not show such a strong correlation with galaxies implies that these systems represent a different class of objects with other properties (i.e., they trace gas in cosmological filaments on much larger scales).

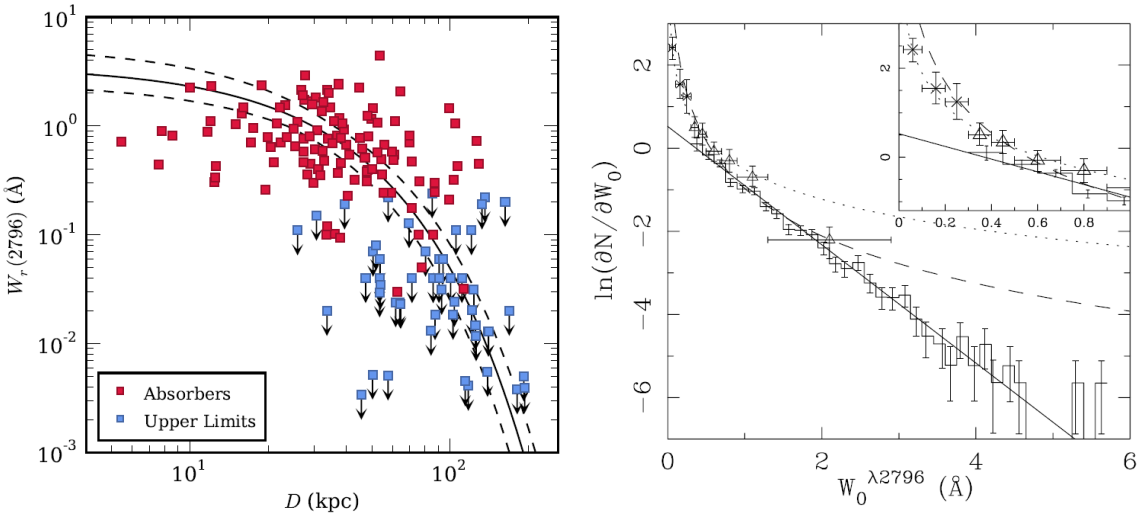

Figure 5.10: **Left**: sample of 169 Mg II λ2796 systems from the MAGIICAT II catalog; plotted is the rest-frame equivalent width, $W_\mathrm{r}(2796)$ versus the impact parameter (here: D). The solid line shows a log-linear maximum likelihood fit, $\log W_\mathrm{r}(2796) = \alpha_1 \mathrm{D} + \alpha_2$ with 1σ uncertainties (dashed curves) and $\alpha_1 = -0.019 \pm 0.002$ and $\alpha_2 = 0.28 \pm 0.11$ (Nielsen et al. 2013).
Right: $W_\mathrm{r}(2796)$ distribution, with a closer look to the $W_\mathrm{r}(2796) < 1.0$ Å region. The power-law fit (dottet line) clearly overpredicts the appearance of strong systems, whereas the exponential fit (solid line) underpredicts the weak ones. This may be an indication of two distinct populations of Mg II absorbers (Nestor et al. 2005).

In the same way as for Ly α absorber, the occurrence of metal absorption in intervening systems has been analyzed with particular focus on the absorber-galaxy connection. Yet, partly because of instrumental and observational restrictions, the main focus of these studies was either low ions like Mg II (see Section 1.4.4) or high ions like C IV, O VI, and Ne VIII (see Section 1.4 and section above). Similar to the results for Ly α, these metal ions show a large variety of (impact-parameter dependent) absorber-galaxy relations. For instance, several studies imply $\rho \lesssim 35$ kpc for strong Mg II absorbers, $\rho \lesssim 200$ kpc for C IV, and $\rho \sim 200 - 300$ kpc for O VI (see Chen et al. 2001; Prochaska et al. 2011, and Figure 6.1). Stocke et al. (2006) have shown that within $\rho = 800$ kpc of all their 23 O VI absorbers in their sample an L^* galaxy can be found. From this follows, for instance, that O VI absorbers are strongly correlated with galaxies and are (typically) not expected to arise in galaxy voids. Tumlinson et al. (2011) found a possible connection between the O VI column density and the specific star formation rate of the host galaxy. It is also evident that the absorber properties depend strongly on the luminosity of the host galaxy. However, there are also several examples with non-detections even for small impact parameters (Prochaska et al. 2011). Therefore, the overall picture on the gas distribution around galaxies is yet incomplete and future studies are desired to further explore the relation between intervening metal absorbers and galaxies also for other highly (and lowly) ionized species.

Table 5.9: Associated galaxies for the subsample sightlines

QSO Sightline	z_{abs}	Galaxy $\Delta z \lesssim 0.005$	impact parameter [arcsec]	[kpc]	z (galaxy)
PG 1259+593	0.0461	SDSSJ130101.06+590006.9	151.16	153.52	0.0473
		SDSSJ130101.05+590007.1	150.62	149.04	0.0462
HE 0226-4110	0.2071	HE 0226-4110 13101	9.89	42.00	0.2065
		HE 0226-4110 09251	30.92	132.10	0.2078
3C 263[1]	0.0635[1]	-	51.50[1]	63.00[1]	0.0632[1]
PG 0838+770	0.0024	UGC 4527	134.21	6.96	0.0024
PHL 1811	0.0807	2MASS J21545996-0922249	23.02	39.51	0.0808
		2MASS J21545870-0923061	58.81	100.45	0.0804

[1]: values taken from Savage et al. (2012)

In summary, there is compelling evidence for a highly complex multi-phase CGM that surrounds low-redshift galaxies. As described above, most of the recent studies have focussed on either highly or lowly ionized species and thus there seems to be a gap in the investigation of the absorber-galaxy connection in intermediately ionized species such as Si III and C III. At this point, this thesis provides new results and constraints that help to improve our understanding of the CGM and the absorber-galaxy connection.

In Table 5.9 we present results for the absorber-galaxy connection of the COS subsample based on a direct search of nearby galaxies with small angular separations from the COS sightlines. For this, the Simbad online database[1] was used, which provides the necessary information on the galaxy positions and redshifts. The impact parameters have been calculated using the conversion of the redshift into a comoving distance based on an online available cosmological calculator[2] together with the ΛCDM parameters described in Section 2.1 (Wright 2006, see Section 2.1.1). To ensure sufficient accuracy of the values derived with this tool, we tested it on more than 10 examples for galaxy distances published in Wakker and Savage (2009). The distance values agree typically within 5%. The final table can be found in the Appendix section. An excerpt for the COS subsample is presented in Table 5.9, where clearly identified galaxy/absorber pairs for the subsample are listed. The final table (Appendix) contains all known galaxies within $\Delta z \lesssim 0.005$ to the associated absorbers for the whole COS sample with the only limitation being the angular distance ($\varphi \lesssim 30$'). Based on the considerations given above, one would expect to find intervening Si III and C III absorbers within a radius of $\rho = 160$ kpc of their host galaxies ($> 0.05L^*$), typically. If we use this value as a cut-off criterion, we find associated galaxies in 34.6% (27/78) of all cases. If we increase the cut-off radius to $\rho = 220$ kpc, this fraction increases to 37.2% (29/78), whereas a cutoff radius of $\rho = 100$ kpc results in a decrease of the fraction down to 20.5%. Consequently, an increase of the considered impact parameter of 38% will result in an additional increase of the galaxy-connected absorber population of only ~ 3%, whereas a decreasing impact parameter apparently forces a drop of ~ 14% in the fraction. This trend indicates that the majority of the intermediate Si III and C III absorbers are typically located within $\rho = 160$ kpc of their host galaxies. This result fits very well into the above discussed picture of the complex multiphase CGM and matches the findings concerning the statistical absorber radii presented in Section 5.4. Referring to fainter galaxies ($L \sim 0.01L^*$), one has to admit that, because of detection limits and missing redshift determinations, their relation to interveing metal absorbers needs to be explored in future studies.

5.5 Conclusions

In this chapter, we have analyzed publicly available *HST*/COS UV spectral data of 47 AGNs. In these spectra, we searched for intervening metal absorption with a focus on the lines of Si II, Si III, and C III. All in all, we detect 78 individual metal absorbers in ~ 65% of all sightlines at a mean absorption redshift of $\langle z \rangle \approx 0.25$. The detected intervening absorbers have been fitted with the `Fitlyman` package implemented in the ESO-*Midas* program to derive column densities, Doppler parameters, and information about the absorption component structure. In most of the detected absorbers we could identify only one or two velocity components, possibly a result of the limited spectral resolution in the COS data.

[1] `http://simbad.u-strasbg.fr/simbad/`
[2] `http://www.astro.ucla.edu/~wright/CosmoCalc.html`

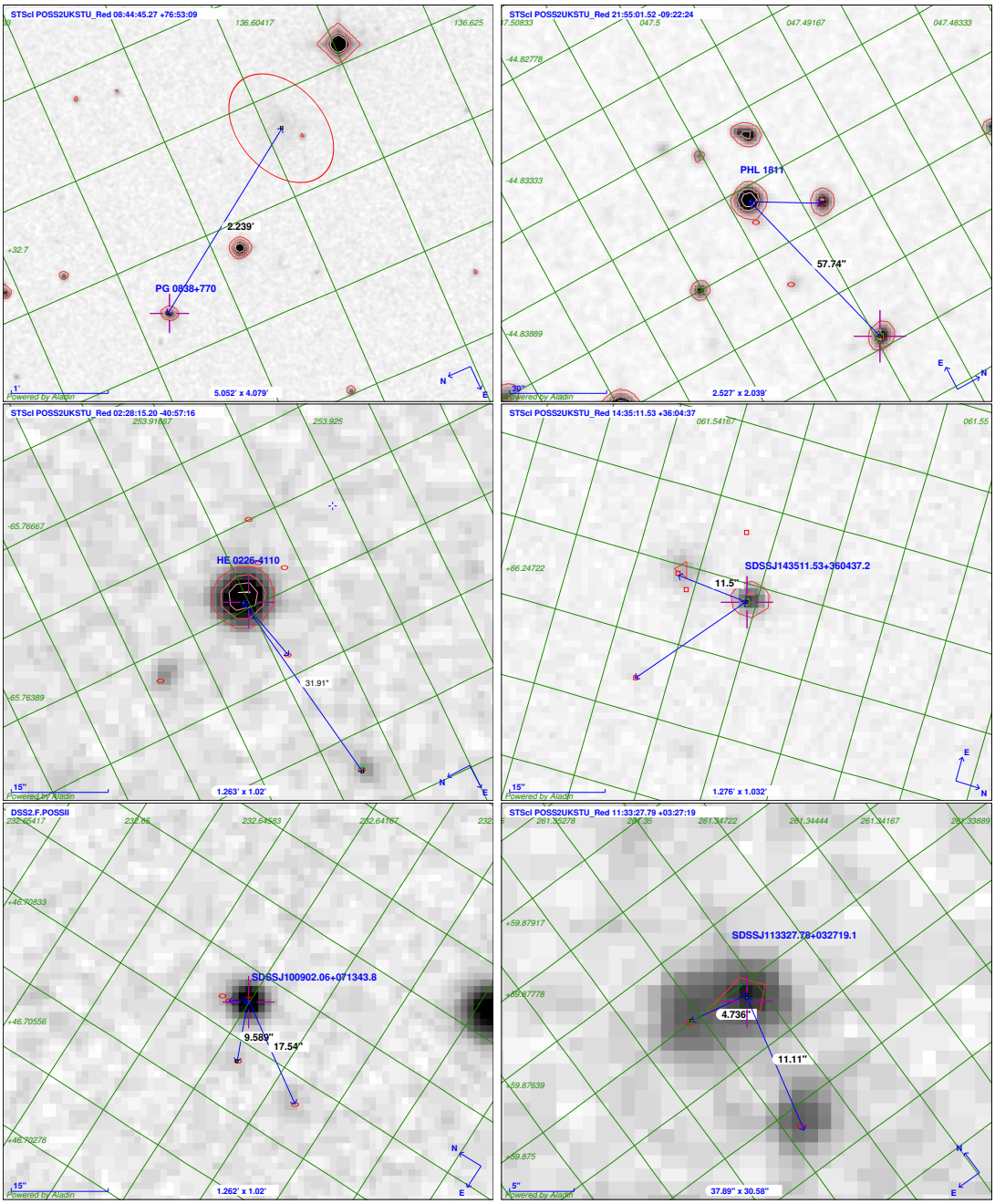

Figure 5.11: Six examples of galaxy-absober pairs. The background AGN is labeled in blue with the arrows pointing towards the associated foreground galaxies where intervening metal systems can be found.

Referring to the H I column density in the absorbers, we find evidence for a bimodal column-density distribution with a separation at $\log N(\mathrm{H\,I}) \approx 17.0$. Combining our results with data from other studies, we suggest the presence of a characteristic H I $\leftrightarrow$ H II transition phase in intervening metal absorbers, which might be responsible for the plateau in the H I column-density distribution function (CDDF). Furthermore, we suggest that these two absorber populations (at least partly) represent the distant analogs of the Galactic high-velocity clouds (HVCs).

In Section 5.2.3, we have analyzed the redshift coverage of our data sample as well as the absorber statistics. We find a slight accumulation of absorbers at $z = 0.2 - 0.3$, which reflects the redshift coverage of the COS data for the above listed ions. We have calculated the number density of the intervening absorbers at low z for different equivalent-width limits and prepared a CDDF for each of the ions of interest. We then have compared the properties of the metal absorbers with the properties of the Galactic HVC absorbers obtained from the *HST*/STIS analysis presented earlier in this thesis. Interestingly, we find a plateau in the CDDF for Si II for the intervening absorbers, similarly as found for Si II in Galactic HVCs. This trend is also visible in Si III and C III. We suggest that these similarities in the shape of the CDDFs indicate characteristic physical conditions (i.e., typical H I optical depths, gas densities, ionizing radiation fields) in the absorbers that are responsible for the observed plateaus and that deserve further attention in subsequent studies. The slopes for the CDDFs that we derived from our analysis are in good agreement with the results from other groups. Moreover, for Si II we derive $\beta = 1.55 \pm 0.22$, a value that is very close to the one derived earlier in this thesis for Galactic HVCs. We regard this as further evidence for a morphological connection between intervening metal absorbers at low z and Galactic HVCs. With the conversion of the Si II column densities of the intervening systems into corresponding values for Mg II we find that these Si II systems belong typically to the class of the so-called weak Mg II absorbers. This would imply that Si II traces CGM regions with typical impact parameters $\rho \leq 100$ kpc from their host galaxies. In the analysis of the Si III and C III absorbers we have demonstrated that for Si III the column densities are in the same range as for Si III in Galactic HVCs. Note that also other studies have discussed the possible connection between intervening metal systems (with relatively low H I column densities) and high-velocity Si III absorbers in the Milky Way halo.

Because of the limited data quality in most of the COS spectra we have selected a suited subsample with data of sufficient quality for a more detailed analysis of the ionization conditions. For the resulting set of 12 sightlines we used the component-modeling technique to re-analyze the component structure in the absorbers and to constrain columnn densities and Doppler parameters in the individual subcomponents. We then set up photoionization models with Cloudy for each component to derive ionization parameters, hydrogen volume densities, and metallicities. We find a large spread in these parameters with mean values of $\langle \log U \rangle = -2.73 \pm 0.09$, $\langle \log n_{\mathrm{H}} \rangle = -2.75 \pm 0.10$, and $\langle \log Z/Z_{\odot} \rangle = -1.07 \pm 0.15$. Most of the systems ($\sim 75\%$) have metallicities < 0.4 solar, which is in good agreement with the theoretical expectations for mildly ionized extended gaseous halos of galaxies at low z. Comparing our results with those derived for Galactic HVCs, we conclude that also the ionization conditions in intervening Si III systems fit into the picture that many of these absorbers represent HVC analogs. The derived range for the ionization parameter, in particular, supports the idea that Si III systems predominantly trace the diffuse interface region between the inner (more neutral) halo regions (and the disk-halo interface) and the hot coronal gas and extended circumgalactic gas regions around low-redshift galaxies.

In the final part of this chapter we have discussed the connection between intervening metal absorbers and their host galaxies. Using the derived number density of absorbers we computed a grid of typical halo radii for the ions Si II, Si III, and C III. For this, we combined the number-density measurements with the covering fractions for high-velocity Si III ($f_c = 0.7$) in the Galactic halo as obtained earlier in our *HST*/STIS analysis. This leads to a characteristic impact parameter for Si III of $\rho = 160$ kpc around $L \geq 0.05L^*$ galaxies. This result can be compared with direct estimates for absorber impact parameters using galaxy catalogs. We have searched for galaxies close to the metal systems in our COS sample with redshift deviations $\Delta z \lesssim 0.005$ between the galaxies and the absorbers. We find that for 34.6% of the absorbers a possible host galaxy is found within a radius of $\rho = 160$ kpc. In summary, we conclude that $\rho \leq 160$ kpc indeed represents a characteristic range for the impact parameters of intervening Si III absorbers at low redshift. This range indicates the characteristic spatial extent of the metal-enriched CGM around the local galaxy population at luminosities $\geq 0.05L^*$.

Chapter 6

Discussion and Summary

6.1 Discussion

In this thesis, new results on the local HVC population and intervening metal absorbers (regarded as HVC analogs) have been presented. In total, more than 100 individual sightlines towards extragalactic background AGNs have been analyzed and the absorber properties have been studied via Voigt-profile fitting and component modeling.

In the first part of this thesis (Chapter 4), the neutral and weakly ionized gas clouds in the Milky Way halo (i.e., HVCs) have been studied based on the analysis of 47 *HST*/STIS sightlines. In the second part of the thesis (Chapter 5), HVC analogs in the halos of more distant galaxies have been studied in absorption towards 57 background sources using *HST*/COS spectral data.

It is nowadays widely accepted that HVCs (and their distant analogs) play an important role in our understanding of gas inflow and outflow processes in galaxies and their connection to the IGM. Using absorption spectroscopy, we have investigated the absorption properties of halo absorbers, to link for the first time the statistics of Galactic HVC absorbers with intervening metal absorbers at low redshift, as such absorbers are believed to arise in halos and circumgalactic environment of other galaxies. In the following, we discuss the implications of our findings for our understanding of metal-absorbing gas structures in the halos of galaxies in the local Universe.

6.1.1 HVC absorption-line statistics

In Chapter 4, 47 *HST*/STIS sightlines have been analyzed to achieve information about column densities, Doppler parameters, covering fractions, and the component structure of Galactic HVCs. From the HVC detection rate of 28/47 we derive an overall HVC covering factor of 59.6%, which is in excellent agreement with the results from Lehner et al. (2012) based on a $\sim$ 3 times larger number of sightlines. These authors have also shown that there is a lack of HVC absorption for high galactic latitudes ($b > 75$ deg), which can also be seen in the data presented in this thesis (see Figure 4.1). This trend can be interpreted in different ways. On the one hand, if one assumes that the HVCs follow a disk-like distribution, it is expected that there are less HVCs at high latitudes. On the other hand, the lack of high-latitude HVCs could be a result of the smaller solid angle that is covered by observations at those high latitudes (Lehner et al. 2012). Clearly, for a more complete picture of the overall sky distribution of HVCs more absorption-line data, that also cover the polar regions, are required. Additionally, Lehner et al. (2012) suggest that the HVC covering fraction, f_c(HVC), is independent of the equivalent width limit in the used data set, i.e., f_c(HVC) remains roughly unchanged with increasing resolution power or decreasing $W_{\rm lim}$. From our analysis we find that, depending on the ions studied, the covering fractions vary between 0.20 (Si IV) and 0.70 (C II), implying that such a general statement must be taken with caution, as the physical conditions in HVCs vary substantially.

In the subsequent discussion we concentrate particularly on high-velocity Si II absorption, because this ion has similar physical properties as Mg II, the latter one being the most frequently studied ion in IGM absorption-line studies. The use of Si II enables us to draw conclusions about the contribution of HVCs to the absorption cross section of strong Mg II absorbers for MW-type galaxies.

With five detectable Si II transitions in the wavelength band covered by the *HST*/STIS data (at λ1190.4, λ1193.3, λ1260.4, λ1304.4 and λ1526.7) the simultaneous fitting of these lines provides very reliable results for the column densities and Doppler parameters of the HVC absorbers. For 19 sightlines, for which high-velocity Si II can be detected, the majority (12/19 $\approx$ 63%) exhibit negative radial velocities. This accumulation at negative HVC velocities for low and intermediate ions has also been found by several other groups (e.g., Blitz et al. (1999); Ben Bekhti et al. (2012); Lehner et al. (2012)).

One may argue that this trend is caused by a selection bias due to the presence of the large HVC complexes at negative velocities, such as complex C and the MS, as well as due to the limited sample size. Another plausible explanation is, however, that the observed distribution reflects a net infall of neutral and weakly ionized material towards the disk of the Milky Way. This interpretation is also supported by models of the extra-planar H I kinematics and distribution presented by Marasco and Fraternali (2011). These authors found evidence for a global infall of neutral hydrogen gas, comparable to results found for other galaxies like NGC 891 (Oosterloo et al. 2007). However, for high ions like O VI this behavior seems to change. Sembach et al. (2003) found a more evenly distributed velocity distribution for Galactic O VI absorbers based on a sample of more than 100 sightlines towards extragalactic background AGNs using FUSE data. This could be seen as evidence that the highly-ionized gas traces both, outflowing as well as infalling gas structures. Here, one has to add that there is also evidence that some of the high-velocity O VI structures might not be restricted to the halo of the Milky Way. Richter (2006) has discussed that for absorbers that exhibit very high radial velocities the transformation from the Local Standard of Rest into the Galactic Standard of Rest or Local Group Standard of Rest velocity frames reduces the velocity dispersion for those O VI systems. This possibly implies that those absorbers may represent intergalactic clouds (or clouds residing in the potential well of the Local Group) rather than systems that are coupled to the Milky Way halo. These findings are also in line with results from theoretical simulations of the Local Group, which predict that there should be a large reservoir of hot gas remaining from the formation of the Local Group (Cen and Ostriker 1999b). However, without having direct information on the distances of these absorbing gas structures, it is very difficult to distinguish between intergalactic/circumgalactic systems and Milky-Way halo systems.

Referring to the column density distribution and the CDDF for Si II in Galactic HVCs, one can see that most of the absorbers have log N(Si II) $\geq$ 13.2. This limit is equivalent to neutral hydrogen column densities of log N(H I) $\geq$ 17.7, if solar abundances are assumed. Since most of the large HVC complexes have sub-solar metallicities, this value has to be regarded as a lower limit ($Z \approx 0.1 - 0.3 Z_{\odot}$, e.g., Richter 2006). The above column density limit is in good agreement with results of other studies which predict peak column densities for the neutral hydrogen in Galactic HVCs of log $N \approx 19 - 20$ (Putman et al. 2012, e.g.,). Our study implies that there is a distinct population of absorbers with log N(Si II) $\leq$ 13.0. These absorbers possibly belong to the class of highly-ionized HVCs and the so-called low-column-density (LCD) HVCs, which have neutral hydrogen column densities of log N(H I) $\leq$ 17.0 (Sembach et al. 2003; Richter et al. 2009). Similar values are also found in intervening metal absorbers (Chapter 5). For the *HST*/COS data, the H I column densities of intervening systems have been measured in a direct way via Voigt-profile fitting. In the right panel of Figure 5.2 one can see a bimodal distribution of H I column densities, which is in agreement with the bimodal column-density distribution of Si II seen in the Galactic HVCs (lower panel of Figure 4.3). The transition between the low-column density and the high-column density peak in the H I distribution occurs at log N(H I) = 17.0, which is close to the column density threshold of optically thick H I gas (log N(H I) = 17.2). This implies that the observed bimodality reflects two distinct populations of halo absorbers that are either optically thick or optically thin in H I.

With respect to the CDDF, the expectation for Si II would be that the slope is similar as for Galactic high-velocity H I, as both species trace roughly the same gas phase. From H I 21cm observations, Lockman et al. (2002) derived a slope of $\beta \approx 1.5$ under the assumption, that the CDDF follows a power law in the form $f(N) = CN^{-\beta}$. For high-velocity Si II in the halo of the MW we obtain a slope of $\beta \approx 1.59 \pm 0.23$, if we restrict our fit to the range log $N \geq 13.7$. Thus, this slope is in good agreement with the value derived for high-velocity H I and is also in line with our results for intervening Si II absorbers, for which we derive $\beta \approx 1.55 \pm 0.22$. These similarities support the idea that high-velocity Si II absorbers in the MW halo and intervening Si II systems trace the same class of objects (i.e., metal-enriched gas structures in the halos of galaxies). One striking feature in all CDDFs is the presence of a plateau. In case of Si II, such a plateau appears around log N(Si II) $\approx$ 13.7 for the Galactic HVCs as well as for the intervening absorbers. A similar plateau is also visible in the CDDFs for intervening Si III and C III (see upper panel of Figure 5.6). This behavior reflects the bimodality in the column densities of these ions, as discussed above. Richter et al. (2011) have shown that for intervening Ca II absorbers dust depletion effects have to be taken into account, in particular for absorbers with high H I column densities. Since silicon is also strongly affected by dust depletion, the slope of the CDDF is expected to steepen at high H I column densities. Therefore, it is difficult to compare CDDFs from different studies without considering the corresponding H I column densities. One important aspect of future absorption-line studies thus will be to establish the (Si II/H I) relation in intervening absorbers to constrain the dust depletion in intervening metal absorbers in a similar way as for Ca II systems (Richter et al. 2011).

Another interesting aspect is the component structure of HVCs and intervening absorbers. Charlton

and Churchill (1998) have shown that it is quite difficult to conclude on the origin of the observed gas relying solely on the velocity information of low and intermediate ions. Also Meiksin (2009) argued that there are (in principle) several fit solutions possible for each absorption feature. Within the theory of absorption lines, it is indeed possible to interpret an absorption structure as an interaction of a large number (or even infinite) amount of smaller subcomponents. In fact, such a scenario is supported by almost all high resolution observations. For instance, Churchill et al. (2003) identified up to 8 individual components in intervening strong Mg II systems, using high-resolution observations. Thus, the expectation is that with increasing data quality the subcomponent structure of an absorption system becomes increasingly complex. In the upper panel of Figure 4.4 and the left panel of Figure 5.2, our results for the component structure of absorbers in the STIS and COS data are shown. One can see that in both cases the vast majority of the absorbers has only one or two velocity components. Because the STIS data has as resolution power that is roughly twice as high as for COS (see Chapter 3), there is a higher detection rate of two component systems in the STIS HVC data compared to the COS data, in which the majority of the absorption systems could be fitted as single-component systems. In conclusion, the observed component structure in HVCs and intervening absorbers does not provide any valuable information on the possible connection between both classes, as it is basically determined by the instrumental properties rather than by the intrinsic physical properties (see Section 5.2).

Closely connected to the component structure of an absorption system is the Doppler parameter, which reflects the line width of an absorption component. For Si II absorption in Galactic HVCs we have fitted a log-normal distribution to the Doppler parameters, as shown in the bottom panel of Figure 4.4. For comparison, investigations of the Lyα forest have shown that also in the diffuse IGM log-normal like distributions for the Doppler parameters can be found (see Meiksin 2009, their Table 2). The origin of this distribution is still not well understood. Meiksin (2009) argued that such a behaviour hints at an internal stochastic process that induces a log-normal distribution. Even the physical processes behind the overall structure formation may have an influence on the shape of this distribution. With the knowledge of the Doppler parameter of an individual absorber it is possible to estimate the local gas temperature (or an upper limit of the temperature, if the contribution of the turbulent part to b is unknown). From this, the typical temperature range for LLSs with neutral hydrogen column densities of $\log N(\mathrm{H\,I}) \geq 17.1$ is on the order of $T \approx 1 - 3 \times 10^4$ K (e.g., Tytler et al. 1999; O'Meara et al. 2001). Thus, the approach of using a canonical value of $T = 10^4$ K for the ionization modeling of intervening metal systems, which have neutral hydrogen column densities in that particular range, appears to be justified. Assuming a temperature for these systems then offers the possibility to separate the thermal from the non-thermal (turbulent) part of the Doppler parameter, which in turn increases the precision of modeling the individual velocity components.

6.1.2 The Milky Way as an absorption line system

Another important aspect of this thesis is the interpretation of the Milky Way halo as an Mg II absorption-line system, if seen from an external vantage point. With the help of Si II and the HALOPATH code we have estimated a mean covering fraction of Mg II in the halo of the MW as well as the contribution of HVCs to the overall number density of strong Mg II absorbers at low z. Also for these results one has to keep in mind that a large fraction of the southern Galactic sky is covered by the Magellanic Stream, which induces a bias in our estimate of the covering fractions. Because such spatially extended tidal features are not the standard for MW-type galaxies at low z, one could argue that the Mg II cross section of HVC analogs in these galaxies might be somewhat smaller. For future studies with a larger sample of sightlines, it would be interesting to exclude the regions around the MS and to compare the absorption statistics with the one derived for the entire sky including the Stream's contribution to the absorption cross section.

For other galaxies it is still hard to identify structures that would represent HVC analogs. However, at least for the Local Group several studies suggest that there is no evidence for significant neutral HVC gas beyond 50 kpc (Lehner et al. 2012; Richter 2012). This statement agrees with our understanding of the gas distribution in the Milky Way halo, where direct distance measurements place the bulk of the HVCs at distances $5 - 15$ kpc from the Galactic plane (e.g., Wakker 2001a; Putman et al. 2003; Wakker et al. 2007 2008; Thom et al. 2008). Also for the other two prominent members of the Local Group, M31 and M33, most of the extraplanar H I features are located at < 50 kpc distances from the disk; most of them in fact are at distances < 15 kpc (Thilker et al. 2004; Putman et al. 2009). Despite the fact that a number of three galaxies is far too small to draw statistically meaningful conclusions, these observations indicate that the HVC phenomenon is typically restricted to the inner halos

of galaxies, if galaxy-interactions are not considered. For more distant galaxies, the HVC/absorber-galaxy connection is a highly debated research topic (see subsequent discussion). Another interesting point regarding the contribution of the HVCs to the number density of strong Mg II systems that has to be considered concerns the origin of the gas. Richter (2012) has shown that the expected number density of intervening absorbers that represent HVC analogs is $d\mathcal{N}/dz < 0.167$, which is $< 34\%$ of the expected value of $d\mathcal{N}/dz(\mathrm{Mg\ II}) = 0.5$ for $z = 0$ derived by Nestor et al. (2005). This discrepancy indicates that the number density of Mg $\mathrm{II}_{\mathrm{strong}}$ systems is dominated by outflowing material (e.g., from galactic winds etc.) rather than from infalling gas (Bouché et al. 2012). This conclusion is supporerted by results from Kacprzak and Churchill (2011), who has shown that the distinction between the infalling and outflowing gas in case of Mg II absorbers can be made based on their equivalent width. These authors concluded that most strong Mg II absorbers are more consistent with outflowing material.

This scenario implies, in turn, that quiescent galaxies, that do not produce extended winds or outflows (such as the MW or M31), contribute only a little to the observed number density of strong Mg II systems at low redshift. This picture is also supported by the study of Rao et al. (2013), who has investigated the outer regions of M31 with the help of 10 background quasars. They confirm the existence of HVCs in the halo of M31 based on Mg II absorption data. However, they find significant absorption of low ions only at impact parameters < 32 kpc within the $\log N(\mathrm{H\ I}) = 18.3$ boundary of the H I disk of M31. This extent is less then what was expected (Rao et al. (2013)) and less than what is seen in the MW halo, suggesting that the distribution of gas in the halos of Milky Way/M31 type galaxies is difficult to understand, if only a few sightlines are available (see also Chapter 4 and 5).

6.1.3 Metallicity and ionization conditions

In the second part of Chapter 5 we have set up different ionization models for a subsample of the intervening absorbers in the COS sample. As documented in Table 5.5, the allowed parameter range of the modeled physical quantities for individual systems is quite large. Nevertheless, the derived mean logarithmic values for the metallicity ($\langle \log (Z/Z_{\odot}) \rangle = -1.07$), the ionization parameter ($\langle \log U \rangle = -2.73$), and the hydrogen volume density ($\langle \log n_{\mathrm{H}} \rangle = -2.75$) are in line with results found by other groups.

Most likely, the relatively large spread in these physical quantities presented in Chapter 5 partly reflect the change in physical conditions in the absorbers as a function of distance (impact parameter) from their host galaxies. From the Galactic H I 21cm HVCs we know that the majority of those systems are located at distances of $\lesssim 15-20$ kpc from the Galactic disk (Wakker et al. 2007; Thom et al. 2008). As we will discuss later, the maximum impact parameter of intervening Si III systems is on the order of ~ 160 kpc for 0.05 L^* galaxies. If one now assumes a gradient in the metallicity as well as in the ionization conditions from the inner halo regions to the CGM and IGM, such a gradient should be visible in our sample of intervening Si III, as they are expected to span a large range of impact parameters. In such a scenario, intervening absorbers may arise in a transition region between the metal-enriched disk of a galaxy, which has typically near solar metallicities, and the diffuse, low-metallicity IGM. Mixing processes between these different halo layers possibly are also relevant. The observed metallicity spread of intervening absorbers presented in Figure 5.9 ($\log (Z/Z_{\odot}) = -2.5$ to 0) fits into this picture.

Regarding this aspect, Shull et al. (2009) and Collins et al. (2009) have presented detailed analyses of Galactic Si III absorption in HVCs. They found mean logarithmic metallicities of HVC Si III absorbers of -1.4, which is ~ 0.3 dex below the result for intervening Si III derived in this work ($\langle \log Z \rangle \approx -1.1$). These authors already mentioned that their derived mean value is quite low compared to the metallicity of complex C found by Collins et al. (2007) and other groups. The complex C metallicity is found to be $\log (Z/Z_{\odot}) = -0.89$ and should give an approximate value for the metallicity of infalling IGM material since it is supposed that complex C represent an infalling stream of low metallicity IGM gas (see Section 1.3). Mixing processes for complex C are, however, not considered in this simple scenario. Note that the mean logarithmic metallicity for the intervening absorbers presented in our study ($\langle \log (Z/Z_{\odot}) \rangle = -1.07$) is only slightly below the complex C value.

Similar considerations can be done for the ionization parameter U. In view of the potential well of galaxies, it is expected that the gas density decreases with increasing impact parameter, so that systems at larger impact parameters should have (on average) a larger ionization parameter (see Equation 2.20). In the work of Shull et al. (2009) and Collins et al. (2009) the authors found typical values of $\log U \approx -3.0$ for Galactic high-velocity Si III, which is ~ 0.3 dex *below* the mean value found for intervening metal absorbers in this work. On the other hand, Danforth and Shull (2008) have shown that the typical logarithmic ionization parameter in low-redshift IGM absorbers exposed to the diffuse UV background is -2.1, which is 0.6 dex *above* the result for the intervening Si III absorbers studied in this work. Thus,

one can conclude that these absorbers still are coupled to the CGM of galaxies. Another relevant analysis of low ions in Galactic low-column densitiy HVCs was presented by Richter et al. (2009). In their Figure 6 the authors outlined a typical range for the ionization parameters for these ions, which is in good agreement with the values found in this work.

One important observational aspect in our study is, that a positive Si III detection in intervening metal systems almost always involves a significant column density in other low or high ions. This can be understood if one considers the ionization potential of Si III ($E_{\rm SiIII} = 33.49$ eV, see Section 2.4.3). The Si III ion traces diffuse ionized gas at intermediate densities in the transition between a weakly ionized colder phase (with ions like Si II and C II) and a warm/hot ionized phase (with high ions such as Si IV, C IV, and O VI). Future studies of multi-ion absorbers based on a larger absorber sample will be necessary to further explore the physical connection between the different gas phases traced by these ions. However, one general problem for the ionization modeling of such multi-phase metal absorbers concerns the determination of hydrogen column densities of individual absorption components in saturated systems. This issue is critical, since the hydrogen column density is one of the basic key parameters for the determination of the ionization parameter in an individual component using Cloudy. Only for those low-z absorbers, that have complementary *FUSE* data available this problem can be solved by considering higher Lyman-series lines of H I (e.g., Tilton et al. 2012).

In Section 4.4.2 we have discussed the connection between Si II and Mg II with regard to ionization properties, covering fractions and abundances, based on our measurements of the Milky Way HVCs. Based on the considerations presented in the previous sections we are now able to classify the intervening Si II absorbers into the scheme of weak/strong Mg II absorbers. If we assume a minimum velocity gap between *individual* absorption systems of $\Delta v = 20$ km s^{-1} (as defined for Galactic HVCs), intervening Si II absorbers with W_λ(Si II λ1260) ≥ 140 mÅ represent the analogs to strong Mg II absorbers (Narayanan et al. 2008b). As a result from our *HST*/COS measurements then follows that $23/32 \approx 72\%$ of the detected Si II systems trace strong Mg II absorbers. This fraction is in very good agreement with the results measured for the Milky Way presented earlier: there, we have shown that the majority of the HVCs would be seen as strong Mg II absorbers if observed from an external vantage point (see Section 4.4.2). This is in line with our idea that at least a fraction of the intervening Mg II absorbers represent HVC analogs. With regard to the redshift-dependend number density of intervening strong Mg II absorbers, $d\mathcal{N}/dz$(Mg II$_{\rm strong}$), we can only roughly estimate this quantitiy from our intervening Si II systems becacuse of the different detection thresholds for both ions in spectral data. If we assume that every "strong" Si II absorber traces a strong Mg II absorber along the measured lines of sight, we can use the calculated fraction of $\sim 72\%$ in combination with the number density of Si II to obtain $d\mathcal{N}/dz$(Mg II$_{\rm strong}$) ≈ 0.67. In view of the limited sample size and the uncertainty for the conversion from Si II to Mg II, this value is in very good agreement with the estimate of $d\mathcal{N}/dz$(Mg II$_{\rm strong}$) ≈ 0.5 from the extrapolation of the Mg II number density at higher redshift down to $z = 0$ in SDSS data (Nestor et al. 2005).

6.1.4 Impact parameters and host galaxies

Since the HVC analogs discussed in this work are expected to arise in the halos and circumgalactic environment of low-redshift galaxies, it is an important task to identify these galaxies and measure the typical impact parameters of the corresponding metal systems (HVC analogs) to their host galaxies. This task is not straight-forward, however, because the connection between the absorption strength (in terms of column density and equivalent width), frequency, and impact parameters of intervening absorbers in relation to the properties of their host galaxies (e.g., luminosity) is not well established. At least for H I, Rao et al. (2011) have shown that the typical impact parameters for LLS galaxies in the redshift range $0.1 \lesssim z \lesssim 1$ is $\sim$36.4 kpc, whereas it is $\sim$ 33.3 kpc for the sub-DLA galaxies and $\sim$ 17.4 kpc for galaxies that give rise to DLA systems. Furthermore, they found that at least the most important absorber parameters, such as the column density, log $N_{\rm HI}$, or the impact parameter, are not correlated to the luminosity of the absorber host galaxy. On the other hand, Kacprzak and Churchill (2011) have argued that, in view of the observed number density of Mg II systems, LLS should be found up to distances of $\sim$ 100 kpc from their host galaxies, which is roughly a factor of $\sim$3 more than what has been found by Rao et al. (2011). This lack of clarity can be also found for other species: apart from the well established ions like Mg II and Si II, little is known about the galaxy-absorber relation for other low- and intermediate ions that trace different gas phases and enrichment patterns (e.g., nitrogen with its ions N II, N III, and N V,).

With the combination of the typical covering fraction for Si III derived from our study of the MW halo and the number density of intervening Si III absorbers determined from our COS sample it is

possible to predict the typical radial extent of Si III-bearing gaseous halos of low-redshift galaxies in a statistical manner (see Equation 5.4). Note that for most of the sightlines studied here there are only a few foreground galaxies known that possibly represent the host galaxies of the intervening Si III absorption and that have known redshifts. However, with the information published by Chen et al. (2001); Stocke et al. (2006) and Prochaska et al. (2011) for other high and low metal ions, together with the calculations from Section 5.4, we expect Si III systems to arise within $\rho \lesssim 160$ kpc of galaxies with luminosities $> 0.05\,L^*$. This value fits very well to the *observed* angular distances between absorbers and their host galaxies in those cases, where galaxy redshift information is available (see Section 5.4.1; e.g., Chen et al. 2001; Stocke et al. 2006; Prochaska et al. 2011). Yet another important aspect in this context is, however, that only for 33.3 % of all sightlines studied here nearby galaxies could be detected within this impact-paramter range. Some of these host galaxies may be too faint to be detected, but since their redshift is small, they would need to have very low luminosities (and masses). Another explanation could be that the majority of the intervening systems represent isolated absorbers which have been ejected out of galaxies a long time ago and remain stable until today. There is also the possibility that these systems never have been part of a galaxy. The latter scenario could explain those intervening metal systems by *in situ* star formation in the IGM on small scales by the Population III stars (Meiksin 2009). Thus, it will be an interesting and challenging question for future studies to further pinpoint the relation between intervening metal systems and their host galaxies, based on a large sample of absorber-galaxy pairs that covers a large range in galaxy luminosities. Our current understanding of the relation between ion absorption and impact parameters in the CGM of galaxies is sketched in Figure 6.1.

Moreover, so far it is not clear to what extend the results for more distant galaxies can be transferred to galaxies in the Local Group like the MW or M31. Typically, for MW/M31 type galaxies luminosities of $\sim$ 0.5 - 1.0 L* are expected (e.g., van den Bergh 1999; Tempel et al. 2010). This is above the minimum luminosity of $L = 0.05\,L^*$ for absorber-galaxy pairs discussed above. Therefore, if MW and M31 were typical (sub)-L^* galaxies in the local Universe, one would expect Si III (or C III) absorption at impact parameters up to $\rho \sim 160$ kpc. Yet, for M31 Rao et al. (2013) have shown that there is almost no significant metal absorption beyond $\rho > 57$ kpc. Also in case of the MW, the most distant metals are confirmed at $\rho \sim 50$ kpc in gas of the Magellanic Stream (Lehner et al. 2012). In view of these results, one can conclude that our understanding of the absorption cross section of low and intermediate ions in the CGM is incomplete, or the Milky Way and M31 do *not* represent typical galaxies with respect to their circumgalactic gas distribution. With increasing absorption-line statistics in the next few years, it remains to be seen whether this discrepancy is just a sensitivity issue or if the MW and M31 indeed are two galaxies that have almost no circumgalactic metal absorption beyond $\sim$ 50 kpc.

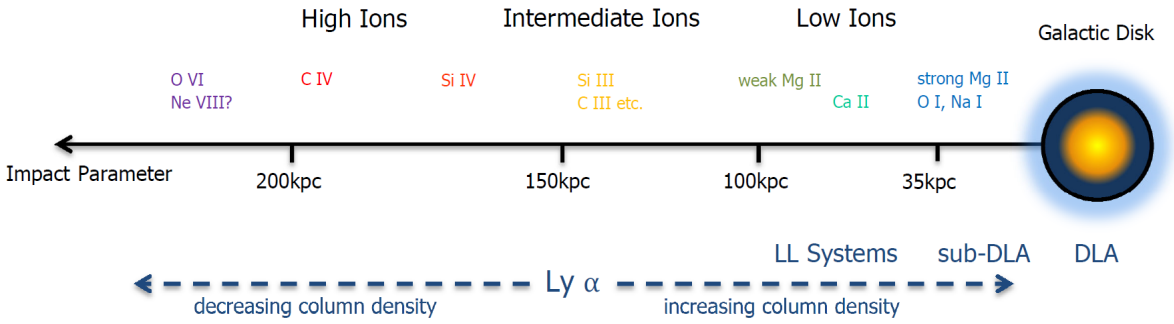

Figure 6.1: Simple illustration of our current understanding of typical impact parameter ranges for different metal ions in gaseous galaxy halos with luminosities $L \geq 0.05\,L^*$.

6.1.5 Future studies

An interesting aspect, which deserves further attention in future studies of the CGM, is the redshift evolution of $\mathrm{d}\mathcal{N}/\mathrm{d}z$ for intervening Si III systems. As described in Section 1.4.4, Nestor et al. (2005) and Narayanan et al. (2007) have shown that there is convincing evidence for a declining number density of weak and strong Mg II systems with declining redshift. Such a trend is also found at higher redshift for Ly α absorbers in the range $z = 4.0 - 1.5$ (e.g., Kim et al. 2001). As summarized in the review of Richter (2006), these systems follow a relation $\mathrm{d}\mathcal{N}/\mathrm{d}z \propto (1+z)^\gamma$ with $\gamma \approx 2.2$ for $1.5 \leq z < 4.0$. Interestingly, this strong evolution seems to disappear for $z \leq 1.5$ (e.g., Weymann et al. 1998; Kim et al. 2001, and

references therein). The physical connection between the CGM and the large-scale IGM (giving rise to the Ly α forest) in terms of baryon budget and metal content yet need to be explored. From line statistics and photoionization models one can conclude that in the range $z \approx 2 - 0$ the contribution of the Ly α forest to the overall baryon density has dropped from $\sim 90\%$ to approximately $\sim 30\%$ (Penton et al. 2004). It is believed that this trend is a result of the on-going structure formation and the appearance of a warm-hot component of the IGM that does not contribute to the Ly α line density. The role of intervening metal absorbers (such as Si III systems) in this context of large-scale structure formation (e.g., as metal-enriched material circulating in the large-scale environment of galaxies) possibly can be studied best in hydrodynamical simulations (e.g., Tepper-García et al. 2011 2013).

Moreover, it is still a matter of debate whether the "cold" accretion or the "warm" and "hot" accretion mode is the more dominant mechanism for the continuous replenishment of the gaseous matter in galaxies. The consequences of such accretion processes for the star-formation activity in galaxies need to be determined in detail, e.g., by combining observational data and semi-analytic models of the gas distribution around galaxies (Richter et al. 2011). Here, many aspects (e.g., the relation between gas-accretion rate and dark-matter halo mass) are not yet fully understood. Based on Mg II absorption measurements, Kacprzak and Churchill (2011) suggest that the H I mass that is cycling through the halo remains fairly constant over time. This scenario appears counter-intuitive on the first look, as there are predictions based on simulations that imply that the total halo mass increases with decreasing redshift (Davé et al. 1999). This discrepancy can be understood if one takes into account that the gaseous material in massive halos mainly resides in a hot phase, which is not accessible through Mg II absorption and which does not contribute to the star-formation because of the large cooling time scale. Clearly, there is large potential to further increase our understanding of the gas circulation in the multiphase circumgalactic environment of galaxies.

One general problem for the comparison between the properties of the gaseous Milky Way halo and the halos of other galaxies is the presence of the Magellanic Stream, which covers a large fraction of the H I 21cm HVC sky and thus introduces a bias in the statistics of Galactic halo absorbers. Recent H I 21cm observations of nearby galaxies suggest that large tidal gas streams might not be as common in the local Universe as previously thought (e.g., Oosterloo et al. 2007; Sancisi et al. 2008). While other spiral galaxies such as M31, M51, M81, M101, and NGC 891 show HVC analogs and extended H I halos, massive tidal features appear to be rare. Thus, one goal for future investigations of the gaseous Milky Way halo must be to provide statistics on the absorption cross-section of high-velocity gas with and without considering material associated with the Magellanic Stream and to develop a "MS-corrected" model of the Galactic HVC distribution. Lehner et al. (2012) suggest that the Galactic HVC population can be divided into the "normal" HVCs with $|v_{\rm LSR}| \leq 210$ km s^{-1} and the so-called "very high-velocity clouds" (VHVCs) with $|v_{\rm LSR}| > 210$ km s^{-1}. They state that almost the entire population of VHVCs is dominated by the MS with only a few exceptions. In contrast, halo gas at low galactic latitudes and low radial velocities typically is situated close to the Galactic disk (e.g., in the disk-halo interface), but it is extremely difficult to disentangle such gas from gas *within* the disk (e.g., Kalberla et al. (2005)). Our understanding of the Milky Way's disk-halo interface region, that is expected to host substantial amounts of outflowing gas from galactic fountain-type processes, is incomplete, as these regions typically are excluded from statistical analyses of the gas distribution in the Milky Way.

The detectability of low, intermediate and high ions in absorption and emission strongly depends on the local physical conditions in the gas. These conditions regulate the ionization balance in the gas and determine the fate of infalling and outflowing material and also its absoption cross section in detectable transitions. While neutral HVCs represent a prominent feature in the Milky Way halo, recent H I 21cm observations (e.g., from the HALOGAS survey; Zschaechner et al. (2012)) imply that they are less prominent in the halos of other galaxies. However, since it is expected that the dominant fraction of the gas mass in the CGM is in the form of ionized gas, the lack of H I 21cm features seen in the halos of more distant galaxies may simply reflect typical physical conditions that are different from those in the Milky Way halo and that do not favour the existence of large, coherent neutral gas structures, but rather favour more ionized gas structures that are invisible in H I 21cm data. As a consequence, a full assessment of the gas distribution in galaxy halos requires the consideration of different ionization stages of tracer species in absorption spectra from multiple sightlines that pass the halos of intervening galaxies at different impact parameters.

As already outlined in the introductory sections, the research field of the IGM and CGM is currently of high interest due to the importance of this material for the ongoing structure formation in the Universe and the evolution of galaxies. One major goal for future *observational* studies must be to increase the amount and quality (e.g., S/N, spectral and spatial resolution) of absorption end emission data of circumgalactic gas in the local Universe to better understand the spatial distribution and kinematics of

the CGM around galaxies. The next generation of UV telescopes (whenever built) hopefully will provide a large number (> 1000) of QSO spectra at high S/N (> 50) and high spectral resolution ($R > 40\,000$). These data then can be used for a "tomography" of galaxy halos in different lowly and highly ionized species along multiple sightlines per halo. With these data, it will also be possible to provide detailed ionization models of the different gas phases in the CGM. In addition, new 21cm radio measurements of the HVC sky around the Milky Way and other galaxies with higher angular resolution than previous surveys are expected to improve our understanding of the spatial structure of neutral gas filaments in galaxy halos and their kinematics (e.g., Kerp et al. 2011). Finally, the steadily increasing number of high-quality optical spectra of stars in the inner and outer Milky Way halo will be of great importance to bracket the distances of Galactic IVCs and HVCs in the direction of these stars, and thus will be used to disentangle the 3D distribution of the different gas phases in the halo.

Going along with new observational campaigns, the next generation of galaxy simulations (embedded in a cosmological framework) will add further important constraints of the complex relationship between galaxies and their gaseous environment. Such simulations will be particularly important to follow the time evolution of infalling and outflowing gas and to characterize processes such as gas stripping from satellites and feedback mechanisms (see, e.g., Putman et al. 2012). Here, a high spatial resolution (down to parsec scales) as well as the inclusion of all relevant physical processes in the simulations represent major tasks to fully take advantage of the power of such simulations to improve our understanding of the CGM.

6.2 Conclusions

In this thesis, gas in the halos and circumgalactic environment of the Milky Way and other galaxies have been investigated by way of absorption spectroscopy, based on UV spectral data obtained with the STIS and COS spectrographs onboard the *HST*. We have studied in detail the statistical properties of metal absorbers in galaxy halos, the physical properties of the absorbing halo structures using photoionization models, the spatial distribution of the different gas phases in galactic halos, and the relation between the Milky Way HVCs and intervening metal absorbers at low redshift. The main conclusions of our study are the following:

1) *Neutral and ionized gas in the Milky Way halo has complex absorption characteristics.*

   We identify Si II with its five detectable transitions in the *HST*/STIS and *HST*/COS wavelength band as the best-suited ion to statistically study the UV absorption characteristics of neutral and weakly ionized gas in Galactic HVCs and their distant analogs. For the 38 individual Si II absorption components in HVCs in our data set we obtain typical column densities in the range $\log N(\mathrm{Si\,II}) = 12.5 - 15.0$. We find that the absorption covering fraction of high-velocity Si II in the Milky Way halo is $f_\mathrm{c}(\mathrm{Si\,II}) = 0.67$ for a column-density limit of $\log N(\mathrm{Si\,II}) \geq 12.25$. This is a factor of two higher than the filling factor of H I in HVCs for $\log N(\mathrm{H\,I}) \geq 17.8$. We conclude that Si II is a sensitive tracer for neutral and partly ionized halo gas with H I column densities below the detection limit of H I 21cm HVC surveys. About 70% of the high-velocity Si II absorption is detected at negative radial velocities, pointing towards a net infall of neutral and weakly ionized gas traced by Si II. Most of these halo Si II absorbers are composed of $1-2$ velocity subcomponents that have Doppler parameters in the range $b = 5 - 15$ km s^{-1}. Non-thermal line broadening mechanisms dominate the observed Si II b-values in HVCs.

2) *Only the most massive Galactic HVCs would represent strong intervening Mg* II *absorbers in QSO spectra.*

   During the last decades, the Mg II ion has been used as prime tracer of multi-phase gas in and around galaxies at low and high redshift. Recent studies have shown that intervening strong Mg II absorbers ($W_{2796} > 0.3$ Å) generally are associated with luminous galaxies ($L > 0.5\,L^*$) at impact parameters $\rho < 35$ kpc, whereas weak Mg II absorbers typically arise at larger impact parameters in the range $35 - 100$ kpc (Steidel et al. 2002; Kacprzak et al. 2010). Since Mg II absorbers predominantly arise in neutral and weakly ionized gas that has a large absorption cross section, they are believed to be reliable tracers of HVC analogs around distant galaxies. One major aspect of this thesis was to pinpoint the relation between Galactic HVCs and intervening weak/strong Mg II absorbers in the context of the origin of the circumgalactic medium.

   In a first step, we have combined information from Si II and Mg II absorption in Galactic HVCs to determine the covering fraction of strong Mg II absorption (with equivalent widths $W_{2796} > 0.3$ Å) in the Milky Way halo. Because Si II and Mg II have similar ionization potentials and both elements have a similar cosmic abundance, we have used high-velocity Si II as tracer for Mg II absorption for sightlines, where no Mg II data are available. We find that the covering fraction of strong Mg II absorption in the Galactic halo is $f_\mathrm{c,sMgII,halo,i} = 0.34 \pm 0.09$ from our position within the Milky Way disk. This value is similar to the covering fraction of H I in HVCs at column densities $\log N(\mathrm{H\,I}) \geq 17.8$. Therefore, our analysis implies that only the most massive Galactic HVCs would represent strong Mg II absorbers if seen as intervening absorbers from an external vantage point.

2) *HVCs contribute with less then 34% to the number density of strong Mg* II *absorbers at $z = 0$.*

   Since the local HVC population is visible only from an interior perspective, one has to rely on analytic models and simulations to compare the properties of Galactic HVCs with halo absorbers of other galaxies. With the investigation of the absorption signatures of various low and high ions along 47 randomly chosen sightlines we are able to estimate covering fractions, f_c, between 0.20 (Si IV) and 0.70 (C II, Si III) in HVCs for the relevant column density thresholds chosen for our data. In a second step, we have combined these results with the geometrical Milky Way/M31 halo model of Richter (2012) to estimate the cross section of strong Mg II absorption in the Milky Way HVCs, if they would be seen as a QSO absorber from an exterior vantage point. For disk

and halo components together we obtain a mean covering fraction of strong Mg II absorption of $\langle f_{\rm c,sMgII} \rangle = 0.31$ for a halo radius of $R = 61$ kpc. This result implies that $\sim 52\%$ of the cross section of strong Mg II absorption in the Milky Way comes from the HVC population in the Galactic halo. Furthermore, our results indicate that the contribution of HVCs to the number density ($\mathrm{d}\mathcal{N}/\mathrm{d}z$) of strong Mg II absorbers at $z = 0$ is small, but not negligible ($< 34\%$). These findings are in line with the idea that most of the intervening strong Mg II absorbers are related to gaseous outflows and galactic winds arising in the extended halos of more actively star-forming galaxies. In the case of the MW and M31, this means that these rather "quiescent" galaxies, which do not produce extended winds and outflows, contribute only little to the observed number density of strong Mg II systems.

3) *The typical impact parameter for intervening Si III absorbers for $L \geq 0.05\,L^*$ galaxies is < 160 kpc.*

One major aspect in our understanding of the nature of intervening metal absorbers concerns their spatial connection to nearby galaxies. Since the metals observed in intervening absorbers are produced in stars *within* galaxies, one expects to find galaxies associated with intervening metal absorbers at characteristic length scales. In the most simple picture of the spatial distribution of metal absorbers around galaxies we expect that neutral and weakly ionized metals typically arise close to the central parts of the galaxies, whereas high ions like C IV and O VI are tracing the extended CGM and transition zone to the surrounding IGM.

In this work, we have combined the covering fractions of intermediate ions in HVCs and the number density of intervening metal absorbers determined from COS data to derive (in a statistical way) the characteristic halo radii for Si III absorption in $\geq 0.01\,L^*$ and $\geq 0.05\,L^*$ galaxies. Adopting a covering fraction of $f_c(\mathrm{Si\,III}) = 0.7$, as measured in the MW, we estimate $R_{\rm h,SiIII}(0.05\,L^*) = 160$ kpc and $R_{\rm h,SiIII}(0.01\,L^*) = 55$ kpc for Si III absorption. These radii are in line with a scenario, in which the absorption cross section of galaxies and their halos increase with increasing ionization fraction of the gas, as traced by the different ionization stages of metal ions such as Mg II, Si II, Si III, C III, C IV, and O VI (see also Chen et al. 2001; Stocke et al. 2006; Kacprzak et al. 2008; Prochaska et al. 2011).

4) *A substantial fraction of intervening metal absorbers may represent HVC analogs around distant galaxies.*

As part of the detailed investigation of intervening Si II, Si III, and C III absorption along 57 *HST*/COS sightlines towards extragalactic background sources we searched for similarities in the statistical properties and physical conditions of intervening metal absorbers and Galactic HVCs. For this, we have analyzed different aspects, such as the component structure, the absorber frequencies, the column density distribution, the ionization conditions, and the impact parameters to nearby galaxies.

We detect a bimodality in the H I column density distribution of intervening metal absorbers at low z, a trend that is also seen in the population of Galactic HVCs. For intervening absorbers with $\log N(\mathrm{H\,I}) < 17.0$ one can speculate that they represent distant analogs of the class of so-called low-column-density HVCs (Richter et al. (2009)). They are probably also related to the population of weak intervening Mg II absobers that have typical impact parameters of $\sim 35 - 100$ kpc (Narayanan et al. 2008b). The similarity of the Si II and Mg II ions can be used to obtain further constraints. For the intervening metal absorbers analyzed in our study we find that $\sim 72\%$ of the detected Si II systems should be also visible as strong Mg II absorbers if NUV data were available. Thus, intervening Si II systems trace (mostly optically thick) gasesous structures that have a relatively large absorption cross section (large compared to the expected cross section of gaseous disks), in line with the idea that they arise in the extended gaseous halos of galaxies.

Finally, we have analyzed the ionization conditions of intervening metal absorbers detected in a subsample of 12 *HST*/COS sightlines that have data with a high S/N. If intermediate ions like Si III and C III represent tracers for galactic halos that have properties similar to the Milky Way halo, one would expect that corresponding halo absorbers should exhibit comparable physical conditions (i.e., similar ionization parameters and similar metallicities). With the set up of Cloudy photoionization models for the 12 individual systems we could confirm that these metal absorbers indeed have average ionization properties that are similar to those in Galactic high-velocity clouds

(e.g., Shull et al. 2009; Richter et al. 2009; Collins et al. 2009; Yao et al. 2011). Despite the large spread in the ionization parameters, our results agree well with expectations for diffuse ionized gas in the CGM of galaxies. For the metallicity of the intervening absorbers, we find a characteristic range $0.003 < Z/Z_{\odot} < 1.50$, while for the hydrogen density our analysis yields $-4.34 < \log n_{\rm H} < -1.94$. The ionization parameters in the absorbers span a range of $-1.20 > \log U > -3.60$. From these ranges we derive mean logarithmic values for the metallicity, density, and ionization parameters in the 12 absorbers of $\langle \log (Z/Z_{\odot}) \rangle = -1.07$, $\langle \log n_{\rm H} \rangle = -2.75$, and $\langle \log U \rangle = -2.73$. These mean values are in good agreement with results from other groups. We suggest that circumgalactic gas structures traced by intermediate ions such as Si III and C III arise in the outer regions of galactic halos at relatively low gas densities (compared to the inner halos), but with an average metallicity that is substantially higher than the surrounding IGM. We have identified candidates for the host galaxies of the interving absorbers in more than 34% of all investigated sightlines with detected intervening Si III absorption. Without considering in detail the luminosity of these galaxies, we find that the typical impact parameter of intervening Si III absorbers to their host galaxies is $\rho \leq 160$ kpc, as expected for galaxies with luminosities $L \geq 0.05\,L^{*}$.

In conclusion, our study provides compelling evidence for a tight morphological connection between Galactic HVCs and intervening metal absorbers at low redshift. The analysis of Si II, Si III, and C III in Milky Way halo absorbers and in intervening systems indicate a complex multi-phase nature of the CGM around galaxies, whose role in the formation and evolution of galaxies deserves further attention in upcoming studies.

Bibliography

Alpher, R. A., Bethe, H., and Gamow, G. (1948) , *Phys. Rev.* **73**, 803

Asplund, M., Grevesse, N., and Sauval, A. J. (2005) , In *Cosmic Abundances as Records of Stellar Evolution and Nucleosynthesis.* (T. G. Barnes, III and F. N. Bash eds.), Vol. 336 of *Astronomical Society of the Pacific Conference Series*, p. 25

Ben Bekhti, N., Winkel, B., Richter, P., Kerp, J., Klein, U., and Murphy, M. T. (2012) , *A&A* **542**, A110

Ben Bekhti, N. B., Murphy, M., Richter, P., and Westmeier, T. (2008) , *Ca ii and Na i Absorption Signatures from the Circumgalactic Gas of the Milky Way*, p. 273

Bennett, C. L., Halpern, M., Hinshaw, G., Jarosik, N., Kogut, A., Limon, M., Meyer, S. S., Page, L., Spergel, D. N., Tucker, G. S., Wollack, E., Wright, E. L., Barnes, C., Greason, M. R., Hill, R. S., Komatsu, E., Nolta, M. R., Odegard, N., Peiris, H. V., Verde, L., and Weiland, J. L. (2003) , *ApJS* **148**, 1

Bergeron, J. and Boisse, P. (1991) , *Advances in Space Research* **11**, 241

Bian, F., Fan, X., Jiang, L., McGreer, I., Dey, A., Green, R. F., Maiolino, R., Walter, F., Lee, K.-S., and Davé, R. (2013) , *ApJ* **774**, 28

Blitz, L., Spergel, D. N., Teuben, P. J., and Hartman, D. (1999) , *ApJ* **514**, 818

Bouché, N., Murphy, M. T., Péroux, C., Contini, T., Martin, C. L., Forster Schreiber, N. M., Genzel, R., Lutz, D., Gillessen, S., Tacconi, L., Davies, R., and Eisenhauer, F. (2012) , *MNRAS* **419**, 2

Braun, R., Thilker, D. A., Walterbos, R. A. M., and Corbelli, E. (2009) , *ApJ* **695**, 937

Brooks, A. M., Governato, F., Quinn, T., Brook, C. B., and Wadsley, J. (2009) , *ApJ* **694**, 396

Brown, T. (2002) , In *HST/*STIS *Data Handbook; Version 4.0*

Cen, R. and Ostriker, J. P. (1999a) , *ApJL* **519**, L109

Cen, R. and Ostriker, J. P. (1999b) , *ApJ* **514**, 1

Charlton, J. C. and Churchill, C. W. (1998) , *ApJ* **499**, 181

Chen, H.-W., Lanzetta, K. M., Webb, J. K., and Barcons, X. (2001) , *ApJ* **559**, 654

Chen, H.-W., Wild, V., Tinker, J. L., Gauthier, J.-R., Helsby, J. E., Shectman, S. A., and Thompson, I. B. (2010) , *ApJL* **724**, L176

Churchill, C., Steidel, C., and Kacprzak, G. (2005) , In *Extra-Planar Gas.* (R. Braun ed.), Vol. 331 of *Astronomical Society of the Pacific Conference Series*, p. 387

Churchill, C. W., Vogt, S. S., and Charlton, J. C. (2003) , *AJ* **125**, 98

Coc, A., Vangioni-Flam, E., Descouvemont, P., Adahchour, A., and Angulo, C. (2004) , *ApJ* **600**, 544

Collins, J. A., Shull, J. M., and Giroux, M. L. (2003) , In *The IGM/Galaxy Connection. The Distribution of Baryons at z=0.* (J. L. Rosenberg & M. E. Putman ed.), Vol. 281 of *Astrophysics and Space Science Library*, p. 169

Collins, J. A., Shull, J. M., and Giroux, M. L. (2004) , *ApJ* **605**, 216

Collins, J. A., Shull, J. M., and Giroux, M. L. (2005) , *ApJ* **623**, 196

Collins, J. A., Shull, J. M., and Giroux, M. L. (2007) , *ApJ* **657**, 271

Collins, J. A., Shull, J. M., and Giroux, M. L. (2009) , *ApJ* **705**, 962

Corbelli, E. and Bandiera, R. (2002) , *ApJ* **567**, 712

Crain, R. A., Theuns, T., Dalla Vecchia, C., Eke, V. R., Frenk, C. S., Jenkins, A., Kay, S. T., Peacock, J. A., Pearce, F. R., Schaye, J., Springel, V., Thomas, P. A., White, S. D. M., and Wiersma, R. P. C. (2009) , *MNRAS* **399**, 1773

Cruddace, R., Paresce, F., Bowyer, S., and Lampton, M. (1974) , *ApJ* **187**, 497

Danforth, C. W. (2009) , In *American Institute of Physics Conference Series.* (M. E. van Steenberg, G. Sonneborn, H. W. Moos, and W. P. Blair eds.), Vol. 1135 of *American Institute of Physics Conference Series*, pp. 8–15

Danforth, C. W. and Shull, J. M. (2008) , *ApJ* **679**, 194

Davé, R., Hellsten, U., Hernquist, L., Katz, N., and Weinberg, D. H. (1998) , *ApJ* **509**, 661

Davé, R., Hernquist, L., Katz, N., and Weinberg, D. H. (1999) , *ApJ* **511**, 521

Davé, R. and Oppenheimer, B. D. (2007) , *MNRAS* **374**, 427

Davis, T. M. and Lineweaver, C. H. (2004) , *Publication of the Astronomical Society of Australia* **21**, 97

de Boer, K. S. (2007) , *Physics and the interstellar medium*, Argelander Institute: Universität Bonn

de Heij, V., Braun, R., and Burton, W. B. (2002) , *A&A* **391**, 67

Dicke, R. H., Beringer, R., Kyhl, R. L., and Vane, A. B. (1946) , *Physical Review* **70**, 340

Draganova, N. (2013) , *On the diversity of O VI absorbers at high redshift*

Draine, B. T. (2010) , *Physics of the interstellar and intergalactic medium*

Faber, S. M., Willmer, C. N. A., Wolf, C., Koo, D. C., Weiner, B. J., Newman, J. A., Im, M., Coil, A. L., Conroy, C., Cooper, M. C., Davis, M., Finkbeiner, D. P., Gerke, B. F., Gebhardt, K., Groth, E. J., Guhathakurta, P., Harker, J., Kaiser, N., Kassin, S., Kleinheinrich, M., Konidaris, N. P., Kron, R. G., Lin, L., Luppino, G., Madgwick, D. S., Meisenheimer, K., Noeske, K. G., Phillips, A. C., Sarajedini, V. L., Schiavon, R. P., Simard, L., Szalay, A. S., Vogt, N. P., and Yan, R. (2007) , *ApJ* **665**, 265

Fabian, D., Savage, B. D., Tripp, T. M., Sembach, K. R., and FUSE Science Team (2000) , In *American Astronomical Society Meeting Abstracts #196*, Vol. 32 of *Bulletin of the American Astronomical Society*, p. 711

Ferland, G. J., Porter, R. L., van Hoof, P. A. M., Williams, R. J. R., Abel, N. P., Lykins, M. L., Shaw, G., Henney, W. J., and Stancil, P. C. (2013) , *Instituto de Astronomía, Universidad Nacional Autónoma de México* **49**, 137

Fernández, X., Joung, M. R., and Putman, M. E. (2012) , *ApJ* **749**, 181

Finkbeiner, D. P. (2003) , *ApJS* **146**, 407

Fontana, A. and Ballester, P. (1995) , *The Messenger* **80**, 37

Ford, H. A., Lockman, F. J., and McClure-Griffiths, N. M. (2010) , In *Astronomical Society of the Pacific Conference Series*. (R. Kothes, T. L. Landecker, and A. G. Willis eds.), Vol. 438 of *Astronomical Society of the Pacific Conference Series*, p. 163

Fox, A. J., Petitjean, P., Ledoux, C., and Srianand, R. (2009) , *ApJS* **320**, 27

Fox, A. J., Savage, B. D., and Wakker, B. P. (2006) , *ApJS* **165**, 229

Fox, A. J., Savage, B. D., Wakker, B. P., Richter, P., Sembach, K. R., and Tripp, T. M. (2004) , *ApJ* **602**, 738

Fox, A. J., Wakker, B. P., Smoker, J. V., Richter, P., Savage, B. D., and Sembach, K. R. (2010) , *ApJ* **718**, 1046

Fraternali, F., Binney, J., Oosterloo, T., and Sancisi, R. (2007) , *New Astronomy Review* **51**, 95

Fukugita, M., Hogan, C. J., and Peebles, P. J. E. (1998) , *ApJ* **503**, 518

Galilei, G., Kepler, J., Foscarini, P. A., and Bernegger, M. (1663) , *Systema cosmicvm*

Gamow, G. (1948) , *Nature* **162**, 680

Ganguly, R., Sembach, K. R., Tripp, T. M., and Savage, B. D. (2005) , *ApJS* **157**, 251

Ghavamian, P., Aloisi, A., Lennon, D., Hartig, G., Kriss, G. A., Oliveira, C., Massa, D., Keyes, T., Proffitt, C., Delker, T., and Osterman, S. (2009) , *Preliminary Characterization of the Post- Launch Line Spread Function of COS*, Technical report

Gibson, B. K., Giroux, M. L., Penton, S. V., Stocke, J. T., Shull, J. M., and Tumlinson, J. (2001) , *AJ* **122**, 3280

Grcevich, J. and Putman, M. E. (2009) , *ApJ* **696**, 385

Green, J. C., Froning, C. S., Osterman, S., Ebbets, D., Heap, S. H., Leitherer, C., Linsky, J. L., Savage, B. D., Sembach, K., Shull, J. M., Siegmund, O. H. W., Snow, T. P., Spencer, J., Stern, S. A., Stocke, J., Welsh, B., Béland, S., Burgh, E. B., Danforth, C., France, K., Keeney, B., McPhate, J., Penton, S. V., Andrews, J., Brownsberger, K., Morse, J., and Wilkinson, E. (2012) , *ApJ* **744**, 60

Haardt, F. and Madau, P. (1996) , *ApJ* **461**, 20

Haardt, F. and Madau, P. (2012) , *ApJ* **746**, 125

Harries, T. J., Hilditch, R. W., and Howarth, I. D. (2003) , *MNRAS* **339**, 157

Hartmann, J. (1904) , *ApJ* **19**, 268

Heitsch, F. and Putman, M. E. (2009) , *ApJ* **698**, 1485

Herenz, P., Richter, P., Charlton, J. C., and Masiero, J. R. (2013) , *A&A* **550**, A87

Herschel, J. F. W. (1815) , *Royal Society of London Proceedings Series I* **2**, 334

Hindman, J. V., McGee, R. X., Carter, A. W. L., Holmes, E. C. J., and Beard, M. (1963) , *Australian Journal of Physics* **16**, 552

Hubble, E. P. (1929) , *Leaflet of the Astronomical Society of the Pacific* **1**, 93

Hui, L. and Gnedin, N. Y. (1997) , *MNRAS* **292**, 27

Jaacks, J., Choi, J.-H., Nagamine, K., Thompson, R., and Varghese, S. (2012) , *MNRAS* **420**, 1606

Jenkins, E. B., Bowen, D. V., Tripp, T. M., and Sembach, K. R. (2005) , *ApJ* **623**, 767

Kacprzak, G. G. and Churchill, C. W. (2011) , *ApJL* **743**, L34

Kacprzak, G. G., Churchill, C. W., Ceverino, D., Steidel, C. C., Klypin, A., and Murphy, M. T. (2010) , *ApJ* **711**, 533

Kacprzak, G. G., Churchill, C. W., Steidel, C. C., and Murphy, M. T. (2008) , *AJ* **135**, 922

Kacprzak, G. G., Churchill, C. W., Steidel, C. C., Murphy, M. T., and Evans, J. L. (2007) , *ApJ* **662**, 909

Kalas, P., Graham, J. R., and Clampin, M. (2005) , *Nature* **435**, 1067

Kalberla, P. M. W. (2003) , *ApJ* **588**, 805

Kalberla, P. M. W., Burton, W. B., Hartmann, D., Arnal, E. M., Bajaja, E., Morras, R., and Pöppel, W. G. L. (2005) , *A&A* **440**, 775

Kalberla, P. M. W. and Haud, U. (2006) , *A&A* **455**, 481

Keeney, B. A., Stocke, J. T., Rosenberg, J. L., Danforth, C. W., Ryan-Weber, E. V., Shull, J. M., Savage, B. D., and Green, J. C. (2013) , *ApJ* **765**, 27

Kepler, J. (1609) , *Astronomia nova.*

Kerp, J., Winkel, B., Ben Bekhti, N., Flöer, L., and Kalberla, P. M. W. (2011) , *Astronomische Nachrichten* **332**, 637

Kerr, F. J. (1958) , *AJ* **63**, 51

Kim, T.-S., Cristiani, S., and D'Odorico, S. (2001) , *A&A* **373**, 757

Kimble, R. A., Woodgate, B. E., and Bowers (1998) , *ApJL* **492**, L83

Komatsu, E., Smith, K. M., Dunkley, J., Bennett, C. L., Gold, B., Hinshaw, G., Jarosik, N., Larson, D., Nolta, M. R., Page, L., Spergel, D. N., Halpern, M., Hill, R. S., Kogut, A., Limon, M., Meyer, S. S., Odegard, N., Tucker, G. S., Weiland, J. L., Wollack, E., and Wright, E. L. (2011) , *ApJS* **192**, 18

Lehner, N. (2002) , *ApJ* **578**, 126

Lehner, N., Howk, J. C., Thom, C., Fox, A. J., Tumlinson, J., Tripp, T. M., and Meiring, J. D. (2012) , *MNRAS* **424**, 2896

Lehner, N., Howk, J. C., Tripp, T. M., Tumlinson, J., Prochaska, J. X., O'Meara, J. M., Thom, C., Werk, J. K., Fox, A. J., and Ribaudo, J. (2013) , *ApJ* **770**, 138

Lehner, N., Savage, B. D., Richter, P., Sembach, K. R., Tripp, T. M., and Wakker, B. P. (2007) , *ApJ* **658**, 680

Lockman, F. J., Murphy, E. M., Petty-Powell, S., and Urick, V. J. (2002) , *ApJS* **140**, 331

Lu, L., Sargent, W. L. W., Savage, B. D., Wakker, B. P., Sembach, K. R., and Oosterloo, T. A. (1998) , *AJ* **115**, 162

Maloney, P. (1993) , *ApJ* **414**, 41

Marasco, A. and Fraternali, F. (2011) , *A&A* **525**, A134

Mastropietro, C., Moore, B., Mayer, L., Stadel, J., and Wadsley, J. (2004) , In *Satellites and Tidal Streams.* (F. Prada, D. Martinez Delgado, and T. J. Mahoney eds.), Vol. 327 of *Astronomical Society of the Pacific Conference Series*, p. 234

Meiksin, A. A. (2009) , *Reviews of Modern Physics* **81**, 1405

Meiring, J. D., Tripp, T. M., Prochaska, J. X., Tumlinson, J., Werk, J., Jenkins, E. B., Thom, C., O'Meara, J. M., and Sembach, K. R. (2011) , *ApJ* **732**, 35

Milutinović, N., Rigby, J. R., Masiero, J. R., Lynch, R. S., Palma, C., and Charlton, J. C. (2006) , *ApJ* **641**, 190

Misawa, T., Charlton, J. C., Kobulnicky, H. A., Wakker, B. P., and Bland-Hawthorn, J. (2009) , *ApJ* **695**, 1382

Morris, S. L., Weymann, R. J., Dressler, A., McCarthy, P. J., Smith, B. A., Terrile, R. J., Giovanelli, R., and Irwin, M. (1993) , *ApJ* **419**, 524

Mortlock, D., Warren, S., Patel, M., Venemans, B., McMahon, R., Hewett, P., Simpson, C., Theuns, T., Rottgering, H., Kuiper, R., Bolton, J., and Harhnelt, M. (2011) , In *Galaxy Formation*

Morton, D. C. (1991) , *ApJS* **77**, 119

Morton, D. C. (2003) , *ApJS* **149**, 205

Narayanan, A., Charlton, J., Misawa, T., Green, R., and Kim, T.-S. (2008a) , *ApJ* **689**, 782

Narayanan, A., Charlton, J. C., Misawa, T., Green, R. E., and Kim, T.-S. (2008b) , *ApJ* **689**, 782

Narayanan, A., Misawa, T., Charlton, J. C., and Kim, T.-S. (2007) , *ApJ* **660**, 1093

Narayanan, A., Savage, B. D., and Wakker, B. P. (2012) , *ApJ* **752**, 65

Nestor, D. B., Turnshek, D. A., and Rao, S. M. (2005) , *ApJ* **628**, 637

Newton, I. (1722) , *Aritmetica Universalis : sive de compositione et resolutione Aritmetica Liber*

Nielsen, N. M., Churchill, C. W., Kacprzak, G. G., and Murphy, M. T. (2013) , *ApJ*

Norberg, P., Cole, S., Baugh, C. M., Frenk, C. S., Baldry, I., Bland-Hawthorn, J., Bridges, T., Cannon, R., Colless, M., Collins, C., Couch, W., Cross, N. J. G., Dalton, G., De Propris, R., Driver, S. P., Efstathiou, G., Ellis, R. S., Glazebrook, K., Jackson, C., Lahav, O., Lewis, I., Lumsden, S., Maddox, S., Madgwick, D., Peacock, J. A., Peterson, B. A., Sutherland, W., Taylor, K., and 2DFGRS Team (2002) , *MNRAS* **336**, 907

O'Meara, J. M., Tytler, D., Kirkman, D., Suzuki, N., Prochaska, J. X., Lubin, D., and Wolfe, A. M. (2001) , *ApJ* **552**, 718

Oosterloo, T., Fraternali, F., and Sancisi, R. (2007) , *AJ* **134**, 1019

Oppenheimer, B. D. and Davé, R. (2009) , *MNRAS* **395**, 1875

Oppenheimer, B. D., Davé, R., Katz, N., Kollmeier, J. A., and Weinberg, D. H. (2012) , *MNRAS* **420**, 829

Penton, S. V., Stocke, J. T., and Shull, J. M. (2004) , *ApJS* **152**, 29

Penzias, A. A. and Wilson, R. W. (1965) , *ApJ* **142**, 419

Petitjean, P., Webb, J. K., Rauch, M., Carswell, R. F., and Lanzetta, K. (1993) , *MNRAS* **262**, 499

Planck Collaboration, Ade, P. A. R., Aghanim, N., Armitage-Caplan, C., Arnaud, M., Ashdown, M., Atrio-Barandela, F., Aumont, J., Baccigalupi, C., Banday, A. J., and et al. (2013) , *ArXiv e-prints, submitted to A&A* , 67 [arXiv:1303.5076]

Portas, A., Brinks, E., Usero, A., Walter, F., de Blok, W. J. G., and Kennicutt, Jr., R. C. (2009) , In *IAU Symposium*. (J. Andersen, J. Bland-Hawthorn, and B. Nordström eds.), Vol. 254 of *IAU Symposium*, p. 52P

Press, W. H. and Schechter, P. (1974) , *ApJ* **187**, 425

Prochaska, J. X., Weiner, B., Chen, H.-W., Mulchaey, J., and Cooksey, K. (2011) , *ApJ* **740**, 91

Prochter, G. E., Prochaska, J. X., and Burles, S. M. (2006) , *ApJ* **639**, 766

Putman, M. E. (2004) , In *High Velocity Clouds*. (H. van Woerden, B. P. Wakker, U. J. Schwarz, and K. S. de Boer eds.), Vol. 312 of *Astrophysics and Space Science Library*, p. 101

Putman, M. E., Bland-Hawthorn, J., Veilleux, S., Gibson, B. K., Freeman, K. C., and Maloney, P. R. (2003) , *ApJ* **597**, 948

Putman, M. E., de Heij, V., Staveley-Smith, L., Braun, R., Freeman, K. C., Gibson, B. K., Burton, W. B., Barnes, D. G., Banks, G. D., Bhathal, R., de Blok, W. J. G., Boyce, P. J., Disney, M. J., Drinkwater, M. J., Ekers, R. D., Henning, P. A., Jerjen, H., Kilborn, V. A., Knezek, P. M., Koribalski, B., Malin, D. F., Marquarding, M., Minchin, R. F., Mould, J. R., Oosterloo, T., Price, R. M., Ryder, S. D., Sadler, E. M., Stewart, I., Stootman, F., Webster, R. L., and Wright, A. E. (2002) , *AJ* **123**, 873

Putman, M. E., Peek, J. E. G., and Joung, M. R. (2012) , *ARAA* **50**, 491

Putman, M. E., Peek, J. E. G., Muratov, A., Gnedin, O. Y., Hsu, W., Douglas, K. A., Heiles, C., Stanimirovic, S., Korpela, E. J., and Gibson, S. J. (2009) , *ApJ* **703**, 1486

Rao, S. M., Belfort-Mihalyi, M., Turnshek, D. A., Monier, E. M., Nestor, D. B., and Quider, A. (2011) , *MNRAS* **416**, 1215

Rao, S. M., Sardane, G., Turnshek, D. A., Thilker, D., Walterbos, R., Vanden Berk, D., and York, D. G. (2013) , *MNRAS*

Ribaudo, J., Lehner, N., and Howk, J. C. (2011a) , *ApJ* **736**, 42

Ribaudo, J., Lehner, N., Howk, J. C., Werk, J. K., Tripp, T. M., Prochaska, J. X., Meiring, J. D., and Tumlinson, J. (2011b) , *ApJ* **743**, 207

Richter, P. (2006) , *ArXiv Astrophysics e-prints*, 32 [arXiv:astro-ph/0602343]

Richter, P. (2012) , *ApJ* **750**, 165

Richter, P., Charlton, J. C., Fangano, A. P. M., Bekhti, N. B., and Masiero, J. R. (2009) , *ApJ* **695**, 1631

Richter, P. and de Boer, K. S. (2004) , In *High Velocity Clouds*. (H. van Woerden, B. P. Wakker, U. J. Schwarz, & K. S. de Boer ed.), Vol. 312 of *Astrophysics and Space Science Library*, p. 183

Richter, P., de Boer, K. S., Widmann, H., Kappelmann, N., Gringel, W., Grewing, M., and Barnstedt, J. (1999) , *Nature* **402**, 386

Richter, P., Fox, A. J., Wakker, B. P., Lehner, N., Howk, J. C., Bland-Hawthorn, J., Ben Bekhti, N., and Fechner, C. (2013) , *ApJ* **772**, 111

Richter, P., Krause, F., Fechner, C., Charlton, J. C., and Murphy, M. T. (2011) , *A&A* **528**, A12

Richter, P., Paerels, F. B. S., and Kaastra, J. S. (2008) , *Space Sci Rev* **134**, 25

Richter, P., Savage, B. D., Sembach, K. R., and Tripp, T. M. (2006) , *A&A* **445**, 827

Richter, P., Savage, B. D., Tripp, T. M., and Sembach, K. R. (2004) , *ApJS* **153**, 165

Richter, P., Sembach, K. R., Wakker, B. P., Savage, B. D., Tripp, T. M., Murphy, E. M., Kalberla, P. M. W., and Jenkins, E. B. (2001) , *ApJ* **559**, 318

Riess, A. G., Filippenko, A. V., Challis, P., Clocchiatti, A., Diercks, A., Garnavich, P. M., Gilliland, R. L., Hogan, C. J., Jha, S., Kirshner, R. P., Leibundgut, B., Phillips, M. M., Reiss, D., Schmidt, B. P., Schommer, R. A., Smith, R. C., Spyromilio, J., Stubbs, C., Suntzeff, N. B., and Tonry, J. (1998) , *AJ* **116**, 1009

Rigby, J. R., Charlton, J. C., and Churchill, C. W. (2002) , *ApJ* **565**, 743

Rudie, G. C., Steidel, C. C., Shapley, A. E., and Pettini, M. (2013) , *ApJ* **769**, 146

Ryan-Weber, E. V., Webster, R. L., and Staveley-Smith, L. (2003) , *MNRAS* **343**, 1195

Sancisi, R., Fraternali, F., Oosterloo, T., and van der Hulst, T. (2008) , *Astronomy and Astrophysics Reviews* **15**, 189

Saul, D. R., Peek, J. E. G., Grcevich, J., Putman, M. E., Douglas, K. A., Korpela, E. J., Stanimirović, S., Heiles, C., Gibson, S. J., Lee, M., Begum, A., Brown, A. R. H., Burkhart, B., Hamden, E. T., Pingel, N. M., and Tonnesen, S. (2012) , *ApJ* **758**, 44

Savage, B. D., Kim, T.-S., Keeney, B., Narayanan, A., Stocke, J., Syphers, D., and Wakker, B. P. (2012) , *ApJ* **753**, 80

Savage, B. D., Lehner, N., and Narayanan, A. (2011a) , *ApJ* **743**, 180

Savage, B. D., Lehner, N., Wakker, B. P., Sembach, K. R., and Tripp, T. M. (2005) , *ApJ* **626**, 776

Savage, B. D., Narayanan, A., Lehner, N., and Wakker, B. P. (2011b) , *ApJ* **731**, 14

Savage, B. D. and Sembach, K. R. (1991) , *ApJ* **379**, 245

Schaye, J., Aguirre, A., Kim, T.-S., Theuns, T., Rauch, M., and Sargent, W. L. W. (2003) , *ApJ* **596**, 768

Schneider, P. (2006) , *Einführung in die extragalaktische Astronomie und Kosmologie*

Schruba, A. (2013) , In *IAU Symposium*. (T. Wong and J. Ott eds.), Vol. 292 of *IAU Symposium*, pp. 311–318

Sembach, K. R., Gibson, B. K., Fenner, Y., and Putman, M. E. (2002) , *ApJ* **572**, 178

Sembach, K. R., Howk, J. C., Savage, B. D., and Shull, J. M. (2001) , *AJ* **121**, 992

Sembach, K. R., Savage, B. D., Lu, L., and Murphy, E. M. (1999) , *ApJ* **515**, 108

Sembach, K. R., Tripp, T. M., Savage, B. D., and Richter, P. (2004a) , *ApJS* **155**, 351

Sembach, K. R., Wakker, B. P., Savage, B. D., Richter, P., Meade, M., Shull, J. M., Jenkins, E. B., Sonneborn, G., and Moos, H. W. (2003) , *ApJS* **146**, 165

Sembach, K. R., Wakker, B. P., Tripp, T. M., Richter, P., Kruk, J. W., Blair, W. P., Moos, H. W., Savage, B. D., Shull, J. M., York, D. G., Sonneborn, G., Hébrard, G., Ferlet, R., Vidal-Madjar, A., Friedman, S. D., and Jenkins, E. B. (2004b) , *ApJS* **150**, 387

Shone, A. M., Morris, S. L., Crighton, N., and Wilman, R. J. (2010) , *MNRAS* **402**, 2520

Shull, J. M., Jones, J. R., Danforth, C. W., and Collins, J. A. (2009) , *ApJ* **699**, 754

Shull, J. M., Smith, B. D., and Danforth, C. W. (2012a) , *ApJ* **759**, 23

Shull, J. M., Stevans, M., Danforth, C., Penton, S. V., Lockman, F. J., and Arav, N. (2011) , *ApJ* **739**, 105

Shull, J. M., Stevans, M., and Danforth, C. W. (2012b) , *ApJ* **752**, 162

Sing, D. K., Vidal-Madjar, A., Désert, J.-M., Lecavelier des Etangs, A., and Ballester, G. (2008) , *ApJ* **686**, 658

Spinrad, H., Filippenko, A. V., Yee, H. K., Ellingson, E., Blades, J. C., Bahcall, J. N., Jannuzi, B. T., Bechtold, J., and Dobrzycki, A. (1993) , *AJ* **106**, 1

Spitzer, Jr., L. (1956) , *ApJ* **124**, 20

Springel, V., Frenk, C. S., and White, S. D. M. (2006) , *Nature* **440**, 1137

Steidel, C. C. (1995) , In *QSO Absorption Lines*. (G. Meylan ed.), p. 139

Steidel, C. C., Kollmeier, J. A., Shapley, A. E., Churchill, C. W., Dickinson, M., and Pettini, M. (2002) , *ApJ* **570**, 526

Stocke, J. T., Keeney, B. A., Danforth, C. W., Shull, J. M., Froning, C. S., Green, J. C., Penton, S. V., and Savage, B. D. (2013) , *ApJ* **763**, 148

Stocke, J. T., Penton, S. V., Danforth, C. W., Shull, J. M., Tumlinson, J., and McLin, K. M. (2006) , *ApJ* **641**, 217

Stocke, J. T., Shull, J. M., and Penton, S. V. (2004) , *ArXiv Astrophysics e-prints*, 25 [arXiv:astro-ph/0407352]

Su, M., Slatyer, T. R., and Finkbeiner, D. P. (2010) , *ApJ* **724**, 1044

Tempel, E., Tamm, A., and Tenjes, P. (2010) , *A&A* **509**, A91

Tepper-García, T., Richter, P., and Schaye, J. (2013) , *MNRAS*

Tepper-García, T., Richter, P., Schaye, J., Booth, C. M., Dalla Vecchia, C., Theuns, T., and Wiersma, R. P. C. (2011) , *MNRAS* **413**, 190

Thilker, D. A., Braun, R., Walterbos, R. A. M., Corbelli, E., Lockman, F. J., Murphy, E., and Maddalena, R. (2004) , *ApJL* **601**, L39

Thom, C., Peek, J. E. G., Putman, M. E., Heiles, C., Peek, K. M. G., and Wilhelm, R. (2008) , *ApJ* **684**, 364

Tilton, E. M., Danforth, C. W., Shull, J. M., and Ross, T. L. (2012) , *ApJ* **759**, 112

Tripp, T. (2008) , In *37th COSPAR Scientific Assembly*, Vol. 37 of *COSPAR Meeting*, p. 3212

Tripp, T. M., Bowen, D. V., Sembach, K. R., Jenkins, E. B., Savage, B. D., and Richter, P. (2004) , *ArXiv Astrophysics e-prints*, 12 [arXiv:astro-ph/0411151]

Tripp, T. M., Sembach, K. R., Bowen, D. V., Savage, B. D., Jenkins, E. B., Lehner, N., and Richter, P. (2008) , *ApJS* **177**, 39

Tripp, T. M., Wakker, B. P., Jenkins, E. B., Bowers, C. W., Danks, A. C., Green, R. F., Heap, S. R., Joseph, C. L., Kaiser, M. E., Linsky, J. L., and Woodgate, B. E. (2003) , *AJ* **125**, 3122

Tumlinson, J., Thom, C., Werk, J. K., Prochaska, J. X., Tripp, T. M., Weinberg, D. H., Peeples, M. S., O'Meara, J. M., Oppenheimer, B. D., Meiring, J. D., Katz, N. S., Davé, R., Ford, A. B., and Sembach, K. R. (2011) , *Science* **334**, 948

Tytler, D., Burles, S., Lu, L., Fan, X.-M., Wolfe, A., and Savage, B. D. (1999) , *AJ* **117**, 63

van den Bergh, S. (1999) , *Journal of the Royal Astronomical Society of Canada* **93**, 175

Wakker, B. P. (1991) , In *The Interstellar Disk-Halo Connection in Galaxies*. (H. Bloemen ed.), Vol. 144 of *IAU Symposium*, pp. 27–40

Wakker, B. P. (2001a) , *ApJS* **136**, 463

Wakker, B. P. (2001b) , *ArXiv Astrophysics e-prints*, 6 [arXiv:astro-ph/0109210]

Wakker, B. P. (2004) , In *Recycling Intergalactic and Interstellar Matter*. (P.-A. Duc, J. Braine, and E. Brinks eds.), Vol. 217 of *IAU Symposium*, p. 2

Wakker, B. P., Lockman, F. J., and Brown, J. M. (2011) , *ApJ* **728**, 159

Wakker, B. P. and Savage, B. D. (2009) , *ApJS* **182**, 378

Wakker, B. P., York, D. G., Howk, J. C., Barentine, J. C., Wilhelm, R., Peletier, R. F., van Woerden, H., Beers, T. C., Ivezić, Ž., Richter, P., and Schwarz, U. J. (2007) , *ApJL* **670**, L113

Wakker, B. P., York, D. G., Wilhelm, R., Barentine, J. C., Richter, P., Beers, T. C., Ivezić, Ž., and Howk, J. C. (2008) , *ApJ* **672**, 298

Welty, D. E., Frisch, P. C., Sonneborn, G., and York, D. G. (1999) , *ApJ* **512**, 636

Westmeier, T. and Koribalski, B. (2008) , *ATNF Proposal* p. 1700

Weymann, R. J., Jannuzi, B. T., Lu, L., Bahcall, J. N., Bergeron, J., Boksenberg, A., Hartig, G. F., Kirhakos, S., Sargent, W. L. W., Savage, B. D., Schneider, D. P., Turnshek, D. A., and Wolfe, A. M. (1998) , *ApJ* **506**, 1

Wilson, G., Kaiser, N., Luppino, G. A., and Cowie, L. L. (2001) , *ApJ* **555**, 572

Winkel, B., Ben Bekhti, N., Darmstädter, V., Flöer, L., Kerp, J., and Richter, P. (2011) , *A&A* **533**, A105

Wolfire, M. G., McKee, C. F., Hollenbach, D., and Tielens, A. G. G. M. (1995) , *ApJ* **453**, 673

Wright, E. L. (2006) , *PASP* **118**, 1711

Yao, Y., Shull, J. M., Danforth, C. W., Keeney, B. A., and Stocke, J. T. (2011) , *ApJ* **730**, 143

Zaninetti, L. (2008) , *AJ* **135**, 1264

Zschaechner, L. K., Rand, R. J., Heald, G. H., Gentile, G., and Józsa, G. (2012) , *ApJ* **760**, 37

Zwaan, M. A., van der Hulst, J. M., Briggs, F. H., Verheijen, M. A. W., and Ryan-Weber, E. V. (2005) , *MNRAS* **364**, 1467

Zwicky, F. (1933) , *Helvetica Physica Acta* **6**, 110

Declaration

I Peter Herenz, confirm that this work submitted for assessment is my own and is expressed in my own words. It has not been presented for a degree to any institution before. Any uses made within of the works of other authors in any form (e.g. ideas, equations, figures, text, tables, programes) are properly acknowledged at the point of their use. A full list of references employed has been included.

Signed:

Date: January 8, 2014

Appendix A

Supplementary material on HVCs

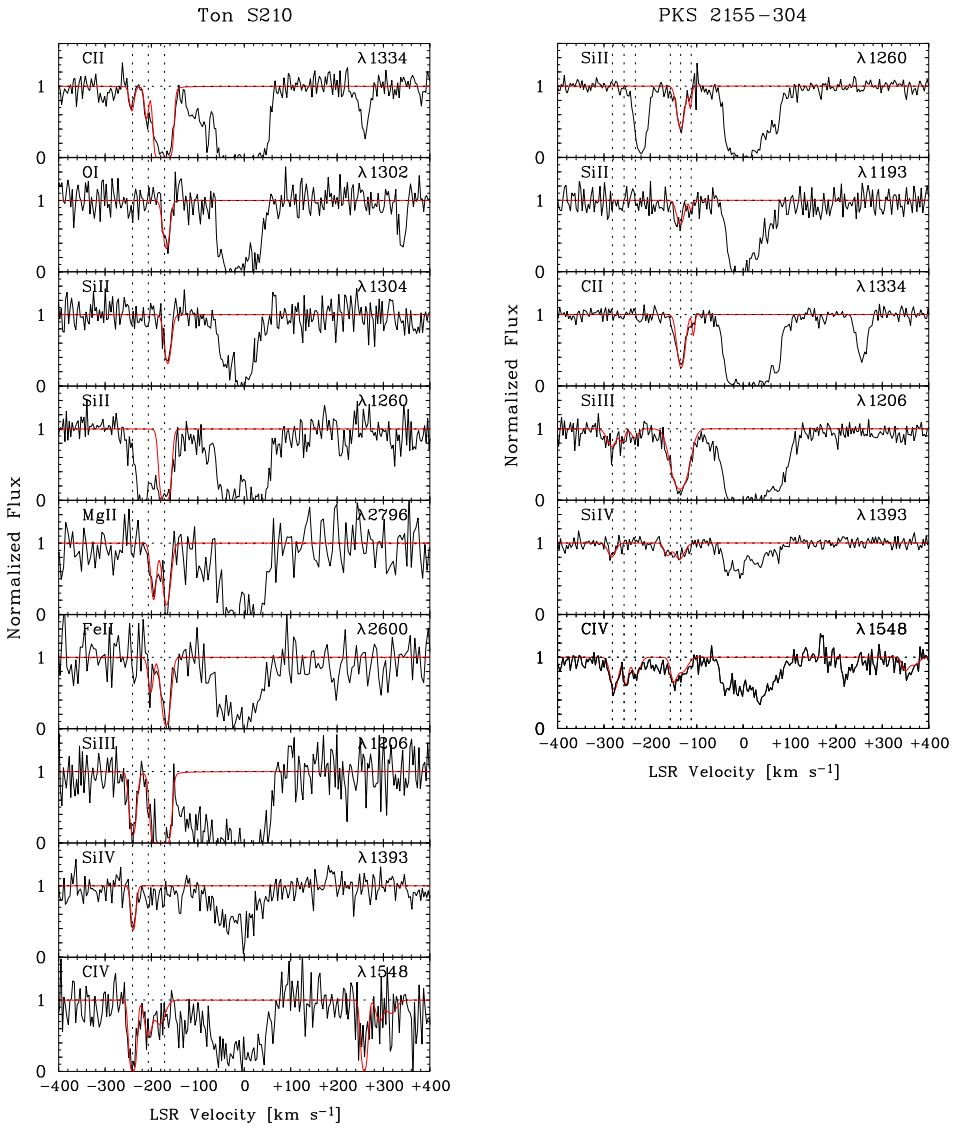

Figure 6.2: Additional continuum-normalized absorption profiles of weakly and highly ionized species towards different QSO sightlines recorded with the E140M and E230M echelle gratings of STIS. The data are plotted against the LSR radial velocity. Identified HVC absorption components are marked with dashed lines. The red plotted lines render the best Voigt-profile fit.

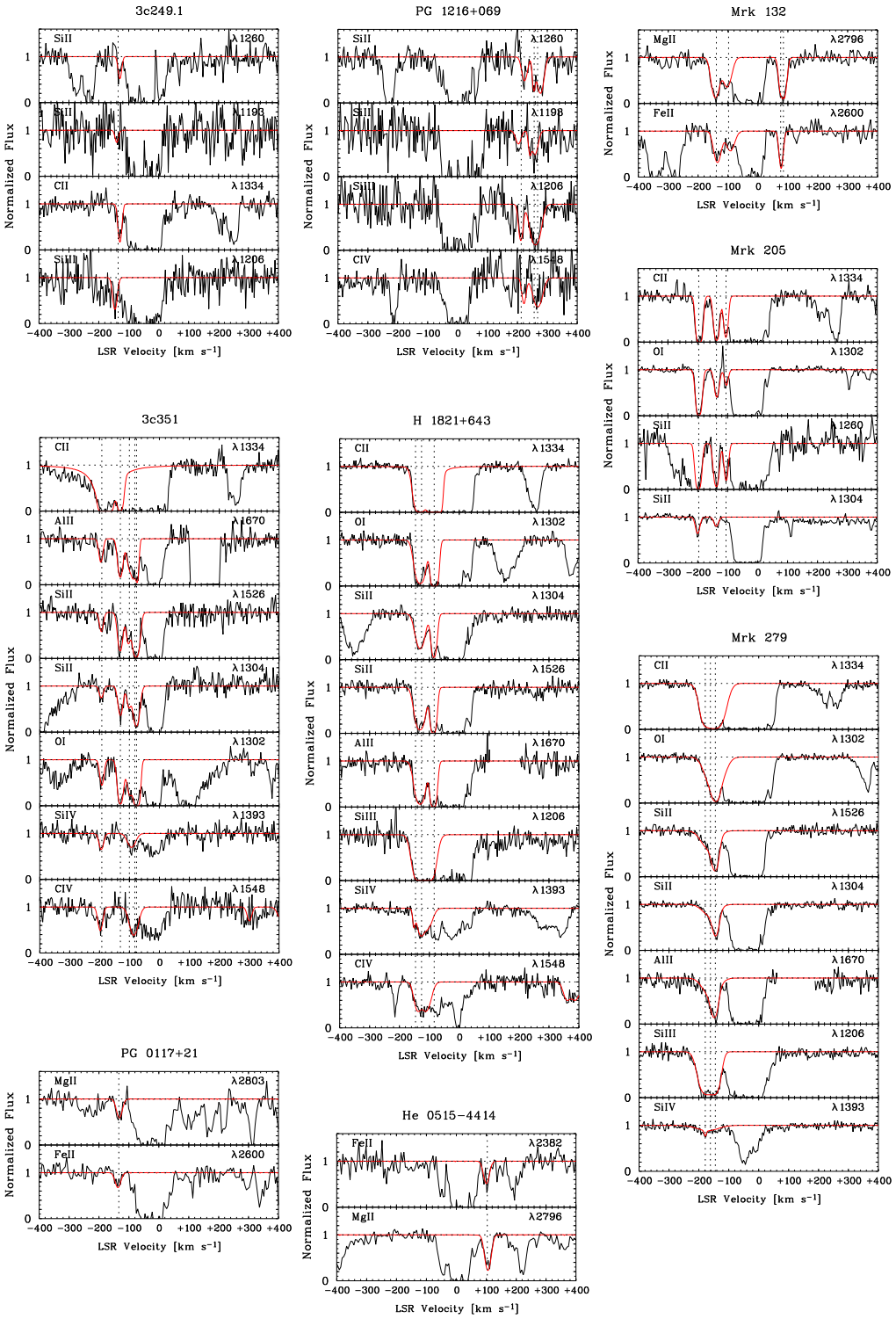

Figure 6.3: Continuum-normalized absorption profiles of weakly and highly ionized species towards different QSO sightlines recorded with the E140M and E230M echelle gratings of STIS. The data are plotted against the LSR radial velocity. Identified HVC absorption components are marked with dashed lines. The red plotted lines render the best Voigt-profile fit.

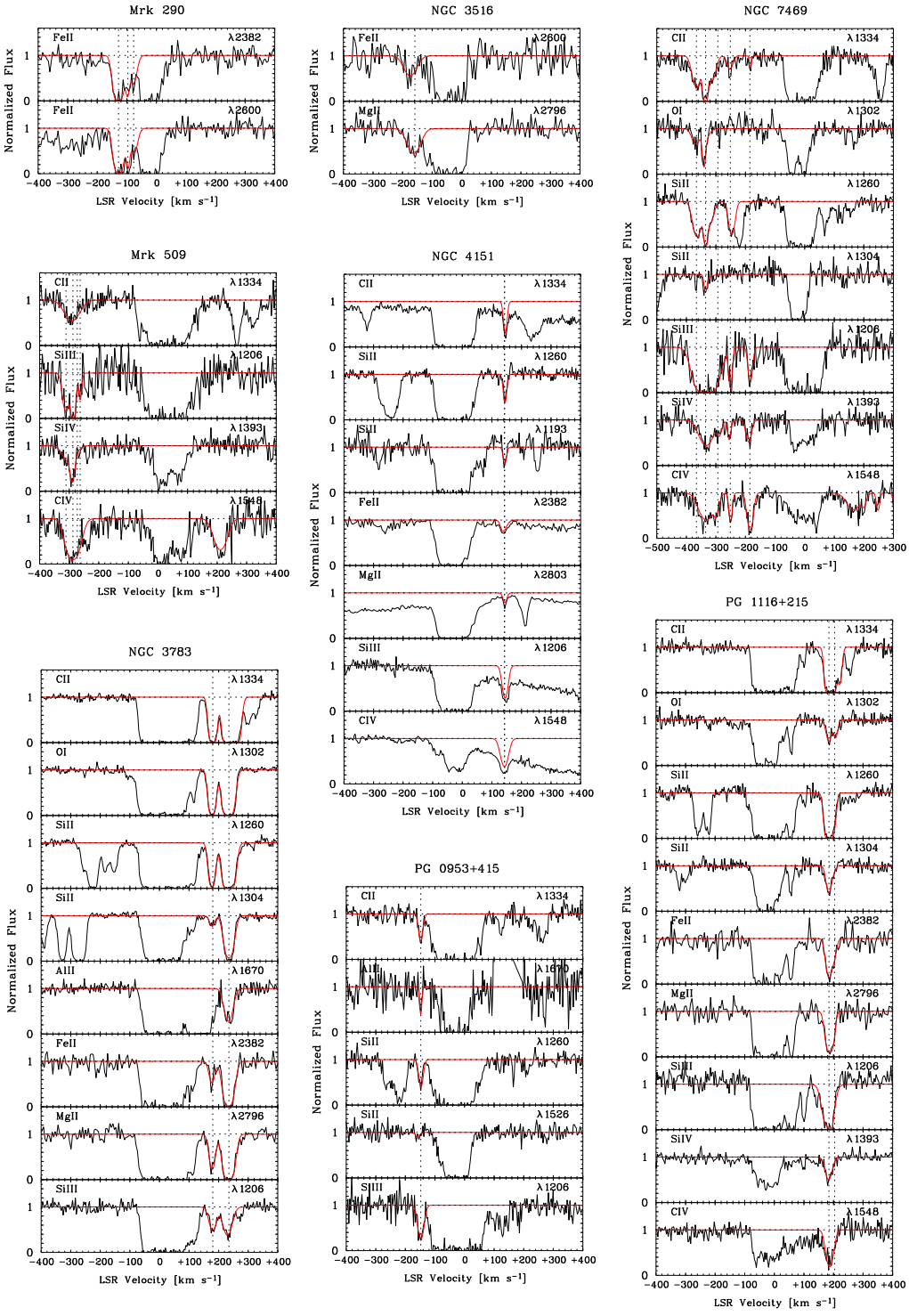

Figure 6.4: Additional continuum-normalized absorption profiles of weakly and highly ionized species towards different QSO sightlines recorded with the E140M and E230M echelle gratings of STIS. The data are plotted against the LSR radial velocity. Identified HVC absorption components are marked with dashed lines. The red plotted lines render the best Voigt-profile fit.

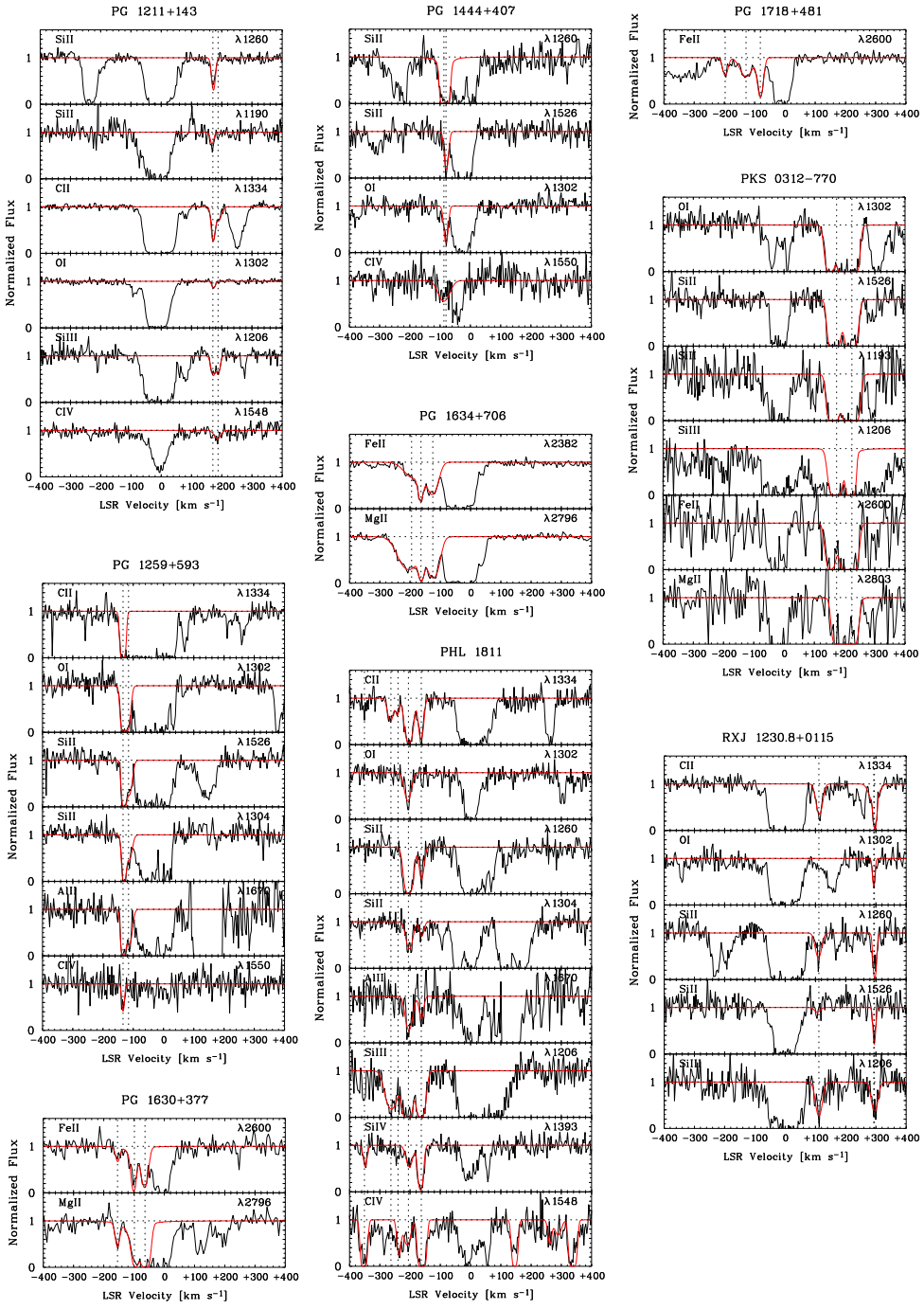

Figure 6.5: Additional continuum-normalized absorption profiles of weakly and highly ionized species towards different QSO sightlines recorded with the E140M and E230M echelle gratings of STIS. The data are plotted against the LSR radial velocity. Identified HVC absorption components are marked with dashed lines. The red plotted lines render the best Voigt-profile fit.

Table 6.1: Summary of HVC absorption-line measurements[a] - part I

Sightline	$v_{\rm LSR}$ [km s^{-1}]	Ion	log N [N in cm^{-2}]	b [km s^{-1}]
PKS 0312−770	+174	Si II	14.92±0.95	14.2±5.9
		C II	13.82±1.06	14.2±5.9
		O I	14.99±0.14	14.2±5.9
		Fe II	13.97±0.26	14.2±5.9
		Mg II	15.22±0.34	14.2±5.9
		Si III	...	...
	+224	Si II	14.73±0.33	16.6±3.1
		O I	14.76±1.02	16.6±3.1
		Mg II	15.08±0.29	16.6±3.1
		Fe II	15.05±0.41	16.6±3.1
		Si III	...	...
PG 0953+415	−147	Si II	12.60±0.06	8.5±1.5
		C II	13.52±0.07	8.5±1.5
		Si III	12.77±0.09	11.9±2.5
3C249.1	−135	Si II	12.37±0.08	6.6±1.7
		C II	13.75±0.07	6.6±1.7
		Si III	12.59±0.18	8.6±5.4
3C351	−193	Si II	13.20±0.06	7.9±1.3
		C II	...	...
		O I	13.89±0.05	7.9±1.3
		Al II	12.17±0.07	7.9±1.3
		Si III	14.52±0.59	8.6±1.2
		Si IV	12.62±0.10	9.5±3.7
		C IV	13.23±0.08	9.5±3.7
	−130	Si II	13.80±0.05	9.4±0.9
		C II	14.31±0.26	9.4±0.9
		O I	14.58±0.07	9.4±0.9
		Al II	12.64±0.06	9.4±0.9
	−101	Si II	14.19±0.06	11.6±1.0
		O I	14.30±0.07	11.6±1.0
		Al II	12.49±0.07	11.6±1.0
	−82	Si II	13.51±0.10	7.8±1.3
		Al II	12.54±0.12	7.8±1.3
		O I	15.14±0.26	7.8±1.3
		Si IV	12.79±0.07	17.8±0.8
		C IV	13.60±0.06	17.8±0.8
	−76	Al II	12.73±0.41	4.0±1.3
PG 1116+215	+184	Si II	13.80±0.03	11.3±0.7
		C II	15.29±0.09	11.3±0.7
		O I	13.91±0.05	11.3±0.7
		Fe II	13.36±0.19	11.3±0.7
		Mg II	12.99±0.24	11.3±0.7
		Si III	13.23±0.25	20.0±4.0
		Si IV	12.99±0.05	14.6±2.3
		C IV	13.76±0.07	14.6±2.3
	+203	Si II	12.64±0.27	7.9±3.3
		C II	13.76±0.05	7.9±3.3
		O I	13.66±0.07	7.9±3.3
		Fe II	12.57±0.48	7.9±3.3
		Mg II	12.74±0.41	7.9±3.3
		Si III	14.42±1.13	4.0±3.6

[a] We do not list column-density limits based on saturated lines.

Table 6.2: Summary of HVC absorption-line measurements[a] - part II

Sightline	$v_{\rm LSR}$ [km s^{-1}]	Ion	log N [N in cm^{-2}]	b [km s^{-1}]
PG 1259+593	−134	Si II	14.60±0.56	5.6±1.6
		C II	15.20±0.51	5.6±1.6
		Al II	13.44±0.44	5.6±1.6
		O I	14.31±0.52	5.6±1.6
	−116	Si II	13.72±0.16	10.8±3.7
		O I	14.69±0.32	10.8±3.7
		Al II	12.58±0.12	10.8±3.7
PG 1634+706	−195	Fe II	13.19±0.05	41.1±2.3
		Mg II	13.30±0.03	41.1±2.3
	−164	Fe II	13.15±0.07	8.2±1.7
		Mg II	13.08±0.12	8.2±1.7
	−125	Fe II	13.36±0.03	22.0±1.3
		Mg II	13.28±0.02	22.0±1.3
PG 1718+481	−197	Fe II	12.80±0.05	10.2±2.5
	−128	Fe II	13.17±0.04	25.4±3.7
	−81	Fe II	13.37±0.05	9.7±1.0
PHL 1811	−351	Si III	...	...
		Si IV	12.68±0.13	7.3±3.6
		C IV	14.57±0.19	7.3±3.6
	−263	C II	13.52±0.16	11.4±5.6
		Si III	13.14±0.07	22.9±3.3
	−240	C II	13.13±0.37	6.9±4.3
		C IV	13.43±0.11	6.9±4.3
	−206	Si II	13.48±0.06	13.7±2.0
		C II	14.25±0.10	13.7±2.0
		O I	14.15±0.05	13.7±2.0
		Al II	12.63±0.13	13.7±2.0
		C IV	13.41±0.08	13.7±2.0
		Si IV	12.92±0.09	13.7±2.0
		Si III	13.61±0.21	13.7±2.0
	−163	Si II	12.70±0.09	8.7±1.6
		C II	13.92±0.10	8.7±1.6
		Al II	12.16±0.19	8.7±1.6
		Si III	13.39±0.23	13.5±3.5
		Si IV	13.48±0.27	8.3±2.3
		C IV	15.00±0.17	8.3±2.3
H 1821+643	−146	Si IV	12.40±0.13	3.8±1.6
	−126	Si II	14.21±0.02	18.5±0.9
		C II	14.62±0.03	18.5±0.9
		O I	14.78±0.04	18.5±0.9
		Al II	13.09±0.04	18.5±0.9
		Si III	...	...
		C IV	13.47±0.06	14.2±4.8
		Si IV	13.03±0.06	14.2±4.8
	−84	Si II	14.28±0.08	9.4±1.0
		C II	...	...
		O I	15.33±0.25	9.4±1.0
		Al II	13.24±0.20	9.4±1.0

[a] We do not list column-density limits based on saturated lines.

Table 6.3: Summary of HVC absorption-line measurements[a] - part III

Sightline	$v_{\rm LSR}$ [km s^{-1}]	Ion	log N [N in cm^{-2}]	b [km s^{-1}]
PG 0117+21	−134	Mg II	12.72±0.06	11.1±2.1
		Fe II	12.73±0.10	11.1±2.1
PG 1211+143	+170	Si II	12.64±0.04	6.7±0.8
		C II	13.61±0.03	6.7±0.8
		O I	13.14±0.06	6.7±0.8
		Si III	12.28±0.14	9.2±3.5
	+188	C IV	12.81±0.13	14.3±6.0
		Si III	12.11±0.19	6.5±3.2
		C II	13.24±0.07	11.6±2.1
PG 1216+069	+267	Si II	12.98±0.08	12.7±2.6
	+256	Si II	12.60±0.17	4.8±2.5
		Si III	13.16±0.09	19.2±2.9
		C IV	13.65±0.11	19.1±6.1
	+212	Si II	12.60±0.09	11.3±3.1
		Si III	12.69±0.13	8.1±2.5
		C IV	13.23±0.14	8.1±2.5
PG 1444+407	−88	C IV	13.82±0.12	24.3±8.3
	−81	Si II	13.69±0.25	7.5±2.4
		C II	...	...
		O I	14.16±0.05	7.5±2.4
PG 1630+377	−155	Fe II	12.60±0.15	7.5±2.3
		Mg II	12.47±0.09	7.5±2.3
	−99	Fe II	...	...
		Mg II	...	...
	−64	Fe II	13.49±0.12	11.5±9.8
		Mg II	13.72±0.45	11.5±9.8
RXJ 1230.8+0115	+111	Si II	12.66±0.07	12.6±2.9
		C II	13.74±0.04	12.6±2.9
		Si III	12.77±0.10	12.6±2.9
	+292	C II	13.60±0.10	18.6±5.0
	+295	Si II	13.55±0.13	3.7±0.5
		C II	14.34±0.36	3.7±0.5
		O I	13.77±0.12	3.7±0.5
		Si III	12.66±0.11	13.0±4.2
NGC 3516	−158	Mg II	12.94±0.07	27.6±5.7
		Fe II	13.25±0.07	27.6±5.7
NGC 3783	+180	Si II	13.31±0.03	11.2±0.6
		O I	14.84±0.04	11.2±0.6
		Mg II	12.88±0.05	11.2±0.6
		Fe II	12.86±0.08	11.2±0.6
		C II	14.57±0.04	11.2±0.6
		Si III	12.60±0.04	15.2±2.0
	+234	Si II	13.88±0.04	17.4±0.9
		C II	...	...
		Mg II	13.61±0.05	17.4±0.9
		Al II	12.72±0.04	17.4±0.9
		Fe II	13.84±0.06	17.4±0.9
		O I	15.13±0.03	17.4±0.9
		Si III	12.81±0.03	19.0±1.8

[a] We do not list column-density limits based on saturated lines.

Table 6.4: Summary of HVC absorption-line measurements[a] - part IV

Sightline	$v_{\rm LSR}$ [km s^{-1}]	Ion	log N [N in cm^{-2}]	b [km s^{-1}]
NGC 4151	+143	Si II	12.53±0.04	6.4±1.0
		C II	13.56±0.04	6.4±1.0
		Mg II	12.23±0.04	6.4±1.0
		Fe II	12.00±0.04	6.4±1.0
		C IV	13.56±0.06	16.2±2.5
		Si III	12.71±0.04	11.3±0.8
		Fe II	12.38±0.28	13.2±8.1
NGC 7469	−366	Si II	13.07±0.05	17.0±1.8
		C II	13.91±0.04	17.0±1.8
		O I	13.89±0.09	17.0±1.8
	−335	Si II	13.29±0.15	5.3±1.3
		C II	15.07±0.32	5.3±1.3
		O I	14.11±0.17	5.3±1.3
		Si III	...	...
		Si IV	13.37±0.06	30.1±5.5
		C IV	13.80±0.04	30.1±5.5
	−293	Si III	...	...
		Si IV	12.55±0.23	10.1±4.3
		C IV	13.12±0.14	10.1±4.3
	−251	Si II	12.88±0.05	12.3±1.7
		C II	13.25±0.08	12.3±1.7
		Si III	...	...
		Si IV	12.60±0.11	6.2±2.3
		C IV	13.22±0.08	6.2±2.3
	−185	C II	12.86±0.60	1.7±4.1
		Si III	...	...
		C IV	13.67±0.06	11.5±2.5
		Si IV	12.88±0.08	11.5±2.5
HE 0515−4414	+103	Fe II	12.88±0.09	11.3±0.9
		Mg II	12.88±0.03	11.3±0.9
PKS 2155−304	−280	Si III	12.12±0.12	13.1±4.6
		Si IV	12.36±0.07	10.5±1.4
		C IV	13.19±0.04	10.5±1.4
	−254	C IV	12.89±0.09	5.5±1.7
		Si III	11.69±0.21	6.2±3.3
	−232	C IV	12.88±0.11	10.8±3.8
		Si III	11.67±0.22	9.3±5.0
	−157	Si IV	12.21±0.12	8.4±3.4
		C IV	12.91±0.26	8.4±3.4
	−135	Si IV	12.54±0.07	13.8±6.8
		C IV	12.88±0.27	13.8±6.8
		Si II	12.63±0.02	9.6±0.8
		C II	13.75±0.08	9.6±0.8
		Si III	13.15±0.05	21.7±2.0
	−111	Si II	11.79±0.15	1.0±1.6
		C II	13.17±0.15	1.0±1.6

[a] We do not list column-density limits based on saturated lines.

Table 6.5: Summary of HVC absorption-line measurements[a] - part V

Sightline	$v_{\rm LSR}$ [km s^{-1}]	Ion	log N [N in cm^{-2}]	b [km s^{-1}]
Mrk 132	+76	Mg II	12.63±0.84	5.8±3.0
		Fe II	13.28±0.12	5.8±3.0
	+85	Mg II	12.95±0.45	8.2±4.5
	−139	Mg II	13.10±0.08	14.1±2.5
		Fe II	13.28±0.07	14.1±2.5
	−98	Mg II	12.87±0.11	17.5±6.9
		Fe II	13.05±0.08	17.5±6.9
Mrk 205	−197	Si II	13.41±0.03	8.8±0.7
		C II	14.59±0.08	8.8±0.7
		O I	14.77±0.03	8.8±0.7
	−138	Si II	13.13±0.04	9.3±0.9
		C II	14.14±0.06	9.3±0.9
		O I	14.00±0.02	9.3±0.9
	−106	Si II	12.81±0.11	7.4±2.1
		C II	13.90±0.07	7.4±2.1
		O I	13.57±0.04	7.4±2.1
Mrk 279	−179	Si IV	11.87±0.19	3.3±3.5
		Si III	...	...
	−161	Si II	13.76±0.09	33.6±2.5
		Al II	12.59±0.16	33.6±2.5
		C II	...	...
		O I	14.69±0.05	33.6±2.5
		Si III	...	...
		Si IV	12.74±0.08	33.6±2.5
	−145	Si II	13.89±0.06	13.1±1.4
		C II	13.59±0.20	13.1±1.4
		O I	14.49±0.12	13.1±1.4
		Al II	12.69±0.15	13.1±1.4
		Si III	...	...
Mrk 290	−128	Fe II	...	...
	−97	Fe II	...	...
	−78	Fe II	...	...
Mrk 509	−311	Si III	12.93±0.15	12.7±5.7
	−287	Si III	14.23±0.77	4.7±4.0
		Si IV	13.01±0.16	7.6±2.1
	−273	C II	13.90±0.06	27.1±4.3
		C IV	14.16±0.04	27.1±5.8
		Si IV	13.06±0.13	27.1±5.8
	−263	Si III	12.31±0.21	5.2±3.2
Ton S210	−241	Si III	12.83±0.16	7.5±2.1
		C II	13.06±0.10	5.6±2.1
		Si IV	12.81±0.10	5.6±1.9
		C IV	14.35±0.33	5.6±1.9
	−207	C II	13.16±0.19	4.5±2.8
		Mg II	12.85±0.35	4.5±2.8
		Fe II	12.79±0.25	4.5±2.8
		Si III	12.55±0.66	9.0±5.6
		C IV	13.20±0.16	9.0±5.6
	−172	Si II	13.81±0.08	8.3±1.3
		C II	...	...
		O I	14.05±0.08	8.3±1.3
		Mg II	12.94±0.20	8.3±1.3
		Fe II	13.62±0.24	8.3±1.3
		Si III	13.54±0.44	14.4±11.1
		C IV	13.15±0.16	14.4±11.1

[a] We do not list column-density limits based on saturated lines.

Appendix B

Supplementary material on intervening absorbers

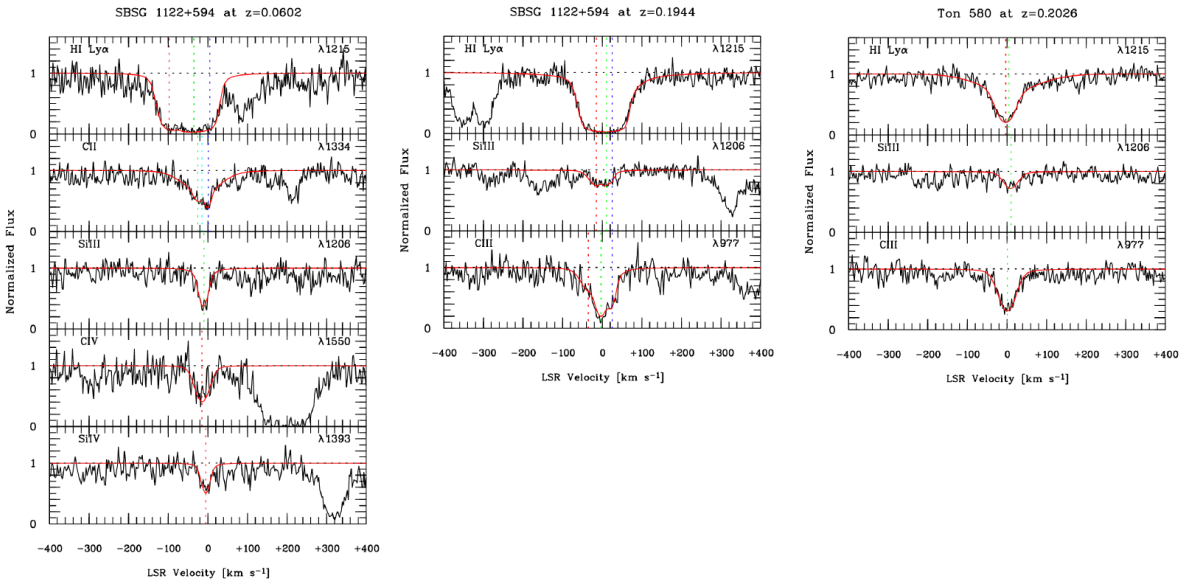

Figure 6.6: Continuum-normalized absorption profiles of low and high ions towards different QSO sightlines recorded with the *HST*/COS instrument. The figures are created with the ESO-*Midas* program using the modeling technique. The red solid lines show the best obtained Voigt-profile model. The vertical dashed lines indicate individual components. Equal colors correspond to the same component.

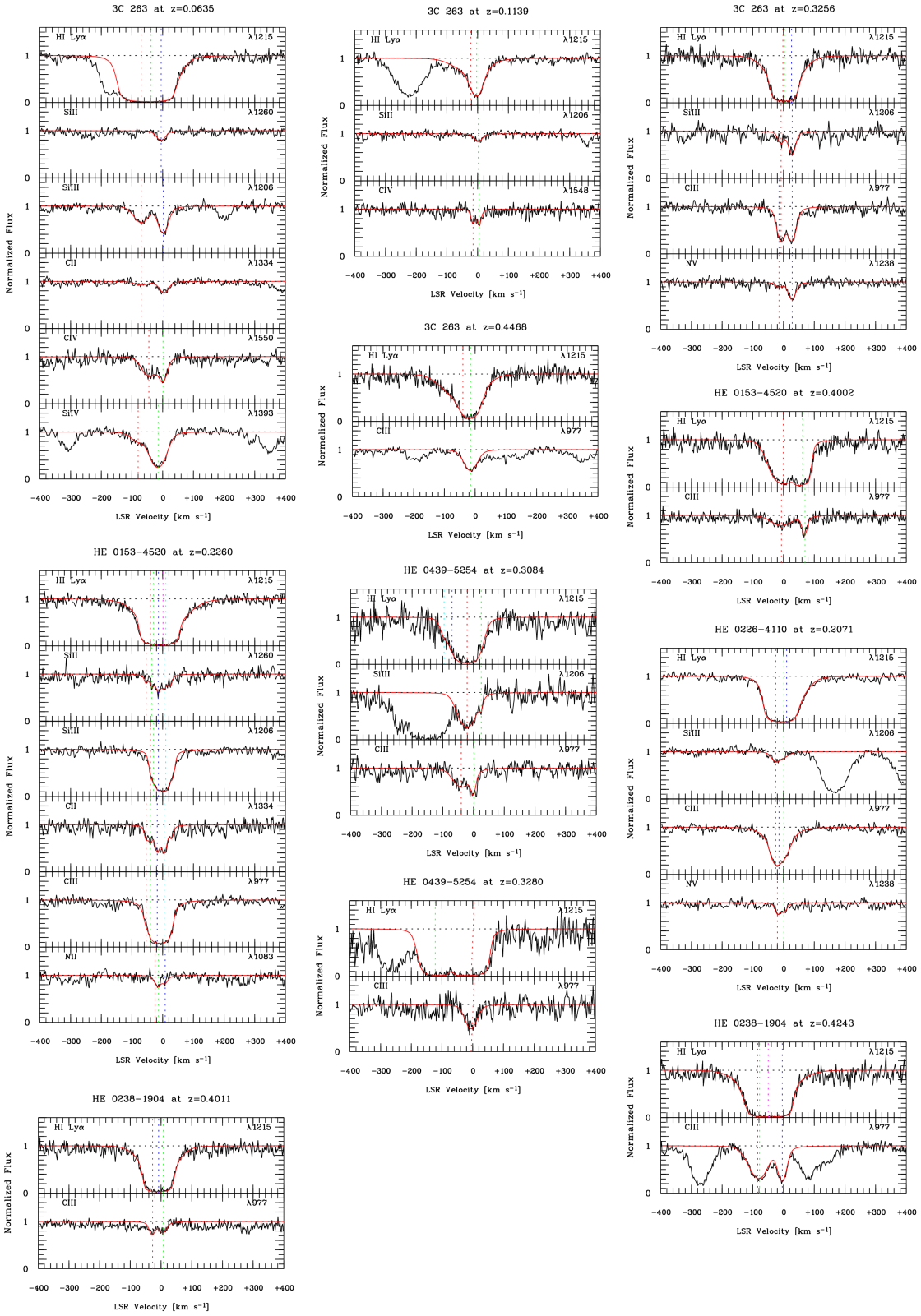

Figure 6.7: Continuum-normalized absorption profiles of low and high ions towards different QSO sightlines recorded with the *HST*/COS instrument. The figures are created with the ESO-*Midas* program using the modeling technique. The red solid lines show the best obtained Voigt-profile model. The vertical dashed lines indicate individual components. Equal colors correspond to the same component.

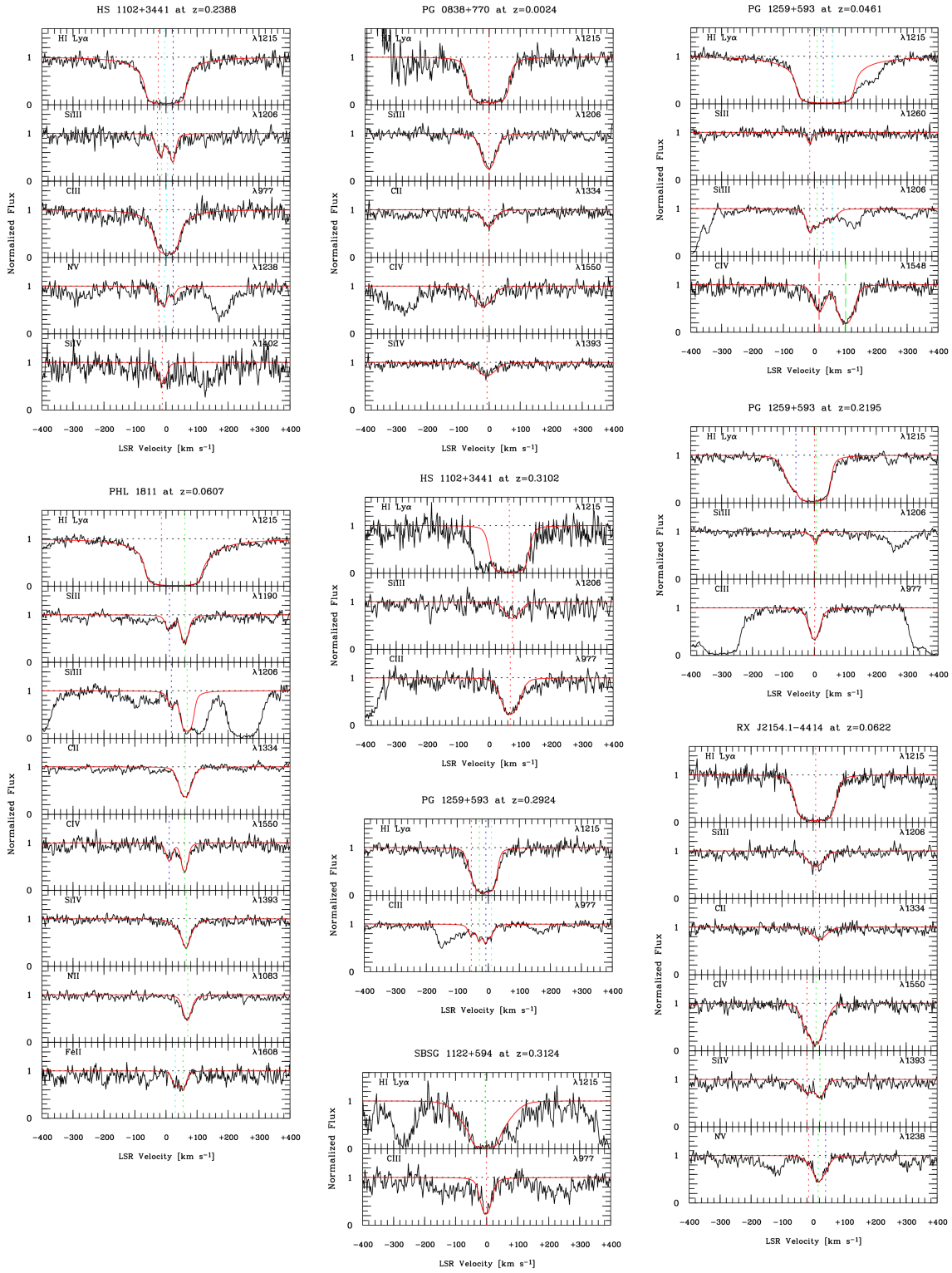

Figure 6.8: Continuum-normalized absorption profiles of low and high ions towards different QSO sightlines recorded with the *HST*/COS instrument. The figures are created with the ESO-*Midas* program using the modeling technique. The red solid lines show the best obtained Voigt-profile model. The vertical dashed lines indicate individual components. Equal colors correspond to the same component.

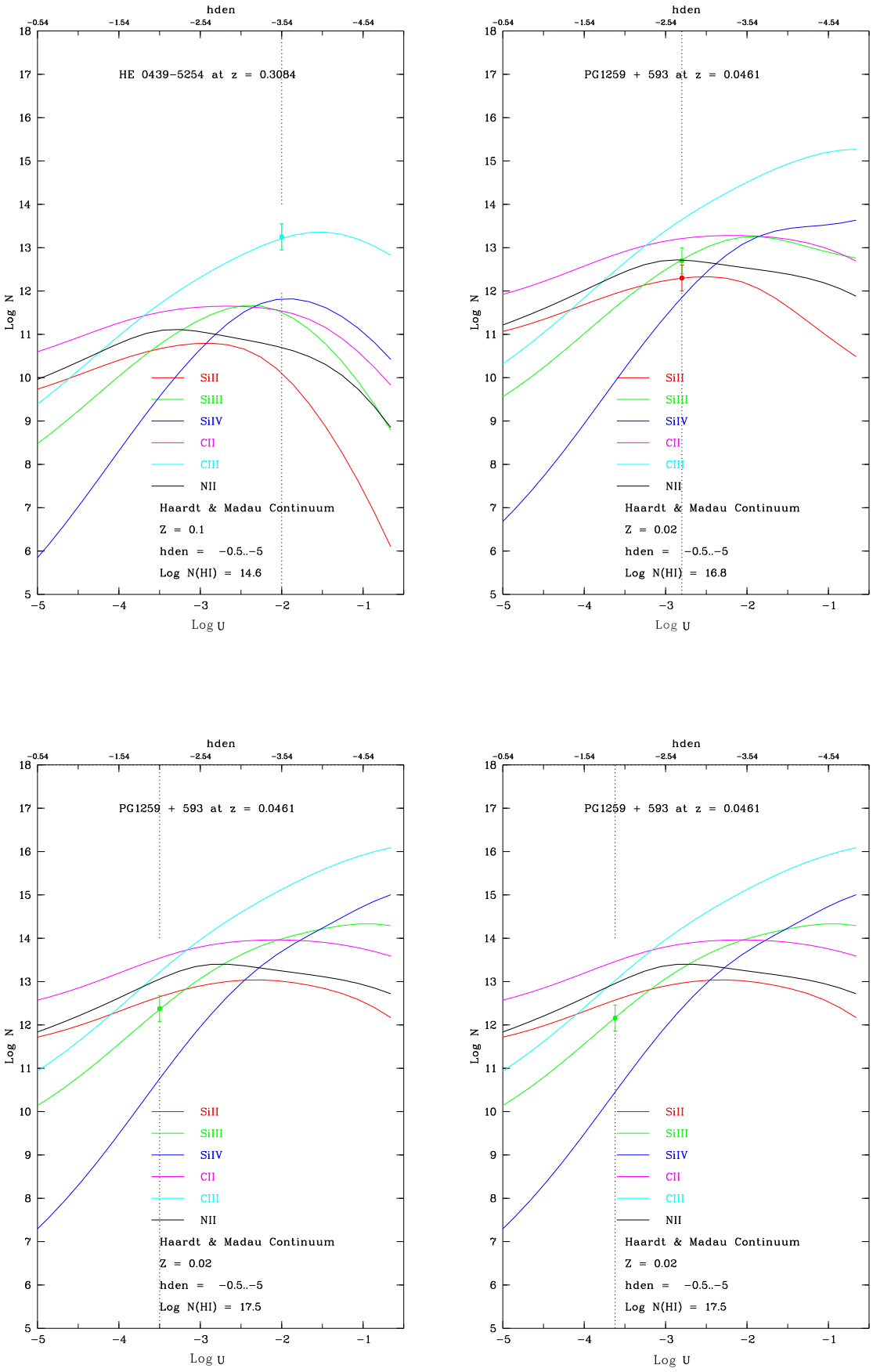

Figure 6.9: Models for the ionization conditions of individual absorption systems derived with the Cloudy program.

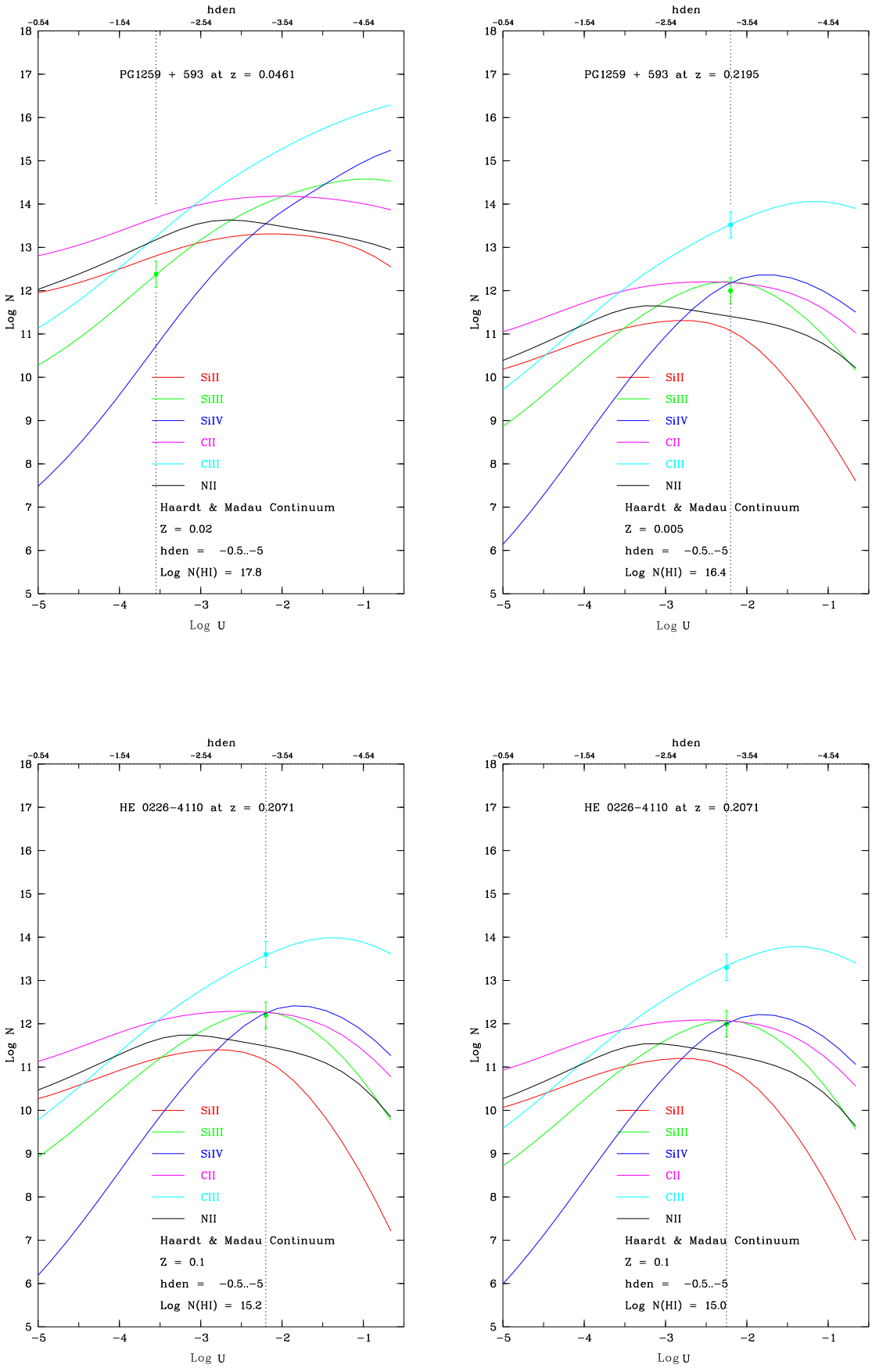

Figure 6.10: Models for the ionization conditions of individual absorption systems derived with the Cloudy program.

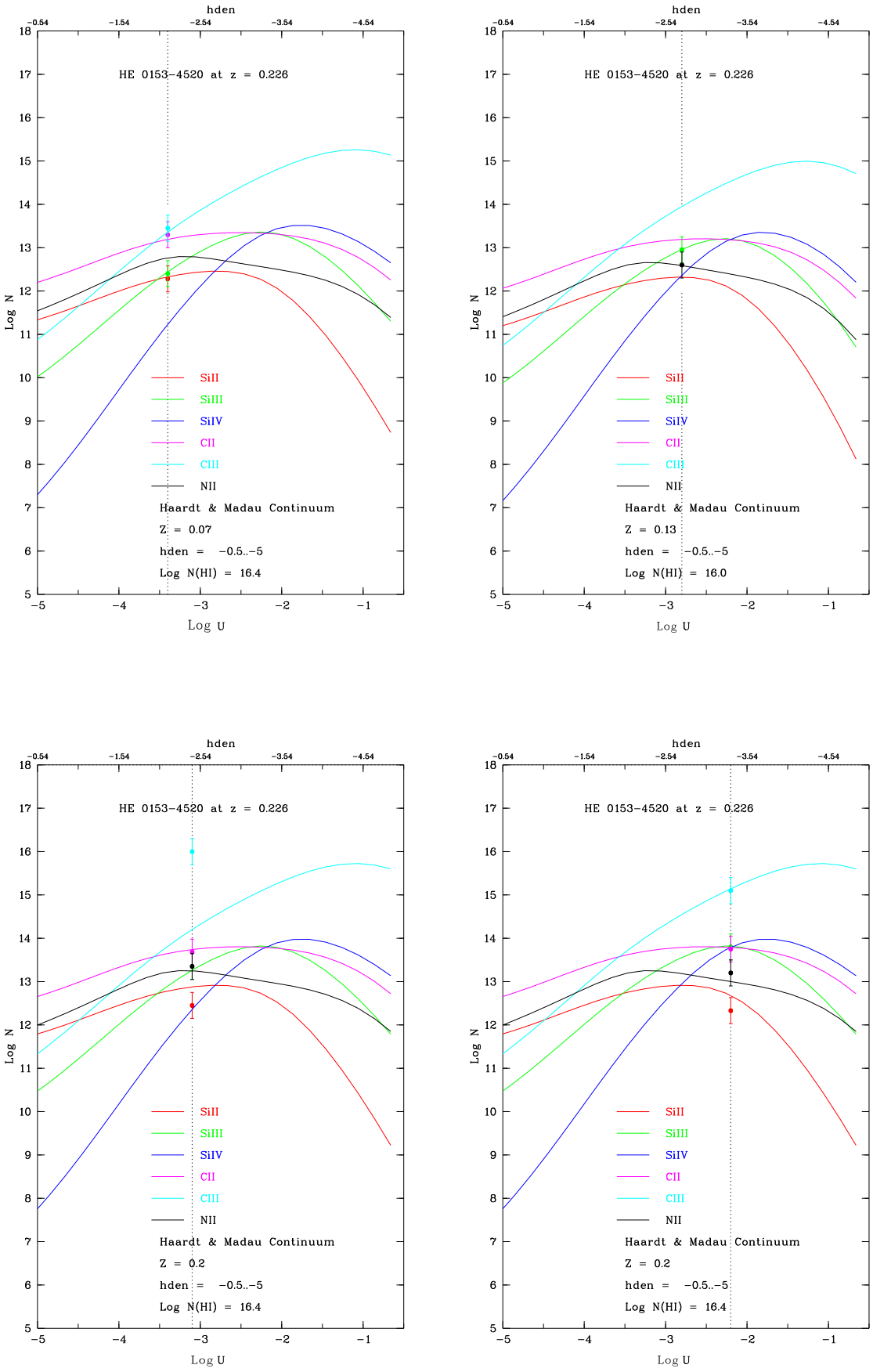

Figure 6.11: Models for the ionization conditions of individual absorption systems derived with the Cloudy program.

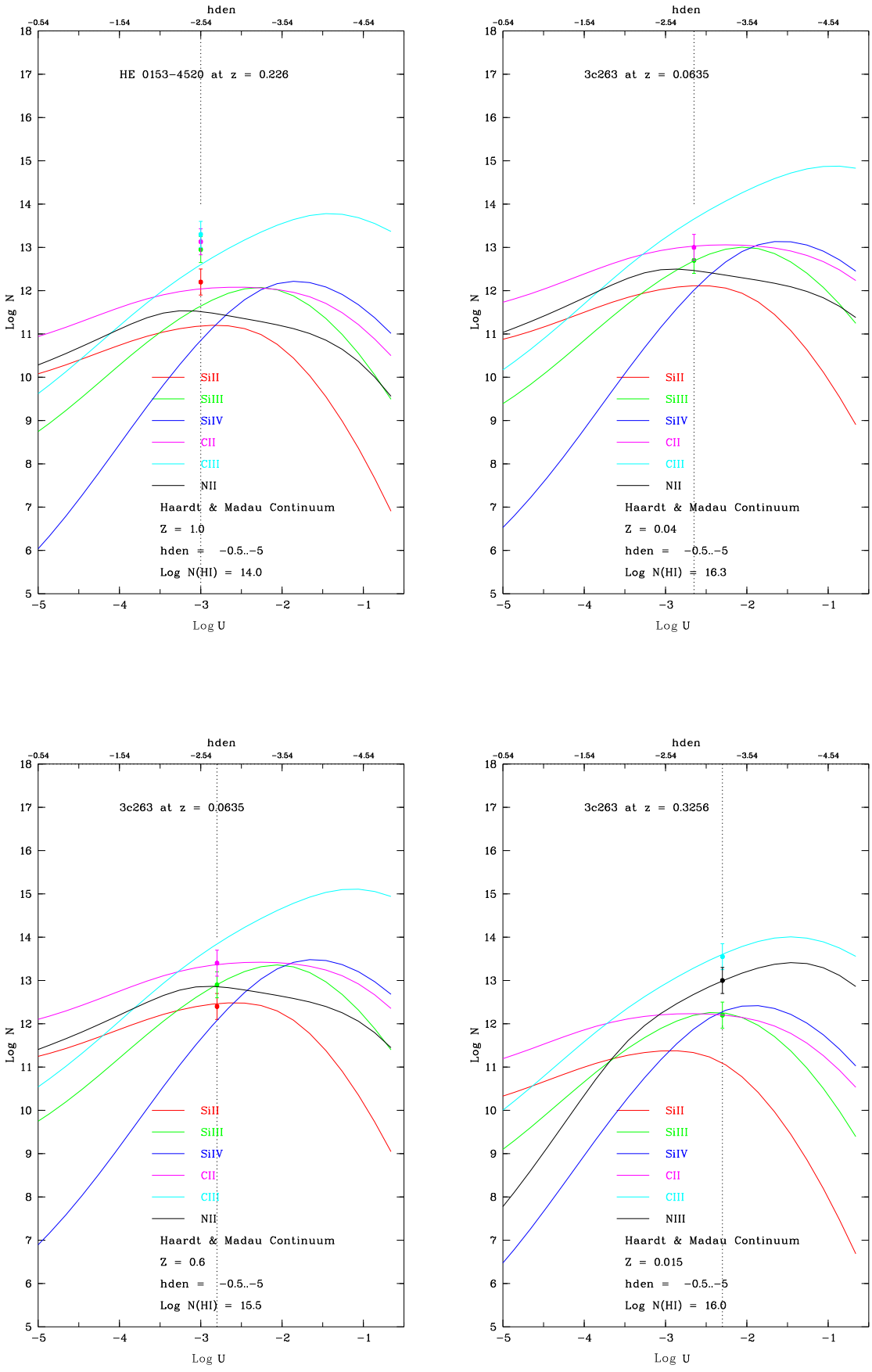

Figure 6.12: Models for the ionization conditions of individual absorption systems derived with the Cloudy program.

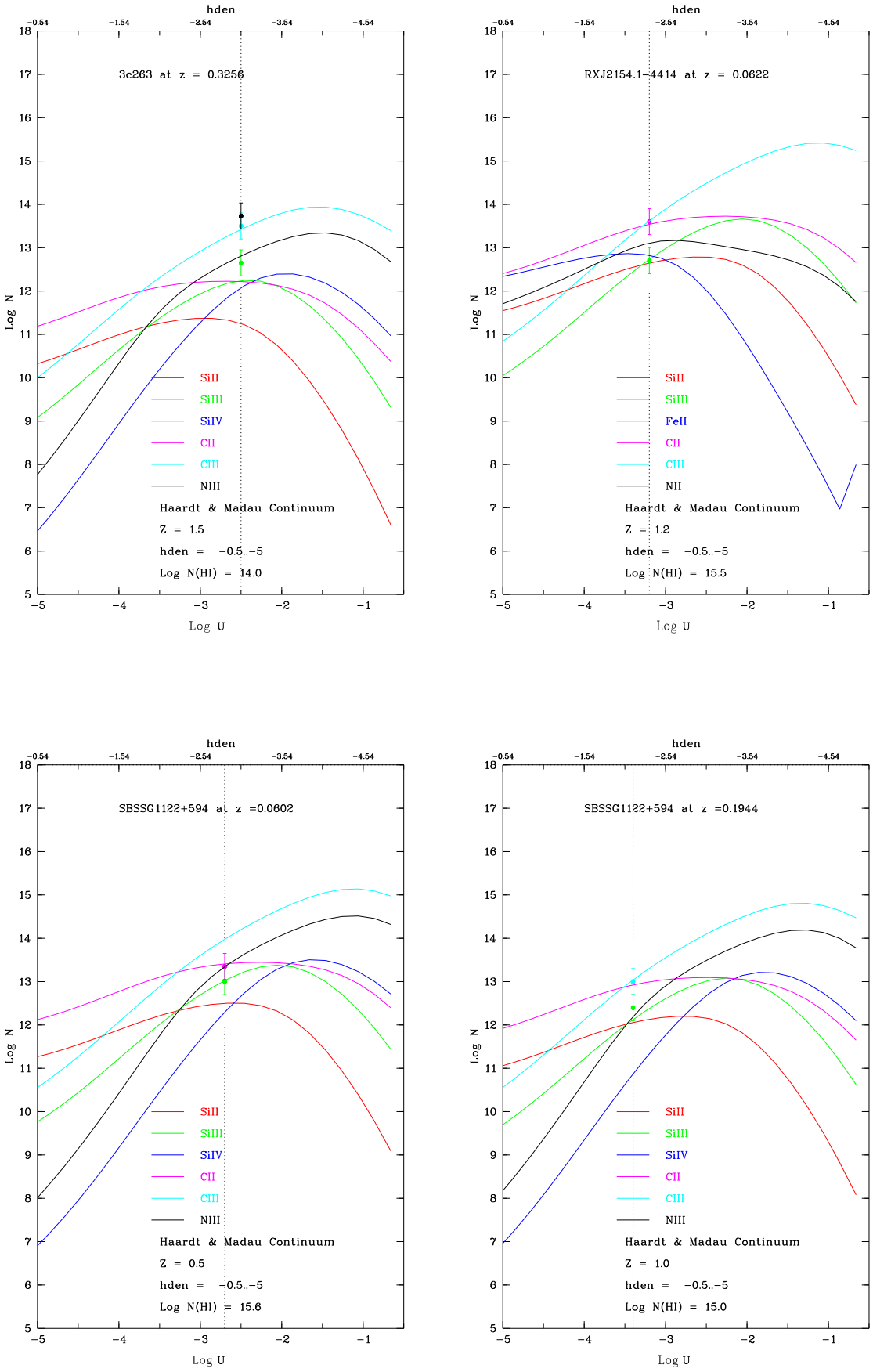

Figure 6.13: Models for the ionization conditions of individual absorption systems derived with the Cloudy program.

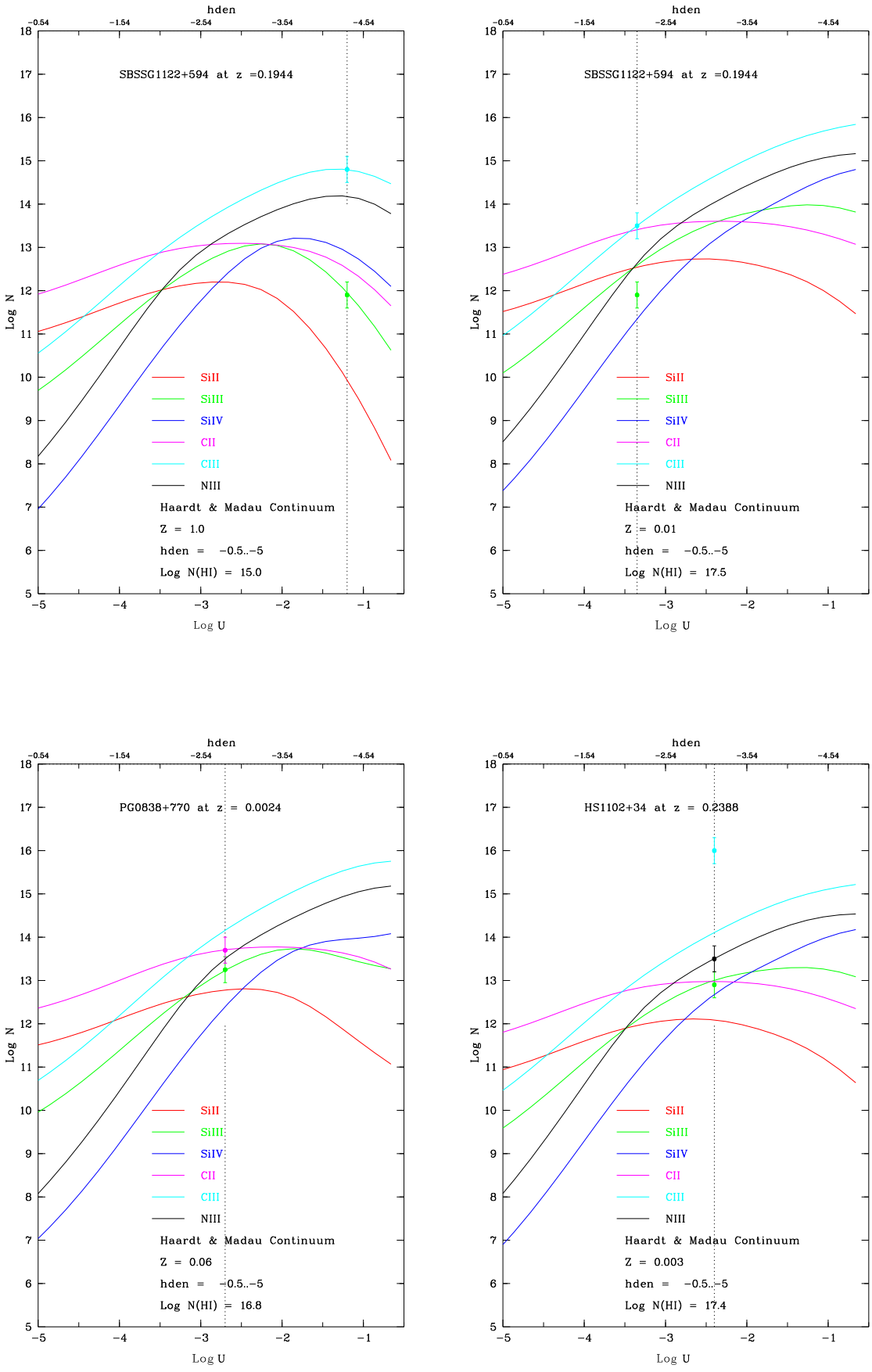

Figure 6.14: Models for the ionization conditions of individual absorption systems derived with the Cloudy program.

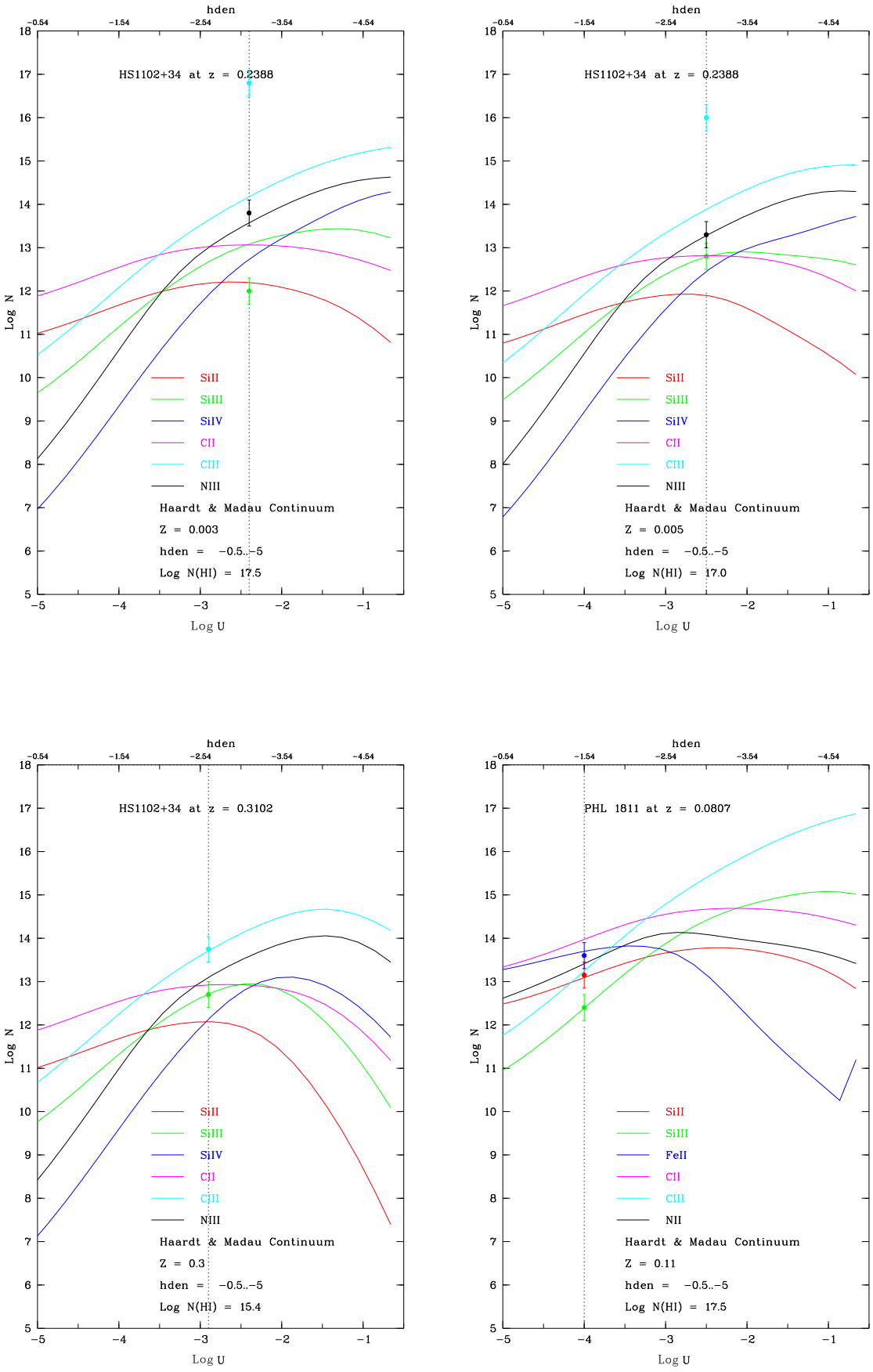

Figure 6.15: Models for the ionization conditions of individual absorption systems derived with the Cloudy program.

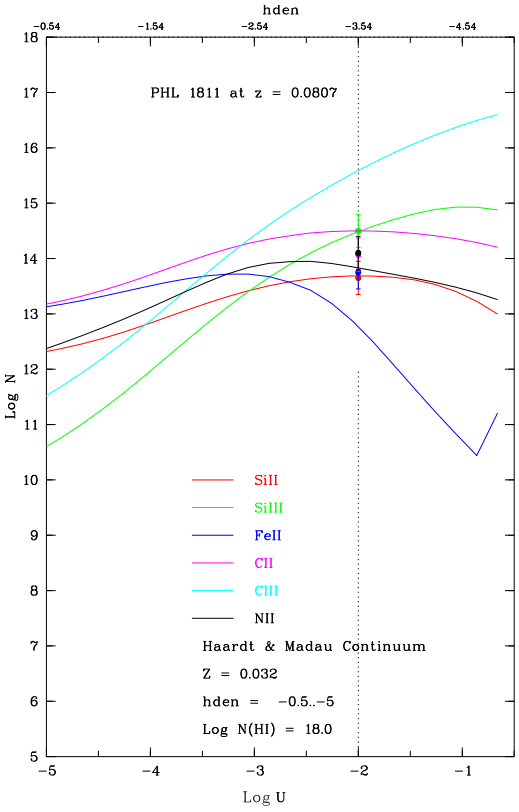

Figure 6.16: Model for the ionization conditions of individual absorption systems derived with the Cloudy program.

Table 6.6: Model data part 1

QSO	z_{abs}	$\bar{v}_{LSR}$ [km s^{-1}]	Ion	b_{turb} [km s^{-1}]	b_{tot} [km s^{-1}]	log N [cm^{-2}]	log U	log n(H) [n(H) in cm^{-3}]	$Z/Z_{\odot}$
HE 0439-5254	0.3084	-95	H I Lyα	5.0	13.83	13.00			
		-70	H I Lyα	11.5	17.28	13.00			
		-27.3	H I Lyα	31.2	33.76	14.60	-2.0[1]	-3.54[1]	0.1[1]
			C III	31.2	31.42	13.25			
			Si III	31.2	31.30	13.25			
		1	C III	1.0	3.86	13.70			
		25	H I Lyα	1.0	12.94	12.60			
			Si III	1.0	2.63	12.20			
	0.3282	-122	H I Lyα	30.0	32.66	14.90			
		-5	H I Lyα	20.0	23.80	16.30			
			C III	20.0	20.34	13.30			
PG 1259+593	0.0461	-15	H I Lyα	6.0	14.23	16.80	-2.8	-2.34	0.02
			Si II	6.0	6.48	12.30			
			Si III	6.0	6.48	12.70			
		9	H I Lyα	5.0	13.83	17.50	-3.5	-2.04	0.02[2]
			Si III	5.0	5.56	12.38			
		15	C IV	21.0	21.33	13.70			
		29	H I Lyα	4.0	13.51	17.50	-3.6	-1.94	0.02[2]
			Si III	4.0	4.68	12.16			
		58	H I Lyα	18.0	22.14	17.80	-3.55	-1.99	0.02[2]
			Si III	18.0	18.16	12.30			
		101	C IV	25.0	25.28	14.15			
	0.2195	-60	H I Lyα	32.0	34.50	13.80			
		1	H I Lyα	15.0	19.78	16.40	-2.2	-3.34	0.005
			Si III	15.0	15.20	12.00			
			C III	15.0	15.46	13.52			
		6	H I Lyα	1.0	12.94	16.40			
			Si III	1.0	2.63	11.90			
	0.2924	-55	H I Lyα	3.0	13.24	13.20			
			C III	3.0	4.78	12.60			
		-29	H I Lyα	1.0	12.94	14.10			
			C III	1.0	3.86	12.85			
		-8	H I Lyα	1.0	12.94	13.60			
			C III	1.0	3.86	12.97			
		10	H I Lyα	1.0	12.94	14.10			
			C III	1.0	3.86	12.50			
HE 0226-4110	0.2071	-25	H I Lyα	15.0	19.78	15.20	-2.2	-3.34	0.1
			Si III	15.0	15.20	12.20			
			C III	15.0	15.46	13.60			
		-20	N V	5.0	6.07	13.10			
		-15	C III	55.0	55.13	13.20			
		1	H I Lyα	20.0	23.80	15.00	-2.25	-3.29	0.1
			Si III	20.0	20.15	12.00			
			C III	20.0	20.34	13.30			
			N V	10.0	10.58	13.10			
		10	H I Lyα	55.0	56.49	14.00			
HE 0153-4520	0.226	-54	C II	1.0	3.86	13.20			
			C III	1.0	3.86	13.00			
			Si II	1.0	2.63	12.05			
		-39	H I Lyα	1.0	12.94	16.40	-3.4	-2.14	0.07
			Si II	1.0	2.63	12.28			
			Si III	1.0	2.63	12.40			
			C II	1.0	3.86	13.30			
			C III	1.0	3.86	13.45			
		-28.3	H I Lyα	1.0	12.94	16.00	-2.8	-2.74	0.13
			Si III	1.0	2.63	12.95			
			N II	1.0	3.59	12.60			
		-15.5	H I Lyα	6.0	14.23	16.40	-3.1[1]	-2.44[1]	0.2[1]
			C II	6.0	7.06	13.68			
			C III	6.0	7.06	16.00			
			Si II	6.0	6.48	12.45			
			Si III	6.0	6.48	13.35			
			N II	6.0	6.92	13.35			
		1	H I Lyα	80.0	81.03	14.00			
		7.2	H I Lyα	7.0	14.68	16.40	-2.2[1]	-3.34[1]	0.2[1]
			C II	7.0	7.93	13.75			
			C III	7.0	7.93	15.10			
			Si II	7.0	7.41	12.33			
			N II	7.0	7.80	13.20			
			Si III	7.0	7.41	13.80			
		30.2	H I Lyα	2.0	13.05	14.00	-3.0	-2.54	1.0
			Si II	2.0	3.15	12.20			
			C II	2.0	4.23	13.13			
			C III	2.0	4.23	13.30			
			Si III	2.0	3.15	12.95			
	0.4002	-4	H I Lyα	40.0	42.00	14.25			
			C III	40.0	40.17	13.00			
		66	H I Lyα	4.0	13.51	15.25			
			C III	4.0	5.47	13.00			

Notes:
[1]) Uncertain value for some reason. See text section for explanations.
[2]) With the metallicity derived from the Si II/Si III ratio from another component in this system.

Table 6.7: Model data part 2

QSO	z_{abs}	$\bar{v}_{LSR}$ [km s^{-1}]	Ion	b_{turb} [km s^{-1}]	b_{tot} [km s^{-1}]	log N [cm^{-2}]	log U	log n(H) [cm^{-3}]	$Z/Z_{\odot}$
3C263	0.0635	-80	Si IV	27.0	27.11	12.80			
		-70	H I Lyα	27.0	29.92	16.30	-2.7	-2.84	0.04
			C II	27.0	27.26	13.00			
			Si III	27.0	27.11	12.70			
		-45	C IV	27.0	27.26	13.90			
		-38	H I Lyα	62.0	63.33	14.50			
		-15	Si IV	28.0	28.11	13.70			
		-1	H I Lyα	16.0	20.55	15.50	-2.8	-2.4	0.6
			Si II	16.0	16.18	12.40			
			C II	16.0	16.43	13.40			
			Si III	16.0	16.18	12.90			
		1	C IV	15.0	15.46	13.85			
	0.1139	-22	H I Lyα	65.0	66.27	13.50			
		-15	C IV	4.0	4.78	13.00			
		-3	H I Lyα	15.0	19.78	13.80			
		-0.5	Si III	15.0	15.20	12.15			
		5	C IV	4.0	5.47	13.07			
	0.3256	-8.3	H I Lyα	10.0	16.32	16.00	-2.3	-2.34	0.015
			N III	10.0	10.58	13.00			
			C III	10.0	10.67	13.55			
			Si III	10.0	10.29	12.20			
		3	H I Lyα	60.0	61.37	13.90			
		27.5	H I Lyα	11.0	16.95	14.00	-2.5[1]	-3.04[1]	1.5[1]
			N III	11.0	11.53	13.73			
			C III	11.0	11.61	13.50			
			Si III	11.0	11.27	12.65			
	0.4468	-40	H I Lyα	70.0	71.18	13.90			
		-15	H I Lyα	25.0	28.13	14.10			
			C III	25.0	25.28	13.24			
Ton 580	0.2026	-1	H I Lyα	21.0	24.65	13.80			
			C III	21.0	21.33	13.60			
		5	H I Lyα	100.0	100.83	13.60			
		10	Si III	21.0	21.14	12.50			
RX J2154.1-4414	0.0622	-18.3	C IV	20.0	20.34	13.90			
			Si IV	20.0	20.15	12.90			
			N V	20.0	20.29	13.00			
		12	H I Lyα	28.0	30.83	15.50	-3.2	-2.34	1.2
			Si III	28.0	28.11	12.70			
			C II	28.0	28.25	13.60			
		15.7	C IV	15.0	15.46	14.40			
			N V	15.0	15.39	13.80			
			Si IV	15.0	15.20	13.00			
		40	C IV	15.0	15.46	13.60			
			N V	15.0	15.39	13.30			
SBSS G1122+594	0.0602	-98	H I Lyα	15.0	19.78	14.35			
		-23.3	H I Lyα	10.0	16.32	15.60	-2.7[1]	-2.74[1]	0.5[1]
			C II	10.0	10.67	13.35			
			Si III	10.0	10.29	13.0			
		-5	Si IV	10.0	10.29	13.10			
		-15	C IV	20.0	20.34	13.75			
			C II	60.0	60.12	14.00			
		3	H I Lyα	5.0	13.83	14.50			
			C II	5.0	6.23	13.60			
	0.1944	-21.7	H I Lyα	20.0	23.80	15.00	-3.4[1]	-2.14[1]	1.0[1]
			C III	20.0	20.34	13.00			
			Si III	20.0	20.15	12.40			
		5.7	H I Lyα	5.0	13.83	15.00	-1.2[1]	-4.34[1]	1.0[1]
			C III	5.0	6.23	14.80			
			Si III	5.0	5.56	11.90			
		25	H I Lyα	5.0	13.83	17.50	-3.4[1]	-2.14[1]	0.01[1]
			C III	5.0	6.23	13.50			
			Si III	5.0	5.56	11.90			
	0.3124	-5	H I Lyα	70.0	70.18	14.20			
		-2.5	H I Lyα	15.0	19.78	15.50			
			C III	15.0	15.46	13.70			
PG 0838+770	0.0024	-13.5	C IV	34.0	34.20	13.70	-2.7	-2.84	0.06
			Si IV	34.0	34.09	13.10			
		-1	H I Lyα	20.0	23.80	16.80			
			Si III	20.0	20.15	13.25			
			C II	20.0	20.34	13.70			
HE 0238-1904	0.4011	-28	H I Lyα	7.0	14.68	15.20			
			C III	7.0	7.93	12.70			
		-8	H I Lyα	60.0	60.31	13.90			
		7	H I Lyα	13.0	18.31	15.00			
			C III	13.0	13.52	12.70			
	0.4243	-84	H I Lyα	37.0	39.18	13.80			
			C III	37.0	37.19	13.50			
		-78	H I Lyα	24.0	27.25	14.60			
			C III	24.0	24.29	13.10			
		-50	H I Lyα	90.0	90.92	14.00			
		-4	H I Lyα	13.0	18.31	15.00			
			C III	13.0	13.52	13.50			

Notes:
[1]) Uncertain value for some reason. See text section for explanations.
[2]) With the metallicity derived from the Si II/Si III ratio from another component in this system.

Table 6.8: Model data part 3

QSO	$z_{\rm abs}$	$\bar{v}_{\rm LSR}$ [km s^{-1}]	Ion	$b_{\rm turb}$ [km s^{-1}]	$b_{\rm tot}$ [km s^{-1}]	log N [cm^{-2}]	log U	log n(H) [cm^{-3}]	$Z/Z_{\odot}$
HS 1102+34	0.2388	-28.0	Si III	1.0	2.63	12.30			
		-22.2	H I Lyα	1.0	12.94	17.40	-2.4[1]	-3.14[1]	0.003[1]
			N III	1.0	3.59	13.50			
			C III	1.0	3.86	16.00			
			Si III	1.0	2.63	12.90			
		-12	Si IV	14.0	14.21	13.35			
		1	H I Lyα	4.0	13.51	17.50	-2.4[1]	-3.14[1]	0.003[1]
			N III	4.0	5.28	13.80			
			C III	4.0	5.47	16.80			
			Si III	4.0	4.68	12.00			
		23	H I Lyα	6.0	14.23	17.00	-2.5[1]	-3.04[1]	0.005[1]
			Si III	6.0	6.48	12.80			
			C III	6.0	7.06	16.00			
			N III	6.0	6.92	13.30			
	0.3102	69.3	H I Lyα	28.0	30.83	15.40	-2.9	-2.64	0.3
			C III	28.0	28.25	13.75			
			Si III	28.0	28.11	12.70			
PHL 1811	0.0807	10.6	H I Lyα	10.0	16.32	17.50	-4.0	-1.54	0.11
			C IV	10.0	10.67	13.55			
			Si II	10.0	10.29	13.15			
			Si III	10.0	10.29	12.40			
			Fe II	10.0	10.15	13.60			
		60	C IV	10.0	10.67	13.90			
		60	Si IV	38.0	38.08	13.10			
		62.8	H I Lyα	10.0	16.32	18.00	-2.0	-3.54	0.032
			C II	20.0	20.34	14.07			
			Si II	10.0	10.29	13.65			
			Si III	10.0	10.29	14.50			
			Fe II	10.0	10.15	13.75			
			N II	10.0	10.58	14.10			
		65	Si IV	10.0	10.29	13.10			

Notes:
[1]) Uncertain value for some reason. See text section for explanations.
[2]) With the metallicity derived from the Si II/Si III ratio from another component in this system.

Table 6.9: Associated galaxies to the sightlines I

I

QSO Sightline	z_{absorber}	Galaxy $\Delta z \lesssim 0.005$	impact parameter [arcsec]	[kpc]	z (galaxy)
HE 0439-5254	0.3084	no			
	0.3280	no			
PG 1259+593	0.0461	yes	151.16	137.55	0.0473
			356.03	323.99	0.0471
			826.40	752.02	0.0467
	0.2195	yes	1240.60	5197.28	0.2221
	0.2924	no			
HE 0226-4110	0.2071	yes	9.89	39.19	0.2065
			30.92	122.52	0.2078
			83.90	332.44	0.2077
			339.48	1345.15	0.2078
			359.10	1422.89	0.2074
			537.20	2128.60	0.2072
			642.56	2546.08	0.2068
HE 0153-4520	0.2260	no			
	0.4002	no			
3C263	0.0635	yes	50.50	63.00	0.0632
	0.1139	yes	1719.61	3817.56	0.1140
			1728.55	3837.40	0.1138
	0.3256	no			
	0.4468	no			
Ton 580	0.2026	no			
RX J2154.1-4414	0.0622	no			
SBSS G1122+594	0.0400	no			
	0.0602	yes	1441.89	1709.20	0.0604
	0.1944	no			
	0.3124	no			
PG 0838+770	0.0024	yes	134.21	6.44	0.0024
HE 0238-1904	0.4011	no			
	0.4243	no			
HS 1102+3441	0.2388	no			
	0.3102	no			
SDSS J161916	0.0964	no			
	0.1323	no			
SDSS J094331	0.3532	yes	19.49	127.70	0.3529
			19.50	127.77	0.3530
	0.3547	no			
SDSS J143511	0.2027	yes	11.45	44.45	0.2024
	0.2624	yes	20.94	103.94	0.2623
			1460.58	7249.74	0.2630
	0.3730	no			
SDSS J141910	0.1789	yes	30.28	104.24	0.1792
	0.2890	no			
	0.4256	no			

Table 6.10: Associated galaxies to the sightlines II

II

QSO Sightline	z_{absorber}	Galaxy $\Delta z \lesssim 0.005$	impact parameter [arcsec]	[kpc]	z (galaxy)
SDSS J124511	0.4494	no			
	0.6891	no			
SDSS J122035	0.1300	no			
	0.2733	yes	37.77	194.82	0.2737
SDSS J101622	0.1659	yes	16.09	51.50	0.1661
			944.46	3022.99	0.1657
	0.2524	yes	6.04	28.9	0.2520
	0.4322	no			
SDSS J113327	0.2373	yes	4.69	21.16	0.2367
			10.48	47.29	0.2364
			33.02	148.99	0.2370
SDSS J100902	0.0586	no			
	0.1141	no			
	0.2277	yes	17.41	75.53	0.2278
	0.3372	no			
	0.3558	yes	2.98	19.66	0.3556
			9.33	61.55	0.3557
SDSS J091440	0.2276	yes	123.96	537.57	0.2265
	0.2443	yes	27.44	127.29	0.2443
SDSS J092554	0.2476	yes	21.57	101.33	0.2475
			24.62	115.66	0.2467
	0.2526	no			
SDSS J111239	0.0248	yes	832.29	409.16	0.0249
			1393.06	648.84	0.0249
	0.2469	yes	13.96	65.41	0.2467
SDSS J091029	0.1423	yes	45.52	125.57	0.1427
	0.2634	yes	34.46	171.66	0.2641
	0.3747	no			
	0.4194	no			
SDSS J155304	0.0829	yes	859.79	1397.67	0.0825
	0.4754	no			
SDSS J124154	0.1471	no			
	0.2056	yes	6.24	24.56	0.2053
			988.18	3888.75	0.2054
	0.2180	yes	26.77	111.41	0.2178
SDSS J080359	0.2533	yes	19.92	95.63	0.2535
	0.4286	no			
PHL 1811	0.0807	yes	23.02	36.44	0.0808
			58.81	93.03	0.0804
			776.59	1229.28	0.0807
SDSS J115758	0.2565	yes	1228.38	5967.34	0.2565
SDSS J225738	0.3786	yes	467.87	3267.94	0.3793
SDSS J133045	0.1923	yes	28.97	106.91	0.1924
SDSS J161649	0.3210	no			
SDSS J123335	0.2220	yes	38.20	161.77	0.2221
	0.2849	no			
SDSS J004222	0.0949	yes	8.64	16.04	0.0950
SDSS J123304	0.3189	yes	6.47	38.56	0.3185
SDSS J155048	0.3126	yes	23.34	136.54	0.3125
	0.4274	no			
SDSS J040148	0.2195	yes	24.28	101.72	0.2197
	0.3238	no			
SDSS J155504	0.1892	yes	10.41	37.82	0.1893
	0.3650	no			

Table 6.11: Fitting Data for the COS Subsample I

QSO	System (redshift)	$v_{\rm LSR}$ [km s^{-1}]	Ion	Fit log N [N in cm^{-2}]	Fit b [km s^{-1}]
HE 0439-5254	0.3084	-64	H I Lyα,β	13.50±0.09	11.70±3.2
			C III	12.72±0.09	11.70±3.2
		-12	H I Lyα,β	14.41±0.03	31.20±3.7
			Si III	13.17±0.04	31.20±3.7
			C III	13.27±0.04	31.20±3.7
		31	H I Lyα	14.18±0.57	1.30±0.4
			H I Lyα	14.18±0.57	1.30±0.4
			Si III	12.21±0.57	1.30±0.4
	0.3280	-119	H I Lyα,β,γ	14.80±0.02	39.80±1.6
		-6	H I Lyα,β,γ	15.44±0.05	36.80±1.3
			C III	13.12±0.06	36.80±1.3
PG 1259+593	0.0461	-10	H I Lyα	13.66±0.13	20.20±1.3
			Si II	12.01±0.10	20.20±1.3
			Si III	12.69±0.02	20.20±1.3
			C IV	13.51±0.03	21.50±2.4
		75	H I Lyα	14.70±0.03	77.10±2.2
			C IV	14.03±0.02	28.90±1.2
	0.2195	-60	H I Lyα,β,γ	13.88±0.08	37.50±3.6
		-1	H I Lyα,β,γ	15.09±0.01	29.50±0.5
			Si III	11.96±0.08	29.50±0.5
			C III	13.31±0.02	18.90±0.08[1]
	0.2924	-13	H I Lyα,β,γ,δ	14.48±0.01	30.60±0.4
			C III	13.11±0.02	30.60±0.4
HE 0226-4110	0.2071	-25	H I Lyα,β,γ,δ	14.87±0.04	23.30±1.1
			Si III	11.45±0.79	23.30±1.1
			C III	13.14±0.09	23.30±1.1
			N V	13.16±1.24[2]	1.20±4.1[2]
		-5	H I Lyα,β,γ,δ	14.72±0.04	39.70±0.7
			Si III	12.27±0.10	39.70±0.7
			C III	13.57±0.03	39.70±0.7
			N V	12.82±0.15[2]	7.40±8.5[2]
HE 0153-4520	0.2260	-10	H I Lyα,β,γ,δ,ϵ	17.77±0.05	22.00±0.2
			Si II	12.78±0.02	22.00±0.2
			Si III	13.87±0.04	22.00±0.2
			Si IV	13.56±0.02	33.00±2.0
			C II	13.98±0.03	22.00±0.2
			C III	14.74±0.04	22.00±0.2
			N II	13.43±0.06	22.00±0.2
	0.4002	8	H I Lyα,β	14.34±0.03	56.60±3.0
			C III	12.96±0.04	56.60±3.0
		71	H I Lyα,β	14.07±0.05	19.80±1.8
			C III	12.77±0.05	19.80±1.8
Ton 580	0.2026	1	H I Lyα,β,γ	14.28±0.02	21.40±0.7
			Si III	12.30±0.05	21.40±0.7
			C III	13.36±0.04	21.40±0.7
RX J2154.1-4414	0.0622	10	H I Lyα	14.59±0.08	44.20±2.4
			C II	13.45±0.06	44.20±2.4
			Si III	12.71±0.03	44.20±2.4
			Si IV	13.04±0.04	35.30±1.3
			C IV	14.44±0.02	35.30±1.3
			N V	13.79±0.02	35.30±1.3

[1] No acceptable fit possible with fixed b values.
[2] Uncertain

Table 6.12: Fitting Data for the COS Subsample II

QSO	System (redshift)	$v_{\rm LSR}$ [km s^{-1}]	Ion	Fit log N [N in cm^{-2}]	Fit b [km s^{-1}]
3C263	0.0635	-168	H I Lyα	13.89±0.05	32.90±2.8
		-75	H I Lyα	14.65±0.10	26.90±2.1
			Si III	12.60±0.02	26.90±2.1
			Si IV	12.82±0.06	26.30±4.2
			C II	13.00±0.05	26.90±2.1
			C IV	13.78±0.04	26.30±4.2
		-6	H I Lyα	17.91±0.04	16.30±1.0
			Si II	12.25±0.04	16.30±1.0
			Si III	12.75±0.04	16.30±1.0
			Si IV	13.62±0.01	32.10±1.2
			C II	13.34±0.02	16.30±1.0
			C IV	13.94±0.04	32.10±1.2
	0.1139	-1	H I Lyα,β	13.81±0.01	28.20±0.9
			Si III	12.11±0.06	28.20±0.9
			C IV	13.20±0.06	19.60±3.7
	0.3256	-5	H I Lyα,β,γ,δ,ϵ	15.18±0.03	25.20±1.2
			Si III	12.11±0.11	25.20±1.2
			C III	13.40±0.03	25.20±1.2
		31	H I Lyα,β,γ,δ,ϵ	14.95±0.05	11.80±1.0
			Si III	12.43±0.06	11.80±1.0
			C III	13.17±0.05	11.80±1.0
			N III	13.56±0.04	11.80±1.0
	0.4468	-78	H I Lyα,β	13.53±0.06	42.60±4.8
		-8	H I Lyα,β,γ	14.20±0.02	35.60±1.5
			C III	13.24±0.01	35.60±1.5
SBSS G1122+594	0.0602	-103	H I Lyα	13.70±0.33	22.80±9.0[2]
		-29	H I Lyα	14.30±0.09	54.50±11.6[2]
			C II	13.91±0.07	54.50±11.6[2]
		-7	H I Lyα	13.07±0.53	13.40±2.6
			C II	13.45±0.13	13.40±2.6
			Si III	12.72±0.06	13.40±2.6
			Si IV	12.93±0.07	16.80±4.4
			C IV	13.38±0.07	16.80±4.4
	0.1944	3	H I Lyα,β,γ	17.90±0.03	17.10±0.3
			Si III	12.32±0.03	17.10±0.3
			C III	14.02±0.13	17.10±0.3
	0.3124	-2	H I Lyα,β,γ,δ,ϵ	14.86±0.02	32.70±1.1
			C III	13.34±0.04	32.70±1.1
PG 0838+770	0.0024	-6	H I Lyα	16.54±0.10	25.30±1.1
			C II	13.53±0.03	25.30±1.1
			Si III	13.02±0.02	25.30±1.1
			Si IV	12.76±0.05	21.50±3.4
			C IV	13.36±0.05	21.50±3.4
HE 0238-1904	0.4011	-11	H I Lyα,β,γ,δ	14.86±0.01	32.00±0.4
			C III	12.81±0.14	32.00±0.4
	0.4243	-77	H I Lyα,β,δ	14.62±0.03	37.20±1.6
			C III	13.57±0.02	37.20±1.6
		-66	H I Lyα,β,δ	13.71±0.22[2]	3.7±5.0[2]
			C III	12.55±0.22[2]	3.7±5.0[2]
		-5	H I Lyα,β,δ	14.53±0.03	27.00±1.3
			C III	13.44±0.02	27.00±1.3
HS 1102+3441	0.2388	-4	H I Lyα,β,γ,δ,ϵ	15.67±0.02	33.10±0.3
			Si III	12.67±0.06	33.10±0.3
			C III	14.02±0.03	33.10±0.3
			N III	13.70±0.05	33.10±0.3
		42	H I Lyα,β,γ,δ,ϵ	14.73±0.25	2.20±0.4
			Si III	13.59±0.65	2.20±0.4
			C III	8.04±1.41[2]	2.20±0.4
			N III	13.60±0.17	2.20±0.4
	0.3102	-7	H I Lyα,β,γ,δ	14.36±0.03	27.00±2.0
		73	H I Lyα,β,γ,δ	14.93±0.02	37.80±1.3
			Si III	12.51±0.07	37.80±1.3
			C III	13.60±0.02	37.80±1.3

[1] No acceptable fit possible with fixed b values.
[2] quite Uncertain

Table 6.13: Fitting Data for the COS Subsample III

QSO	System (redshift)	$v_{\rm LSR}$ [km s^{-1}]	Ion	Fit log N [N in cm^{-2}]	Fit b [km s^{-1}]
PHL 1811	0.0807	4	H I Lyα	17.73±0.05	13.10±2.2
			Si III	12.12±0.07	13.10±2.2
			C IV	13.55±0.06	19.50±4.1
		63	H I Lyα	17.91±0.04	14.30±1.1
			Si II	13.43±0.02	14.30±1.1
			C II	14.01±0.01	14.30±1.1
			Si III	13.41±0.06	14.30±1.1
			N II	13.92±0.02	14.30±1.1
			Fe II	13.81±0.04	14.30±1.1
			Si IV	13.23±0.02	16.90±2.2
			C IV	13.87±0.03	16.90±2.2

[1] No acceptable fit possible with fixed b values.
[2] quite Uncertain